Pablo José Gracia González

Novel fluorescence-based tools and applications for characterizing emerging pathways of α-synuclein amyloid aggregation, disaggregation and inhibition

Director/es

Cremades Casasín, Nunilo

Universidad Zaragoza
1542

Tesis Doctoral

NOVEL FLUORESCENCE-BASED TOOLS AND APPLICATIONS FOR CHARACTERIZING EMERGING PATHWAYS OF A-SYNUCLEIN AMYLOID AGGREGATION, DISAGGREGATION AND INHIBITION

Autor

Pablo José Gracia González

Director/es

Cremades Casasín, Nunilo

UNIVERSIDAD DE ZARAGOZA
Escuela de Doctorado

Programa de Doctorado en Bioquímica y Biología Molecular

2022

PhD THESIS

Novel fluorescence-based tools and applications for characterizing emerging pathways of α-synuclein amyloid aggregation, disaggregation and inhibition

Thesis presented by Pablo José Gracia González to aim for the doctor degree by the University of Zaragoza

Thesis advisor: Dra. Nunilo Cremades Casasín

June 2022, Zaragoza

Institute for Biocomputation and Physics of Complex Systems (BiFi)
Department of Biochemistry and Molecular and Cellular Biology

PhD program in Biochemistry and Molecular Biology

Dr. Nunilo Cremades Casasín, lecturer at the Department of Biochemistry and Molecular and Cellular Biology

CERTIFIES:

That the PhD thesis "Novel fluorescence-based tools and applications for characterizing emerging pathways of α-synuclein amyloid aggregation, disaggregation and inhibition" was realized by Pablo José Gracia González at the Institute for Biocomputation and Physics of Complex Systems (BiFi) of the University of Zaragoza under her supervision and that it meets, to her judgement, the required conditions to aim for the degree of doctor in Science.

Zaragoza, June 2022

Nunilo Cremades Casasin

You know the name you were given,

but you don't know your own name

"Book of evidences" (1998:9)

Foreword

Foreword

To the people that I hold dear,

As far as writing this thesis is concerned, I saved the best for last. You. 5 years of life lessons to think about now. *It's not the easiest section to write, I reckon, but likely the most rewarding,* I wrote initially. Against all odds, I've sprayed these lines quickly, in barely twenty minutes. Let's say thinking of my thesis from an emotional perspective induced a state of flow in my brain. Unconstrained and instinctive. Visceral words erupting from my bowels. Like the emerging concept of a gut-brain connection in neurobiology. Today is a radiant late spring morning and, through the window and across the Gállego valley I can see the Mallos de Riglos and the small homonymous village that seems embedded in the inmeasurable three hundred-meter tall red conglomerate rockwalls. Like the living organ of a gigantic body that took tremendous time and geological forces to form. Like my human heart inside my scientific thesis. The beating drum that makes me dedicate these lines, intentionally even if arguably poetic, to you who, in different moments and ways walked with me and made it possible to get here. Disclaimer: I know a cliché when I see one and I absolutely oppose them but I decided to go with *I do not want to mention many people personally. No need. You know who you are.* Overused or not, there it is.

I would like to use these lines to acknowledge the fact that, even though a PhD thesis is measured by its scientific output, publications and vast knowledge acquired along the way, there is a personal dimension to it without which we are not ready to survive. I feel enormously grateful to every person out there who has widened and nourished my personal dimension. Hopefully, and for some people I know it for certain, I have given you something of mine during this time, too, that has helped you or made you happy in some way. The thesis is tough, keeping the motivation levels high seems unachievable at times, frustration and existential crisis hide behind every corner and, yet, we, my dear friends, manage to make it through and contribute to scientific community with our work and findings. I myself had ups and downs when it comes to personal relationships and bonding with some of you, but you can rest assured that my heart is with you. Getting to know and sharing time with good, loving people are the best thing that can happen to us, when the planet is goind go the drain and our society rots in the landfill ir carefully created for itself. So, here is a shout out to you all who help me and other people to get over this. Thank you heartfully.

I still want to appreciate some people in particular *–oh surprise!-*. Nunilo has been my PhD advisor and the person constantly working to keep the squad motivated and believing in what we do. This is not trivial as many of you know. If you add to the equation being a mother to two children and having a few other scientific kids pipetting around, I guess you get an idea of what Nunilo has done. Thank you for truly caring about me and my work, for trusting me and treating me with respect as a young researcher. We don't get this easily these days.

Obviously I want to acknowledge the support of my family who have no relationship with the scientific research universe but always encouraged me to *find out something new about Parkinson's disease* or asked how things were going with *the fluorescence stuff*. Having somebody that will stand by your side no matter what is priceless, we shall never forget it. I love you and I deeply appreciate that you respect that what do is my call, even –*especially*- when you would have done differently. We will always be growing together, as you and I get older. Every step of the way.

To Rachel: I really just wanted your name to be here to see your smile and happy silly face when this is over and printed. I don't really have anything surprising to tell you and even less in a text that more people can read, but I still want to make a toast. To you and your ability to look after me, wait for me, accept me as I am and even help me better myself. I thank you for your lust for freedom and open-mindedness toward life which removes veils for me. To us and our companionship, to our understanding and true love, and to whatever the future holds for us. In some abstract way, you are in all those figures and graphs and, more than anything, in my heart. Not tied like the tomatoes to the cane structure in our veg patch, but near me, in sync, having fun. Seeding, planting and harvesting year after year at a nature-inspired pace. And then keeping the seeds to grow some more, with care and dedication.

To the team BiFi: here is where the lifeline sentence *you know who you are* saves me the dreadful possibility of forgetting a name. I feel lucky to have shared time with you and call me your friend. You brighten things up. We used to go out on thursdays. We had to several coffee breaks a day to catch up and gossip. We held dinner parties and hiked mountains together, camped out, went to emergencies because food allergy is sneaky. Still, life is weird and time warps sometimes in a way that makes me strangely dizzy. Why did I detach from some of you for a while? I did not stop caring about you, but yet I could not get myself together and foster our friendship as it deserved. I'm sorry about that. That's why I'm coming clean in front of you now. We are having a party, my friends, we deserve it. Besides, some of you are experts at that discipline so now that I'm living the countryside fantasy and embracing my old man habits even more, you sure will have lots to teach me.

To my friends and people who inspired me along the way: I'm going through many changes of late and all of them are related to a number of you. We share dreams, treks, trips, rivers and lakes, good cooking hours and couch potatoing times watching films, remembering childhood. We carry 15 kg on our bikes for the weekend, fix the world over beer and fancy cheese. We get involved in social movements, try to help make our neighboirhood a better place, knit a human net that can endure bad times. We get political, buy ethical food together. We talk, and talk and talk. I talk a lot sometimes. I mean, *you know who you are*, don't you? Well, thank you big time.

Six years ago I wrote a graduation speech for my master's degree in Dresden. A shoutout and my acknowledgements to Michael and Georg and the other "Schlierfs" who introduced me smoothly into lab work and the world of single molecules. Luckily enough, I'm seeing some of those old dogs this summer. This reinforces the value of human relationships and their long-lasting nature when they are meaningful. In that

speech I used a quote many of you will recognize and I figured I should not change what works fine so here we go: *home is behind, the world is ahead and there are many paths to tread*. Wisdom and courage can be found even in the smallest things and creatures, such as Peregrin Took, who sang those lines. In the search for meaning, most of us need good company. In the search for your own name, as it reads in the opening quote of this thesis, we might end up needing good company as well. So, my dearest people, let's be that company to one another every now and then along those paths we will tread. I thank you with my whole heart and wish you all the best hereforth.

Table of Contents

List of Published Articles and Patents

Pablo Gracia, David Polanco, Jorge Tarancón, Ilenia Serra, Maruan A. Bracci, Javier Oroz, Douglas V. Laurents, Inés García, Nunilo Cremades. Molecular Mechanism for the Synchronized Electrostatic Coacervation and Amyloid Co-Aggregation of A-Synuclein and Tau. In revision in *Nature Communications*, **2022**.

Aitor Franco, **Pablo Gracia**, Adai Colom, José D. Camino, José A. Fernández-Higuero, Natali Orozco, Alexander Dulebo, Leonor Saiz, Nunilo Cremades, José M. G. Vilar, Adelina Prado, Arturo Muga. All-or-none amyloid disassembly via chaperone-triggered fibril unzipping favors clearance of α-sinuclein toxic species. *Proceedings of the National Academy of Sciences of the United States of America*, **2021**, 12:1814.

José D. Camino, **Pablo Gracia**, Nunilo Cremades, The role of water in the primary nucleation of protein amyloid aggregation. *Biophysical Chemistry*, **2021**, 269:106520.

Pablo Gracia and Nunilo Cremades. Detailed Analysis of the Interaction of Molecules to Pathogenic Protein Aggregated Species by Dual-Color Time-Resolved Fluorescence Spectroscopy. *Methods in Molecular Biology*, **2021**, in press.

Jaime Santos, **Pablo Gracia**, Susanna Navarro, Samuel Peña-Diaz, Jordi Pujols, Nunilo Cremades, Irantzu Pallarès and Salvador Ventura. α-Helical peptidic scaffolds to target α-synuclein toxic species with nanomolar affinity. *Nature Communications*, **2021**, (12) 3752.

Ventura, S.; Pallarés, I.; Santos, J.; Cremades, N.; **Gracia, P** (**2020**). Inhibitors of α-synuclein aggregation and uses thereof. (Spain EP20382658). Oficina Española de Patentes y Marcas.

Pablo Gracia, José D. Camino, Laura Volpicelli-Daley, Nunilo Cremades. Multiplicity of α-Synuclein Aggregated Species and Their Possible Roles in Disease. *International Journal of Molecular Sciences*. **2020**, 21(21):8043.

José D. Camino, **Pablo Gracia**, Serene W. Chen, Jesús Sot, Igor de la Arada, Víctor Sebastián, José L. R. Arrondo, Félix M. Goñi, Christopher M. Dobson and Nunilo Cremades. The extent of protein hydration dictates the preference for heterogeneous or homogeneous nucleation generating either parallel or antiparallel β-sheet α-synuclein aggregates. *Chemical Science*, **2020,** (11) 11902-11914.

List of Abbreviations

Abbreviation	Meaning
αS, α-Syn	A-synuclein
WT	Wild-type
PD	Parkinson's disease
LB	Lewy bodies
DLB	Dementia with Lewy bodies
AD	Alzheimer's disease
ALS	Amiotrophic lateral sclerosis
HD	Huntington's disease
Aβ	Amyloid-beta peptide
PrP	Prion protein
FTD	Frontotemporal dementia
NAC	Nonamyloid β component
CTD	C-terminal domain
NTD	N-terminal domain
PHF	Paired helical filament
MTBD	Microtubule-binding domain
Pro-rich	Proline-rich
pLK	Poly-L-lysine
dsDNA	Double stranded deoxyribonucleic acid
ssDNA	Single-stranded deoxyribonucleic acid
IDP	Intrinsically disordered protein
IDR	Intrinsically disordered region
SF	Sonicated fibril
LLPS	Liquid-liquid phase separation
LSPT	Liquid-to-solid phase transition
CC	Complex coacervation
DTT	Dithiotreitol
IPTG	Isopropyl β-d-1-thiogalactopyranoside
PMSF	Phenylmethylsulfonyl fluoride
TCEP	Tris (2-carboxyethyl) phosphine
EDTA	Ethylenediaminetetraacetic acid
EGCG	Epigallocatechin-3-gallate
DMPS	Dimyristoyl phosphatidylserine
SDS	Sodium dodecyl sulfate
SUV	Small unilamellar vesicle

ThT	Thioflavin-T
ANS	8-Anilo-1-naphtalene-sulfonic acid
TEMPOL	4-Hydroxy-2,2,6,6-tetramethylpiperidine-N-oxyl
GFP	Green fluorescent protein
FITC	Fluorescein
PEG	Polyethylene glycol
TFE	2,2,2-Trifluoroethanol
AF488	AlexaFluor 488
Pyr	Pyrene
Mal	Maleimide
Deq	Dequenching
A/W	Air/water
PTFE	Polytetrafluoroethylene
DMEM	Dulbecco's modified Eagle's medium
FBS	Fetal bovine serum
BSA	Bovine serum albumine
PFA	Paraformaldehyde
ATP	Adenosine triphosphate
PBS	Phosphate buffered saline
HEPES	4-(2-Hydroxyethyl)-1-piperazineethanesulfonic acid
NaN$_3$	Sodium azide
HS-AFM	High speed-atomic force microscopy
IR	Infrared
DLS	Dynamic light scattering
NMR	Nuclear magnetic resonance
CW-EPR	Continuous wave-electron paramagnetic resonance
WF	Widefield
CF	Confocal
DIC	Differential interference contrast
BF	Brightfield
AIX	Anion exchange chromatography
SEC	Size exclusion chromatography
TRFM	Time-resolved fluorescence microscopy
FLIM	Fluorescence lifetime imaging microscopy
dcSPFS	Dual-color single-particle fluorescence spectroscopy
TCCD	Two-color coincident detection
FCS	Fluorescence correlation spectroscopy
dcFCCS	Dual-color fluorescence cross-correlation spectroscopy
spFRET	Single-particle Förster resonance energy transfer
PIE	Pulse-interleaved excitation
TCSPC	Time-correlated single photon counting

APD   Avalanche photodiode
LDH   Laser diode head

List of figures, tables and equations

Figures

Tables

Table i.1. Human diseases associated with protein misfolding and amyloid aggregation

Table 3.1. Comparison of the binding parameters of αS type B* oligomers with PSMα3 obtained by dcFCCS and dcSPFS analysis

Table 4.1. Disaggregation parameters obtained by pyrene fluorescence and AF488-dequenching for disaggregation of αS fibrils by the Hsc70 machinery

Table 4.2. Disaggregation parameters obtained by AF488-dequenching for disaggregation of different αS amyloids by the Hsc70 machinery

Equations

Eq. i.1. Fluorescence auto-correlation function

Eq. i.2. Relationship between auto-correlation amplitude, number of molecules, concentration and focal volume

Eq. i.3. 3D-diffusion model for describing auto-correlation functions

Eq. i.4. Stokes-Einstein relationship

Eq. i.5. Fluorescence cross-correlation function

Eq. i.6. Calculating the degree of ligand binding from dcFCCS experiments

Eq. i.7. Calculating the free ligand concentration from relative cross-correlation

Eq. i.8. Model of $N_{\max}$ identical and independent binding sites

Eq. i.9. Corrected fluorescence stoichiometry from single-particle fluorescence spectroscopy data

Eq. i.10. FRET efficiency and Förster radius

Eq. i.11. FRET efficiency from donor and acceptor intensities

Eq. i.12. Corrected FRET efficiency from donor and acceptor intensities

Eq. i.13. FRET efficiency from donor lifetime

Eq. 1.1. Analysis of aggregation kinetics: sigmoidal function

Eq. 1.2. FT-IR spectra global analysis

Abstract

Abstract

Amyloid aggregation is typically referred to as a protein misfolding process involving the transition from a functional, soluble protein into oligomeric intermediates and, eventually, insoluble fibrils with a hallmark cross-β structure. A number of neurodegenerative diseases are associated to this process, including Parkinson's disease (PD), which is characterized by intracellular deposits rich in α-synuclein (αS) in the form of amyloid aggregates, which are referred to as Lewy bodies (LB) or neurites. αS is an intrinsically disordered 140-aminoacid protein widely expressed throughout the body, particularly in the central nervous system. Its amyloid aggregation is also associated with other synucleinopathies such as dementia with Lewy bodies (DLB), multiple system atrophy (MSA) or Alzheimer's disease (AD). While the factors triggering the amyloid self-assembly of αS *in vivo* are still obscure, *in vitro* studies are able to reproduce the aggregation, typically using hydrophobic/hydrophilic interfaces to trigger the first protein-protein contacts, a process termed primary nucleation. The amyloid structures resulting from this (heterogeneous) nucleation show a parallel inter-molecular arrangement. In this work, we were able to induce and analyze the amyloid self-assembly of αS in the absence of interfaces in the bulk of the solution (homogeneous nucleation) under limited hydration conditions. By using pyrene fluorescence spectroscopy we proved that, via this new type of nucleation, the aggregates adopt an antiparallel topology. Moreover, we have observed that this type of nucleation could be favorable in the interior of αS condensates generated by liquid-liquid phase separation (LLPS). By using a combination of biophysical techniques, we quantitatively interrogated the ability of αS and the protein Tau to undergo LLPS. Among these techniques, we used fluorescence lifetime imaging microscopy (FLIM) down to the single-coacervate level, to resolve their maturation without ambiguity, owing to the exquisite temporal and spatial resolution of FLIM. We found that, indeed, αS and Tau form mixed biomolecular condensates by complex elecotrostatic coacervation and, over time, they form amyloid heteroaggregates through liquid-to-solid phase transition (LSPT) in the interior of the condensates. Interestingly, we proved that the valence and occupancy of the heterotypic interactions, and not the polypeptide dynamics, are the main factor governing LSPT. Our results help establishing a relevant scenario for the co-aggregation of both proteins which could explain their joint presence in both PD and AD. Besides, we have contributed to the LLPS-LSPT field by providing a thourough, quantitative description of αS/polycation systems with advanced and complementary techniques and by looking at single coacervates. This could serve as a framework to be used in a wide array of biomolecular condensates, and of particular interest for characterizing the link between these and amyloid aggregation.

Finding molecules with therapeutic or diagnosic potential in neurodegenerative disorders is of utter importance. However, the complexity and heterogeneity of the amyloid conformational landscape, makes amyloid aggregation a tremendously challenging target for typical drug screens based in molecular interaction assays. Here,

we established an experimental strategy which combines dual-color fluorescence correlation spectroscopy and single-particle fluorescence spectroscopy (dcFCCS/dcSPFS) to investigate the binding of small molecules to amyloid species of αS with single-particle resolution and regardless of molecular heterogeneity. By observing binding events individually, we gained direct access to the binding specificity, affinity and stoichiometry of several small amyloid inhibitory peptides, including a human peptidic molecule. We demonstrated its molecular mechanism of action and disentangled the minimum physico-chemical properties behind the binding properties, thus aiding in the rational design of other peptide drug candidates. dcFCCS/dcSPFS could be extended to other multi-ligand/multimeric receptor interaction scenarios and serve as a platform for finding new drugs and amyloid-specific diagnostic probes.

Besides inhibiting the self-assembly process, the disaggregation of amyloid fibrils can be a tool for fighting neurodegeneration. In the cell, such task is performed on αS fibrils by an evolutionary refined chaperone machinery termed the human disaggregase. However, the exact mechanism by which this proteic complex processes the fibrils as well as what is the relationship between aggregate toxicity, structure and disaggregase activity remains under debate. A major challenge is to obtain reliable kinetic data of the disassembly reaction due to artifacts related to the most commonly used amyloid probe, thioflavin-T (ThT). In our work, we have applied pyrene fluorescence together with fluorescence dequenching to solving this problem. We demonstrated an all-or-none disassembly mechanism, where a fibril disassembles entirely into soluble monomers by an unzipping mechanism. Our kinetic data enabled to quantitatively model the disaggregation mechanism on different amyloid assemblies of αS. Our results revealed that the chaperone machinery has likely evolved to tackle small cytotoxic aggregates specifically.

In summary, we have implemented new fluorescence-based tools and applications, including time-resolved and single-particle dual-color fluorescence techniques, to the detailed investigation of amyloid aggregation, phase separation, inhibition and disaggregation of αS. Collectively, our results help to understand key questions of αS amyloid aggregation and potential therapeutic strategies against synucleinopathies. In addition, the experimental approaches presented in this thesis can be also easily extended to understand and tackle other amyloid systems, representing important methodological tools in the fields of amyloid aggregation and neurodegeneration.

Resumen

Resumen

Habitualmente se denomina agregación amiloide a aquel proceso de malplegamiento proteico que comprende la transición de una proteína soluble y funcional a especies oligoméricas intermedias y, en última instancia, fibras insolubles con una estructura característica llamada de lámina β cruzada. Varias enfermedades neurodegenerativas se encuentran asociadas a este proceso, entre las que se encuentra la enfermedad de Párkinson (PD en inglés). Esta se caracteriza por unos depósitos intracelulares, denominados cuerpos o neuritas de Lewy, ricos en α-sinucleína (αS) en forma de agregados amiloides. αS es una proteína intrínsecamente desordenada de 140 aminoácidos que se expresa ampliamente en el cuerpo humano, especialmente en el sistema nervioso central. Su agregación amiloide también está vinculada con otras sinucleinopatías como demencia con cuerpos de Lewy, atrofia sistémica múltiple y enfermedad de Alzheimer (AD en inglés). A pesar de que los factores que provocan el autoensamblado amiloide de αS *in vivo* son desconocidos, algunos estudios *in vitro* son capaces de reproducir tal agregación. Habitualmente, lo hacen mediante el uso de interfases de carácter hidrofóbico/hidrofílico que catalizan los primeros contactos entre proteínas en un proceso llamado nucleación primaria. Las estructuras amiloides formadas mediante este mecanismo de nucleación heterogénea poseen una disposición inter-molecular paralela. En este trabajo, hemos logrado inducir y analizar el autoensamblado amiloide de αS en ausencia de interfases bajo condiciones de hidratación limitada. La agregación ocurre en el seno de la disolución mediante una nucleación, por tanto, homogénea. Mediante el empleo de la espectroscopia de fluorescencia de pireno hemos demostrado que, siguiendo este nuevo mecanismo de nucleación, los agregados adoptan una topología antiparalela. Además, hemos observado que este tipo de nucleación podría estar favorecida en el interior de condensados biomoleculares de αS generados a través de separación de fases líquido-líquido (LLPS en inglés), donde la hidratación de la proteína se ve reducida. Aplicando una combinación de técnicas biofísicas, hemos estudiado cuantitativamente la capacidad de αS y de la proteína Tau para sufrir LLPS. Entre estas técnicas, hemos empleado microscopía de tiempo de vida fluorescente (FLIM en inglés), al nivel de condensados individuales, para demostrar la maduración en el tiempo de estos, gracias a la exquisita resolución temporal y espacial de FLIM. Hemos descubierto que αS y Tau sí forman condensados biomoleculares mixtos y que, con el tiempo, forman heteroagregados amiloides en el interior de estos coacervados mediante la denominada transición de fases líquido-solido (LSPT en inglés). Cabe destacar que hemos esclarecido que el principal factor que regula esta LSPT es la valencia y ocupación de las interacciones heterotípicas, y no la dinámica de las cadenas polipeptídicas como se ha descrito frecuentemente para otros sistemas. Nuestros resultados ayudan a establecer un escenario relevante para la co-agregación de ambas proteínas que podría explicar el hecho de que se observen, conjuntamente, tanto en PD como en AD. Además, hemos contribuido al campo de LLPS-LSPT proporcionando una descripción detallada y cuantitativa de sistemas αS/policatión con técnicas avanzadas y complementarias, incluyendo el estudio de

coacervados individuales. Esto podría servir como base para el estudio de una amplia variedad de condensados biomoleculares y de especial interés para caracterizar la relación entre estos y la agregación amiloide.

Por otra parte, encontrar moléculas con potencial terapéutico o diagnóstico en enfermedades neurodegenerativas es de una importancia extrema. Sin embargo, la complejidad y heterogeneidad en el paisaje conformacional de la agregación amiloide hacen de esta una diana destacablemente complicada para los estudios habituales de cribado de fármacos basados en ensayos de interacción molecular. En esta tesis hemos establecido una estrategia experimental que combina la espectroscopia de correlación cruzada de fluorescencia y la espectroscopia de fluorescencia de partícula individual de dos colores (dcFCCS/dcSPFS en inglés), y la hemos empleado para investigar la unión de pequeñas moléculas a especies amiloides neurotóxicas de αS con resolución de partícula individual y con independencia de las heterogeneidades moleculares del sistema de estudio. Gracias a la observación de los eventos de interacción de uno en uno, hemos resuelto de manera directa la especificidad, afinidad y estequiometría de unión de varios pequeños péptidos inhibidores de la agregación amiloide de αS, entre los cuales se incluye un péptido humano. Hemos descrito en detalle su mecanismo molecular de actuación y desentrañado las propiedades físico-químicas que respaldan la interacción, contribuyendo al diseño racional de otros péptidos candidatos a fármaco. El uso dcFCCS/dcSPFS puede ampliarse a otras situaciones de interacción multi-ligando/receptor multimérico y convertirse en una plataforma experimental para el descubrimiento de nuevos fármacos y marcadores diagnósticos específicos de amiloide.

Por último, además de inhibir el proceso de autoensamblado, la desagregación de fibras amiloides puede ser una herramienta para combatir la neurodegeneración. Dentro de las células, esta tarea es llevada a cabo sobre fibras de αS por una maquinaria especializada de chaperonas conocida como la desagregasa humana. Sin embargo, el mecanismo preciso por el cual este complejo proteico procesa las fibras, así como el posible vínculo entre la toxicidad y estructura de un agregado y la actividad desagregasa sobre el mismo es un tema todavía bajo intenso debate. Uno de los principales retos es la obtención de datos cinéticos fiables y de calidad de la reacción de desensamblado, debido a artefactos de la técnica más extensamente usada: la fluorescencia de la sonda tioflavina-T. En nuestro trabajo hemos aplicado la fluorescencia de pireno junto con la desextinción de fluorescencia para afrontar este problema. Hemos logrado probar un mecanismo de desagregación de todo o nada, por el cual cada fibra se desensambla y libera monómeros solubles de αS mediante un mecanismo de cremallera. Nuestros datos cinéticos han permitido el modelado cuantitativo del mecanismo de desagregación sobre diferentes estructuras amiloides de αS. Estos resultados han revelado que, probablemente, la desagregasa humana ha evolucionado para actuar específicamente sobre agregados pequeños y citotóxicos.

En resumen, hemos implementado nuevas herramientas y aplicaciones de fluorescencia, incluyendo técnicas de fluorescencia resueltas en el tiempo y de partícula única de dos colores, para el estudio detallado de la agregación amiloide, transición de fases, inhibición y desagregación de αS. En conjunto, nuestros resultados contribuyen a responder preguntas clave de la agregación amiloide de αS y de la búsqueda de estrategias terapéuticas contra las sinucleinopatías. Además, los enfoques experimentales presentados en esta tesis se pueden aplicar para comprender y actuar sobre otros sistemas amiloides, siendo por tanto herramientas metodológicas relevantes en el campo de la agregación amiloide y la neurodegeneración.

General Introduction

General Introduction

1. Amyloid aggregation

In this introductory section we discuss fundamental aspects such as the basic description of what amyloid assemblies are, how they are connected to disease and what is known about the self-assembly processes that govern the energy landscape of aggregation as well as the end-point of such reaction: the amyloid aggregates. Besides, we focus on the particular case of the protein α-Synuclein (αS).

1.1. The role of amyloid aggregation in neurodegeneration

A number of neurodegenerative disorders are characterized by protein inclusions that are formed by the conformational conversion of normally soluble proteins or peptides into oligomeric intermediates and eventually amyloid aggregates and fibrils by a process referred to as amyloid aggregation [1, 2]. In each neurodegenerative disease, the distribution and composition of protein aggregates are different [3]. In Alzheimer's disease (AD), for instance, there are 2 types of protein deposits. Amyloid plaques are deposited extracellularly in the brain parenchyma and around the cerebral vessel walls, and their main component is a 40- to 42-residue peptide termed β-amyloid peptide (Aβ) [4]. Neurofibrillary tangles are located in the cytoplasm of degenerating neurons and are composed of aggregates of hyperphosphorylated Tau protein [5]. In patients with Parkinson's Disease (PD), Lewy bodies are observed in the cytoplasm of neurons of the *substantia nigra* in the brain. The major constituent of these aggregates is a protein named α-Synuclein (αS) [6]. In patients with Huntington disease, intranuclear deposits of a polyglutamine-rich version of huntingtin protein are a typical feature of the brain [7]. Patients with amyotrophic lateral sclerosis (ALS) have aggregates mainly composed of superoxide dismutase (SOD) in cell bodies and axons of motor neurons [8]. Finally, the brains of humans and animals with diverse forms of transmissible spongiform encephalopathy are characterized by accumulation of protease-resistant aggregates of the prion protein (PrP) [9]. A summary of human diseases associated with protein misfolding and amyloid aggregation [10, 11] is shown in **Table i.1** [12]**.**

Disease	Precursor Protein	Polypeptide Length (n° of Residues)	Structural Organization of Precursor
Neurodegenerative Diseases			
Alzheimer's disease	Amyloid-β variants	37–44	IDP
Spongiform encephalopathies	Prion protein or its fragments	208	IDP and α-helical
Parkinson's disease	α-synuclein	140	IDP

Frontotemporal dementia with Parkinsonism	Tau	352–441	IDP
Amyotrophic lateral sclerosis	Superoxide dismutase 1	153	β-sheet
Huntington's disease	Huntingtin with polyQ expansion	3144	Mostly IDP
Neuroferritinopathy	Ferritin	175 or 183	α-helical
Familial British dementia	ABri	34	IDP
Familial Danish dementia	ADan	34	IDP
Familial amyloid polyneuropathy	Transthyretin variants	127	β-sheet
Non-Neuropathic Systemic Amyloidosis			
Amyloid light chain amyloidosis	Immunoglobulin light chains or its fragments	~90	β-sheet
Amyloid heavy chain amyloidosis	Immunoglobulin heavy chains or its fragments	~220	β-sheet
Amyloid A amyloidosis	Serum amyloid A protein fragments	45–104	α-helical and unknown fold
Familial Mediterranean fever	Serum amyloid A protein fragments	45–104	α-helical and unknown fold
Apolipoprotein A1 amyloidosis	Apo A-1 fragments	80–93	IDP
Senile systemic amyloidosis	Wild-type transthyretin	127	β-sheet
Familial amyloid cardiomyopathy	Transthyretin variants	127	β-sheet
Haemodialysis-related amyloidosis	β2-microglobulin	99	β-sheet

Lysozyme amyloidosis	Lysozyme variants	130	α-helical and β-sheet
Finnish hereditary amyloidosis	Fragments of gelsolin variants	53 or 71	IDP
Non-Neuropathic Localized Amyloidosis			
Type II diabetes	Islet amyloid polypeptide	37	IDP
Injection-localized amyloidosis	Insulin	21 and 30	α-helical
Gelatinous drop-like corneal dystrophy	Lactoferrin	691	α-helical and β-sheet
Medullary carcinoma of the thyroid	Calcitonin	32	IDP
Localized cutaneous amyloidosis	Galectin 7	136	β-sheet
Atrial amyloidosis	Atrial natriuretic factor	28	IDP
Cataracts	γ-crystallins	variable	β-sheet

Table. i.1. Human diseases associated with protein misfolding and amyloid aggregation. Adapted from [12].

Amyloid aggregates are proteic self-assembled structures, which typically show a fibrillar morphology. They are composed primarily of one type of protein or peptide, although amyloid structures containing more than one protein (hetero-amyloids) have been recently reported [13–15], as discussed further in chapter 2 of this thesis. Upon amyloid aggregation, the protein adopts a hallmark structural architecture, termed the cross-β structure [16–18]. The molecular mechanisms by which proteins adopt this structure is of unquestionable interest, and much progress has been recently made through the development of new experimental approaches, and by combining experimental and theoretical methods using the formalism of chemical kinetics [19–21]. However, there are still important questions that remain to be clarified such as how and why a specific protein starts to self-assemble, how the acquisition of the amyloid structure occurs, and how this process induces toxicity.

The pathogenic effect of amyloid aggregation has been linked with mainly two general factors. On the one hand, a loss of function of the proteins that aggregate, and a gain of toxic function through the generation and accumulation of aggregated forms of the protein [2, 22]. Besides, these assemblies are able in some cases to spread within cells and propagate toxicity from cell to cell [23, 24]. There is continuous discussion as to which protein aggregated species are more damaging to cells, either the fibrillar-end products of the aggregation reaction or the soluble oligomeric intermediate species [20, 22, 25, 26].

Both species of multiple proteins and peptides can induce toxicity by similar mechanisms including membrane perturbation, calcium and metal ion imbalance, oxidative stress, and overload of chaperone and ubiquitin proteasome systems [27–31]. Together, this suggests generic aggregation and toxicity pathways between different amyloidogenic proteins and peptides [1, 22], as well as possible common mechanisms of toxicity between oligomeric and fibrillar species.

1.2 The amyloid aggregation of α-Synuclein (αS) in neurodegeneration

αS is an intrinsically disordered protein of 140 amino acids, widely expressed throughout the body, particularly in the central nervous system, including the dopaminergic neurons of the *substantia nigra pars compacta* (SNc), excitatory neurons in the cortex, amygdala and olfactory bulb and inhibitory neurons in the *globus pallidus*, subthalamic nucleus and *substantia nigra pars reticulata* (SNr) [32]. Its primary sequence, encoded in the SNCA gene, can be divided into three regions. The N-terminal domain (residues 1–60), which has a predisposition to fold into amphipathic α–helices, particularly upon interaction with lipid membranes [33, 34]. The central hydrophobic region (residues 61–95), named nonamyloid β component (NAC) region (due to historical reasons to differentiate this amyloid-prone region in αS from the amyloid β peptide involved in Alzheimer's disease [35, 36], which has a predisposition to fold into either α-helix conformation upon interaction with highly negatively charged lipid membranes [37, 38], or β-sheet structure upon self-assembly [39]. Finally, the proline-rich and highly negatively charged (at neutral pH) C-terminal region (residues 96–140), with no structure-forming propensity.

Controversy is served as to what would be the native conformation of the protein at physiological conditions [40]. Currently, the most accepted paradigm is that the protein remains unfolded (as an intrinsically disordered protein, IDP) [41, 42] in the cytosol, although with some tertiary contacts between the C-terminal and the NAC and N-terminal regions [43, 44], or partially folded into α-helix for the approximately 1/3 fraction of αS [45] that is bound to membranes [46]. Indeed, it has been proposed that the protein forms α-helix-rich oligomers on the cellular membranes and that these oligomeric forms would be the functional state of the protein fuor its role in synaptic vesicle trafficking and neurotransmission release [45]. However, under pathological conditions, αS self-assembles into amyloid aggregates, with the typical cross-β structure, which can ultimately form amyloid-rich inclusions.

The presence of these amyloid inclusions is the histopathological signature of a number of neurodegenerative disorders collectively referred to as synucleinopathies [47, 48]. The three most prevalent synucleinopathies include Parkinson's disease (PD), dementia with Lewy bodies (DLB) and multiple system atrophy (MSA). PD is characterized by motor symptoms such as tremor at rest, slowness of movement, and balance problems and is the second most common form of neurodegeneration following Alzheimer´s disease (AD). The typical motor symptoms of the disease are a consequence of the degeneration of dopaminergic neurons in the SNc in the basal ganglia of the brain resulting in bradykinesia and rigidity [49]. αS inclusions inside neurons are referred to as Lewy bodies (LBs) and Lewy neurites (LNs) in PD and DLB. In MSA, however, αS accumulates

primarily into inclusions found in the cytosol of oligodendrocytes, called glial cytoplasmatic inclusions, although a small percentage of neurons can also have αS inclusions [47]. The aggregation of αS into amyloid aggregates is thought to play a key role in the initiation and spreading of these diseases, although controversy remains whether LBs or smaller polymorphs of aggregates contribute to neuronal defects and toxicity. αS is not only pathologically but also genetically linked to disease. This dual link indicates a central role for αS in the pathogenesis of both the inherited and sporadic forms of these diseases. Indeed, evidence suggests a mechanistic link between even slightly higher-than-normal levels of αS and the formation of αS amyloid aggregates within neurons and the induction of neurodegeneration, likely through the generation and accumulation of toxic, aggregated αS species during the process of amyloid self-assembly [50, 51].

Even though wild-type (WT) αS is responsible for the sporadic forms PD [6], which are the most frequent forms of the disease (around 85 % of the cases), there are variants of the protein that have been linked to disease. In particular, mutations and post-translational modifications (PTMs) seem to play a role in the conversion of the monomeric protein into amyloid aggregates, although their exact link to disease remains largely obscure [52, 53]. The N-terminal acetylation of αS is the major physiological form of the protein [42], even if this PTM does not seem to affect the biophysical properties the protein [42], while a phosphorylation in the serine residue 129 (S129-P) has been linked to disease. Regarding mutations in the SNCA gene, A18T, A29S, and A30P are associated with a relatively typical PD phenotype and mild clinical manifestations [54, 55], but patients with E46K, H50Q, G51D, A53E, or A53T have a severe and rather rapidly progressing clinical phenotype, involving cognitive impairment, psychiatric disturbance, hallucination, autonomic dysfunction, myoclonus, and epilepsy with pyramidal signs [56–61]. Among these, G51D and A53T are especially notable for early onset and severe symptoms. SNCA gene duplication, triplication and polymorphisms also cause PD [62–64]. Autosomal dominant inherited mutations in genes including LRRK2, GBA and VPS35 also cause late onset PD with symptoms similar to sporadic PD, while autosomal recessive mutations in genes including PINK1, PRKN and PARK-7, for example, cause early onset forms of parkinsonism [65, 66]. LRRK2 and GBA mutations can increase the formation of αS inclusions [67–69]. Much research has been carried out on these mutations as they provide valuable tools to understand the pathogenesis of PD, particularly its hereditary forms. However, the precise mechanisms underlying the clinical phenotypes remain elusive.

1.3. Nucleation mechanisms and inter-molecular architecture of αS amyloid aggregates

The transition of a protein from its functional, typically monomeric form to the amyloid state is a highly complex process (see **Fig. i.1A**) that depends on both intrinsic features of the particular protein and the environmental conditions. Early analysis of *in vitro* kinetics of formation of amyloid fibrils show that the overall process typically includes a long nucleation lag phase, where oligomeric species and a sufficient number of fibril nuclei are formed, followed by an exponential phase, reflecting the faster nuclei-dependent growth through monomer addition, generating protofilaments and

eventually mature amyloid fibrils, as compared to the much slower formation of *de novo* aggregates from monomeric protein. This type of mechanism has been described by a nucleation-polymerization model [70]. More complex models have been later developed for analyzing the amyloid aggregation mechanism of certain amyloidogenic proteins. One such model is the so-termed nucleation-conversion-polymerization model which includes a structural conversion of the early formed oligomers into β sheet-enriched, elongation-competent oligomers [71, 72] as illustrated in **Fig. i.1B**. In addition to primary nucleation and template-based aggregate elongation, other secondary processes have been shown to be important in the overall amyloid aggregation process, insofar they give raise to different αS self-assembled species, including fibril fragmentation, disaggregation and fibril-catalyzed secondary nucleation [20, 73–75].
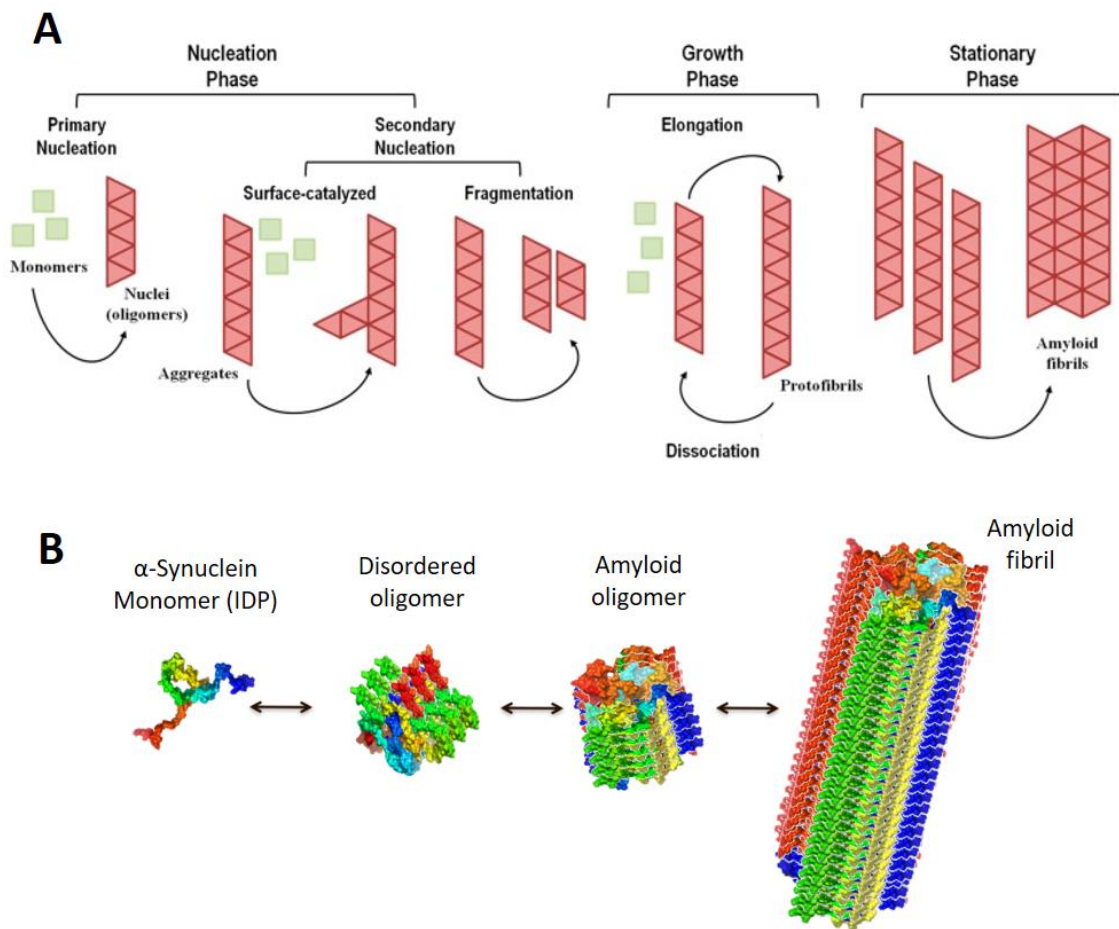
Fig. i.1. **The complex landscape of amyloid aggregation**. **A**) Representative general model for amyloid fibril formation by nucleation-dependent mechanisms (including primary and secondary nucleation) and nucleation-independent mechanisms (absence of nucleation). The stationary phase involves the assembly of protofibrils into mature amyloid fibrils with different morphological structures and a high level of polymorphism. Adapted from [76]. B) Schematic representation of the process of amyloid formation according to a nucleation-conversion-polymerization model. This model has been proposed for the process of αS aggregation when triggered at conditions of heterogeneous primary nucleation [20]: the initially formed oligomers slowly convert into partially formed β-sheet oligomers that further elongate and generate fully-formed mature fibrils. Note that this is a very simplified linear representation of the real funnel-like conformational landscape of the process.

In vivo, exposure of neurons to fibrils generated from recombinant αS induces endogenously expressed αS to form inclusions that closely resemble those found in PD brains, allowing researchers to model inclusion formation, associated impact on neuronal function and research targets that could prevent aggregation [77]. When looking for the reason why monomeric αS converts into amyloid fibrils which, eventually, cause neural cell damage, the hypothesis that high levels of αS contribute to its propensity to fibrillize is supported by multiple genomic studies [62, 66, 78]. Also, impaired mitochondrial function and its associated oxidative stress has been proposed to have a key role in inducing *in vivo* amyloid aggregation and PD-compatible symptoms [79–81]. Finally, hindering the ability of αS to interact with cellular membranes has also been propounded as a possible *in vivo* aggregation mechanism [82]. In spite of the available data and constant scientific efforts, no agreement has been reached as whether the cause for αS pathology dissemination is the templated seeding of αS presently discussed or epiphenomenal causes. Therefore, further studies investigating external factors that might initiate *in vivo* αS aggregation to disease phenotypes remain crucial.

At typical diluted *in vitro* conditions, *i. e.* with typical buffers at neutral pH and physiological ionic strength and temperature, αS is not observed to aggregate for more than 7–10 days of incubation without sample agitation at concentration as high as 500 µM [83, 84]. Typically, aggregation of αS *in vitro* is triggered by subjecting the protein solution to agitation, either shaking or stirring [85], upon which the protein starts to aggregate within 1–3 days, depending on protein concentration. Under those conditions, nucleation initiates at the air/water interface, in the absence of any other hydrophobic/hydrophilic interface such as the hydrophobic coatings of sample containers or stirring bars [74, 84, 86]. When nucleation initiates at an active interface, it is referred to as heterogeneous nucleation [86, 87]. Given the propensity of the N-terminal region of αS to acquire amphipathic α-helices, the protein preferentially partitions or adsorbs at hydrophobic/hydrophilic interfaces, in order to simultaneously maximize the hydrophilic interactions in the aqueous environment and the hydrophobic force at the hydrophobic surface [88]. At the interface, the protein initiates its self-assembly (under high hydration conditions), likely as a result of the local increase in protein concentration and the selection of nucleation-efficient conformations upon adsorption. Interestingly, this is not a unique property of αS, since hydrophobic/hydrophilic interfaces have been found to be critical for the aggregation of many other amyloidogenic proteins and peptides, including IDPs such as Aβ peptide [89], and folded proteins such as insulin [90].

When αS aggregation is triggered by heterogeneous primary nucleation, the pre-nucleus of amyloid structure formed at a given hydrophobic/hydrophilic interface would inevitably adopt a parallel intermolecular β-sheet arrangement given the restrictions in the disposition and orientation of the polypeptide chains anchored through their N-terminal amphipathic region to the interface. We hypothesized that aggregation could be triggered by homogeneous nucleation *in vitro, i. e.,* in the bulk of the solution without any interface. In this scenario, there is no restriction in the orientation of the protein molecules in the bulk, and the antiparallel orientation of the β-sheets would be preferred

over the parallel arrangement, as the stability of the hydrogen bonds in such configuration is generally higher [91, 92].

Indeed, our group has recently observed, mainly in the doctoral work of Dr. José Daniel Camino, that αS can form amyloid aggregates without the need of a nucleation-active surface through homogeneous nucleation under limited hydration conditions (see chapter 1). When the protein undergoes this process, there is a preference for remarkably different amyloid polymorphs. Specifically, there is a preference for an antiparallel β-sheet arrangement, in contrast to the parallel β-sheet architecture adopted when heterogeneous nucleation dominates [84]. The formation of amyloid aggregates rich in intermolecular antiparallel β-sheets under limited hydration conditions has been also reported for the neurotoxic type B* oligomers formed upon lyophilization [93] as well as other amyloidogenic peptides, and a multitude of a priori non-amyloidogenic proteins belonging to different structural classes, as well as disordered peptides such as poly-L-lysine [87, 92, 94, 95].

Water activity and, therefore, the protein hydration state have been recently demonstrated to be a key determinant not only for tuning αS self-assembly (maintaining αS monomeric and preventing it from misfolding and self-assembling under highly hydration conditions), but also for dictating the preference for the type of primary nucleation (heterogeneous -vs- homogeneous) and the type of structural amyloid polymorph generated (parallel -vs- antiparallel β-sheet structure) [84]. Conditions of very poor water activity such as those encountered inside protein-rich droplets, generated by liquid-liquid phase separation (LLPS, *see* **Fig. i.2**), have been reported to be particularly efficient in triggering αS amyloid aggregation both *in vitro* and *in vivo* [84, 96–99]. It would be of great interest, therefore, to characterize the nucleation mechanism behind LLPS-mediated αS amyloid aggregation as well as the molecular features of such aggregates. Besides, bringing *in vitro* LLPS conditions towards more physiological scenarios would also be a remarkable advance in the field.

Considering this background, we postulate that the formation of antiparallel β-sheet amyloid aggregates might be a general process of the polypeptide chains that is triggered under limited hydration conditions by a mechanism of homogeneous primary nucleation similar to that we have described recently for αS [84] (see chapter 1 of this thesis). Depending on the microenvironment that αS encounters in the cell, therefore, alternative amyloid aggregation mechanisms and pathways would be triggered, leading to the formation of remarkably different amyloid polymorphs.

2. Phase transitions in intrinsically disordered proteins (IDPs) and their link to neurodegeneration

One of the defining traits of globular proteins is their ability to undergo a spontaneous intramolecular phase transition, commonly referred to as folding, by which they acquire their native structure. However, IDPs also experience phase transitions, be it intramolecular such as a folding-upon-binding, or intermolecular. Among the latter, we find a diverse set of macrosystemic phenomena taking place in protein solutions, such as new phase nucleation in bulk, on the interface, and on the impurities, protein

crystallization, protein aggregation, the formation of amyloid fibrils, and intermolecular liquid–liquid or liquid–gel phase transitions associated with the biogenesis of membraneless organelles in the cells.

2.1. Liquid-liquid phase separation (LLPS) and biomolecular condensates

LLPS is a thermodynamics-driven process in which a homogeneous fluid made of two or more components separates into two distinct phases, a condensed phase (enriched in at least one component) and a dilute phase, both with liquid-like properties but with different compositions [100], as depicted in **Fig. i.2**. The condensed phase initially acquires a spherical droplet shape, which is governed by thermodynamics (**Fig. i.2B**). These droplets, also referred to as biomolecular condensates or protein droplets when the LLPS process involves proteins, have a dynamic structure and so they can fuse, divide or disappear, as LLPS is a totally reversible spontaneous process [101]. The absence of a membrane that delimitates the droplet with its exterior and its liquid-like nature allow for the free exchange of molecules within the droplet and between the droplet and the dilute phase.
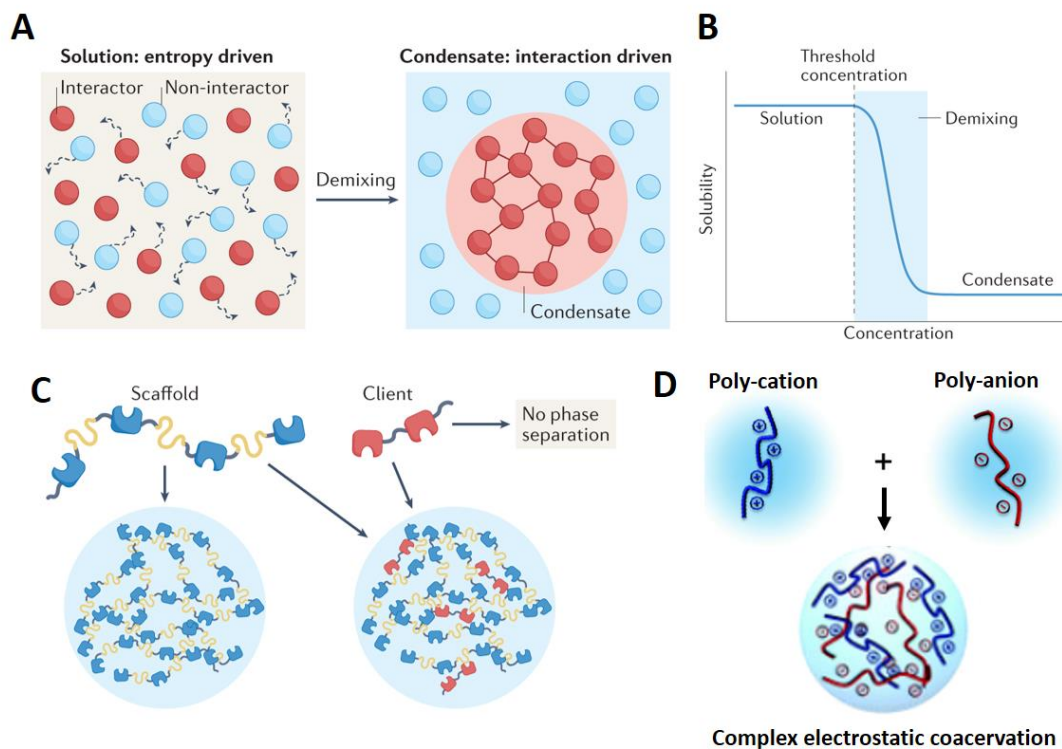
Fig. i.2. **Basic principles of liquid–liquid phase separation and biomolecular condensates.** **A)** Solution behavior of molecules -vs- liquid-liquid phase separation (demixing) and condensate formation and the basic thermodynamic forces governing each process. **B)** Solubility diagram depicting the thermodynamic phase behavior of molecules in LLPS. **C)** Scaffolding vs client molecules: scaffold molecules undergo LLPS effectively while client molecules merely partition into preformed condensates formed by scaffolding molecules. Panels **A-C**) are adapted from [123]. **D)** Electrostatic complex coacervation of generic poly-cation and poly-anions. Adapted from [124].

Biomolecular condensates have been increasingly identified as key regulators of biological processes in the cell, as concluded from *in vitro* and *in vivo* studies [102]. For instance, they act as catalysts of biochemical processes by concentrating enzymes and/or substrates in defined foci [103–106] or modulate enzymatic activity by enzyme sequestration [107, 108], or interfering with factors that affect a given biochemical cellular process [109, 110]. At the molecular level, liquid droplets have also been reported to regulate ribosome biogenesis [111, 112]) and modulate the folding state of proteins and RNA [112–115]. Biomolecular condensates also play a role in synaptic transmission [116], DNA replication [117], autophagy [118, 119] or even mediate protein homeostasis and the heat-shock response [120]. Finally, they are widely acknowledged as cell organizers, since the seggregation of the molecules forming the dense phase of the condensate acts as a compartimentalization mechanism, yet membrane-less [121, 122].

Typically, LLPS has been studied *in vitro* for mixtures of two or more components such as synthetic polymers, proteins, salts, nucleic acids or polysaccharides More recently, growing experimental evidence indicates that this process can also occur inside cells giving rise to what has been referred to as membraneless organelles [100, 125]. These are formed mostly by proteins, either specific multivalent modular folded proteins or particular types of IDPs, and, in some cases, also by RNA/DNA molecules [100, 125, 126]. Studies on physiological biomolecular condensates show a high occurrence of intrinsically disordered proteins in their composition [127]. This could be explained considering the fact that an IDP, owing to the absence of a general structure, can act as a scaffold for multiple interactions with other biomolecules such as RNA [128]. The formation of these phase-separated cellular compartments, as well as the content and relative proportion of these condensates, is tightly regulated by the cell [126], in agreement with the relevant role these membrane-less organelles have in the context of the aforementioned important cellular functions.

2.1.1. Electrostatic coacervation in LLPS

The interactions leading to the formation of liquid protein droplets are transient interactions between the different components of the condensate and can be of different nature. The most common interaction modes occurring inside biomolecular condensates are charge-charge (electrostatic) interactions, π-π stacking, cation-π interactions, hydrogen bonds and hydrophobic interactions, and typically several modes of interaction are simultaneously prevalent in multicomponent biomolecular condensates [129]. When the protein droplets are formed primarily by electrostatic interactions they are referred to as electrostatic coacervates, and they represent a major type of protein liquid droplets [130, 131].

Within these, it is believed that polyelectrolyte complexation is driven by mainly electrostatic attraction in long distances between oppositely charged polymer chains (**Fig. i.2D**) in water and by additional molecular recognition driving forces such as chirality, hydrogen bonding, and hydration in short distances [124, 132], implying that the polyelectrolyte complex is composed of at least one polycation and one polyanion, so-called oppositely charged complexation. When fluid–fluid phase separation occurs, it is referred to as oppositely charged coacervation [133–135].

Electrostatic coacervates can be further classified as simple or complex depending on the number of proteins or biomolecules involved in their formation. In simple coacervates (SC), only one molecule is responsible for triggering and undergoing LLPS [136, 137], while in complex coacervates (CC) two or more types of molecules, in most cases oppositely charged, are required to trigger LLPS [138]. Those molecules required for LLPS in a given system, which form the backbone of the droplet are referred to as scaffolding molecules [139], although other roles can be found in the protein droplets. Some molecules are not essential for forming the biomolecular condensates but they can modulate their formation (modulators) or simply partition into the interior or interface of preformed droplets (clients) [139] as depicted in **Fig. i.2C**. These molecules can, in turn, impact the properties and behavior of the liquid droplets. *In vitro* studies are able to reproduce and characterize electrostatically-driven LLPS with a variety of biomolecular combinations: colloids, proteins, surfactants, or polymers [140, 141].

IDPs or proteins with intrinsically disordered regions (IDRs) or domains contain a much higher fraction of charged residues than folded proteins/domains. Often these sequences are described by a stickers-and-spacers architecture that controls phase transitions [142]. Briefly, stickers are those residues promoting inter-molecular associations while spacers are those non-interacting residues which contribute to the flexibility and conformational freedom of the protein networks arising from LLPS. Owing to this property, IDPs are found to be the major protein class when it comes to electrostatic complex coacervation [143] both *in vitro* and *in vivo* [127, 144, 145]. Examples of this are the proteins FUS [146], TDP-43 [147], hnRNPA1/hnRNPA2 [148, 149], Ddx4 [144] or LAF-1 [145], among others.

2.2 Liquid-to-solid phase transition (LSPT) of IDPs and its link with neurodegeneration

The protein molecules within biomolecular condensates fulfill a variety of cellular tasks and are thus needed for physiological functioning. Consequently, a change in the phase-separating behaviour of the molecular components or a failure in the regulation of the formation/dissolution of these protein droplets can bring about pathological effects. One of such undesired consequences is the liquid-to-solid transition (LSPT, **Fig. i.3**) of the protein droplets with the formation of amyloid aggregates [126, 150].

Many IDPs, often highly charged and flexible, which initially form highly mobile liquid condensates, undergo LSPT and become more viscoelastic and rigid over time and eventually form a gel-like state that is unable to exchange its component molecules with the surrounding medium [149, 151, 152] This transition could either be due to entanglement of biopolymers or stronger association of proteins leading to fibril formation as reported for many protein condensates linked to neurological disorders such as FUS, TDP-43, Tau and hnRNPA1 [149, 151–154] It has been suggested that in these cases, phase separation might increase the nucleation rate for protein aggregation into amyloid fibrils [155]. Given the nature of amyloidogenic peptides and proteins, a high concentration of such molecules with significant flexibility and conformational dynamics in the liquid condensates might promote the formation of toxic oligomers [155] and increase the nucleation rates for the formation of amyloid fibrils [149, 155]. However, the exact role of LLPS and LSPT in amyloid aggregation at the molecular level

is still unknown, and the relationship between LLPS and the established amyloid nucleation theories also remains elusive.
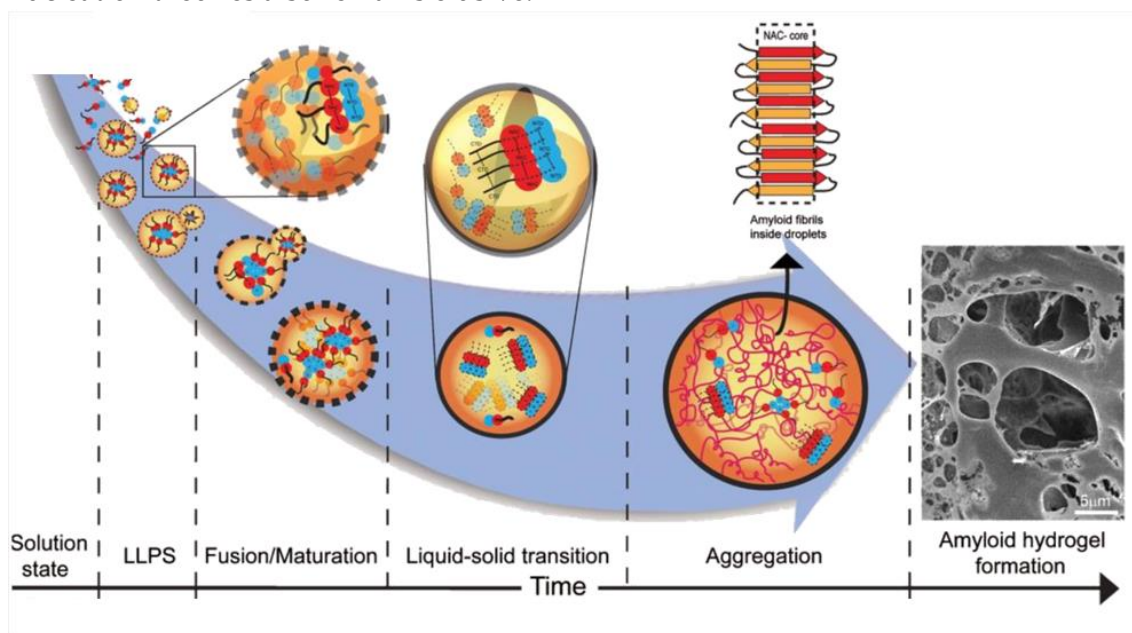
Fig. i.3. Schematic representation of a possible mechanism for LLPS/LSPT-driven amyloid aggregation. A monomeric protein can undergo LLPS and the phase-separated droplets mature from a liquid state to a solid-like state due to fusion and Ostwald ripening. Protein molecules inside these droplets gradually become stiffer and eventually transform into amyloid hydrogel state containing fibrillar aggregates and oligomers. Adapted from [156]

Of particular interest for this thesis are the recent advances made on understanding the LLPS and LSPT behavior of two amyloidogenic proteins involved in neural disorders: Tau and αS. The background on this topic is especifically introduced and discussed in chapter 2.

3. Interaction between amyloids and other molecules for therapy and diagnostics

Over the past decade, much effort has been made in explaining and characterizing the non-covalent binding of soluble chemical species to amyloid aggregates. The motivation behind detecting and tailoring the interactions between these structures and small molecules is essentially two-fold: firstly, amyloidophilic small molecules can act as labels and allow imaging techniques to detect deposited or in-solution amyloid structures in a diagnostic setting [157–159]; secondly, small molecules have the potential to influence the progression of protein aggregation and bias the populations of fibrils and oligomeric species, which are likely to possess increased cytotoxic character, relative to soluble monomers [160–162]). Independently of which molecular species is the most toxic entity on the aggregation pathway, the capability to selectively inhibit or enhance steps on the reaction pathway, and therefore to shift the populations, is expected to foster new therapeutic approaches. Besides, the possibility of labeling, detecting and imaging these protein aggregates in a highly specific manner *in vivo* is a requirement for accurate diagnostic approaches to these disorders.

In the context of this thesis, the search for specific inhibitors of protein aggregation is of particular interest. Since the amyloid deposition process has autocatalytic elements and is greatly accelerated in the presence of preformed aggregates or oligomers [163], these aggregates themselves represent a natural target for intervention in order to inhibit their subsequent proliferation. Interestingly, there are indications that this strategy is adopted by some of the natural mechanisms against protein aggregation, including the action of heat shock proteins [164–166]. The picture of protein aggregation in a disease context that has emerged from the *in vitro* research in the last few years is that the amyloid aggregation phenomenon can be described as a nucleated polymerization mechanism, the overall kinetic behavior of which is governed by a small number of rate constants of elementary steps, such as nucleation, growth of nuclei and multiplications of seeds by fragmentation [73]. Small molecules could in principle interfere with all these elementary steps. One possible strategy is to design a molecule that binds to the aggregates and interferes with the further recruitment of soluble protein by pre-existing aggregates, through a competition for the attachment sites. Interestingly, it has recently been shown that in many cases where a specific mechanism targeting the growth sites on the aggregates was initially proposed, a large contribution to the observed inhibitory effect observed *in vitro* could originate from the sequestration of soluble protein by micellar forms of the surfactant-like small molecules [167, 168]. Obviously, despite blocking or reducing the amyloid growth, making the functional monomeric protein less available is expected to have critical detrimental effects to be avoided when designing therapeutic molecules.

Several natural compounds are effective antiamyloid agents, notably tetracyclines, steroid-polyamine [169] and polyphenols [170, 171]. They are generally non-specific, as documented by their partially overlapping mechanisms and the capability to interfere with the aggregation of several unrelated proteins [172]. The other major class of amyloid therapeutics-intended are rationally designed molecules [173, 174]. Design and development of such molecules can take advantage of knowledge stemming from both theoretical and experimental investigations on the mode of action of natural compounds. In particular, there is surely room for developing more effective compounds starting from the natural ones used as lead compounds. High-throughput screening (HTS) studies of compounds libraries (also in the form of virtual libraries) have built on previous knowledge on inhibition mechanisms, thus disclosing new perspectives for the development of novel classes of inhibitors. Interestingly, high-throughput computational methods are expected to become increasingly useful not only in view of the development of low-molecular weight organic molecules as anti-amyloid agents, but also as a support in the efficient screening of peptide libraries for the selection of the most effective compounds against amyloid aggregation (*i. e.*, for instance, peptide-based inhibitors derived from original amyloid sequences). Among these small molecules we can find the prominent examples of β-breakers peptides [175, 176], whole antibodies [177, 178] and their fragments [179]. Regarding the amyloid aggregation of αS, natural [174, 180, 181] and synthetic [182, 183] compounds have been proven powerful in blocking the self-assembly of the protein into amyloid aggregates, binding to toxic oligomers and abrogating the effect of the toxic amyloid species in cells or even curing

disease traits in animal models [183, 184]. However, these molecules are still not optimal owing to their non-specific inhibition or low affinities.

3.1. The need for a detailed inhibition molecular mechanism

The lack of a detailed mechanism of action of small molecules over amyloid aggregation processes is a bottleneck in drug development for neurodegenerative disorders. A very clear example of this is the Aβ peptide. Although targeting Aβ accumulation has been pursued as a major potential therapeutic strategy against AD [185–188], no compound selected for this purpose has yet entered clinical use [189, 190]. Although these failures have raised doubts about the amyloid hypothesis [191], they can also be attributed to an incomplete knowledge of the molecular mechanisms by which the compounds tested so far affect the nucleation and growth of Aβ aggregates. Indeed, it has been shown that inhibiting Aβ aggregation without a detailed understanding of the underlying microscopic processes could affect the toxicity in unexpected ways [192, 193]. For example, the inhibition of nucleation events may delay or decrease toxicity, whereas the inhibition of elongation may lead to an overall increase in toxicity [192, 193]. Therefore, effective therapeutic strategies must be aimed at targeting precise microscopic steps and specific aggregated species during Aβ self-assembly [19, 192, 194, 195].

Another paradigmatic amyloidogenic protein for which much progress remains necessary in terms of drug development is αS. Interfering with αS amyloid formation and abrogating the associated toxicity is considered a promising therapeutic strategy for synucleinopathies [49, 196, 197]. However, the design of molecular entities that target specific αS toxic assemblies is challenging because of the heterogeneous, dynamic, and transient nature of these species. High-throughput screening initiatives have rendered promising αS aggregation inhibitors [183, 198, 199]. However, these selection procedures are blind to the ligand mechanism of action. In the absence of a structure-activity relationship, it is difficult to evolve the affinity and specificity of the identified hits to generate drugs that can reach clinical stages. The lack of specific and sensitive molecules to detect the pathogenic forms of αS also hinders the early diagnosis of these diseases.

One of the factors contributing to the difficulty in identifying the molecular target of inhibitor compounds stems from the fact that few experimental techniques exist that allow the specific interactions between protein aggregates and small molecules to be studied. Despite the incidence and devastating nature of this family of diseases, there still exist an urgent need for more specific and effective therapeutic and early diagnostic tools based on molecules that either inhibit the toxicity of the amyloid aggregates [200] or that are capable of recognizing the toxic amyloid species specifically [201]. This necessity, in turn, calls for the development of experimental approaches that allow for a detailed and quantitative characterization of the interaction of molecules of interest to the amyloid aggregates, which is not trivial considering the heterogeneity in particle size and binding stoichiometry of these complexes [202].

In addition to that, an optimal interaction assay for identifying molecules of interest would need to be fast, low-sample consuming, cover a wide concentration range, yield

no false positives and to be able to gain direct access to the affinity and also the stoichiometry of the interaction simultaneously. This is not the case for most of the widely used techniques in amyloid inhibition such as thioflavin-T (ThT) fluorescence, where the overall efficacy of the molecule on the aggregation process is assessed but the binding parameters are not directly obtained but estimated assuming theoretical mechanistic models [192], or isothermal titration calorimetry, where the working concentration range, sample volume and possible artifacts arising from sample inhomogeneities are limiting factors [203]. Thus, obtaining a detailed understanding of the mechanism of action and the specific interaction of potential therapeutic or diagnostic molecules to toxic amyloid aggregates remains technically challenging by conventional techniques.

4. The role of molecular chaperones in protein misfolding brain diseases

In a functioning cell, protein biogenesis is a vital process that ensures the conservation of correctly folded protein. Polypeptides are synthesized and delivered to the proper cellular compartment, where they are folded into their native structure. An accumulation of a large amount of unfolded or misfolded polypeptides resulting from a number of pathogenetic sources such as mutations, inefficient folding, error in synthesis, etc, may cause cell toxicity. However, cells have evolved molecular defense mechanisms that enable them to withstand, to variable extents, such damage. One such group of molecules that assist protein homeostasis are molecular chaperones. They are expressed ubiquitously under physiological conditions and play important roles in various cellular processes [204], such as guiding nascent polypeptide chains from the ribosome into a productive folding pathway, rescuing misfolded proteins by promoting their correct folding or even by promoting the disassembly of mature amyloid fibrils [203]. In addition, they also protect the native protein from cellular stress such as free radicals, high temperature, heavy metals, etc., and even promote the refolding of misfolded proteins [203]. Recycling of the proteome and the specific degradation of misfolded proteins that are unable to refold by the molecular chaperones is essential for the adequate proteostasis equilibrium in the cell. There are different protein degradation mechanisms, the most relevant ones being the ubiquitin-proteasome pathway (UPS) and autophagy [205].

Under physiological conditions, the collective activity of molecular chaperones along with UPS and autophagy are an efficient protein quality control (PQC) system to prevent aggregation of misfolded proteins (**Fig. i.4A**). However, there could be stress conditions under which the misfolded proteins resist the action of PQC system and accumulate upto hazardous levels (**Fig. i.4B**). This is the case for several diseases including AD, PD, ALS, and HD, where the accumulation of particular types of misfolded proteins in different brain regions is a distinctive feature [206] (see section 1 of this introduction for related relevant bibliography). Molecular chaperones, among which heat-shock proteins (HSPs) are found, provide protection against the stressful events in the nervous system like mitochondrial dysfunction and Aβ or Tau accumulation that contribute to the oxidative damage in AD [207]. Under these oxidative stress conditions, the expression of HSP-encoding genes is enhanced [203]. Experimental evidences have shown that HSPs can directly inhibit the aggregation of Aβ, NFTs, and promote the binding of

ubiquitin to misfolded proteins [208–210]. After the principal component αS in Lewy bodies, a hallmark of PD, we also find synphililin-1 (an aggregation prone protein), components of PQC, such as ubiquitin, and molecular chaperones including Hsp90, Hsp70, Hsp60, Hsp40, Hsp27, and CHIP [211–213]. The presence of large amounts of various of the components of PQC in Lewy bodies along with αS indicates efforts of molecular chaperones in maintaining proteostasis during the stress conditions. Numerous hypotheses have been linked with protein misfolding associated with ALS, including alteration in protein degradation pathway and cellular trafficking, ER stress, oxidative stress, and prion like misfolding [214]. In HD, for instance, different molecular chaperones have been implicated in the suppression of misfolded protein aggregates.
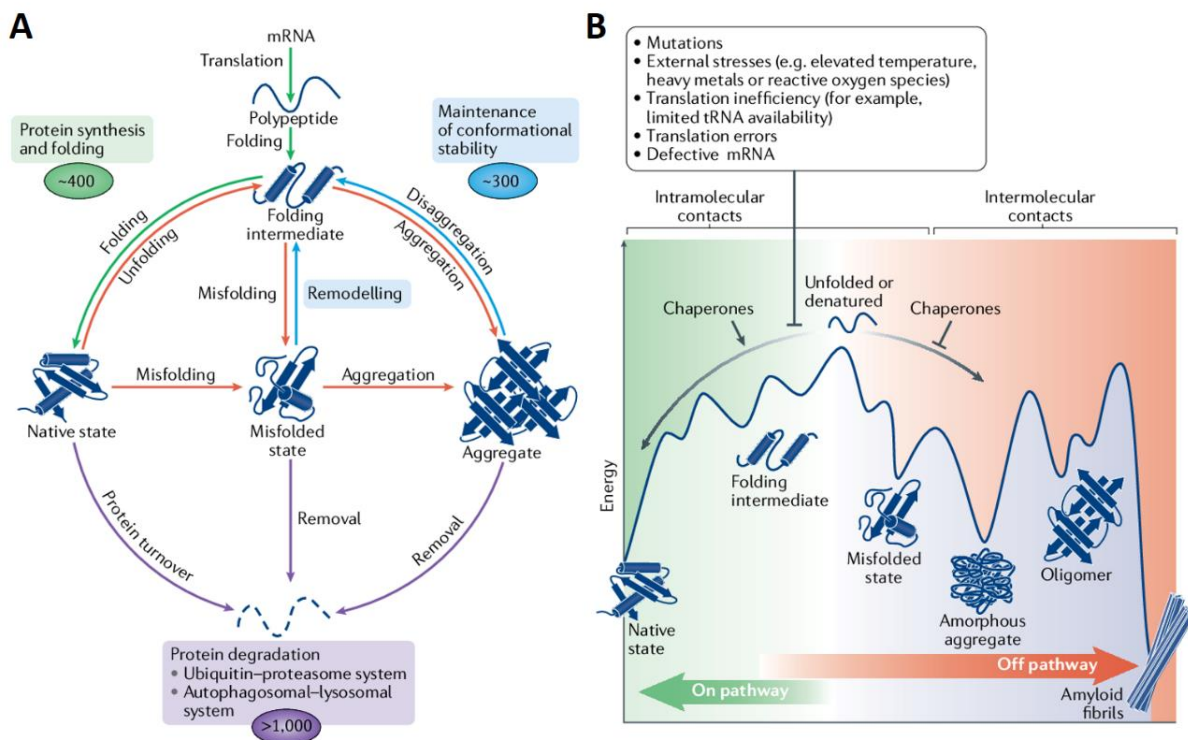
The molecular chaperones Hsp70 and Hsp40 suppress the neurotoxicity induced by mHtt in Drosophila models of HD by directly interacting with exon1 of polyQ in mHtt [215, 216].

Fig. i.4. **The proteostasis network prevents the formation of toxic protein aggregates**. **A)** The proteostasis network contains all the factors that are necessary to control the functional levels of proteins in their native state and minimize non-productive or harmful off-pathway reactions (generation of unfolded proteins or aggregates; red). Proteostasis network components, which comprise ~2,000 proteins in human cells, can be operationally assigned to three major arms: protein synthesis and folding (green), conformational maintenance (blue) and degradation (purple). In humans, ~300 different molecular chaperones orchestrate these processes and function in folding, refolding and disaggregation reactions. They cooperate with the ubiquitin–proteasome system and the autophagosomal–lysosomal machinery in the degradation of misfolded proteins and aggregates. **B)** Proteins sample diverse conformations during folding, increasingly forming native intramolecular contacts as they progress downhill along a rugged energy landscape towards the thermodynamically stable, native state. Folding intermediates and misfolded states may accumulate as kinetically trapped species that need to traverse free-

energy barriers to form functional proteins. Intermolecular contacts between non-native states may result in the formation of various aggregate species, including oligomers, amorphous aggregates and amyloid fibrils, the latter of which may even be thermodynamically more stable than the native state. Molecular chaperones enhance on-pathway reactions that support progression of folding intermediates towards the native state and block off-pathway reactions that lead to misfolded and aggregated species. Various factors, such as mutations, stress, translation aberrations or defects in mRNA, inhibit the on-pathway reactions, favouring protein misfolding and aggregation. Adapted From [217].

In summary, *in vitro* and *in vivo* studies highlight how effectively molecular chaperones restore proteostasis via interacting with different protein species and conformations and facilitating the degradation of misfolded proteins. The involvement of molecular chaperones in disease pathogenesis comes, therefore, as no surprise. Their enhanced expression or activation could possibly delay disease progression, making them promising therapeutic targets for misfolding diseases.

4.1 Disaggregases: chaperone machineries to disassemble protein aggregates

Molecular chaperones and co-chaperones can be grouped in distinct families, including ribosome-binding chaperones, heat shock proteins such as Hsp40s, Hsp70s, Hsp90s, Hsp100, chaperonins, prefoldins and tetratricopeptide repeat (TPR)-domain containing co-chaperones. It has been estimated that this large body of proteins amounts to *ca*. 330 distinct polypeptide chains in the human proteome [218]. Beside the previously discussed key roles in protein homeostasis, molecular chaperones have been recently proposed to promote disassembly of undesired aberrant protein aggregates [219–222]. Although this last function has long been known to involve only chaperones of the ClpB and Hsp104 families present in bacteria, protozoa, plants and fungi [219], it has recently been discovered in higher eukaryotes as well [223, 224]. The mammalian cytosol possesses a potent, ATP-dependent chaperone machinery with disaggregase and reactivation activity [225]. This activity was shown to be provided by the central chaperone Hsp70 in collaboration with a specific subset of J-domain proteins (JDPs or Hsp40s) and nucleotide-exchange factor (NEF) chaperones (such as those from the Hsp110 family), a ternary system capable of solubilizing a wide range of amorphous aggregates [223, 225–227].

Although historically the process of protein disaggregation is connected to the Hsp104/ClpB disaggregase, this machine does not exhibit disaggregation activity on its own but instead strictly requires cooperation with cognate Hsp70 chaperone systems [228, 229]. It is the Hsp70 chaperone that forms the initializing core of the Hsp70/Hsp104 bi-chaperone machinery [230, 231]. Hsp70 chaperones are highly versatile and involved in a multiplicity of cellular processes including folding of newly synthesized proteins, protein transport and degradation, and prevention of protein aggregation [232]. This broad set of activities is made possible by co-chaperones of the DNAJ protein family that target Hsp70 to specific cellular sites including protein aggregates. Hsp70s promiscuously bind to different kinds of protein aggregates, including bacterial inclusion bodies formed upon overproduction of heterologous proteins, stress granules composed of translation factors and translationally repressed mRNA, heat stress-

generated protein aggregates composed of misfolded proteins, and amyloid fibrils formed by disease proteins [224, 233]. This underlines the central role of Hsp70 in aggregate handling. The disaggregation potential of Hsp70 is, however, limited, and aggregate-bound Hsp70 typically requires assistance to be most effective [232]. In this sense, Hsp104/ClpB represent specialized Hsp70 partner chaperones that increase the potential of the Hsp70 machinery in protein disaggregation. Protein disaggregation is thus initiated by Hsp70 binding to the surface of protein aggregates followed by subsequent recruitment of the cooperating Hsp100 disaggregase [234, 235].

4.2 αS amyloid disassembly by the human disaggregase

As we have mentioned, chaperone systems with a disaggregase activity are able to break down different types of protein aggregates. When it comes to amyloid aggregates in particular, equimolar concentrations of the constitutive Hsp70 (Hsc70), the canonical class B-JDP DnaJB1 and the NEF of the Hsp110 family Apg2 were shown to disassemble αS fibrils in a timescale of weeks [236]. A later study revealed that a chaperone complex composed solely of members of the Hsp70, Hsp40, and Hsp110 families (henceforth called human disaggregase) was able to efficiently reverse αS amyloid fibrils within hours [224]. The amount of the NEF was proposed to be the main reason to explain the time-scale differences as substoichiometric levels of the NEF relative to Hsc70 seem critical for good performance [224, 227].

Protein disaggregation by the human disaggregase is initiated by JDPs, recognizing and binding to protein aggregate surfaces [237]. JDPs then recruit Hsp70 to the aggregate through the simultaneous interaction with both the substrate and Hsp70, which results in the stimulation of ATP hydrolysis at the Hsp70 nucleotide-binding domain (NBD) [238]. ATP hydrolysis is coupled to a conformational cycle defined by a large-scale reorganization of the Hsp70 substrate-binding domain (SBD), in which the α-helical lid subdomain closes over the β-sandwich substrate binding pocket in the ADP state, resulting in substrate capture [239, 240]. Although in all JDPs the interaction of the J-domain is responsible for the activation of Hsc70, the adjacent glycine-phenylalanine rich domain (GF) of DnaJB1 blocks the Hsc70-binding site [241]. The interaction of a second site (at the CTDI) of DnaJB1 with the Hsc70 C-terminal tail releases the GF-domain and therefore ends its inhibitory effect [241].

In the absence of DnaJB1, Hsc70 decorates the fibrils randomly [224]. However, the multivalent interaction of DnaJB1 with the fibrils allows for the organized recruitment of Hsc70 in a crowded state [242]. Crowding of Hsc70 molecules at the surface of αS fibrils has an initial entropic energy barrier that is overcome by the DnaJB1-stimulated ATPase activity of Hsc70, which slows down the dissociation of the Hsc70-ADP state and thus, increases an order of magnitude the affinity of the chaperone for fibrils [224, 242]. Such binding reduces the conformational space accessible due to an excluded volume effect caused by the physical barrier formed by the aggregate [242]. In an attempt to restore conformational freedom, and the associated increase in entropic energy, Hsc70 applies a pulling force away from the aggregate surface that drives aggregate dissolution [242]. This entropic pulling mechanism has also been used to explain Hsp70-mediated clathrin uncoating and protein translocation [243, 244].

After ATP-hydrolysis, the timely release of the trapped polypeptides from the fibrils is mediated by the NEF, which stimulates ADP exchange by ATP [245]. Rebinding of ATP and simultaneous opening of the substrate-binding pocket dissociates substrates from Hsp70, promoting localized polypeptide unfolding–refolding events and resetting Hsp70 for the next cycle of substrate binding. Among the several existing Hsp70 NEFs, Bag1, Hsp105a, and Apg2 have been shown to stimulate Hsc70-mediated disassembly of αS fibrils, although with very different efficiencies (Bag1 < Hsp105a < Apg2) [224]. The higher molecular mass of NEFs from the Hsp110 family (Hsp105a and Apg2) seems to be the reason for these differences, as disassembly of amyloids is favored by a bulky NEF like Apg2, which besides exchanging ADP by ATP, also rearranges the fibril-bound Hsc70 molecules, increasing crowding and the formation of productive disaggregase assemblies [242].

From a mechanistic point of view, there is uncertainty about how human chaperones proceed in the disassembly of amyloids. By using αS fibrils capped with his-tagged protomers, Shorter and colleagues showed that Hsc70, DnaJB1, and Apg2, in the presence of HspB5, liberated only his-αS into the soluble fraction, which indicated that disassembly proceeded via depolymerization [236]. A later contribution by Bukau´s group showed a fast disappearance of longer fibrils with a concomitant appearance of shorter species in the presence of Hsc70, DnaJB1, and Apg2, and proposed that apart from depolymerizing, the human disaggregase could also extract monomers from the center of the fibrils, therefore breaking them into smaller fragments [224]. This was proposed under the premise that a depolymerization-only disassembly might be expected to decrease length at a similar rate in all fibrils.

In the light of the current lack of consensus as to what is the precise disaggregation mechanism of the human disaggregase over αS amyloid fibrils, and also considering the evergrowing evidence for the role of intermediate αS oligomers in mediating cytotoxic effects, we set out to characterize the molecular mechanism of the Hsc70 machinery on these aggregates. This is described in chapter 4 of this thesis.

5. Challenges in the study of amyloid aggregation, inhibition and disaggregation

As we have discussed before, amyloid aggregation is a highly complex process. On the one hand, the conversion from monomeric proteins to amyloid fibrils follows molecular mechanisms which remain largely unknown, and the factors triggering self-assembly and acquisition of a β-sheet structure vary among amyloidogenic proteins. Besides, there is still much debate over what species, whether fibrillar or intermediate oligomeric assemblies, are responsible for inducing cytotoxicity, cell-to-cell amyloid propagation and, ultimately, neuropathological effects. Another emerging source of complexity are structural polymorphisms [246–248], which cast lights and shadows on which amyloid structures are actually relevant for disease. In order to circumvent this, protocols to isolate and investigate specific amyloid species *in vitro* and *in vivo* are highly desirable, yet not available for most amyloidogenic protein systems. On the other hand, there is a lack of detail understanding of the particular inhibition mechanisms for the different reported molecules able to bind amyloid assemblies, owing to the aforementioned

structural complexity and heterogeneity of the amyloid aggregation process. Techniques able to directly access the binding properties and mechanisms of potential therapeutic molecules would be desirable so as not to depend on theoretical modelling of often irreproducible kinetic data [192, 249]. For disaggregation experiments, similar challenges are encountered. High resolution structural techniques are required to gain direct access to the disassembly mechanism of disaggregase chaperone systems over amyloid aggregates. Likewise, kinetic methods which do not solely rely on theoretical models and extrinsic dyes that only report on the formation of amyloid fibrils, without distinguishing between structural features of the latter, would be highly beneficial for interpreting data and coming up with more accurate models of the molecular mechanisms of chaperone-mediated aggregate disassembly. The caveats and limitations of the typically used techniques when facing the cahllenges mentioned above, as well as alternative technical approaches applied in this thesis and their advantages are discussed below.

5.1. Extrinsic and intrinsic dyes for monitoring amyloid structures

Amyloid aggregates are often visualized *in vivo* or in fixed samples by fluorescence microscopy using probes such as congo red or thioflavin-S (ThS). *In vitro*, the most widely employed approach to probe and monitor amyloid aggregation is to follow the kinetics of the reaction [250, 251]. However, these are very often highly irreproducible and their analysis relies on theoretical models that are typically very simplistic (for example, nucleation is depicted as a single chemical reaction with a unique associated kinetic rate) [192, 249]. For tracking the changes upon aggregation, disaggregation or even monitoring the aggregation inhibition by a small molecule, extrinsic or intrinsic fluorescent probes can be employed. Extrinsic dyes are the most commonly used approach. They are added to a protein solution which is then subjected to aggregation-inducing conditions and, typically, the binding of the probe, visible as a spectral change, is interpreted as a reporter of the presence of amyloid fibrils. Thus, extrinsic dyes depend on their ability, specificity and mode of binding to a given amyloid structure [252, 253]. By contrast, protocols using these dyes are technically straightforward and standardized. In the case of intrinsic probes, a small fluorescent molecule can be covalently attached to the monomeric form of the protein of interest before inducing aggregation. Then, changes in fluorescence parameters such as polarization [254], lifetime [255] or intensity [256] are used as reporters of aggregation. This multiparametric readout increases the amount and meaning of the information obtained per experiment. Here, the signal changes giving rise to the kinetic curve does not rely on the amyloid-binding properties of an extrinsic fluorescent probe. Besides, site-specific labelling enables accessing sequence-specific information. Protein engineering and fluorescent labelling steps are required for using intrinsic probes, even if they are not labor-intensive.

5.1.1. Thioflavin-T as an amyloid reporter: common uses and caveats

The most commonly used techniques for studying amyloid aggregates are based on fluorescence using extrinsic dyes capable of binding amyloid structures specifically. Among these, one could say thioflavin-T (ThT) is a "swiss knife" and, without any doubt,

the gold standard. In 1959, Vassar and Culling [257] demonstrated its potential as a fluorescence microscopy probe for amyloid fibril deposits in histological samples. Thirty years later, Naiki *et. al.* [258] first quantified amyloid fibrils *in vitro* by spectrophotometrically detecting the fluorescence emission of ThT with excellent linearity between fibril concentration and emission intensity. Since then, ThT and its chemical derivatives have become the most widely used probes for selectively identifying and analyzing formation and disassembly of amyloid fibrils both *in vivo* and *in vitro* [259].

When it binds to β sheet-rich structures such as amyloid fibrils, ThT displays enhanced fluorescence and a characteristic blue shift in the emission spectrum [260, 261] from approximately 510 nm in the free state to 480 nm when bound to amyloid fibrils. The increasing number of structural models for amyloid fibrils strongly suggests that ThT binds by aligning parallel to the long axis of the fiber, intercalating to the repeating side-chain interactions running across β-strands within a β-sheet layer [262, 263]. Therefore, the large size and the rigidity of the fibrils allows the binding of a large amount of ThT, while providing an environment with restricted mobility, which enhances ThT fluorescence emission [256, 264]. Protofibrils are structurally closest to the mature fibrils, and are often described as intermediates in the late stages of fibril formation. Although protofibrils bind ThT and other dyes, the interaction is often weaker than observed for mature fibrils [265–267]. Usually, oligomers are populated during the initial lag- or nucleation phase of amyloid aggregation [20, 268, 269]. Due to their transient appearance, they are difficult to characterize. In addition to size and shape, oligomers are distinct from fibrils in their poor interaction with ThT (resulting in a low fluorescence emission), high intra-sample heterogeneity and the co-existence of different oligomeric states. Furthermore, to complicate matters further, a given amyloid aggregate can bind ThT in more than one type of binding mode with different affinities [270, 271]. ThT has also been used to identify amyloid aggregation during LSPT of amyloidogenic proteins. However, although its amyloid-reporting application in isolated aggregates in aqueous solution is well-established, unspecific partitioning of ThT into biomolecular condensates could occur due to a preference for the chemical properties of either phase. Together with this, the inherent reduced molecular mobility inside the condensates may also induce the spectral changes of ThT that can be taken as a sign of amyloid structures, thus making this dye prone to artifacts in the complex scenario of LLPS and LSPT. Lastly, binding of ThT is also not totally limited to just amyloid fibrils [272], but also found to bind certain specific native state proteins [273, 274], non-amyloid aggregates [272, 275] or even other non-proteic molecules [276–278].

Due to the ease and high throughput of the fibrillization kinetics assay, ThT has been employed in multiple amyloid systems to screen for small molecules inhibiting fibrillation [279]. Changes in its intensity are used as an indicator of fibril assembly or disassembly [259]). If a decrease in signal intensity is observed, it is attributed to the reduction of amyloid assemblies [280, 281], caused by the tested anti-amyloid compound. However, such assays give rise to even more potential artifacts. Small molecule inhibitors often have structures similar to ThT, allowing them to prevent ThT binding by competitive inhibition or by spectral overlap that quenches ThT signals, rather than inhibiting the fibrillation process itself [282]. Even in the absence of spectral

overlap, oxidative products of the small molecules may cause quenching and hence report false positive inhibitors. Small molecules often included in small molecule libraries like catecholamines (dopamine), polyphenols (resveratrol, EGCG), and flavonoids (quercetin) all oxidize to quinones, which can significantly quench ThT signals [282]. A review on Aβ and small molecule inhibitors shows how one would reach false positive conclusions if based only on extrinsic dye-binding assays [279]

5.1.2. Pyrene fluorescence spectroscopy

Pyrene is a flurorescenct polycyclic aromatic hydrocarbon (PAH) consisting of four fused benzene rings, resulting in a flat aromatic system (**Fig. i.5**). The spectral features of pyrene are exquisitely sensitive to the microenvironment of the probe: it exhibits an ensemble of monomer fluorescence emission peaks that report on the polarity of the probe microenvironment [283, 284], and the possibility for the presence of an additional band at longer wavelengths, termed usually pyrene excimer (**Fig. i.5**) which reflects the presence of another pyrene molecule in close spatial proximity (~ 1-10 Å) [285–287]. Its high extinction coefficient allows us to study labeled proteins in solution at physiologically relevant concentrations [288]. The environmentally- and spatially-sensitive features of pyrene allow monitoring protein conformation, conformational changes, protein folding and unfolding, protein-protein, protein-lipid and protein-membrane interactions [287, 289–291]. For site-specific pyrene labelling of proteins, cysteines are the preferred target due to their lower frequency of occurrence compared to lysines. In this case, a maleimide derivative of pyrene is used [287, 292]. In the case of proteins with naturally occurring cysteines, the probe will monitor all cysteines if stoichiometric labeling is achieved. If cysteines are not present at locations of interest, they may be replaced by serines or alanines (which show negligible reactivity with sulfhydryl reagents) provided the function of the protein is not significantly altered [293, 294]; this is followed by introduction of cysteine(s) at desired site(s) by site directed mutagenesis, and labeling with pyrene.

The fluorescence emission spectrum of pyrene is characterized by five major vibronic bands designated Bands I, II, III, IV and V, with well-defined peaks at ~375, 379, 385, 395 and 410 nm, respectively. To differentiate them from the fluorescence arising from dimer interaction (described below), the ensemble of the five vibronic bands is collectively referred to as the monomer bands. The first notable feature useful for analysis of protein conformational changes is the exquisite sensitivity of the peak at 385 nm (corresponding to the third vibronic band) to the polarity of the probe's microenvironment, a consequence of the coupling of electronic and vibronic states [284, 296]. In comparison to the emission intensity of Band I at 375 nm (I_I, which corresponds to the first vibronic band), the intensity of Band III at 385 nm (I_{III}) is significantly enhanced in hydrophobic environments. In contrast, the intensity of Band I is significantly higher than that of Band III in polar environments [283, 297, 298]. The ratio of the fluorescence emission intensities of Band I and III (Py value or I_I/I_{III} ratio) can thus be employed to quantify the degree of polarity in the vicinity of the probed location. For instance, the I_I/I_{III} ratio was used to interrogate the binding mode of αS to lipid membranes using a site-directed pyrene labelling scheme and the role of Ca^{2+} in that interaction [291].
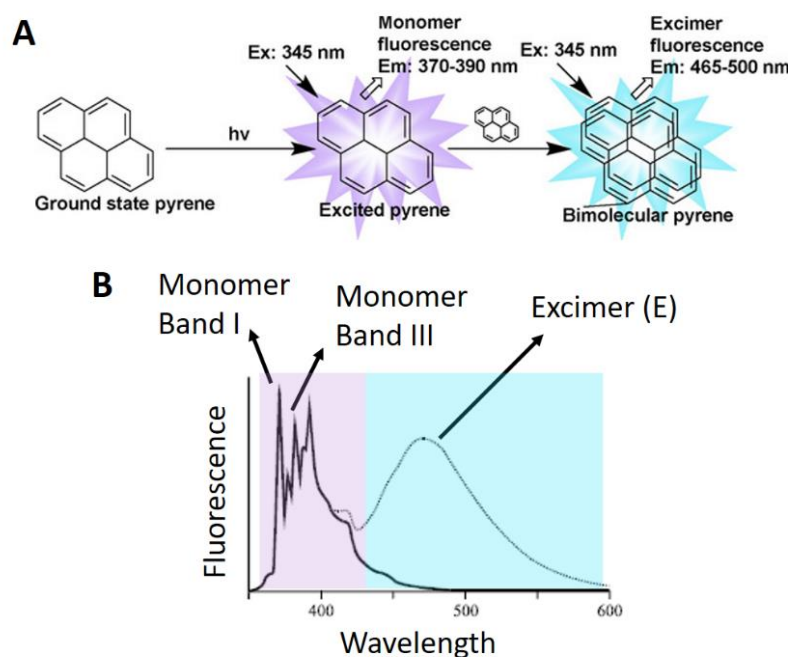
Fig. i.5. **Fundamentals of pyrene fluorescence spectroscopy**. **A**) Pyrene species according to their excitation and fluorescence emission properties are shown. Adapted from [295]**B**) Pyrene spectral properties. The emission from the excited pyrene in its monomeric form is shown in shaded purple and the excimer (bimolecular pyrene) emission band is shown in shaded blue. The microenvironment polarity-reporting emission bands I and III at 375 nm and 385 nm, respectively, are indicated with arrows. Adapted from from [295]

A second notable feature of pyrene fluorescence emission that can be employed for protein conformational analysis is the appearance of a broad emission band at longer wavelengths (ranging from 425 to 550 nm, centered around 460 nm) when two pyrene rings are ~10 Å from each other or closer. It arises due to formation of an excited state dimer also known as pyrene excimer and involves interaction between two pyrene molecules [299, 300]. The unusually long lifetime of pyrene emission (> 100 ns) [283, 297] allows this excited state reaction to occur. Excimer emission may arise in a dose-dependent manner (for example at higher concentration of pyrene-labeled protein in solution or in the context of the plane of a lipid bilayer) or when two pyrenes are spatially proximal to each other in an intra-molecular context. The excimer/monomer (E/M) ratio, calculated by comparing the fluorescence intensity (or quantum yield) of the first monomer peak (typically ~ 375 nm) with respect to the excimer band (generally ~ 460 nm), is a relative indicator of the extent of excimer formation, and therefore the spatial proximity between two pyrene moieties. An illustrative example of the application of the E/M ratio of pyrene was the study of the conformational changes of apolipoprotein ApoLp-III upon binding to lipids [301, 302]. The E/M ratio also contributed to understanding the inter-molecular organization and multimerization of protein assemblies. Taken in conjunction with other studies, excimer emission of pyrene labeled tropomyosin homodimer confirmed the spatial proximity, parallel and in-register

orientation of two neighboring chains [299, 303, 304]. Another example is the helix-helix interaction and oligomerization of ApoE [305].

Interestingly in the frame of this thesis, pyrene fluorescence spectroscopy has been used successfully by the group of Prof. T. Jovin to investigate the early stages of αS amyloid aggregation [305]. Also, Gallea and Celej applied pyrene fluorescence to the structural characterization of oligomeric assemblies of αS [306]. Typical fluorescence methods such as ThT are largely blind to these early molecular events that eventually lead to the formation of mature fibrils. They showed that, upon induction of aggregation, the entire family of steady-state descriptors of pyrene emission (monomer intensity, solvent polarity ratio (I_I/I_{III}), and anisotropy; and excimer intensity) change dramatically, particularly during the early stages in which oligomeric intermediates form and evolve. The pyrene probe senses a progressive decrease in polarity, an increase in molecular mass and close intermolecular association as a function of position in the protein primary sequence and the presence of point mutations.

5.2. Ensemble *versus* single-molecule spectroscopic techniques

In *in vitro* experiments, 100 μl of a biological sample at a concentration of 10 μM contains approximately 10^{14} molecules. One might suppose that their mean average property, which is what ensemble techniques measure, is an adequate representation of the properties of any given single molecule. In some exceptional biological systems this is true; however, in general this is not the case. This is because single biological molecules usually exist in multiple states, intrinsically related to their biological functions. For example, there are many molecules which exist in multiple spatial conformations, such as molecular motors, with each conformation having a characteristic energy state [307]. Although there may be a single conformation/state that is more stable than the others for these tiny molecular machines, several short-lived conformations still exist, which are used in different stages of motion and force generation. The mean conformation would look something close to the most stable of these many different conformations, but this single average parameter does not tell us a great deal about the behaviour of the other short-lived, but essential states. To illustrate this, we can think of a million butterflies flicking their wings (**Fig. i.6A**). Because they are not synchronized and fly as individual elements, some of them will have their wings fully closed, some fully open and most of them will have their wings in a range of intermediate positions. If we can only see the average property of these ensemble butterflies, we will inevitably conclude that their wings are half-open (or half-closed for that matter). However, we know this is not possible and, if we look at them one by one, we will be able to describe the different populations, thus painting a much more realistic picture of the butterflies.

Bulk ensemble average analysis, irrespective of what experimental property is measured, cannot probe multiple states in a heterogeneous molecular system (**Fig. i.6B**). Also, temporal fluctuations in the molecules from a population result in broadening the distribution of a measured parameter from a bulk ensemble experiment [307], which can be difficult to interpret physiologically. These thermal fluctuations are driven by collisions from the surrounding water molecules, which can drive biological molecules into different states [308, 309]. In an ensemble experiment, this may broaden the

measured value, making reliable inference difficult. Furthermore, there is a risk of lack of synchronicity in ensemble experiments [310, 311]. The issue here is that different molecules within a large population may be doing different things at different times;
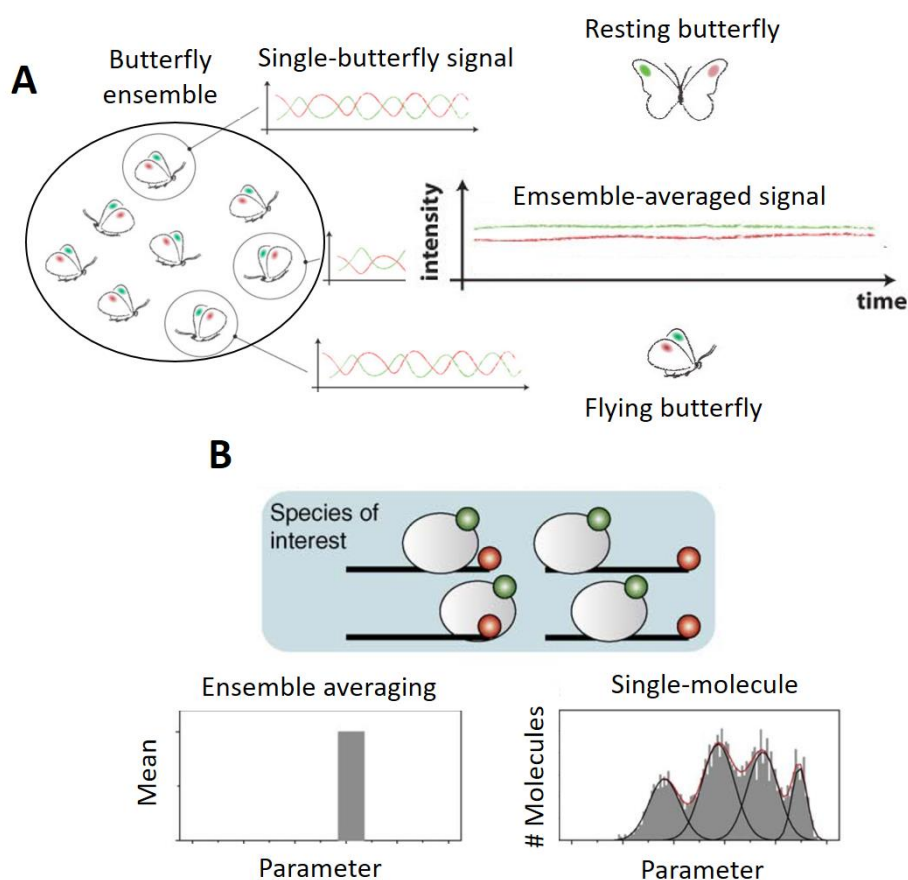
Fig. i.6. **Ensemble versus single-molecule spectroscopic techniques**. **A**) A group of green and red butterflies flying is shown in a circle and the signal fluctuations arising from the green and red colors (in analogy to fluorophores) observed by ensemble averaging or by a single-molecule approach are illustrated. Adapted from the webpage of Prof. Chirlmin Joo (TU Delft). **B**) The top panel shows one molecule with two domains (rod and circle), each of them labelled with either a green or a red dye. Upon conformational changes, up to four species are possible for this molecule. The fluorescence from both colors (be it intramolecular FRET efficiency E, for instance) yields very different readouts: while ensemble averaging (or bulk techniques) can only see the average property of the molecular complexes, while single-molecule observations enable us to tell the four states apart. Adapted from [307].

molecules may for example be in different conformations at a given time, so the average snapshot from the large population encapsulates all such temporal fluctuations resulting in an inaccurate picture. In a nutshell, ensemble biophysical techniques see only a blurred picture of the molecular events behind biological function and often lead to mistaken conclusions.

In recent decades, the development of single-molecule techniques has expanded our ability to monitor one molecule at a time, and has transformed our understanding of complicated biological processes. Investigating biological questions at the single-

molecule level is an inevitable trend in the application of molecular biophysics in both animal and plant systems. At present, single-molecule techniques can be classified into two branches: non-force based approaches, which are by means of fluorescence microscopy or spectroscopy and and nanopores without application of any extra force; and force-based approaches, which are delivered by force-based manipulation and force-based spectroscopy, including the use of optical tweezers, magnetic tweezers, tethered particle motion and atomic force microscopy (AFM) [312, 313]. Single-molecule force-based manipulation techniques are used to mimic and quantify some force-dependent processes, such as chromosome compaction, cell adhesion and muscle contraction. Among the former, fluorescence-based detection takes center stage amongst single-molecule techniques. On the one hand, fluorescence-based approaches not only provide high sensitivity but also high spatial and temporal resolution [314–316]. Using these techniques, fluorescence intensity, bleaching, Förster resonance energy transfer (FRET) [317, 318], fluorescence correlation spectroscopy (FCS) [319–322] and fluorescence lifetime [323–325] can be quantified, illustrating the flexibility and multiparametric nature of these approaches [326]. On the other hand, they can be developed into powerful tools for investigating molecular processes in living cells [327–329]. Overall, using single-molecule techniques, one can precisely control the reaction conditions, and uncover the mechanisms of macromolecule functioning, such as protein/DNA/RNA folding [330–333], protein–protein [334, 335], protein–DNA/RNA [336, 337] and protein-lipid interactions [338, 339]. For molecular assemblies, where the entity of interest is composed of multiple monomers (for instance, multimeric receptors or protein self-assembled aggregates) single molecule (sm) techniques can be referred to as single-particle (sp) techniques.

Another factor to be taken into account when thinking of single-molecule fluorescence experiments is the choice of a fluorophore. This should be, generally speaking, bright (high extinction coefficient and high quantum yield) to maximize signal, photostable (do not photobleach quickly) to allow the fluorophore to be imaged for long periods, small enough to not disrupt the biological activity of the labeled molecule and emit light in the visible region of the spectrum, preferably where the detection system has the highest quantum efficiency [340]. One of the most critical factors affecting single molecule experiments is detecting the low signal coming from a single fluorophore in what is likely a high background noise environment [341]. There is a wide variety of choice when it comes to fluorophore selection, all of which have their advantages and disadvantages based on the above criteria. The most popular of which would be organic dyes (*e. g.* AlexaFluor or Atto dyes), fluorescent proteins (*e. g.* GFP, YFP) and quantum dots [340]. The selection of a labeling method and fluorophore is vitally important and needs to be carefully balanced against the needs of the sample and specific experimental technique, as will be discussed in the following sections. In the case of organic dyes, mostly used for *in vitro* single-molecule techniques such as FRET and FCS (see next sections) [340], the fluorophore will be a small organic molecule attached covalently and, most frequently, site-specifically to a functional group of the biomolecule of interest.

Single-molecule techniques have at least two irreplaceable advantages. They allow single-molecular real-time traces, and they require small amounts of sample (as low as a 1 µL solution of 1 nM of molecule of interest in FCS, for instance) [340], which is

extremely important when handling precious material. By monitoring the action of a single molecule in real time, one can directly observe the behavior of targeted molecules, including static and dynamic details (**Fig. i.6B**), even in living cells [327, 328]. From the fluorescence time trajectories, one may directly capture reaction intermediates [20], which is challenging and often model-dependent in bulk assays. By constructing a histogram, one can directly obtain the distributions of macromolecular properties, which avoids the loss of information caused by averaging the measurements over a population. Thereby, the real heterogeneity of biomolecules can be unambiguously revealed. Additionally, by combining statistical analysis of stochastic trajectories with theoretical calculation [342], one can model the processes of given reactions, which would greatly advance our understanding of the underlying biological mechanisms involved.

5.2.1. Single-particle fluorescence (SPF) in amyloid research

Considering the research area of the present doctoral thesis, the power of single-particle fluorescence techniques in amyloid research deserves to be mentioned. As we have discussed elsewhere before, the amyloid aggregation landscape is heterogeneous in terms of structure, size and physicochemical properties of the protein assemblies. Such complexity hampers the analysis of the size, conformation and structure of the neurotoxic aggregates. In addition, monomers and small aggregates *in vivo* are likely to interconvert in a dynamic equilibrium [20, 343, 344], which would be extremely difficult to investigate under the blurry lens of ensemble averaging. Moreover, at physiological conditions, amyloidogenic proteins exist at a low concentration and vary between intracellular regions and brain cell types. For example, concentrations of αS in cerebrospinal fluid or bound to lipid vesicles might be likely in the low-nanomolar range [345, 346], while the soluble Aβ42 were only found at the picomolar levels in human AD brain entorhinal cortex and superior frontal gyrus regions [347, 348]. Such low concentrations are below the detection capability of conventional biophysical assays, but well within the detection limit of single-particle techniques. Thus, bulk techniques are most certainly insufficient for understanding the molecular mechanisms of aggregation, disaggregation nor to study the interaction of potential drug molecules to amyloid assemblies. These processes are highly complex owing to the heterogeneous nature of the amyloid species involved and the conformational changes that occur along the misfolding pathways and, hence, an accurate understanding of such events cannot be gained by ensemble averaging techniques.

To circumvent these caveats, single-particle techniques, particularly fluorescence-based, have emerged as a powerful experimental strategy over the past years. Even though application examples in amyloid research are mentioned here, the fundamentals of these techniques are described in more detail in section 6 of this introduction. For instance, FCS has been used to characterize the amyloid aggregation process and determine the presence of different oligomeric species, both in well-equilibrated systems *in vitro* and more complicated environments *in vivo* [349, 350]. Mittag et al. [351] fitted FCS data to gaussian distribution models to clearly distinguish different Aβ oligomeric species *in vitro*. FCS can also be used to quantitatively investigate the binding of amyloid proteins on membranes. Fluorescently labeled αS has been demonstrated to preferentially bind to acidic vesicles [351]. Less bulky head groups of anionic lipids enhance this binding

possibly due to the anionic lipids being able to pack more closely together, thus producing a high-charge density [352, 353]. Using FRET and two-color coincident detection (TCCD [354, 355]), direct observation of coincident bursts of oligomer fluorescence revealed two distinct structural types of αS oligomers during αS aggregation *in vitro* [20]. Additionally, they detected toxic αS oligomers originating from disaggregation of mature αS fibrils, suggesting that the disaggregation of fibrils can also be a source of toxic species and result in toxicity [20]. Later, Horrocks and co-workers combined fast flow microfluidics with FRET to investigate the oligomerization of αS [356]. Isolating type A from type B oligomers by dilution, they discovered that type A dissociates but type B stabilizes in the lower ionic strength of the solution. Moreover, type B oligomers from two αS mutant forms (A53T and A30P) displayed different FRET efficiencies, suggesting that the variants contribute to the structural diversity of oligomeric ensembles [356]. Also, recently, FRET has been used to identify the binding of Aβ oligomers to the A 7 nicotinic acetylcholine receptor (α7nAChR) [356], whose loss of activity is believed to impair cognitive performance in AD [356]. The result showed that the Aβ binding site on α7nAChR overlaps with the orthosteric ligand binding sites comprising loop C with a high-binding affinity. FRET was also used to evaluate different α7nAChR-related compounds of interfering with the binding abilities of Aβ to α7nAChR [356]. In addition, FRET was applied for the screening of various compounds against Zn^{2+}–Aβ interaction [356].

6. Time-resolved fluorescence techniques

Fluorescence measurements can be broadly classified into two types of measurements: steady-state and time-resolved. Steady-state measurements, the most common type, are those performed with constant illumination and observation. The sample is illuminated with a continuous beam of light, and the intensity or emission spectrum is recorded. Because of the nanosecond (ns) timescale in which fluorescence occurs [356], most measurements are steady-state measurements. When the sample is first exposed to light, steady state is reached almost immediately. The second type of measurement is time-resolved, which is used for measuring intensity decays or anisotropy decays. For these measurements, the sample is exposed to a pulse of light where the pulse width is typically shorter than the decay time of the sample [357–359]. This intensity decay is recorded with a high-speed detection system that permits the intensity or anisotropy to be measured on the ns-timescale (**Fig. i.7**). A steady-state observation is, thus, simply an average of the time-resolved phenomena over the intensity or anisotropy decay of the sample.

While steady-state fluorescence measurements are simple, nanosecond time-resolved measurements typically require sophisticated and expensive instrumentation [357–359]. Given the relationship between steady-state and time-resolved measurements, what exactly is the value of these more complex measurements? It turns out that much of the molecular information available from fluorescence is lost during the time averaging process. For instance, the precise shape of the anisotropy decay contains information about the shape of the macromolecule and its flexibility. Unfortunately, this shape information is lost during averaging of the anisotropy signal over the decay time [360, 361]. The intensity decays also contain information that is lost during the averaging

process [362]. As we have discussed before, macromolecules can exist in more than a single conformation, and the decay time of an attached probe may depend on the conformation of the biomolecule of interest. The intensity decay could for instance reveal two decay times, and thus the presence of more than one conformational state. The steady-state intensity will only reveal an average intensity dependent on a weighted average of the two decay times. There are numerous additional reasons for measuring time-resolved fluorescence. For instance, in the presence of energy transfer (see next sections of this introduction), the intensity decays reveal how acceptors are distributed in space around the donors [363, 364]. Also, time-resolved measurements reveal whether quenching is due to diffusion or to complex formation with the ground-state fluorophores [365, 366]. Importantly, time-resolved measurements are independent on changes in local concentration and fluorescence bleaching and fluorescence background can be easily subtracted. In fluorescence, much of the molecular information content is available only by time-resolved measurements.

Some of the most widely used time-resolved fluorescence techniques are fluorescence lifetime imaging microscopy (FLIM, **Fig. i.7A-D**) and single-particle techniques (**Fig. i.8**) such as fluorescence correlation spectroscopy (FCS) and Förster resonance energy transfer (spFRET, also called smFRET from "single-molecule"). Regardless of the nature of the output data (be it spectroscopy or microscopy), experiments with these techniques are typically performed on a confocal fluorescence (CF) microscope with high detection sensitivity and particular electronics to achieve high time resolution. An overview on the basis of these techniques and their particular technical requirements are provided in the following sections.

6.1. Fluorescence lifetime imaging (FLIM) microscopy

Conventionally, we define fluorescence lifetime (τ) as the average time that a fluorophore remains in its excited state [358]. Fluorescence lifetime can be measured in either the time-domain or frequency-domain [358], being the former the most widely used, including this doctoral thesis. Briefly, for time-domain methods, the sample is excited by a short laser pulse and the fluorescence decay is calculated either from the time-of-arrival of photons that are binned into a histogram [357, 362, 367, 368] or by time-gated detection [369] or pulse sampling techniques. If multiple fluorescent species are present, all species are summed into a single histogram. Since we have not used frequency-domain lifetime measurements in this thesis, it is not discussed in more detail in this introduction. Both time-domain and frequency-domain offer unique advantages and challenges in different FLIM applications including low photon budget, high dynamic range and high time resolution [323].

FLIM measures the fluorescence decay rate of a fluorophore on the timescale of sub-nanoseconds to hundreds of nanoseconds. Fast electronics coupled with efficient photon detectors have been integral tools for FLIM and other fast temporal measurements. In particular, time-correlated single photon counting (TCSPC) is used to determine the fluorescence lifetime [357, 358, 370]. With TCSPC, the time between sample excitation by a pulsed laser and the arrival of the emitted photon at the detector is measured. TCSPC requires a defined start, provided by the electronics triggering the laser pulse typically

on a photodiode, and a defined stop signal, realized by detection with single-photon sensitive detectors (*e. g.* single photon avalanche diodes, SPADs). The measurement of this time delay is repeated many times (one per each of the thousands of detected
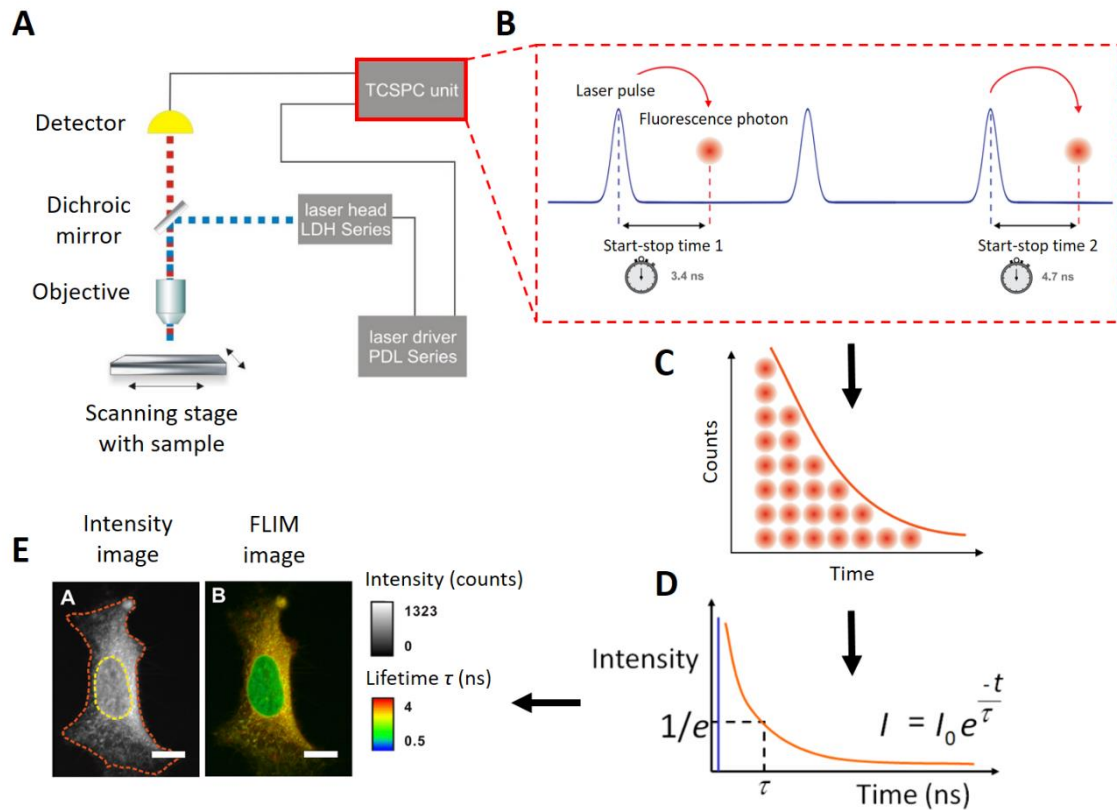
Fig. i.7. **Time-resolved fluorescence and fluorescence lifetime imaging microscopy (FLIM).** **A)** Experimental setup for time-resolved fluorescence data acquisition. The illustration shows a fluorescence microscope (most typically confocal) equipped with pulsed laser diode heads (LDH), laser-driving electronics (PDL) and time-correlated single photon counting (TCSPC) electronics. The stopwatch-like functioning of TCSPC is illustrated in panel **B**). Each fluorescence photon is tagged with the exact time of the excitation pulse it originated from and its arrival time at the detector. Then, the photon arrival time allows for obtaining the histogram shown in **C**). A generic lifetime (τ) decay curve and the basis for obtaining τ is shown in panel **D**. Panels **A-C**) are adapted from [370]. **E)** exemplary results using FLIM. Intensity-based imaging shows no differences between both selected areas (yellow and red dotted lines) while FLIM, applying the analysis shown in **D**) to every pixel of the image, is able to resolve those differences regardless of the fluorescence intensity and concentration of the sample. Adapted from [371].

photons in one experiment) to account for the stochastical nature of the fluorophore emission [372, 373]. The delay times are sorted into a lifetime (τ) histogram that plots theoccurrence of emission over time after the excitation pulse. In order to acquire a fluorescence lifetime image (FLIM), the photons have to be attributed to the different pixels, which is done by storing the absolute arrival times of the photons additionally to the relative arrival time in respect to the laser pulse. Line and frame marker signals from the scanner of the confocal microscope are additionally recorded in order to sort the time stream of photons into the different pixels (**Fig. i.7A-D**).

FLIM offers many unique advantages over intensity-based fluorescence microscopy (**Fig. i.7E**). Fluorescence intensity imaging provides information on the spatial distribution of fluorophores and can discriminate between fluorophores with distinct spectral properties. However, intensity alone cannot distinguish fluorophores with similar spectra or distinguish unique molecular environments around the same fluorophore. Given that τ is unique to each fluorophore, this technique is frequently used to discriminate spectrally overlapping fluorophores using their fluorescence lifetime. FLIM has gained popularity because of its high sensitivity to the molecular environment and changes in molecular conformation. Importantly, the fluorescence lifetime of a fluorophore does not depend on its concentration [323], making FLIM particularly well-suited for *in vivo* imaging [323, 374], where probe concentration is extremely challenging, if even possible, to control. This technique has been extensively used in autofluorescent molecular imaging to study cellular metabolism. FLIM of autofluorescent molecules provides unique insights into cellular health in a nondestructive manner and is often used to study live animals and as a contrast mechanism for fluorescence-guided surgery [375–377]. Exogenous fluorescent molecules that are capable of monitoring microenvironmental parameters, such as temperature, viscosity, pH, and ion concentration, are categorized as FLIM-based sensors [378–380]. These are a key advantage of FLIM given that they report on a whole new layer of information regarding the microenvironment of the probe, beyond intensity. Protein–protein interactions can be monitored using Förster resonance energy transfer (FRET) sensors that are specific for cellular signaling, cellular proliferation, cytokinesis, and other molecular interactions [381–383]. For using exogenous probe-based FLIM, fluorescent labelling of the biomolecules of interest is required, either by fusing a fluorescent protein [340, 384] or by an *in vitro* chemical reaction [340, 385].

In summary, leveraging both endogenous and exogenous fluorophores, FLIM can serve a myriad of applications such as local environmental sensing, detection of molecular interactions and conformational changes, background removal [385] or tissue characterization by auto-fluorescence.

6.2. Fluorescence correlation spectroscopy (FCS)

Fluorescence Correlation Spectroscopy (FCS) is a correlation analysis of temporal fluctuations of the fluorescence intensity [320–322, 386]. It offers insights into the photophysics that cause these characteristic fluorescence intensity fluctuations as well as diffusive behaviour and absolute concentrations of detected particles, as illustrated in **Fig. i.8D** [319]. FCS is based on the analysis of time correlations in fluorescence fluctuations emitted when fluorescently labeled molecules are diffusing in and out of a tiny observation volume [322, 387]. These intensity changes can be quantified in their strength and duration by temporally auto-correlating the recorded intensity signal, leading to the average number of fluorescent particles in the detection volume and their average diffusion time through the volume. Eventually, important biochemical parameters such as the concentration [320, 388] and size [320, 388] or shape of the particle (or molecule) as well as the viscosity of the environment [389, 390] can be determined. For instance, the larger a molecule or a particle is, the more slowly it will freely diffuse through the confocal volume, and the larger the auto-correlation times of its fluctuations

will be. The opposite is true for smaller-sized species. Regarding sample concentration, we need to think of the impact of the amount of molecules on the auto-correlation decay. Shortly, if we have only one molecule in the focus at a given time point, that molecule diffusing out of the focus will have a great impact on the auto-correlation amplitude, which will decay immediately. However, if we have tens of molecules, it is reasonable to think that one of them leaving the focus will not change the auto-correlation signal significantly. This is why the auto-correlation signal depends inversely on the fluorescent species concentration. Essentially, FCS is the fluorescent analog of dynamic light scattering (DLS), but with the ability to distinguish molecules of interest from others spectrally, thus being species-specific and virtually inmune to artifacts arising from any unlabeled molecules. FCS is a very sensitive analytical tool provided that it observes a small number of molecules (nanomolar to picomolar concentrations) in a small volume (typically ~ 1 fL). This concentration range fits to naturally occurring concentrations [391]. Considering all the above, FCS is the perfect method to provide quantitative answers on diffusing molecules from within unperturbed compartments, like cells. Besides, sample volumes as little as 1 μL can be used for fast measurements, making FCS an incredibly sample-efficient technique. The temporal resolution of FCS can reach the low nanosecond range, so it allows detecting molecular diffusion as well as conformational changes and dye photophysics [319, 392] both *in vitro* and *in vivo* [393–395].

Regarding its implementation, FCS is often performed in a confocal system where the fluorescence emitted from the labeled molecules in the observation volume is collected by the same high numerical aperture objective lens, and propagate along the opposite direction to that of the excitation light. After passing through a dichroic mirror, the fluorescence is focused through a pinhole onto an avalanche photodiode (APD). The fluorescence emitted in the out-of-focus region is rejected by the pinhole, and therefore, it does not reach the detector. Consequently, the pinhole reduces the axial extension of the observation volume. Such confined observation volume enhances the signal-to-noise ratio significantly and also reduces the measurement time needed to obtain a decent correlation curve. Despite a continuous-wave (CW) laser is available for FCS, the usage of pulsed lasers for excitation and time-correlated single-photon counting (TCSPC) for detection is preferable for the rejection of environmental background and also allows performing dual-color FCCS [396, 397] (see next section, 6.2.1) in a pulsed interleaved excitation (PIE) [398] scheme. Using pulsed lasers allows even more sophisticated analysis possibilities like fluorescence lifetime correlation spectroscopy (FLCS) [399, 400] to eliminate background or spectral crosstalk from the analysis and also offers a way around after-pulsing artifacts [399]. In these approaches, several excitation sources are interleaved so that fluorescence excited by a light pulse decays completely before arrival of the next excitation pulse. The information on the excitation source for every detected photoelectron event is known, and hence the cross-talk between two spectral channels is eliminated.

In an FCS experiment, the fluorescence as a stream of single photon arrival times is the primary, raw data. Although already containing the full information of the single molecule dynamics, these raw data have to undergo several steps of processing until the parameters of interest (*e. g.* concentrations or diffusion coefficients) can be determined

[319, 320]. Due to the free diffusion of molecules by nature, an intensity fluctuation over time $F(t)$ will take place when the molecules are diffusing in and out of the observation volume. Then, in a first step, the auto-correlation of $F(t)$ is calculated with:

$$G(\tau) = \frac{\langle \delta F(t)\, \delta F(t+\tau) \rangle}{\langle F(t) \rangle^2} - 1 \qquad \textbf{(Eq. i.1)},$$

where $G(\tau)$ is the auto-correlation amplitude at a given τ, $F(t)$ is the fluorescence intensity at time t, $\langle F(t) \rangle = (1/T) \int_0^T F(t)\, \delta t$ denotes the time average of the signal, $\delta F(t) = (F(t) - F(t)$ are the fluctuations around the mean value $F(t)$ and τ is the correlation or lag time. The auto-correlation curve measures the self-similarity of the signal, reflecting the probability that the signal at different times still belongs to the same molecular event. Therefore, the decay time τ_D (also termed diffusion time) of the auto-correlation curve is related to the residence time of the molecules in the detection volume. The amplitude is inversely proportional to the average number of observed molecules N in the detection volume V (or V_{eff}), which is calibrated experimentally (see chapter 3 of this thesis) and therefore to the concentration C of the fluorescent particles in solution, such that

$$G(0) = \frac{1}{N} = \frac{1}{VC} \qquad \textbf{(Eq. i.2)},$$

where $G(0)$ is the auto-correlation amplitude when $\tau = 0$. In general, it is not only the diffusion through the detection volume that leads to fluctuations in the intensity. Other sources are internal dynamics, the rotation of the fluorophores connected to varying excitation probabilities, or photophysical fluctuations, $e.\ g.$ due to population of the triplet state. From the inspection of $G(\tau)$ it is already possible to learn a lot about the dynamics of the fluorescent molecules. A precise quantitative determination of the parameters of interest, however, requires the fitting of the experimental auto-correlation curve by a model function, the correlation function, which describes the sources of the intensity fluctuations. The correlation function depends on the parameters of interest (fitting parameters), which are varied during the fitting process to minimize the difference between the experimental correlation curve and the model at each time point τ. The particular expression of the correlation function used for data analysis depends on both the shape of the detection volume, $i.\ e.$ on the optical set-up, and the molecular sources of fluorescence intensity fluctuations. A good approximation for molecules undergoing free diffusion through a confocal detection volume is a three-dimensional gaussian profile:

$$G(\tau) = \frac{1}{N}\left(1 + \frac{\tau}{\tau_D}\right)^{-1}\left(1 + \frac{\tau}{S^2 \tau_D}\right)^{-1/2} \qquad \textbf{(Eq. i.3)},$$

where $N = VC$ is the average number of particles in the effective detection volume $V = \pi^{3/2} w_0^3 S$, where S is the aspect ratio of the detection volume and w_0 is its size ($1/e^2$ radius). The diffusion time $\tau_D = w_0^2/4D$ can be used to calculate the diffusion coefficient D. However, to determine concentrations and diffusion coefficients from N and τ_D, it is necessary to know the parameters describing the geometry of the detection volume, $i.\ e.$

w_0 and S. These parameters are usually determined by a calibration measurement using a dye with a known diffusion coefficient. Clearly, the biomolecular concentration, *e. g.* of a protein, is an interesting parameter. But what does its diffusion coefficient D tell us? According to the Stokes-Einstein-equation it depends mainly on two important parameters: the hydrodynamic radius of the diffusing molecule R_H and the micro-viscosity of the surrounding medium η:

$$D = \frac{k_B T}{6\pi \, \eta \, R_H} \tag{Eq. i.4}.$$

6.2.1. Dual-color fluorescence cross-correlation spectroscopy (dcFCCS) for studying molecular interactions

If one wanted to measure molecular binding, conventional FCS is only available when the interaction leads to a resolvable change in diffusion time, compared to individual molecules, and depends on accurately fitting the autocorrelation curves with a model [399]. For instance, in globular proteins the diffusion coefficient is approximately proportional to the cubic root of the molecular weight, and therefore at least an order of magnitude change in the molecular weight upon binding is required to observe the binding reaction in the fluorescence auto-correlation. This application will be further handicapped when uninteresting molecules are bound to the fluorescently labeled molecules [399]. Dual-color FCS (dcFCCS) is a preferable technique to detect molecular binding without these limitations [396, 397]. dcFCCS is an extension of FCS which correlates signal originating from two different fluorophores detected in two channels with each other, as depicted in **Fig. i.8D**. When two spectrally different fluorophores are attached to two molecules, dcFCCS results in information of the degree of coinciding occurrence in the optical volume [396, 397, 401]. Through this we can learn about the degree of interaction between the fluorophores. This technique therefore offers access to molecular binding at low molecular concentrations in solution [174] as well as unperturbed systems like living cells [402]. Remarkably, tiny fractions of doubly labeled particles can be detected on the background of larger amounts of singly labeled particles, irrespective of whether their diffusion coefficients differ significantly or not.

The concept of dcFCCS was first proposed by Eigen and Rigler [397], and was first realized experimentally by Schwille *et. al* [396]. In dcFCCS, two species of interest are labeled with two different types of spectrally distinct fluorophores, respectively, indicated with the subscript "r" (red) and "g" (green) for simplicity. The following equations and theory assume that the "red" molecules are the receptor and the "green" molecules are the ligand. Upon the excitation of the red and green fluorophores, the fluorescence from each of the fluorophores (F_g and F_r, respectively) is separated and counted into two detection channels, respectively. The auto-correlations of the intensity traces $F_g(t)$ and $F_r(t)$ from the two-color channels are calculated with **Eq.** i.1 yielding, respectively, $G_g(\tau)$ and $G_r(\tau)$. When molecules interact, they form complexes containing both fluorophores. In turn, this introduces a synchronized intensity fluctuation in the two channels when the complexes diffuse into and out of the focal volume. Accordingly,

the presence of the complexes can be analyzed with the cross-correlation $G_{gr}(\tau)$ of the two-color intensity traces:

$$G_{gr}(\tau) = \frac{\langle \delta F_g(t)\, \delta F_r(t+\tau)\rangle}{\langle F_r(t)\rangle\langle F_g(t)\rangle} - 1 \qquad \textbf{(Eq. i.5).}$$

There is only a positive contribution to the cross-correlation amplitude if the two species interact and diffuse as a single entity through the detection volume. Therefore, dual-color FCS measures dynamic co-localization of differently colored molecules during their transit through the focal volume. Then, the degree of binding can be quantified from the amplitude of the cross-correlation curve $G_{gr}(\tau)$ and the ligand autocorrelation (G_L) curve with $G_{gr}(0)/G_L(0)$ (relative cross-correlation). From here, Krüger *et. al.* developed a theoretical framework which was tested experimentally to obtain binding parameters from dcFCCS experiments [338]. In summary, the degree of ligand binding N_L (number of bound ligand molecules) can be calculated from the absolute cross-correlation amplitude as

$$\langle N_L\rangle = G_{gr}(0)\, V_{gr}\, C_L^0 \qquad \textbf{(Eq. i.6),}$$

where the absolute ligand concentration C_L^0 is obtained directly from the autocorrelation function (in this case, $G_g(0)$) and the free ligand concentration C_L^{free} from the relative cross-correlation as

$$C_L^{free} = C_L^0 \left(1 - \frac{1 + \langle N_L\rangle}{\langle N_L\rangle} \frac{G_{gr}(0)}{G_r(0)} \frac{V_{gr}}{V_r}\right) \qquad \textbf{(Eq. i.7).}$$

If we perform a ligand titration experiment, plotting N_L versus C_L^{free} yields a standard, binding model-independent ligand binding curve [402]. The half-saturation point of this curve allows for an estimation of the affinity of the ligand for the receptor. Further, the ligand binding curve (N_L versus C_L^{free}) is the basis for testing any specific binding model [402]. One can use the model of N_{max} identical and independent binding sites (non-cooperative binding [402]), which is also referred to as the Langmuir isotherm:

$$\langle N_L\rangle = N_{max}\left(\frac{C_L^{free}/N_A}{K_D + \left(C_L^{free}/N_A\right)}\right) \qquad \textbf{(Eq. i.8),}$$

where N_A is Avogadro's number and the dissociation constant K_D indicates the molar concentration of free protein at which half of the binding sites are occupied.

More details on the theoretical basis behind these equations can be found in [338]. The effect of artifacts such as spectral cross-talk on cross-correlation amplitudes is extensively discussed in [402]. Technical aspects, including a discussion of the focal geometry, background and spectral cross-talk correction, as well as detailed treatment of the two-component binding equilibria as studied by dcFCCS, are presented in [402]. In this thesis, as mentioned above, a PIE scheme in combination with time-gated detection was used to remove spectral cross-talk and background noise.

6.3. Dual-color single-particle fluorescence spectroscopy (dcSPFS)

Freely-diffusing molecules in single-molecule or single particle confocal fluorescence techniques can take different paths as they diffuse through the laser focus, giving rise to a variation in the excitation rate of the fluorophore and hence the fluorescence intensity detected (**Fig. i.8A, B**). In order to address this issue, ratiometric methods have been developed where two different fluorophores are attached to the same biomolecule and the ratio of their fluorescence intensities is measured as they diffuse across the laser-excited volume [403–405]. In these techniques, an experimental setup similar to that described for FCS is used, including TCSPC, PIE and SPADs. However, two lasers are typically used in dcSPFS, and are required for performing PIE-dcSPFS. Generally speaking, the two fluorophores are excited independently by two different spatially overlapped lasers and coincident fluorescent photons are detected as the molecule diffuses across the laser-excited focal volume V_{eff} or simply V [404, 405]. Two-color coincidence detection (TCCD, **Fig. i.8C**) [354, 406] is based on detecting fluorescence photons emitted at two distinct frequency bands arising from continuous excitation of the confocal volume by one or two lasers. Although in some cases one laser is sufficient, it is usually very advantageous to be able to excite the two fluorophores with two independent lasers. This allows the fluorophores to be placed at any convenient positions on the biomolecule without any requirement to place them close for FRET (see next section), which may not be possible if there is no information on the structure of the complex. In addition, a broader application of TCCD allows us to sensitively detect associated molecules when the fluorophores are placed in different subunits of a biomolecular complex [354, 406, 407]. Analysis of the frequency and intensity of coincident fluorescence bursts on both channels allows us to quantify and determine the amount and stoichiometries of the associated molecules [354, 407]. One important advantage of TCCD is that it removes the constraints on the labelling of biological molecules, allowing single-molecule methods to be applied to systems whose structure and stoichiometry is unknown, and this has allowed the application of TCCD to a wide range of biological and biomedical problems. In addition, TCCD allows ultrasensitive detection of biomolecules and the measurement of intramolecular dynamics [407]. TCCD has also been shown to be less sensitive to background fluorescence than single-colour detection and to be capable of detecting femtomolar levels of molecular complexes [407].

A Free diffusion-based time-resolved single-particle fluorescence detection

~100 pM

Glass chamber ~10 uL

Objective

Dichroic mirror

Optical fiber

130 ps

Pulsed lasers

Pinhole

Polarizing beam splitter

F1

II

APD1

TCSPC

Avalanche photodiodes

APD2

Simultaneous direct monitoring of each particle

B

Red channel

Green channel

Intensity

Time

Intensity ratios

C TCCD, Stoichiometry

Blue dye

Red dye

Red (counts)

Blue (counts)

Time

FRET

FRET efficiency, E

E

E

Fluorophore distance R_{AD} (nm)

Fluctuation analysis

D FCS

$G(\tau)$

slower diffusion

higher concentration

τ [ms]

Green intensity $I_g(t)$

Red intensity $I_r(t)$

Fluorescence intensity

Time t

Many dimers:

G
R
GR

Diffusing particles

Green/red observation volume

dcFCS

Green autocorrelation
Red autocorrelation
Cross-correlation

Correlation function

Increasing relative concentration of

No

Lag time T

78

Fig. i.8. **Dual-color single-particle time-resolved fluorescence spectroscopy**. Dual-color single-particle time-resolved fluorescence spectroscopy. **A)** A typical experimental setup based on a confocal microscope for spTCCD, spFRET, FCS and scFCCS is shown. Briefly, two pulsed laser diode heads (LDH) are used in pulse-interleaved excitation (PIE) mode and avalanche potodiodes (APDs) serve as single molecule-sensitive detectors. LDHs and APDs are synchronized with a time-correlated single photon counting (TCSPC) device, which enables exquisite temporal resolution as well as further data analysis such as a correlation in FCS/dcFCCS. In this example, 3 molecules labelled doubly with a green and red dye each pass through the focal volume (depicted here as a green laser beam for simplicity) and, every time they go across the volume the emitted green and red photons are detected as it is depicted in panel **B**). This photon stream can then be analyzed considering the intensity ratios (**C**) or by fluctuation analysis (**D**). **C)** TCCD analysis (left) quantifies the ratio between green (here shown as blue) and red photons for each individual molecule and enables stoichiometry determination. In this example, the presence of molecular complexes is investigated. Adapted from [407]. FRET efficiency *E* (right) depends in inter-dye distance and enables quantifying molecular changes within the 2-10 nm range. **D)** FCS analysis from fluorescence intensity fluctuations (center) allows obtaining diffusion and concentration of labelled freely diffusing molecules and dcFCCS (right) is capable of quantifying molecular binding of two distinctly labelled molecules by monitoring those diffusion events where both dyes are present, termed, therefore, co-diffusion. Panel D) is adapted from [407].

Coincident events are analysed to extract the amount and stoichiometry of the complex studied [354, 355]. The frequency of coincident fluorescence bursts provides quantification of the complex, via the association quotient [355]. The apparent stoichiometry (S_{app}) is then obtained by forming ratio histograms of $\ln(F_g/(F_g+F_r))$, where F_r and F_g are the number of fluorescence photons detected during the coincident burst in the red and the green channel respectively [355, 408]. However, whenever FRET is present in a dual-color sample (as it is the case in the present thesis, *see* chapter 3), to accurately determine *S* we need to take into account certain corrections that are inherent to the technique in intensity-based calculations [409]: i) the bleedthrough of photons emitted by the donor into the acceptor channel (α) and ii) the direct excitation of acceptor molecules with the donor specific wavelength (δ). Additionally, a correction factor for the different detection efficiencies θ^{det} in both channels is defined as γ and, similarly, a correction factor for the different excitation efficiencies in both channels is defined as β. α and δ can be experimentally obtained while γ and β can be calculated from the technical data of the dyes and the microscope setup [409]. By applying these corrections, we can calculate *S* as

$$S = \frac{F_{DA} - \alpha F_{DD} - \delta F_{AA} + \gamma F_{DD}}{F_{DA} - \alpha F_{DD} - \delta F_{AA} + \gamma F_{DD} + (F_{DD}/\beta)} \qquad \textbf{(Eq. i.9)}.$$

The subscripts are expressed in a FRET context, where F_{DD} and F_{AA} are the donor ("green" dye) and acceptor ("red" dye) emission after direct excitation, respectively, and F_{DA} is the sensitized emission or acceptor indirect excitation through energy transfer of after donor excitation.

Finally, If the molecular brightness η_B (the number of photons emitted by one molecule per unit of time) of each species is known, this ratio can be used to obtain the number of

molecules of each species (color) that are forming the molecular complex. More details on the application of this approach to obtain stoichiometries of molecular complexes can be found in chapter 3 of this thesis.

6.3.1. Single-particle Förster resonance energy transfer (spFRET)

Förster resonance energy transfer (FRET) describes the physical phenomenon of energy transfer between two photosensitive molecules, rendering convenient for real-time dynamic research of molecules under various physiological conditions [332, 333, 410, 411]. FRET was first proposed in 1948 by Theodor Förster [318]. In FRET, energy from the excited donor chromophore may transfer to an acceptor chromophore in proximity through nonradioactive dipole–dipole coupling provided that the emission spectra of the donor and the absorption spectra of the acceptor overlap to some extent. Besides the overlap of spectra, the donor should have a sufficiently durative fluorescence lifetime and sit close enough to the acceptor to permit energy transfer to occur. So it is necessary to find a suitable donor–acceptor pair to satisfy the conditions for effective energy transfer. FRET efficiency (E) is inversely proportional to the sixth power of the distance (r) separating donor and acceptor [285, 318, 358], expressed as the formula below:

$$E = \frac{1}{1 + \left(\frac{r}{R_0}\right)^6} \tag{Eq. i.10},$$

where R_0 is the distance when the energy transfer efficiency is 50 %, called Förster distance, depending on the refractive index of the solution, the overlap integral of the donor emission spectrum with the acceptor absorption spectrum and their relative dipole moment orientation. Typically, the distance between the chromophore pair can be well distinguished at the range of 1–10 nanometers, making FRET efficiency extremely sensitive to small changes of distance in the scale where a large number of biomolecular conformational changes occur (**Fig. i.8C**). Therefore, FRET is a sensitive tool to obtain structural information of macromolecules and determine the distance between two molecules within several nanometers. FRET is referred to as an effective "spectroscopic ruler" due to the above characteristics. Several methods have served as options for FRET detection. One of the most common methods is to measure the increase of acceptor emission arising from the energy transfer from the donor (F_{DA}) [409] such as

$$E = \frac{F_{DA}}{F_{DA} + F_{DD}} \tag{Eq. i.11}.$$

Because this approach is based on fluorescence intensities, te same correction factors mentioned in the previous section must be used in order to determine FRET efficiency E accurately, such that

$$E = \frac{F_{DA} - \alpha F_{DD} - \delta F_{AA}}{F_{DA} - \alpha F_{DD} - \delta F_{AA} + \gamma F_{DD}} \tag{Eq. i.12}.$$

Similarly, FRET efficiency can also be inferred from the donor fluorescence lifetime changes [409] using the following equation

$$E = 1 - \frac{\tau_{\mathrm{DA}}}{\tau_{\mathrm{DD}}} \qquad \textbf{(Eq. i.13)},$$

where τ_{DA} and τ_{DD} are the fluorescence lifetimes of the donor dye in the presence and absence (donor-only sample) of FRET, respectively. This approach is far less sensitive to artifacts than intensity-based methods and thus is not correction-dependent. However, time-resolved fluorescence equipment is required for lifetime-based FRET efficiency determination, making it a less widely accessible method. Another strategy is to monitor the photobleaching rates of the donor in the presence and absence of an acceptor, as the acceptor competes with the photobleaching pathways [412, 413].

smFRET provides *E* values of lots of individual molecules wherein the single pair of donor and acceptor is excited and detected, which allows a more precise analysis of heterogeneous populations. smFRET is able to monitor the short-lived populations in transition states [20, 317, 414, 415]. that are hard to characterize by ensemble FRET. Moreover, by tracking specific molecules, smFRET can measure system changes in equilibrium [415]. Intramolecular smFRET is usually used to identify dynamic or static (in equilibrium) subtle structural differences of biomacromolecular states, especially for proteins. It is, therefore, particularly useful to study protein folding and conformational reconfiguration upon binding or during functioning. On the other hand, intermolecular smFRET is highly suitable for characterising bimolecular interactions. Some typical examples, including receptor and antigen interactions [416, 417], vesicle fusion [418–420] and ion channel dynamics also relate to the conformational changes and equilibrium properties of molecules [421]. More details on our application of single-particle fluorescence spectroscopy to investigate the formation of molecular complexes can be found in chapter 3 of this thesis.

Overall, time-resolved and single-particle dual-color fluorescence techniques are among the most powerful tools at hand for 'looking' at real time dynamics and interactions of biomolecules and macromolecular complexes with spectral specificity and exquisite spatial and temporal resolution.

Chapter 1

Pyrene Fluorescence Spectroscopy reveals Antiparallel Architecture of *α*-Synuclein Amyloid Fibrils formed through Homogeneous Nucleation in Limited Hydration Conditions

Introduction

A number of neurodegenerative disorders collectively known as synucleinopathies exhibit the aberrant aggregation of α-synuclein (αS) as a common differential trait [47]. This aggregation has been extensively reproduced *in vitro* over the past decades revealing the currently established cross-β structure of amyloid aggregates [258]. Owing to the ability of the fluroescent probe thioflavin-T (ThT) to bind amyloid structures, the kinetics of this process has been characterized. Typically, it follows a sigmoidal kinetic profile that reflects a nucleated self-assembly reaction with an energetically-disfavored primary nucleation-associated lag-phase [422, 423] and a subsequent energetically-favored exponential templated growth phase. While significant advances have been made in our understanding on some of the microscopic processes that take place during the macroscopic self-assembly reaction, the factors that initiate primary nucleation and the molecular reorganizations that occur during the early stages remain largely unknown and a hot topic with open questions in the field. The nature of the early aggregate nuclei formed will govern the structural features of the eventually neurotoxic, mature amyloid aggregates generated, which seems to be disease-specific [424]. Therefore, it seems evident that characterizing primary nucleation in detail is of outmost importance to further understand the overall amyloid aggregation mechanism and design new strategies to inhibit or prevent it. In fact, it must be noted that the amyloid aggregates found *in vitro* in different synucleinopathies differ structurally from those generated *in vitro* [425, 426]. Besides this, in cellular and animal models of synucleinopathies, the mere overexpression of αS is insufficient for inducing aggregation, and additional treatments are required for it [427], which suggests that particular, yet unknown, cellular microenvironments are optimum for triggering αS nucleation.

These two major discrepancies between *in vitro* aggregation and what is observed in disease could likely stem from particular experimental conditions and requirements to trigger and study amyloid aggregation of αS in the test tube. Specifically, a combination of strong stirring or shearing forces, over-physiological protein concentrations (50-100 µM, [85, 428] and the presence of hydrophilic/hydrophobic interfaces [428–430] have been widely used to promote aggregation. Among these, the latter seem to play a major role in causing the first contacts between αS monomers thus leading to the formation of the primary aggregation nuclei under the typical *in vitro* conditions used [424, 430]. The aggregation process, thus, is generally triggered at particular types of surfaces in what is called heterogeneous nucleation [428, 431]. A variety of hydrophilic/hydrophobic interfaces have proven capable of recruiting αS monomers owing to the amphipathic nature of the protein [88]: the air/water interface [428–430] (in a test tube, plate well, microscopy slide…), non-physiological, anionic lipid vesicles [432, 433] or polytetrafluoroethylene (PTFE) beads [75, 433–435]. Recently, αS has also been shown to undergo amyloid aggregation *in vitro* and *in vivo* under what is known as liquid-liquid phase separation (LLPS) [97, 98, 436].

The amyloid structures resulting from all these experimental conditions, except for LLPS, where it was unknown before our investigations, give rise to the well-known parallel β-sheet architecture [39, 424, 437], where each monomer of αS (protomer) is stacked to its neighbors perpendicularly to the fibril axis and in parallel with its neighboring protomers. To address the aforementioned open questions regarding primary nucleation and broaden the conformational landscape of αS amyloid aggregation, we tested whether nucleation may occur in the bulk of a solution without the need of an interface. Interestingly, we found that αS can indeed self-assemble into amyloid structures in the absence of a hydrophobic/hydrophilic interface under conditions of low hydration. When doing so, the lag-phase was either reduced dramatically or virtually non-existent and the protein concentration required was also decreased by an order of magnitude down to physiological concentrations. Strikingly, the characterization of the resulting aggregates by infrared (IR) spectroscopy suggested an antiparallel topology of the monomeric units under these conditions, an amyloid architecture only seen in other proteins and, for αS, in type B* oligomers up to now [87, 92, 94, 438–440]. Because the interpretation of IR spectra for determining parallel and antiparallel β-sheets in amyloids is still under debate [441, 442], we decided to develop a new experimental strategy to confirm this novel topology. With this, we expected to establish an unambiguous approach to understand the primary nucleation mechanism of these and possible upcoming amyloid aggregation pathways. To this end, we resorted to the small organic fluorescent probe pyrene, which exhibits some unique spectral properties and has proven useful in studying αS aggregation in previous studies [443]. When two pyrene rings are found in close proximity (1 nm or less), a new fluorescent species termed "excimer" arises, which shows an emission band at approximately 470 nm in addition to the typical bands of monomeric pyrene at 375-395 nm (Bands I, II, III and IV) (see general introduction for more detailed information). Moreover, the relative intensity of the so-called pyrene monomer bands I and III report on the polarity of the probe and thus reveals valuable information regarding the microenvironment where the probe is located. For more detailed information and relevant literature, *see* section 5 of the general introduction. We hypothesized that fluorescence spectroscopy of pyrene-labelled proteins would thus be a powerful tool for telling apart parallel and antiparallel amyloid topologies in aggregates generated under different conditions. By applying this approach to αS, we could validate the data obtained by IR and, overall, the novel homogeneous nucleation and the role of protein hydration in amyloid aggregation proposed by our group. To this end, we labelled αS with a maleimide derivative of pyrene (pyr-maleimide) in different positions of the aminoacidic sequence and set up a quantititive ratiometric analysis to study the molecular arrangement of amyloid assemblies formed under different aggregation conditions. In our work, the combination of pyrene fluorescence spectroscopy and the kinetic and structural studies performed by Dr. José Camino shows how water plays a critical role in selecting one amyloid path over multiple others. Interestingly, we also found that homogeneous nucleation seems to trigger amyloid aggregation of αS under conditions of liquid-liquid phase separation.

Specific aims

- Establish and optimize a pyrene fluorescence-based methodology to discriminate the parallel or antiparallel topology of amyloid aggregates of αS.

- Gain insight into the stability of αS amyloid aggregates formed by heterogeneous and homogeneous primary nucleation mechanism and the reversibility between both mechanisms.

- Determine whether the pyrene strategy can be complementary to IR spectroscopy in terms of amyloid topology identification.

- Elucidate the type of nucleation mechanism that triggers amyloid aggregation of αS upon liquid-liquid phase separation.

Results & Discussion

1. Reduced hydration conditions trigger fast amyloid aggregation of αS in the absence of a hydrophilic/hydophobic interface

During his PhD thesis, Dr. José Camino made a tremendous effort to discover and characterize novel amyloid aggregation routes of αS *in vitro*. His findings are the starting point of my work in this chapter and, together with my results, were published in Chemical Science in 2020 [292]. First, we recapitulated the aggregation of αS using hyprophilic/hydophobic interfaces such as air/water (500 μM αS) and small unilamellar vesicles (SUVs, 100 μM αS) made of dimyristoyl phosphatidylserine (DMPS) in aggregation buffer (AB) (PBS, pH 7.4 (**Fig. 1.1**). As expected, a sigmoidal thioflavin-T (ThT) kinetic profile was obtained with a lag-time (τ_{lag}) of several hours (> 10 h, **Fig. 1.1A**), corresponding to a slowheterogeneous nucleation process with a high kinetic barrier. The aggregates formed at the end of the reaction (plateau phase) were isolated by centrifugation and their IR spectra were analyzed (**Fig. 1.1B**), yielding very similar results independently of the hyprophilic/hydophobic interface used. In particular, the typical IR absorption band at ca. 1625 - 1615 cm^{-1} associated with intermolecular β-sheet, hallmark of amyloid aggregates [444, 445], was observed. Together with the absence of an absorption band at ca. 1690 cm^{-1}, the presence of a band peaking at ca. 1620 cm^{-1} is indicative of an intermolecular parallel β-sheet architecture. Atomic force microscopy (AFM) revealed the typical fibrillar shape of the aggregates (**Fig. 1.1C**). Under this conditions, in the absence of a hydrophilic/hydrophobic interface, αS did not aggregate even at concentrations as high as 500 μM αS during more than two weeks of incubation at 37 ºC (not shown, *see* [292]).
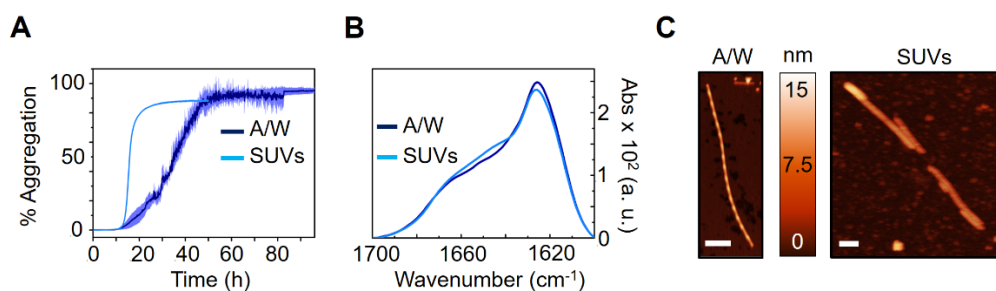
Fig. 1.1. Characterization of αS aggregation at typical hydrophobic/hydrophilic interfaces. **A**) Aggregation kinetics of 500 μM αS under shaking conditions (700 rpm) in air/water (A/W) interface dark blue) and 100 μM αS under quiescent conditions in the presence of DMPS SUVs (light blue). The standard deviation from a triplicate experiment for each curve is shown in lighter colors. **B**) IR spectra of the conditions shown in **A**). **C**) Representative AFM images of the aggregates formed in the conditions shown in **A**) and **B**). Scale bar: 200 nm. Data adapted with permission of Dr. José D. Camino.

However, when additives known to reduce the protein hydration layer in aqueous solutions such as methanol (MeOH) or NaCl were added in the same buffering conditions, much faster aggregation reactions were observed (**Fig. 1.2**) even in the absence of shaking and shearing. Despite not being found in the cell at high

concentrations, we found these additives a good model for understanding the role of water and protein hydration in amyloid nucleation, in line with previous reports [446, 447]. Microfluidic mixing and surface tension experiments performed by Dr. José Camino (not shown) further proved that, for the first time to our knowledge, we found experimental conditions where no active interface was required for triggering amyloid aggregation, pointing to a homogeneous nucleation mechanism. In particular, two kinetic aggregation regimes were observed upon increasing MeOH concentrations from 5 to 40 % (v/v) or NaCl concentrations from 0.5 to 3.5 M (similar behaviors were observed using other types of alcohols or kosmotropic salts). In the presence of either of these additives at moderate concentrations, the aggregation τ_{lag} was reduced but remained in a timescale of hours, thus still implying a high nucleation energy barrier (**Fig. 1.2A** and **B**). At a certain additive concentration, however, τ_{lag} was remarkably reduced from hours to seconds (or even lower), indicating that under these conditions the energy barrier is drastically low, and nucleation seems to occur almost instantly.
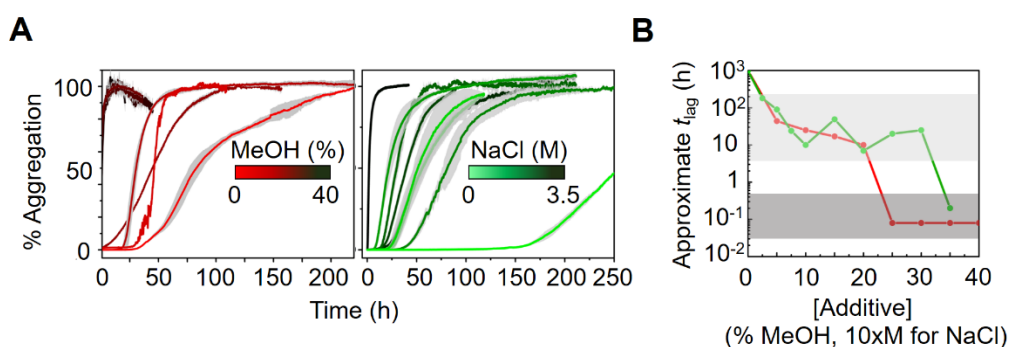
Fig. 1.2. Kinetic characterization of αS aggregation in the presence of different alcohol and salt. **A**) Aggregation kinetics of 100 μM αS under quiescent conditions in the presence of increasing concentrations of MeOH (left) or NaCl (right). Darker colors indicate higher concentrations of the additive. The gray-shaded pattern show the standard deviation from a triplicate experiment for each curve. **B**) The approximate aggregation τ_{lag} is shown for the different alcohol (red) and NaCl (green) concentrations. The parallel and antiparallel aggregation regimes are denoted as light and dark gray rectangles, respectively. Data adapted with permission of Dr. José D. Camino.

To investigate these two regimes in more detail, we focused on conditions that were representative of each of them. In particular, 10 % vs 35 % MeOH (M10 and M35) and 2 M vs 3.5 M NaCl (N2 and N3.5) were compared (**Fig. 1.3**). Morphologically, all the aggregates formed upon the addition of dehydrating agents were smaller and almost globular as seen by AFM (**Fig. 1.3C**). Alongside these differences, IR spectra revealed a low-frequency shift of the main β-sheet band and a new absorption band at 1690 cm^{-1} (**Fig. 1.3B**) that was not present in those aggregates formed in the presence of hydrophilic/hydrophobic interfaces. This low-frequency band was putatively pointing toward an antiparallel arrangement of the β-sheeted protomers within the aggregates, as it was proposed previously [442, 448, 449]. Due to the current lack of agreement in the field regarding the interpretation of this IR signature [441], a new experimental strategy based on the fluorescence probe pyrene was envisioned.
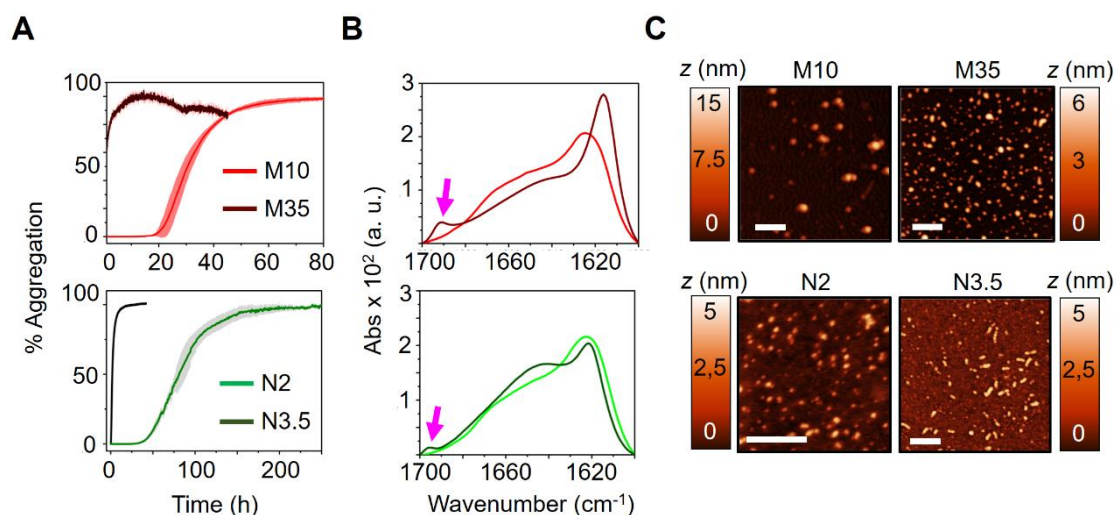
Fig. 1.3. Structural characterization of αS aggregation in the presence of low and mild alcohol and salt concentrations. **A**) Aggregation kinetics of 100 μM αS in quiescent conditions in the presence of 10 % (red) and 35 % (maroon) MeOH (top) or 2 M (light green) or 3.5 M (dark green) NaCl (bottom). **B**) IR spectra of the aggregates formed under conditions shown in A). Pink arrows indicate the presence of an absorption band at 1690 cm^{-1} for some of the reported spectra. **C**) AFM images of the aggregates formed in the conditions shown in **A)** and **B**). Scale bar: 200 nm. Data adapted with permission of Dr. José D. Camino.

2. Site-specific pyrene ratiometric analysis reveals an antiparallel topology of novel αS amyloid polymorphs generated through homogeneous nucleation

Considering how the excimer formation of pyrene responds to proximity between two probes and the relative distances between β-stands of different protein units in the parallel β-sheet arrangement of the cross-β amyloid structure, we hypothesized that a parallel aggregate, where the αS monomers find themselves in register with one another, would exhibit intermolecular excimer signal, as it has been reported previously [443]. In contrast to this, an antiparallel architecture of the aggregate would render the pyrene rings too far from each other (> 1 nm) and therefore no excimer emission (I_{470} or I_E) should be expected (**Fig. 1.4B**). Also, the polarity of the pyrene probe should decrease upon aggregation due to a loss of probe solvent accessibility within the amyloid assembly and, leading to a decrease in the intensity of Band I respect to Band III (I_I/I_{III} ratio). To test this, we site-specifically labelled engineered single-cysteine mutants of αS at different positions along its primary sequence (positions 6, 24, 56, 69, 85, 90 and 140) with maleimide-pyrene using thiol-maleimide chemistry (see methods for more information). **Fig. 1.4A** shows a representative schematic for a labeled monomer of αS. The fluorescence spectrum of monomeric αS labeled with pyrene at position 85 (Pyr85-αS, 100 % labelling) showed no excimer emission and a I_I/I_{III} ratio of 1.44 (**Fig. 1.4B**).
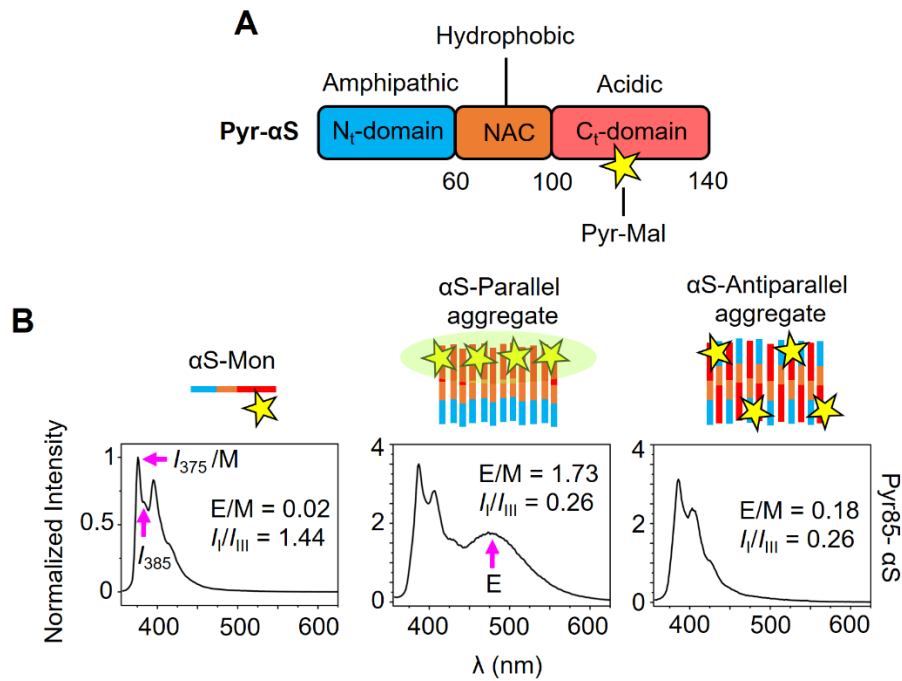
Fig. 1.4. Basis of pyrene fluorescence spectroscopy for studying amyloid topology. A) Schematic of the protein sequence and specific regions of αS. The amphipatic N-terminus, hydrophobic amyloid-driving NAC and acidic C-terminal domains are shown. A covalently-bound pyrene-maleimide molecule is depicted as a yellow star. **B)** Typical pyrene spectra for nonomeric αS (left), parallel (center) and antiparallel relative inter-molecular β-sheet orientations are shown and the analysed emission bands are indicated by pink arrows. Representative experimental values for the E/M and I_I/I_{III} ratios are given for the Pyr85-αS variant. Pyrene molecules are shown as yellow stars and the formation of the pyrene excimer is represented as a green halo. Spectra were normalized to I_{375}.

Opposed to this, the aggregates generated by heterogeneous primary nucleation at the air/water interface, the reference in the field, showed a clear peak at 470 nm, confirming the formation of the pyrene excimer (**Fig. 1.4B**). Concomitant to this, the I_I/I_{III} ratio decreased to 0.26, reporting on the apolarity of the probe's microenvironment in the typical parallel β-sheet αS amyloid aggregates. However, when we aggregated the same labelled monomeric αS under homogeneous nucleation conditions using 35 % MeOH, a spectrum with no excimer signal was obtained, suggesting an antiparallel arrangement of the protein monomers (**Fig. 1.4B**). The aggregated nature of the sample was confirmed by centrifugation and by the low I_I/I_{III} ratio, which corresponded exactly to that of the parallel aggregates, indicating that the probe is located in a similar apolar microenvironment in both parallel and antiparallel β-sheet amyloid aggregates, drastically different to the probe's polar environment in the monomeric protein state. With this, we proved that pyrene excimer formation is a useful tool to identify the parallel or antiparallel topology of amyloid aggregates.

Next, we set out to validate the method using the variety of amyloid polymorphs generated by either heterogeneous interface-associated or homogeneous nucleation, which Dr. José Camino established in the first place. Aside from the referential air/water

(A/W) interface, medium-low concentrations of additives such αS 10 % MeOH, 2 M NaCl or 5 % trifluoroethanol (reagent) were used for heterogeneous nucleation. All data shown in **Fig. 1.5** was obtained in aggregation buffer using 100 μM Pyr85-αS except for A/W, where 500 μM Pyr85-αS were used. For all of these conditions, the same spectra were obtained, showing a high excimer/monomer (E/M) ratio (I_{470}/I_{375}), as shown in **Fig. 1.5A, B**. We termed this the parallel aggregate fingerprint. On the other hand, when homogeneous nucleation conditions such as 35 % MeOH, 3.5 M NaCl or 15 % TFE were used, the E/M ratio was almost identical, although with a distinct I_I/I_{III} pattern, to that of the monomeric αS (**Fig. 1.5A, B**), confirming the antiparallel configuration of these polymorphs. We termed this, by analogy, the antiparallel aggregate fingerprint.
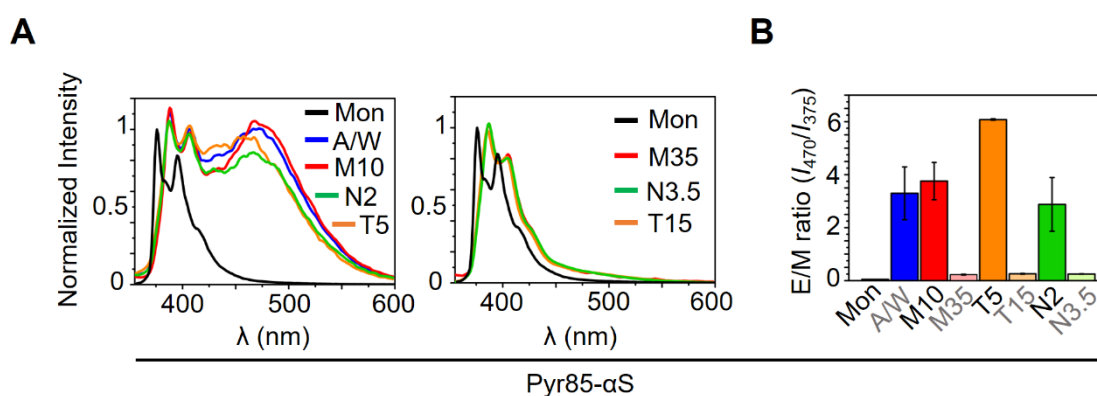
Fig. 1.5. Pyrene excimer quantification in parallel and antiparallel αS amyloid assemblies. **A**) Representative pyrene fluorescence spectra of αS monomer (black line in both left and right panels) and parallel (left panel) or antiparallel (right panel) aggregates, labelled in position 85 of the protein primary sequence (Pyr85-αS), formed at 500 μM at the air-water interface in PBS with shaking (blue line), or at 100 μM in quiescence in PBS with 10 % or 35 % MeOH (red lines), 2 M or 3.5 M NaCl (green lines) and 5 % or 15 % TFE (orange lines). For a better comparison, spectra were normalized to I_{375}. **B**) Excimer/Monomer (E/M) ratio of pyrene fluorescence emission of the αS aggregates described in **A**). Error bars show the standard deviation from a triplicate experiment.

For practical purposes, we performed all experiments henceforth with MeOH and NaCl αS model additives. Since we were dealing with different chemicals at concentrations where they may act as co-solvents, we checked for possible artifacts of these on the spectral properties of pyrene (**Fig. 1.6**). We observed that neither MeOH nor NaCl at their highest concentrations used (35 % and 3.5 M, respectively), altered the E/M or I_{470}/I_{375} ratio of monomeric αS or A/W fibrils. This clearly indicates that the pyrene spectral changes directly report on structural features of the aggregates. Additionally, we tested possible artifacts arising from the % of pyrene-labelled αS in the sample and observed that using 20 % labelling was sufficient for observing a significant different between the E/M ratios parallel and antiparallel aggregates (not shown) and, therefore, we chose to use this labelling ratio henceforth.

In order to prove that our fingerprinting approach was not an artifact of the location of the probe, we tested the rest of the aforementioned labelling positions for parallel and

antiparallel fingerprinting in MeOH and NaCl heterogeneous and homogeneous nucleation conditions (**Fig. 1.7**). While 56, 69, 85 and 90 are located in the β-sheet amyloid core, position 24 is located close to the N-terminal part of the amyloid core and positions 6 and 140 are located at the very N-terminal and C-terminal ends of the protein sequence, respectively. As can be seen in **Fig. 1.7**, fluorescent spectra show an excimer band for all positions for 10 % MeOH and 2 M NaCl, especially in those protein variants labeled at the positions where the A/W-fibrils are known to have their amyloid core.
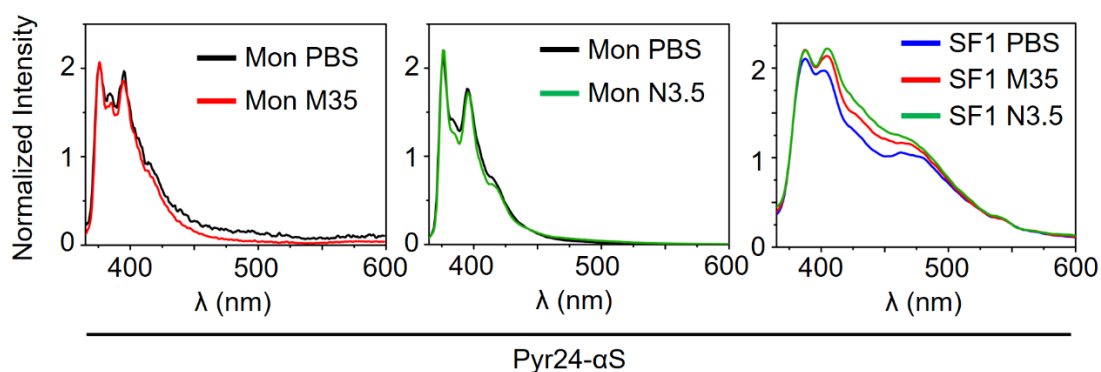
Fig. 1.6. Pyrene fluorescence control experiments. Effect of the solvent on the E/M and I_I/I_{III} ratios. Representative pyrene fluorescence spectra of αS (Pyr24-αS) monomer (top and middle) in PBS (black) or in the presence of 35 % MeOH (red) or 3.5 M NaCl (green). The bottom panel shows representative pyrene fluorescence spectra of αS sonicated fibrils (SF1) in PBS (blue), 35 % MeOH (red) or 3.5 M NaCl (green). Spectra were normalized to I_{375}.

This can be better visualized by the ratiometric E/M analysis (**Fig. 1.8**). Even if the E/M ratio is low for other positions, it is still considerably high for positions away from the core (**Fig. 1.8A**), suggesting that they might be involved in transient interactions that brings that part of the monomers in close contact to each other temporarily. In contrast, all positions exhibit a very low E/M ratio for 35 % MeOH and 3.5 M NaCl, closer to that of the monomeric αS, further confirming the antiparallel architecture of these polymorphs. The fact that all aggregates rendered a I_I/I_{III} ratio much lower than that of the free monomer at all positions (**Fig. 1.8B**) confirms the aggregated nature of all assemblies, which provide a less polar microenvironment for the pyrene probe due to the tight intermolecular packing of hydrophobic areas of the αS protomers.

Lastly, we asked ourselves whether the homogeneous nucleation and its associated antiparallel amyloid topology is always related to a lack of τ_{lag}. For this, we incubated αS (100 % Pyr24-αS) in 35 % MeOH at very low, physiologically relevant concentrations (5 μM) and monitored its aggregation by ThT fluorescence (**Fig. 1.9**), which revealed a lag-phase of around 24 h in the reaction, a feature that we typically observe in heterogeneous nucleation processes. However, pyrene spectra and their ratiometric analysis revealed that, as compared to 10 % MeOH, the aggregates formed at this condition were antiparallel and must arise, hence, from homogeneous nucleation. This shows how the pyrene fluorescence approach complements widely used techniques

such as ThT fluorescence, considering that ThT kinetic analysis alone, as we see here, might lead to confusion regarding the type of nucleation of an amyloid aggregation reaction.
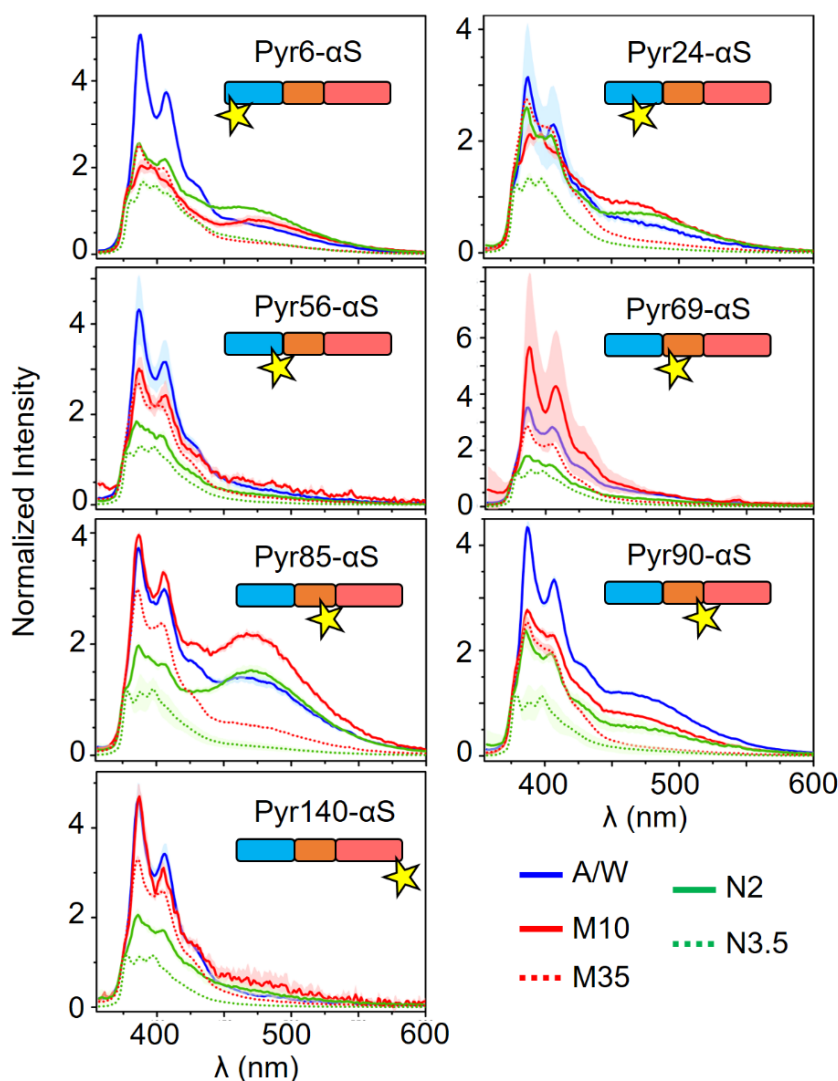
Fig. 1.7. Pyrene spectra of distinct αS aggregates at different labelling positons. Pyrene fluorescence spectra of αS aggregates, labeled in position 6, 24, 56, 69, 85, 90 and 140 of the protein primary sequence, formed at the air-water interface in PBS with shaking (blue), or in quiescence in PBS with 10 % MeOH (solid red line), or 2 M NaCl (solid green line), as well as aggregates formed in the bulk of the solutions in PBS with 35 % MeOH (dotted red line) or 3.5 M NaCl (dotted green line). Spectra were normalized to I_{375}. Shaded colors show the standard deviation from a triplicate experiment.

Together, our results confirmed the suitability of this pyrene-based approach to ascertain the topology of the aggregates in a sequence-specific manner thereby gaining detail into the homogeneous nucleation mechanism. Lastly, we were able to confirm in a robust manner that limited hydration of αS leads to amyloid aggregates with an antiparallel architecture. We believe the pyrene-based methodology we developed could be widely applicable to other amyloidogenic proteins, provided it is straightforward and

inexpensive, thus adding a powerful tool to the biophysical toolbox of any research group.
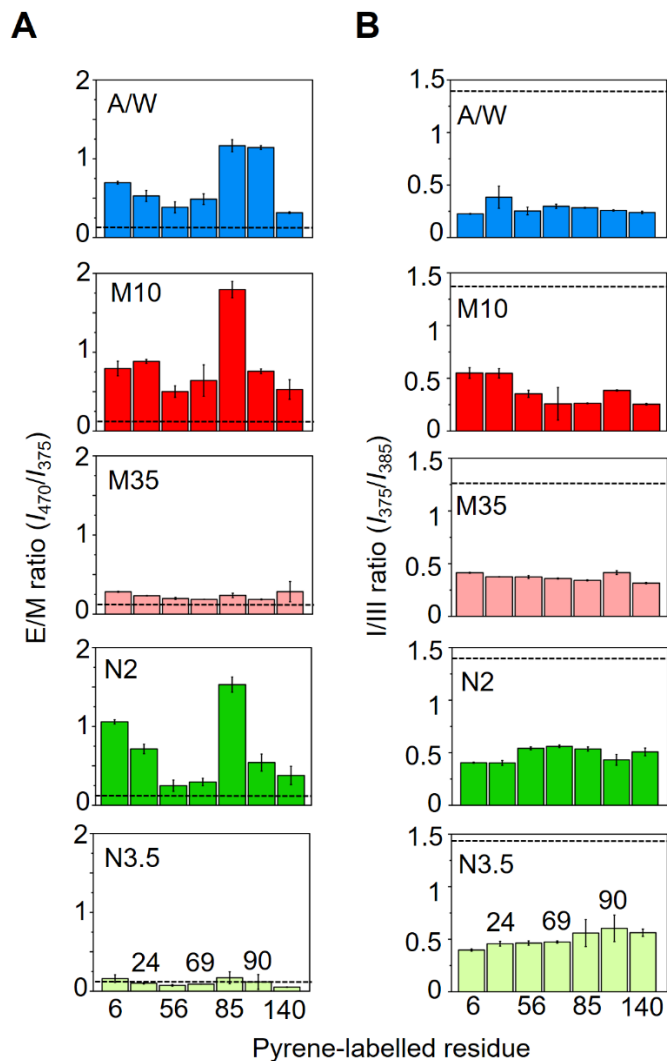
Fig. 1.8. Ratiometric pyrene fluorescence analysis of distinct αS aggregates at different labelling positions. The E/M (**A**) and I_I/I_{III} (**B**) ratio analysis are shown for the pyrene fluorescence spectra of αS aggregates formed by agitation in the A/W interface (blue) or in the presence of 10 % MeOH (red), 2 M NaCl (green), 35 % MeOH (light red) or 3.5 M NaCl (light green). Results for labelling positions 6, 24, 56, 69, 85, 90 and 140 of the protein primary sequence are shown. Error bars show the standard deviation of a triplicate experiment.

3. Antiparallel aggregates formed by homogeneous nucleation possess a different stability than parallel aggregates

Given that amyloid is the most stable protein conformation known to date [450, 451], the question arose whether the nucleation pathway played any role on the stability of αS aggregates. In particular, we wanted to address the possible differences between the stability of parallel and antiparallel polymorphs and test whether the polymorphs generated in the presence of additives were also stable in their absence. By

centrifugation, SDS-PAGE, IR and pyrene spectroscopy, we found that parallel aggregates remain stable in solution without significant disaggregation upon being
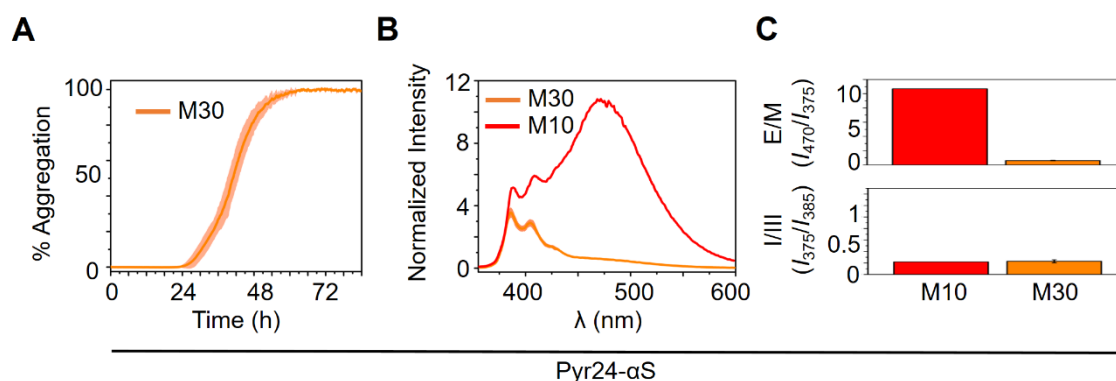
Fig. 1.9. αS aggregation at 5 μM protein concentration in PBS pH 7.4, 35 % MeOH. A) Aggregation kinetics of 5 μM αS in PBS pH 7.4 (37 °C) in the presence of 30 % MeOH with 50 μM ThT. **B**) Fluorescence spectra of 5 μM pyrene-labelled αS aggregates formed in the presence of 10 % (red) and 35 % (orange) MeOH. Only labelled αS was used, carrying the pyrene moiety in position 24. Spectra were normalized to I_{375}. Shaded colors show the standard deviation from a triplicate experiment. **C**) E/M (top) and I_I/I_{III} (bottom) ratiometric analysis of the conditions shown in **B**). Error bars show the standard deviation of a triplicate experiment. The data indicate that αS is able to aggregate at low protein concentrations, in the very low micromolar range, under conditions of homogeneous nucleation with the formation of antiparallel β-sheet aggregates.

transferred into just buffer, but lose a significant amount of β-sheet content (concomitant with an increase in random coil structure). In contrast to this, antiparallel aggregates completely and quickly dissociated when transferred into additive-less aggregation buffer, indicating a very low stability under highly hydrating conditions. Next, we investigated the stability of parallel and antiparallel polymorphs under conditions where the other polymorph is preferentially formed. To this end, the pyrene spectra of M10 and N2 aggregates were studied in 35 % MeOH and 3.5 M NaCl, respectively, while M35 and N3.5 aggregates were assessed in 10 % MeOH and 2 M NaCl, respectively (**Fig. 1.10**). Here and henceforth, we used 100 uM protein (20 % pyrene-labelled) and the Pyr24-αS variant, as it gives a good contrast between parallel and antiparallel fingerprints and is away from the amyloid core of the aggregates, preventing possible structural destabilizations due to probe incorporation. All polymorphs turned to be stable in their "opposite" buffer condition according to SDS-PAGE (not shown). When looking at the excimer band and the band I of the spectra, we saw only slight differences upon buffer exchange, indicating that the aggregates are undergoing no significant structural changes (**Fig 1.10**).

When performing this assay using all the pyrene-labelled αS variants (**Fig. 1.11**), a similar trend as for Pyr24-αS was observed, with small variations of both the E/M and I_I/I_{III} ratios for both MeOH and NaCl-induced parallel and antiparallel conditions. On the one hand, the I_I/I_{III} ratios stay at very low values (**Fig. 1.11B** indicating that, indeed, the

aggregates did not dissociate upon condition inversion. On the other hand, the E/M ratios decreased or increased slightly for all positions (**Fig. 1.11A**), suggesting a structural rearrangement of the relative position of the monomers within the polymorphs.
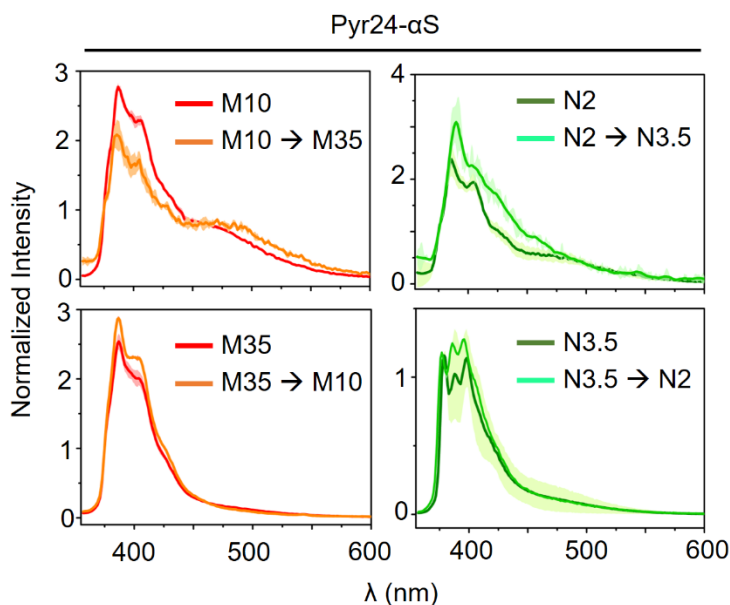
Fig. 1.10. Structural stability of distinct αS aggregates in different environments seen by pyrene fluorescence spectroscopy. Left and right panels show the stability assays of aggregates formed in the presence of MeOH and NaCl, respectively. Pyrene fluorescence spectra of αS labeled at position 24 of the protein primary sequence (Pyr24-αS) are shown. The figure legend indicates the initial aggregation conditions in which the spectra were acquired (MeOH 10 %, MeOH 35 %, NaCl 2M and NaCl 3.5 M in top-left, bottom-left, top-right and bottom-right, respectively) and the buffer change conditions, where the spectra were acquired after incubating the aggregates formed in MeOH 10 %, MeOH 35 %, NaCl 2M and NaCl 3.5 M in their opposite conditions, as it is depicted by arrows. Shaded colors show the standard deviation from a triplicate experiment. Spectra were normalized to I_{375}.

Together, our results reveal that the degree of protein hydration in the conditions of heterogeneous and homogeneous nucleation is responsible for tuning the intermolecular interactions within amyloid assemblies. Specifically, as we demonstrate, it has a critical impact on the kinetics and thermodynamics of αS amyloid aggregation.

4. Pyrene fluorescence and IR spectroscopy are a powerful combination to study the topology and stability of αS amyloid polymorphs

There is mounting evidence supporting that the structural properties of amyloid assemblies are critical for their toxicity [424, 452]. However, structural techniques with residue resolution, such as x-ray crystallography or nuclear magnetic resonance (NMR), are not always accessible and often require large amounts of sample. IR spectroscopy, on the other hand, informs on the secondary structure of proteins and has been widely used for amyloid research [453], although sequence-specific information is missing.

Alongside this, there is a lack of consensus when it comes to interpreting the low frequency band at approximately 1690 cm^{-1}. To overcome these technical limitations, we
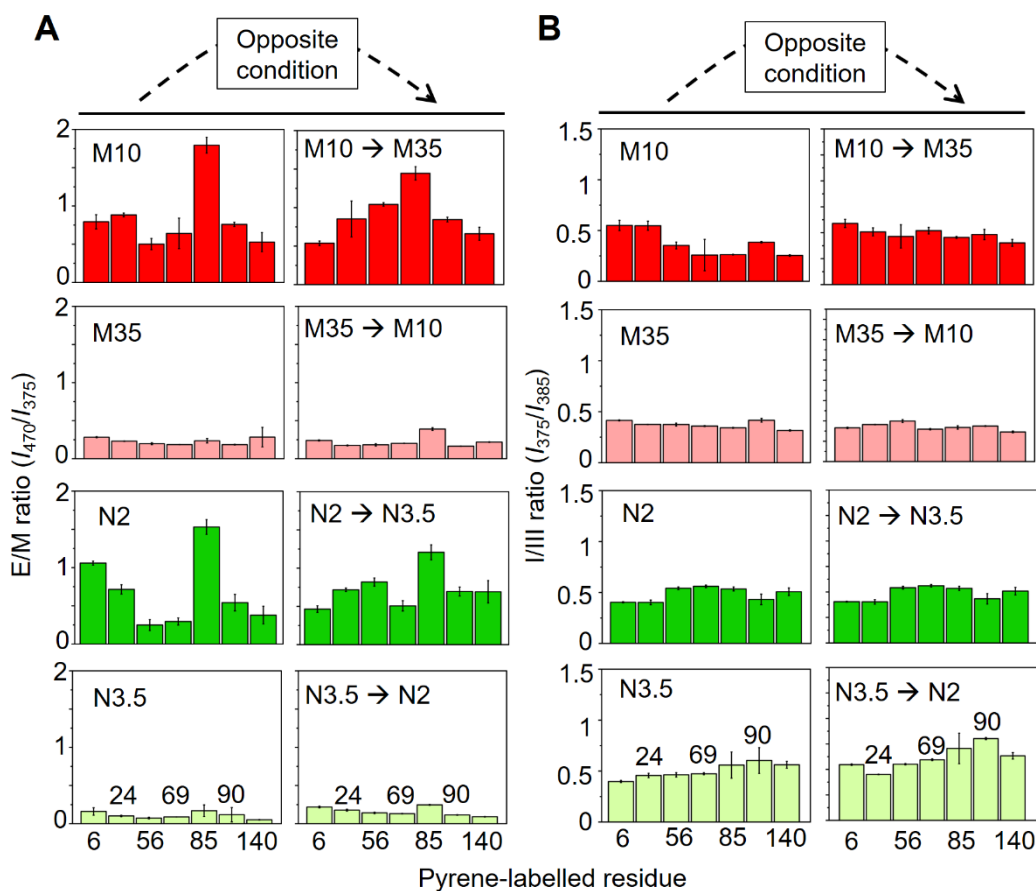
Fig. 1.11. Ratiometric pyrene analysis of the structural stability of distinct αS aggregates in different environments. The E/M (**A**) and I_I/I_{III} (**B**) ratiometric analysis are shown for the experiment shown in **Fig. 1.10** at the different labelling positions of the primary sequence of αS. For each panel (**A**) and **B**)), the left graphs show the results from the initial condition and the right graphs show the ratiometric analysis after changing to the opposite condition. Error bars show the standard deviation of a triplicate experiment.

came up with the pyrene fluorescence strategy, which is simpler in terms of equipment and can use much smaller amounts of protein (down to 250 nM can render a good quality spectrum on an average fluorescence spectrometer). Here, we have demonstrated that this experimental approach nicely recapitulates and confirms the results obtained by IR for antiparallel αS amyloid polymorphs formed by homogeneous nucleation and that it can be implemented for discriminating between parallel and antiparallel topologies of, virtually, any amyloid assembly.

In line with this, we asked how good IR spectroscopy would match pyrene fluorescence stability data of the different polymorphs (**Fig. 1.12**). In the article we published in Chemical Science, Dr. José Camino analyzed the stability of the aggregates formed upon MeOH by IR, as it is shown in figure **1.12A, B and D**. First, we analyzed the structural changes for parallel and antiparallel polymorphs upon inverting their buffer conditions,

finding that in all cases aggregates (M10) undergoes a significant gain of random coil content in detriment of β-structure, although key features of parallel and antiparallel topologies (the high frequency peak position and the 1690 cm⁻¹) remain unaltered, confirming the lack of disassembly. Remarkably, these results are in great agreement with the ratiometric pyrene analysis shown in **Fig. 1.12C**. Lastly, we studied the thermodynamics of MeOH-triggered aggregation by both IR and pyrene fluorescence by estimating the % of antiparallel aggregates at increasing concentrations of MeOH (**Fig. 1.12D**). This way, the transition from a heterogeneous to a homogeneous nucleation regime was monitored. From IR data, the intensity of the 1690 cm⁻¹ was represented as a function of % MeOH and for pyrene fluorescence the E/M ratio was used. We found a sharp transition with a sigmoidal shape within the range of 15 – 25 % MeOH and a remarkable overlap between the IR- and the pyrene-derived curves (**Fig. 1.12D**), thus validating the combined use of these two techniques.
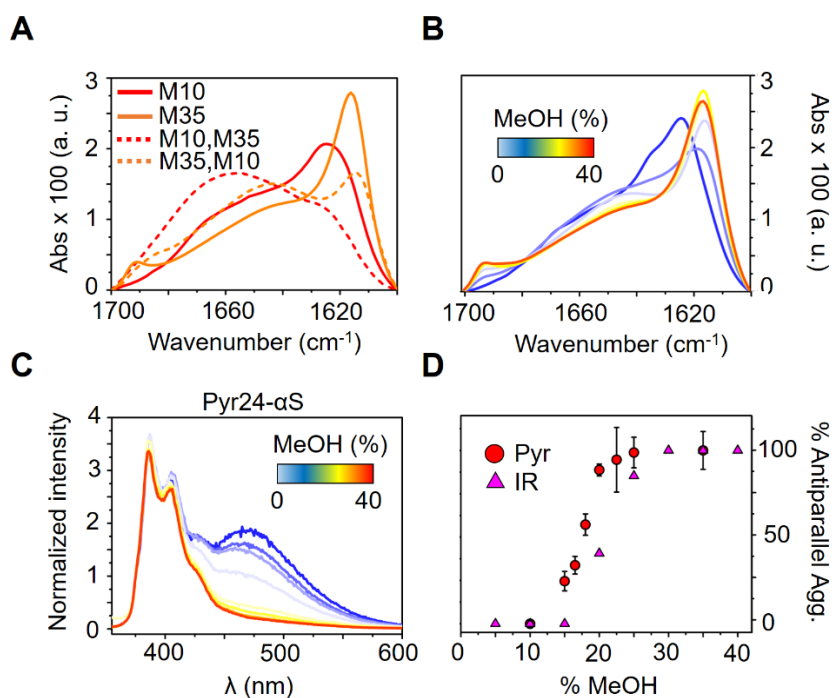
Fig. 1.12. Structural analysis of αS aggregates formed in the presence of different percentages of MeOH. A) IR spectra of aggregates formed with 100 μM αS in PBS pH 7.4 (37 °C) in the presence of 10 % and 35 % MeOH and after changing those conditions to MeOH 35 % and MeOh 10 %, respectively. **B**) Representative IR and **C**) I_{375}-normalized pyrene fluorescence spectra of aggregates formed with 100 μM αS in PBS pH 7.4 (37 °C) in the presence of different methanol concentrations. A heat colorscale shows the MeOH increase as warmer colors. **D**) Transition from a parallel to an antiparallel β-sheet structure is observed using both methods, in both cases yielding virtually superimposable transition sigmoidal curve. Red circles and pink triangles show pyrene fluorescence and IR data, respectively. Error bars show the standard deviation from a triplicate experiment. IR data adapted with permission of Dr. José D. Camino.

Both heterogeneous and homogeneous nucleation pathways may coexist within the transition regime, as it can be inferred from the step-wise behavior, again highlighting

the role of hydration in selecting one or another amyloid nucleation mechanism. However, the data shown in this chapter suggests that, once a given polymorph is formed, there is no reversibility of the aggregation mechanism. Thus, gaining information about the structure-toxicity relationship and on how to modulate the nucleation pathway the protein takes seems of uttermost importance in the short term.

5. Liquid-liquid phase separation of α synuclein can lead to antiparallel amyloid aggregation through homogeneous nucleation

We have demonstrated the homogeneous nucleation of αS *in vitro* resulting in antiparallel amyloid assemblies as a consequence of a reduction in protein hydration. However, the conditions shown so far in this work are far from physiological, even if they serve as good models for studying aggregation. It must be noted that limited hydration conditions may also occur inside the cell, for example inside of protein liquid droplets, also referred to αS biomolecular condensates or membrane-less compartments, which are macromolecule-dense liquid-like droplets typically formed by a liquid-liquid phase separation (LLPS) process. In fact, there is increasing evidence linking LLPS of neurodegeneration-related intrinsically disordered proteins (IDPs) with amyloid aggregation both *in vitro* and *in* [156, 454]. Among others, the amyloid aggregation of αS through LLPS has been described before and after the course of our work on this topic [98, 436, 455]. Provided that biomolecular condensates are very crowded particles with limited solvent accessibility [456–459], the question thus arises whether homogeneous nucleation is the mechanism behind amyloid aggregation of αS by LLPS.

In order to tackle this, we first set out to reproduce the conditions used by Ray *et. al.* [436], until the moment to pursue these experiments, the only conditions under which αS was reported to undergo LLPS *in vitro*. Namely, a drop 200 μM αS in a buffer (Tris 25 mM, NaCL 150 mM, pH 7.4) containing 10 % Polyethylene Glycol-8000 (PEG8) was casted directly onto a PEGylated well of a microplate, then sealed and observed over 20 h. 1 μM AlexaFluor488-labelled αS at position 122 (AF488-122-aS) was used to monitor droplet formation. On a separate sample but without AF488-aS, 50 μM ThT was added to monitor amyloid aggregation. We observed that after 20 min LLPS is triggered and droplets containing αS with liquid-like features appear in the solution (**Fig. 1.13**), while the ThT signal remained negative. After approximately 2 h, ThT-positive particles already were visible (not shown), indicating very fast aggregation which could be arguably arising from homogeneous nucleation owing to its characteristic high speed. Ultracentrifugation analysis revealed a small size of these aggregates, also compatible with the AFM data for other antiparallel polymorphs. After 20 h, all the protein was deposited at the bottom of the sample and was ThT-positive, thus indicating a virtually complete amyloid aggregation of the sample after LLPS. When no PEG was added no LLPS nor subsequent amyloid aggregation were observed (**Fig. 1.14**). Interestingly, when PEG was present but the sample was prepared in bulk instead of casted as a drop onto the bottom of the well, no LLPS nor aggregation occurred either, indicating that the amyloid aggregation we observed (**Fig. 1.13**) indeed arises from the LLPS process.

Next, we applied the pyrene fluorescence strategy that we had set up previously for determining the nucleation pathway of the observed LLPS-aggregation. We repeated the exact same experiment as before but using 20 % Pyr24-αS as a probe and no AF488 nor ThT (**Fig. 1.13A, B**). At initial times (t = 0), E/M and I_I/I_{III} ratiometric analysis show no excimer formation and a high polarity, in agreement with a monomeric conformation of αS. After 20 h, however, the I_I/I_{III} greatly reduced, indicating the aggregation of the protein and in agreement with the ThT analysis. Interestingly, the E/M ratio does not increase significantly and resembles that of the other antiparallel β-sheet amyloid polymorphs reported in this chapter. This strongly suggests that the amyloid aggregates formed in synchrony with LLPS present an antiparallel configuration and thus arise from homogeneous nucleation inside the αS condensates.
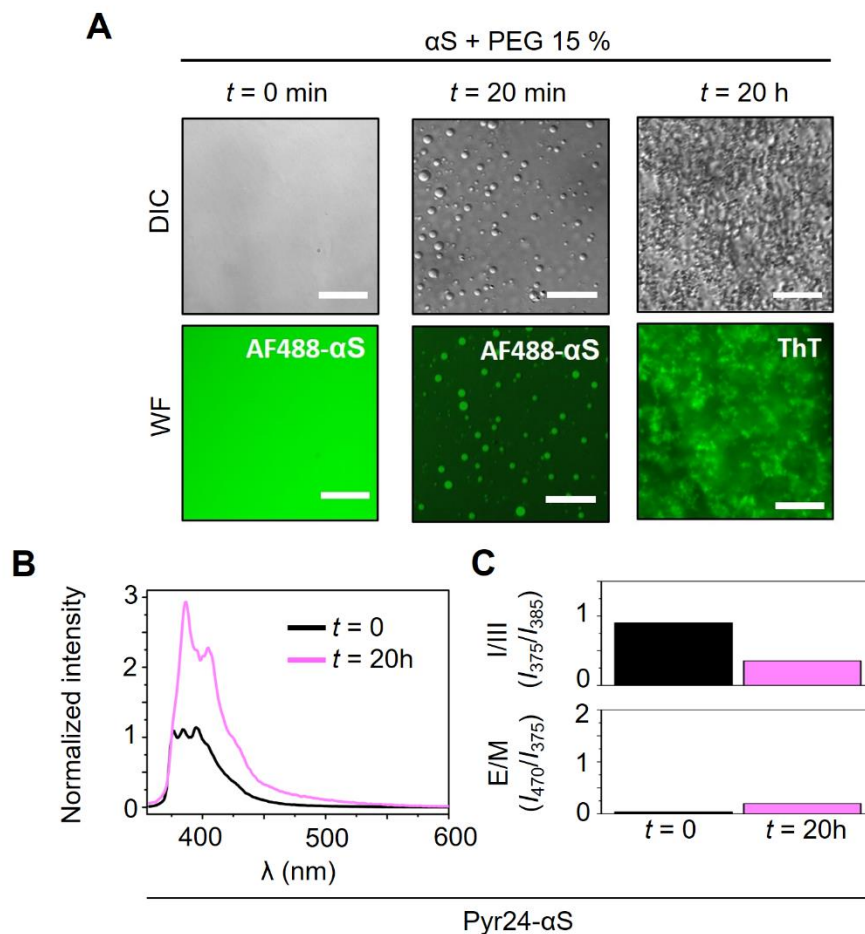
Fig. 1.13. Analysis of the amyloid aggregates formed by the liquid-to-solid transition (LSPT) of αS droplets generated by LLPS. αS droplet formation was triggered by incubating 200 μM protein in 25 mM Tris, 50 mM NaCl, pH 7.4 in the presence of 10 % PEG8000 in a drop set up. **A)** Representative images acquired by differential interference contrast (DIC, top panels) and widefield fluorescence (WF) microscopy (bottom panels). After 20 min of incubation (center), protein droplets were already observed. After 20 h of incubation (right), the protein sample was full of amyloid aggregates. For the left and center WF fluorescence images, 1 μM AF488 αS was added to the protein solutions and the AF488 fluorescence signal was recorded. In the right WF fluorescence image, all the protein was unlabeled and 100 μM ThT was added at time = 0. A GFP excitation/emission filter set was used for the fluorescence microscopy acquisitions

in all cases. Scale bar: 25 μm. **B)** Representative I_{375}-normalized pyrene spectra (top) at time 0 h (black) and 20 h (pink) of incubation of a protein sample treated as in **A)** which also contained 20 μM pyrene-αS labeled at position 24. Error bars are the standard deviation from two independent experiments. **C)** E/M (bottom) and I_I/I_{III} (top) ratiometric analysis of the data shown in **B)**.
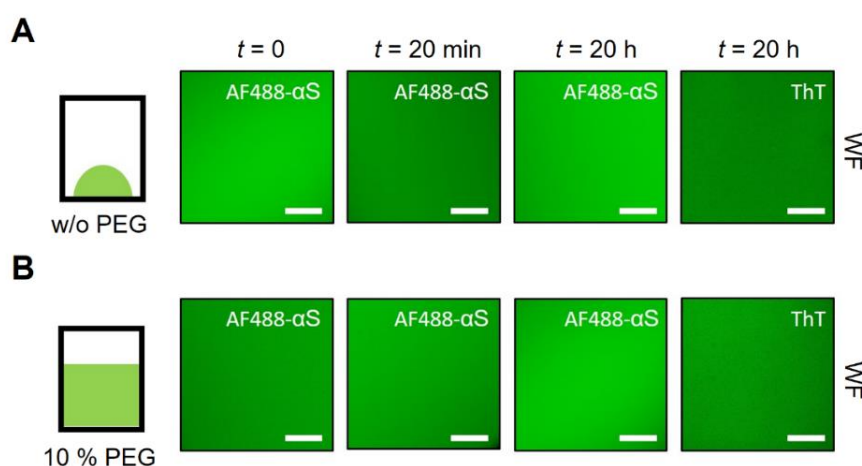
Fig. 1.14. Analysis of the formation of αS droplets by LLPS. Representative WF microscopy images of protein samples containing 200 μM αS and 1 μM AF488-αS without PEG in a droplet setup (**A**) and with 10 % PEG in a microplate well (**B**). Images of the reaction are shown at t = 0, t = 20 min and t = 20 h, respectively. Right panels are equivalent to center-right panels with the exception that the sample contained only unlabeled αS and 100 μM thioflavin-T (ThT). Scale bar is 25 μm. A GFP excitation/emission filter set was used for all acquisitions. The images in the top panels show that 10% PEG is needed in order to trigger αS LPPS, and that, under those conditions (without PEG), no protein droplets or aggregates are, therefore, formed. In addition, the images in the bottom panels show that αS LLPS was not favored even after 20 h of incubation of protein solutions with 10 % PEG when the protein solutions were covering ca. 1/3 of the microplate wells, indicating that a casted drop setup is needed for αS LLPS at the time scales analyzed in this study. When the protein solutions were placed in a drop setup on the surface of the wells of the microplates, LLPS was triggered and αS droplets were observed after 20-min incubation (see Fig. 12 in the main text). The aggregates generated inside the αS droplets by a liquid-to-solid transition (2 h for observing aggregation, 20 h for almost complete aggregation) showed a pyrene signature of intermolecular antiparallel β-sheet amyloid structure, thus suggesting that they were formed by homogeneous primary nucleation in the particular microenvironment of the interior of the αS droplets, with a particularly low water activity in comparison with the solution conditions outside the protein droplets. DIC microscopy imaging of the samples yielded the same result, *i. e.,* no LLPS nor protein aggregation was observed (not shown). Two independent triplicate experiments were performed.

Our data supports the hypothesis that a reduction of protein hydration leads to an accelerated, homogeneous primary nucleation. In particular, we proposed in a review article published in Biophysical Chemistry [460] that, even though homogeneous nucleation is disfavored under hydrating conditions where heterogeneous nucleation governs the aggregation energy landscape, protein condensates formed by LLPS might

be just the dehydrated scenario needed to prompt homogeneous nucleation (**Fig. 1.15**), as it could putatively happen in the cell.
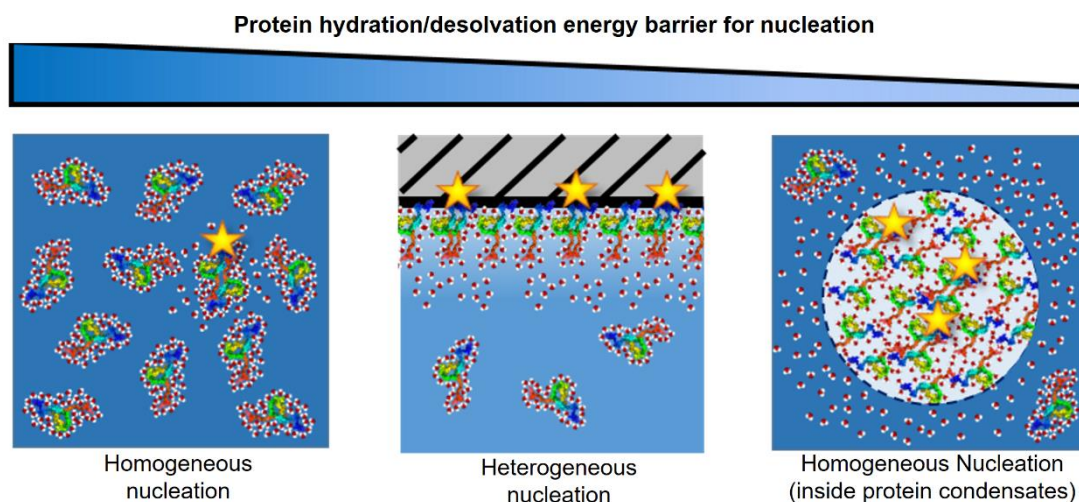
Fig. 1.15. Water strongly modulates the energy barrier for both heterogeneous and homogeneous amyloid nucleation. While the self-assembly of both hydrophobic and hydrophilic IDPs would be thermodynamically favoured due to a large water entropy contribution, a large desolvation energy barrier is expected, particularly for the nucleation of hydrophilic IDPs. Under highly hydrating conditions, primary nucleation is slow (left panel), being facilitated by the presence of nucleation-active surfaces (heterogeneous nucleation, center panel). Under conditions of poor water activity, such as those in the interior of protein droplets generated by LLPS (right panel), however, the desolvation energy barrier is significantly reduced, and nucleation can occur very rapidly in the bulk of the solution (homogeneous nucleation), giving rise to structurally distinct amyloid polymorphs. Water, therefore, plays a key role in modulating the transition free energy of amyloid nucleation, thus governing the initiation of the process, and dictating the type of preferred primary nucleation and the type of amyloid polymorph generated, which could vary depending on the particular microenvironment that the protein molecules encounter in the cell.

These results highlight the virtues of using pyrene αS a structural reporter for probing amyloid assemblies and, on themselves, shed new light into the possible molecular mechanisms governing LLPS-associated amyloid aggregation. However, the experimental setup used for this study, which is based in the aforementioned previous reports, shows certain flaws and, in our view, is far from reliable. This is why, with these preliminary results in hand, we set out to establish new and physiologically relevant experimental conditions to induce LLPS of αS *in vitro* so as to further understand its link with amyloid aggregation and, in a wider context, with neurodegeneration.

Materials & Methods

Protein expression and purification. Wild type (WT) αS and αS variants were expressed in *Escherichia coli* strain BL21 (DE3) and purified as described previously [461, 462]. The cysteine-containing αS variants (acquired from Genscript) were expressed and purified as described for the WT protein but including 5 mM DTT in all purification steps.

Aggregation assays. In ThT-monitored aggregation assays, 100 μM monomeric αS was incubated in PBS buffer pH 7.4, 50 μM ThT, 0.01 % azide, in the presence of given concentrations co-solvents or salts at 37 °C until reaction was complete. 500 μM αS was used for aggregation in PBS in the absence of co-solvents or salts under shaking conditions (700 rpm using *in situ* orbital agitation in the plate reader). Non-Binding 96-Well Microplate (μClear®, Black, F-Bottom/Chimney Well) (Greiner bio-one North America Inc., USA) were used and the plates were covered with adhesive foil to prevent evaporation. All buffer samples and additive stock solutions were pre-filtered with 0.22 mm filters and both the multi-well plates and microfluidic devices were thoroughly cleaned before use. Kinetic reads were recorded in a FLUOstar plate reader (BMG Labtech, Germany); excitation at 450 ± 5 nm and emission at 485 ± 5 nm. For pyrene-labeled αS, aggregation assays were performed as described for the WT protein with a 1:10 labeled-to-unlabeled αS ratio and containing 200 μM TCEP to prevent disulfide bridge formation between cysteines during the aggregation.

Fourier-Transform infrared (FT-IR) spectroscopy. αS end-point aggregates, after two centrifugation-resuspension cycles in order to remove unreacted monomers from the solution were resuspended in deuterated buffer to a final protein concentration of ca. 4 mg/ml. Samples were then deposited between two CaF$_2$ polished windows separated by a PTFE Spacer (Harrick Scientific Products Inc., USA). Spectra were collected in transmission mode at room temperature using a VERTEX 70 FTIR Spectrometer (Bruker, USA) equipped with a cryogenic MCT detector cooled in liquid nitrogen. IR spectra were processed and analyzed using standard routines in OPUS (Bruker, USA), RAMOPN (NRC, National Research Council of Canada) and Spectra-Calc-Arithmetic© (Galactic Inc., USA) [442]. Global fitting analysis of IR spectra of αS aggregates generated at different MeOH concentrations were performed as indicated in Supp. Info. These experiments were performed and analysed by Dr. José Camino.

Atomic force microscopy. Aggregated αS samples were diluted to a protein concentration 0.1 - 0.5 μM and deposited on cleaved Muscovite Mica V-5 (Electron Microscopy Sciences; Hatfield, Pensilvania, USA). Slides were washed with double distilled water and allowed to dry before imaging acquisition on a Bruker Multimode 8 (Bruker; Billerica, USA) using a FMG01 gold probe (NT-MDT Spectrum Instruments Ltd., Russia) in intermittent-contact mode in air. Images were processed using Gwyddion and the width measurements were corrected for the tip shape and size (10 nm). These experiments were performed and analysed by Dr. José Camino.

Kinetic data analysis. Aggregation kinetic data were fitted to the following sigmoidal equation:

$$F = F_i + \frac{(F_f + m_f \cdot t)}{1 + e^{\frac{-(t-t_{50})}{\tau}}}$$

Eq. (1.1)

where F is the fluorescence intensity, F_i is the fluorescence signal at time zero, $F_f + m_f t$ describes the final baseline at the plateau phase, t_{50} is the time at which F is half of the maximum intensity and τ is a characteristic time constant that represents the inverse of the apparent growth rate. The lag time, t_{lag} is estimated as $t_{50} - 2\tau$ as described previously [463]. This equation is typically used to analyze amyloid formation kinetics without the assumption of any specific model, so it does not reflect the complexity underlying the amyloid aggregation process, but provides descriptive, empirical parameters that can be used in comparative studies. This analysis was performed by Dr. José Camino.

Determination of the aggregation yield. The fraction of aggregated αS was estimated by quantifying the relative concentration of the insoluble and the soluble fractions. After reaction was complete (in the plateau phase), the sample was ultracentrifuged at 627.000 g for 90 minutes in a Beckman Coulter Optima® TLX (Beckman, USA) at room temperature, using a Beckman Coulter TLA 120.2 rotor. The soluble fraction was collected and the protein concentration of the soluble fraction determined spectrophotometrically (by absorbance at 275 nm, using a molar extinction coefficient of 5600 M^{-1} cm^{-1}) for samples in the absence of ThT. For samples containing ThT, an aliquot of the soluble fraction was loaded in a 15 % acrylamide gel, together with an aliquot of the initial protein sample before aggregating, and the concentration of protein in the soluble fraction of the aggregated samples was estimated by comparing band intensities, after Coomassie staining, using the ImageJ software (NIH Image). These experiments were performed by Dr. José Camino.

Lipid Vesicle Preparation. Small unilamellar vesicles (SUV) were prepared from dimyristoyl phosphatidylserine (DMPS, Avanti Polar Lipids, USA) by sonication as described previously [432]. The concentration of lipid stocks and the final solution of SUVs in HEPES buffer pH 6.5 was estimated from the Fiske phosphorus assay [464]. In this way the protocol for the generation of SUVs with a 100 % efficiency vas validated. The same protocol then was used to generate SUVs in phosphate buffer pH 6.5. These experiments were performed by Dr. José Camino.

Labelling of αS with N-(1-pyrenyl) maleimide. The cysteine-containing αS variants were labelled with N-(1-pyrenyl) maleimide (Santa Cruz Biotechnology). A stock solution of the pyrene reagent was prepared in DMSO. The DTT present in each cysteine αS variant solution was replaced with 5 mM Tris(2-carboxyethyl) phosphine (TCEP, Sigma Aldric), exchanging buffer with a Sephadex G-25, PD-10 desalting column (GE Healthcare). The labelling reactions were performed with 100 µM protein solutions in 25 mM Tris-NaCl, 150 mM NaCl, TCEP 5 mM, pH 7.25 at 4 °C in the dark, with a 5-fold

molar excess of the pyrene reagent. The final DMSO concentration in the labelling reactions was, in all cases, lower than 1 %. The reactions were terminated at ca. 12-15 h by adding 10 mM DTT to the solutions, and the labelled protein was separated from the unreacted reagent with a PD-10 column. The labelling efficiency (10 - 95 %) was calculated by MALDI-TOF and, additionally, spectrophotometrically using a molar extinction coefficient of 36,000 $M^{-1}.cm^{-1}$ at 343 nm for pyrene and a correction for the pyrene absorbance at 275 nm using the same dye concentration in DMSO.

Pyrene-labelled αS aggregation assays. For pyrene-labelled αS, aggregation assays were performed as described for the WT protein with the following modifications: a 1:10 labelled-to-unlabelled ratio cysteine-containing αS mixture was aggregated at a total 100 µM protein concentration in PBS pH 7.4 containing 200 µM TCEP to prevent disulfide bridge formation between cysteines during the reaction. When required, MeOH or NaCl were added to the mixture at a given final concentration. After aggregation, the residual monomer was removed by ultracentrifugation as described for the WT protein. Pellets were solubilised in 100 µL of the aggregation buffer, sonicated for 1 min in a sonication bath and pyrene spectra were immediately measured. Bath sonication ensured adequate dispersion of the aggregated samples, with no significant aggregate clustering, while avoiding disaggregation and any apparent structural changes in the aggregates.

Steady-state pyrene fluorescence spectroscopy. The emission spectra of the aggregated pyrene-labelled αS variants excited at 343 nm were collected at room temperature in a Cary Eclipse Fluorescence Spectrophotometer (Varian, Palo Alto, California, United States) with slit-widths of 5/5 nm. An averaging time of 100 ms was used. The fluorescence spectra of the final aggregates of each pyrene-labelled variant were normalized to the intensity at 375 nm (I_{375}) and subsequently analysed to quantify the E/M ratio by dividing I_{470}/I_{375}, as described elsewhere [287, 443, 465, 466].

αS aggregate stability assays. Identical protocols for IR and pyrene fluorescence analysis of aggregate stability were used. The pyrene-labelled aggregates were generated with a 1:10 labeled-to-unlabeled αS ratio as explained above. Once the aggregates were generated and washed to remove unreacted monomers from the solution, a first spectrum was collected corresponding to the aggregates under the same conditions as they were generated. Then, the aggregates were ultracentrifuged, as described above, resuspended in a buffer of equal composition as the aggregation buffer but with a different alcohol or salt concentration, bath-sonicated and incubated for 20 h at 37 °C. After this time, possible monomeric protein generated from aggregate disaggregation was removed from the protein sample by ultracentrifugation. The pellet was then resuspended in the same buffer and the aggregate solution was later bath-sonicated to avoid aggregate clustering due to ultracentrifugation. Then, the IR or pyrene fluorescence emission spectrum were collected, representing the aggregate spectra at the new alcohol concentration. The IR experiments were performed by Dr. José Camino.

Estimation of the fraction of parallel and antiparallel β-sheet aggregates at the end of the aggregation reactions at different MeOH concentrations by FT-IR spectra global analysis. A global fitting analysis of the IR spectra of αS aggregates generated at different MeOH concentrations in the range of 5-40 % MeOH was performed in order to estimate the fraction of parallel and antiparallel β-sheet aggregates present at the end of the αS aggregation reactions under the different solution conditions. For this, the following equation was used:

$$X_i = X_{\nearrow\nearrow} \cdot a_i \cdot (A + B \cdot [MeOH]) + X_{\nearrow\swarrow} \cdot (1 - a_i) \cdot (C + D \cdot [MeOH]) \quad \textbf{(Eq. 1.2)}$$

where the observed absorbance value at each wavenumber, X_i, is assumed to be a linear combination of the values of each structural aggregate (parallel, $X_{\nearrow\nearrow}$, or antiparallel, $X_{\nearrow\swarrow}$) and its population (a_i, and $1 - a_i$, respectively). This analysis was performed by Dr. José Camino.

Liquid-liquid phase separation assays. 200 µM αS was incubated at 25 °C for 20h in Tris 25 mM, NaCl 50 mM, pH 7.4 in the presence or absence of 10 % PEG8000. For widefield fluorescence microscopy, either 1 µM AF488-labelled N122C αS or 100 µM thioflavin-T were included. For pyrene fluorescence spectroscopy and E/M ratio analysis, 10 % of the total protein concentration was pyrene-labelled at position 24 (Pyr-24-αS). LLPS was initiated by casting a 10 µL droplet inside a non-binding microplate well (Greiner bio-one North America Inc., USA) for 20 minutes. Then, the wells were sealed and the reaction was allowed to proceed for 20 h in a humidity chamber to avoid evaporation. Assays were also performed in the bulk exactly in the same manner as described above with the sole exception that microplate wells were filled with 150 µL of the reaction mixture. Two independent triplicate assays were performed. For pyrene fluorescence spectroscopy, end-point LLPS reactions were ultracentrifuged for 2 h at 627.000 xg in a Beckman Coulter Optima® TLX (Beckman, USA) at room temperature, using a Beckman Coulter TLA 120.2 rotor, then the pellet was solubilized in the original reaction conditions and pyrene spectra were acquired as described above. Two independent assays were performed.

Differential interference contrast (DIC) and widefield fluorescence (WF) microscopy. Images were acquired on a Leica Dmi8 inverted fluorescence microscope (Leica Microsystems, Germany) at room temperature. A halogen lamp or a mercury metal halide bulb EL6000 (for DIC and WF imaging, respectively) served as illumination sources. For WF microscopy, the light was focused on and collected from the sample using a 40x air objective lens (Leica Microsystems, Germany) and the excitation and emission light was filtered with a standard GFP filter set with bandpass filters of 460-500 nm and 512-542 nm for excitation and emission, respectively. For DIC microscopy, the same objective was used to collect the reflected light. Collected light was detected on a Leica DFC7000 CCD camera (Leica Microsystems, Germany). Exposure times were 50 ms for DIC microscopy imaging and 20 ms for WF microscopy imaging. Intensity was

software-enhanced for the ThT images for comparative purposes due to the low degree of ThT binding to these aggregates. Images were analysed using ImageJ (NIH, USA).

Chapter 2

Molecular Mechanism for the Synchronized Electrostatic Coacervation and Amyloid Co-Aggregation of α-Synuclein and Tau

Introduction

Besides membranous compartments, spatial segregation in the cell can be achieved through the formation of protein-rich liquid-like dense bodies, named biomolecular condensates or liquid protein droplets. These are formed by a process known as liquid-liquid phase separation (LLPS) [467] through weak, multivalent transient interactions, commonly between proteins and proteins with RNA, fulfilling a wide array of functions in essentially all living systems [468]. A large number of proteins that can undergo LLPS present low-complexity sequences that remain disordered to a large extent in native conditions, as well as when forming biomolecular condensates [469–471]. A number of experimental studies have spotlighted the flexible, typically disordered and 'multivalent' nature of the constituent proteins in these liquid-like condensates [142]. However, less is known about the particular molecular determinants governing the growth and maturation of these condensates into more solid-like states.

There is mounting evidence supporting the hypothesis that aberrant protein-driven LLPS and the transition of the liquid droplets to solid-like structures might be a relevant cellular pathway leading to the formation of insoluble, toxic aggregates that are often a hallmark of degenerative diseases. In fact, a number of LLPS-associated intrinsically disordered proteins (IDPs), often highly charged and flexible, have been long linked to neurodegeneration through amyloid aggregation processes. More specifically, biomolecular condensates of IDPs such as FUS [151] or TDP-43 [472] have been shown to age into gel or even solid-like structures, through a process known as liquid-to-solid phase transition (LSPT). This maturation occurs as a function of time or as a response to certain post-translational modifications [146, 473, 474] or pathological mutations [151, 475–477]. Nevertheless, a detailed understanding of the molecular determinants and complex protein interaction networks governing pathological LSPT remains obscure.

One of these proteins is Tau, a microtubule-associated disordered protein whose amyloid aggregation is typically related to Alzheimer's disease [5, 478, 479], but also more recently linked to Parkinson's disease (PD) and other synucleinopathies [480, 481]. Tau has been shown to trigger LLPS through electrostatic interactions [482], resulting in liquid droplets which are referred to as electrostatic coacervates. Such type of non-specific interactions have likewise been observed to be the driving force of numerous biomolecular condensates in nature [483]. In the case of Tau, electrostatic coacervates can be formed through either simple coacervation (homotypic interactions), where oppositely charged regions of the protein trigger the de-mixing process, or complex coacervation through the interaction with typically negatively charged polymers [484] (heterotypic interaction). To the best of our knowledge, the only polymers so far reported to undergo complex coacervation with Tau are RNA molecules or heparin [484].

Recently, α-synuclein (αS) has been shown to concentrate in protein condensates with liquid-like behavior both in cellular and animal models [97, 436]. *In vitro* studies have proposed that αS undergoes LLPS by simple coacervation through primarily hydrophobic homotypic interactions, although this process requires particularly high protein concentrations and atypically long incubation times [292, 436]. Whether the αS-containing condensates observed *in vivo* are formed through this or other LLPS processes

is a key question that remains unsolved. Similarly, although αS amyloid aggregates are observed inside neurons in PD and other synucleinopathies, the precise mechanisms by which αS undergoes amyloid aggregation inside cells are still unclear, as the mere overexpression of the protein seem to be unable to elicit this process. Additional cellular insults are typically required [427], suggesting that particular cellular locations or microenvironments are necessary for the *de novo* nucleation of αS amyloid assemblies inside cells. A particularly aggregation-prone cellular environment could be the interior of protein condensates [485].

Intriguingly, αS and Tau have been found to co-localize in the disease hallmark inclusions of individuals with PD and other synucleinopathies [486, 487] and a synergistic pathological relationship between these two proteins has been experimentally reported [488, 489], suggesting a potential cross-talk between αS and Tau aggregation in neurodegenerative disorders. αS and Tau have been found to interact and promote each other's aggregation both *in vitro* and *in vivo* [490, 491], and hetero-aggregates composed of both proteins have been observed in the brains of patients suffering from synucleinopathies [492]. However, the molecular basis underlying the interplay between αS and Tau, and the mechanisms of their co-aggregation are poorly understood. αS has been reported to interact with Tau through electrostatic attractions between the highly negatively charged C-terminal region of αS and the central proline-rich region of Tau, which is also enriched in positively charged residues. Owing to this interaction, αS has been recently reported to exhibit a client role in LLPS with Tau. In particular, partition of αS into preformed Tau/RNA electrostatic coacervates has been observed [493].

Taking this background into account and building on the results presented in chapter 1 of this thesis, where we demonstrated the ability of αS to undergo LLPS in somewhat extreme conditions, we turned to Tau/αS as a putative complex coacervation system with physiological relevance. Besides, we wanted to explore LLPS and LSPT as a possible αS amyloid aggregation pathway. In this study, we used a combination of advanced biophysical techniques to characterize the precise role of each protein in LLPS, the strength and chemical nature of the heterotypic interactions leading to complex coacervation, the dynamics of αS within the coacervates and the potential transition of these liquid droplets into solid-like, amyloid aggregates by LSPT. For this, we studied αS in the presence of disordered poly-cations in a controlled environment at low micromolar concentrations and physiologically relevant conditions, following the typical thermodynamically-driven LLPS behavior. From the experimental technique point of view, the widely used amyloid-binding thioflavin-T (ThT) probe shows limitations when monitoring amyloid formation in liquid-to-solid transitions owing to its molecular rotor working principle (*i. e.* its sensitivity to the viscosity of the media through its internal fluorescence quenching effect) [494, 495] and not fully specific binding to other non-amyloid structures [272, 275], as explained elsewhere in this thesis (see general introduction section 5.1.1 for more detailed information). In order to circumvent this, we combined conventional ThT fluorescence microscopy with state-of-the-art time-resolved confocal fluorescence microscopy (TRFM). In particular, we used a combination of fluorescence lifetime imaging (FLIM) and FRET microscopy to gain

access into the microscale changes in the protein-protein networks within αS/polycation liquid droplets upon LSPT.

In this work we collaborated with Dr. Inés García, Ilenia Serra and Maruan A. Bracci at the University of Zaragoza, experts in EPR spectroscopy, and Dr. Douglas V. Laurents and Dr. Javier Oroz from the Rocasolano Institute for Chemical Physics at the Centro Superior de Investigaciones Científicas (Spain), experts in NMR. Our joint work is currently under revision in the journal Nature Communications and I am co-first author, wrote the article and prepared all the figures.

Specific aims

- Establish a physiologically relevant model for αS LLPS based on αS/polycation electrostatic complex coacervation.

- Provide a detailed, quantitative characterization of the LLPS process.

- Disentangle the role of protein-protein interactions and protein dynamics in the behavior of αS/polycation coacervates and their LSPT over time.

- Apply fluorescence lifetime imaging microscopy (FLIM) to monitoring the ageing and LSPT of αS/polycation coacervates.

- Prove the amyloid co-aggregation of αS and Tau coupled to their LLPS and LSPT.

- Propose a model for αS/Tau LLPS-LSPT as a potential amyloid-triggering process relevant in disease.

Results

1. αS forms electrostatic complex coacervates with poly-L-lysine.

αS has a highly anionic C-terminal tail at neutral pH (**Fig. 2.1A**), which we hypothesized could undergo LLPS by electrostatic complex coacervation with a poly-cationic disordered polypeptide molecule. As an initial co-driving model molecule for LLPS, we used poly-L-lysine of 100 residues (pLK), given the positively charged and disordered polymeric nature of this molecule at neutral pH [496]. First, we confirmed the electrostatic interaction of pLK with the C_t-domain of αS by solution NMR spectroscopy (**Fig. 2.1B**) using C^{13}/N^{15}-labelled αS in the presence of increasing αS:pLK molar ratios. The interaction of pLK with the C_t-domain of αS is evident by both chemical shift perturbations and loss of peak intensities in this protein region. Interestingly, when we mixed αS with pLK at αS concentrations of ca. 5 - 25 μM in the presence of small amounts of polyethylene glycol (5 - 15 % PEG-8) (the typical LLPS buffer: 10 mM HEPES pH 7.4, 100 mM NaCl, 15 % PEG-8), we immediately observed protein droplet formation by widefield fluorescence (WF) and brightfield (BF) microscopy (**Fig. 2.1C**).
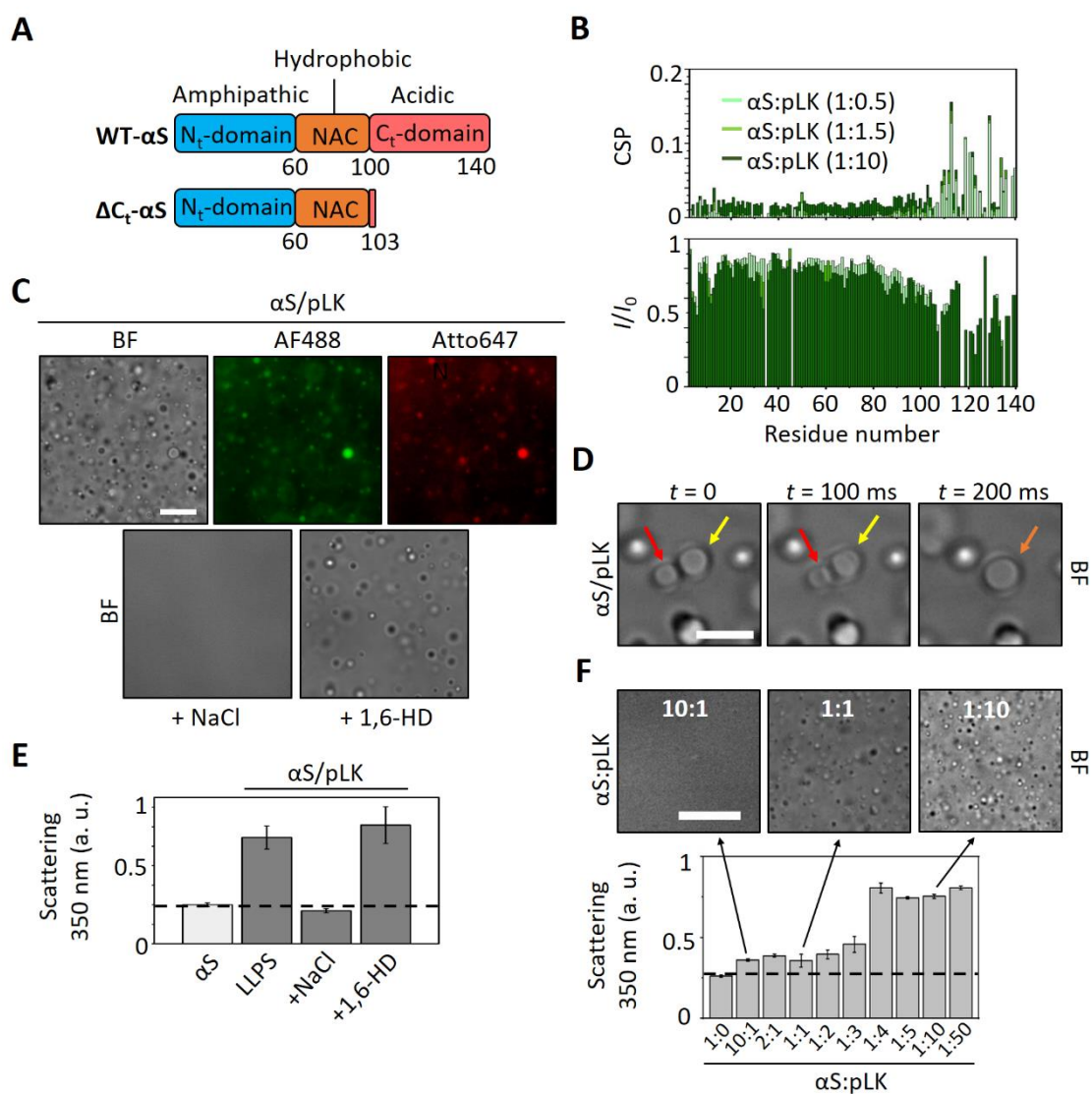
Figure 2.1. Complex electrostatic coacervation of αS with poly-L-lysine. A) Schematic of the different protein regions in WT-αS and the ΔCt-αS variant used in this study. The amphipathic N-terminal domain, the hydrophobic amyloid-forming (NAC) region and the negatively charged C-terminal domain are shown in blue, orange and red, respectively. **B**) NMR analysis of αS/pLK interaction in the absence of macromolecular crowding. Chemical shift perturbation (CSP, top) and intensity ratio (I/I_0, bottom) analysis of HSQC spectra of C^{13}, N^{15}-labeled αS (150 μM) in the presence of increasing concentrations of pLK (αS:pLK molar ratios of 1:0.5, 1:1.5 and 1:10 are shown in light green, green and dark green, respectively). **C**) Brightfield (BF, top left and bottom images) and widefield fluorescence (WF, top center and right images) microscopy images of αS/pLK coacervates (1:10 molar ratio) at an αS concentration of 25 μM (1 μM AF488-labelled αS or Atto647N-labelled pLK for WF imaging) in the absence (top) or presence of 500 mM NaCl (bottom left) or 10 % 1,6-hexanediol (1,6-HD; bottom right). Scale bar = 20 μm. **D**) Representative BF microscopy images of an αS/pLK (1:10 molar ratio) droplet fusion at an αS concentration of 25 μM; arrows indicate individual liquid droplets (red and yellow arrows) merging into one new droplet (orange arrow) within 200 ms. Scale bar = 20 μm. **E**) Light scattering (at 350 nm) of αS/pLK coacervates, at an αS concentration of 25 μM in the absence or presence of 500 mM NaCl or 10 % 1,6-HD. **F**) BF images (top) and light scattering analysis (at 350 nm, bottom) of αS/pLK coacervates at an αS concentration of 25 μM at increasing αS:pLK molar ratios. Scale bar = 10 μm for all images except for **F** (20 μm).

Droplets of 1 - 5 μm in size, containing condensed αS (spiked with 1 μM AlexaFluor488-labelled αS, AF488-αS) are readily formed, and their electrostatic nature is evident from their resistance against 10% 1,6-hexadienol (1,6-HD) and their sensitivity to increasing NaCl concentrations (**Fig. 2.1C**). The liquid-like nature of the αS/pLK electrostatic complex coacervates was proved by their ability to fuse within milliseconds (**Fig. 2.1D**). By means of turbidimetry, we quantified droplet formation under these conditions, confirmed the electrostatic nature of the main interactions involved in their stability (**Fig. 2.1E**), and evaluated the effect of different polymer ratios on the LLPS process (**Fig. 2.1F**). Although droplet formation is observed within a wide range of polymer ratios, the process is highly favored when pLK is in excess with respect to αS. LLPS was also observed when a chemically different crowding agent, dextran-70 (70 kDa), was used or when different sample formats are employed (including drop-on-glass slide, microplate well of different materials, or Eppendorf or quartz capillary tubes - data not shown).

2. αS forms electrostatic complex coacervates with Tau by liquid-liquid phase co-separation

Based on our observation of αS/pLK electrostatic complex coacervation, we hypothesized that αS is capable of undergoing LLPS through electrostatic interactions with Tau. In particular, we set out to demonstrate that αS is capable of not only partitioning into preformed Tau liquid droplets, as previously proposed [493], but also to induce the co-separation of both proteins from the solvent (LLPcoS) by electrostatic complex coacervation. We observed that when 10 μM αS and 10 μM Tau441 (containing 1μM AF488-αS and 1μM Atto647N-Tau, respectively) are mixed together in LLPS buffer, they readily form protein condensates, which contain both proteins as seen by WF microscopy (**Fig. 2.2A**). The co-localization of both proteins in the droplets was confirmed by confocal (CF) microscopy (**Fig. 2.3A**). A similar behavior was observed when dextran-70 was used as crowding agent (**Fig. 2.3C**). By using FITC-labelled PEG

or dextran, we found that both crowding agents distribute homogeneously over the whole sample without showing a seggregative nor an associative behavior (**Fig. 2.3D**). Instead, this indicates that they favor phase separation through macromolecular crowding effects in this system, being PEG a preferentially stabilizing crowding agent, as observed for other LLPS systems [497, 498]. These protein-rich droplets are sensitive to NaCl (1 M) but not to 1,6-HD (10 % v/v), thus confirming their electrostatic nature (**Fig. 2.4A, B**). Observation of droplet fusion events within milliseconds by BF microscopy verify their liquid-like behavior (**Fig. 2.2B**).
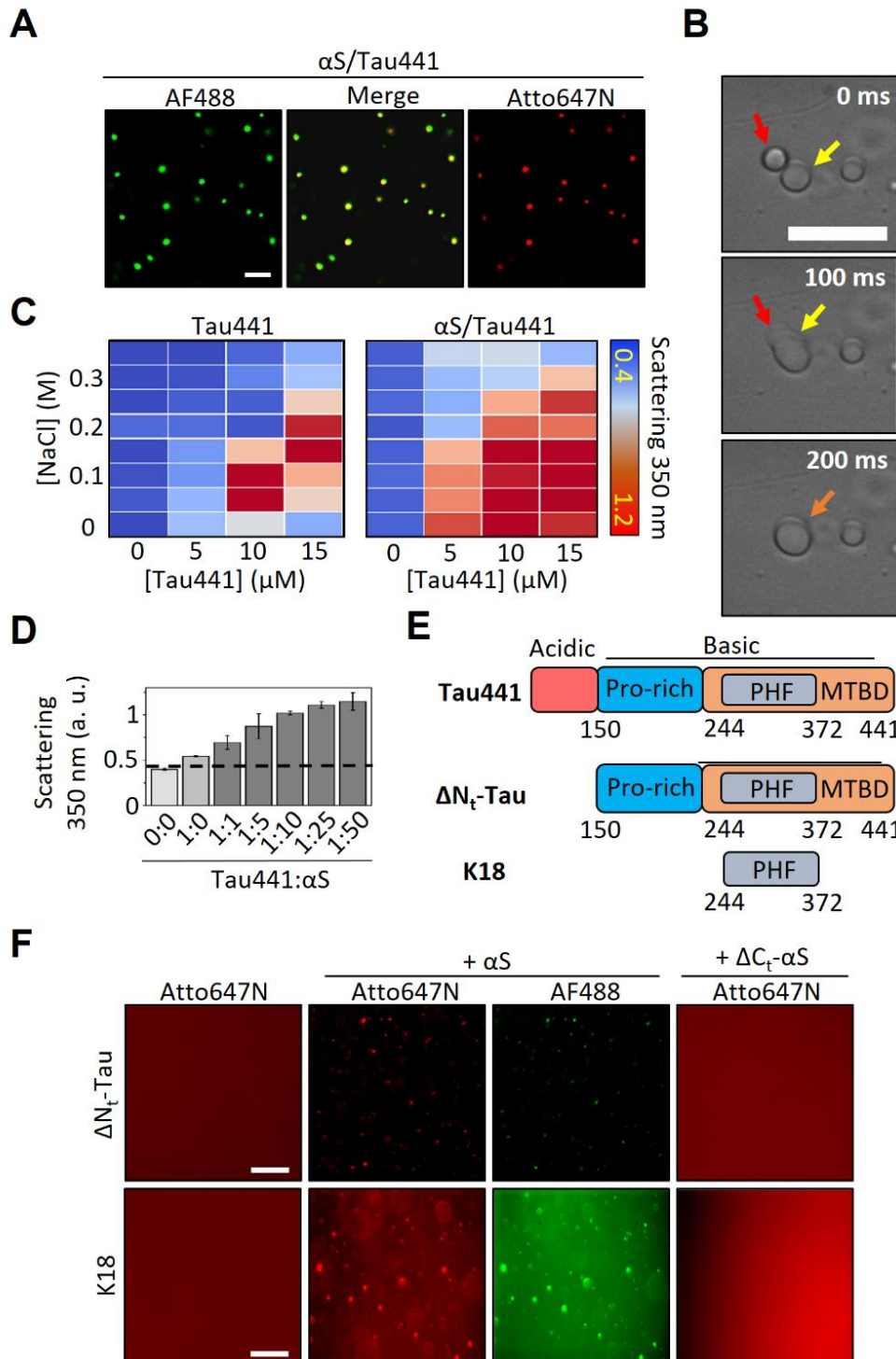
Figure 2.2. Complex electrostatic coacervation of αS with Tau. A) Confocal (CF) microscopy images of αS/Tau441 coacervates (10 μM each protein, 0.5 μM AF488-labelled αS and Atto647N-labelled Tau441). **B**) Representative differential interference contrast (DIC) microscopy image of an αS/Tau441 droplet fusion event (10 μM each protein). **C**) Light scattering-based (at 350 nm) phase diagram of Tau441 LLPS (0 - 15 μM) in the absence (left) or the presence (right) of 50 μM αS. Warmer colors indicate more scattering. **D**) Light scattering of αS/Tau441 coacervate samples with increasing concentrations of αS (Tau441 at 5 μM). **E**) Schematic of the Tau protein variants used in this study and the different protein regions: the negatively charged N-terminal domain (in red), the proline-rich region (in blue), the microtubule-binding domain (MTBD, in orange) and the amyloid-forming paired helical filament (PHF) region located within the MTBD (in gray). **F**) WF microscopy images of αS or ΔC_t-αS coacervation with ΔN_t-Tau (top, 10 μM each protein) or K18 (bottom, 50 μM each protein), using 1 μM AF488-labelled αS and Atto647N-labelled ΔN_t-Tau or K18. Scale bars in one image indicate the scale bar throughout each entire panel and are 20 μm for all panels. Data in **B, C and F** adapted with permission from Jorge Tarancón and David Polanco.

In order to test whether αS actually plays an active role in this LLPS process, we first investigated the effect of αS on the stability of the droplets by turbidimetry using increasing NaCl concentrations (**Fig. 2.2C**). The higher values of light scattering (at 350 nm) with higher salt concentrations in the sample containing αS evidence a stabilizing role of αS in this LLPS system. A similar effect can be observed upon increasing the concentration of αS (thus the αS:Tau441 ratio) up to ca. 10-fold with respect to Tau concentration (5 μM) (**Fig. 2.2D**). To further prove that αS plays an active role, rather than merely a client molecule, we decided to investigate the behavior of a LLPS-impaired Tau mutant, lacking the negatively charged N-terminal region (residues 1-150, *see* **Fig. 2.2E**), termed ΔN_t-Tau. We verified by WF microscopy and turbidimetry that ΔN_t-Tau does not undergo LLPS by itself (**Fig. 2.2F** and **Fig. 2.4C**), as it was previously reported [482]. However, when αS was added to the dispersed solutions of this truncated Tau variant, the LLPS process was fully restored with droplet densities resembling those of solutions of full-length Tau and αS under similar conditions and protein concentrations. The role of the C-terminal region of αS in the LLPS process was demonstrated by the inhibition of droplet formation when a C terminus-truncated variant of αS (ΔC_t-αS), lacking residues 101-140, was used instead of the full-length protein (**Fig. 2.2F** and **Fig. 2.4C**). Co-localization of αS and ΔN_t-Tau was confirmed by confocal fluorescence microscopy (**Fig. 2.3B**).

To further validate the mechanism of LLPS between Tau441 and αS, an additional Tau variant was used; namely the paired helical filament core fragment (PHF) within the microtubule-binding domain (MTBD), also typically referred to as K18 fragment when containing the four characteristic repeat domains (**see Fig. 2.2E**). αS has been recently reported to bind Tau preferentially at the proline-rich domain that precedes the microtubule-binding domain in sequence [493]. However, this latter region is also rich in positively charged residues, particularly lysines (15.2% of the residues), which prompted us to test for the ability of this region to also contribute to αS/Tau complex coacervation. We observed that K18 is unable to trigger LLPS by itself (**Fig. 2.2F**) under the conditions tested (LLPS buffer with either 15% PEG or 20% dextran) at concentrations up to 100 μM. However, when we added 50 μM αS to 50 μM K18, rapid formation of protein droplets containing both K18 and αS was observed by turbidimetry

Fig. 2.4C) and WF microscopy (**Fig. 2.2F**). As expected, ΔCt-αS was not able to rescue the LLPS behavior of K18. We noted that for αS/K18 coacervation, slightly higher protein concentrations were needed to trigger LLPS as compared to αS/ΔNt-Tau or αS/Tau441 under otherwise identical conditions. This is consistent with a stronger interaction of the C-terminal region of αS with the proline-rich domain of Tau, as compared to the microtubule-binding domain. Nonetheless, both Tau regions are likely involved in the process of LLPS though electrostatic complex coacervation with αS.
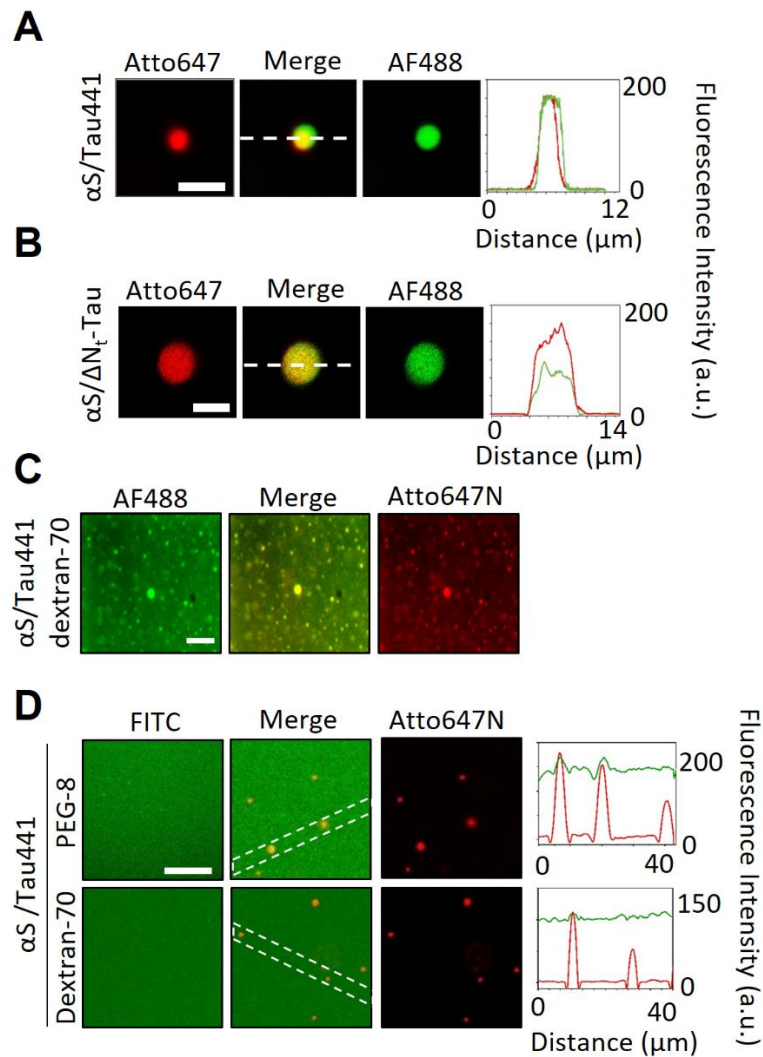
Figure 2.3. Spatial distribution of αS, Tau441, ΔNt-Tau and macromolecular crowders in the coacervate samples. Representative confocal fluorescence (CF) microscopy images of colocalizing αS/Tau441 (**A**), 10 μM each protein) and αS/ΔNt-Tau (**B**), 25 μM each protein) coacervates. The intensity profiles obtained at the center of the image (shown as discontinuous lines in the center of the merge image) are shown for the fluorescence intensity of αS-AF488 (green) and Tau441- or ΔNt-Tau-Atto647N (red). **C**) Representative WF microscopy images of αS/Tau441 coacervates (25 μM each protein) in 20 % dextran-70 (w/v). **D**) Representative CF microscopy images of αS/Tau441 LLPS in different crowders. In green, the fluorescence intensity of FITC-labelled crowders (1 % with respect to the total crowder concentration) is shown and, in red, Atto647N-labelled αS (1 μM). For the coacervate samples in the presence

of PEG-8, αS and Tau were used at 10 µM each protein and PEG at 15 % (w/v), while for the coacervate samples in the presence of dextran-70, the proteins were used at 25 µM each, and the crowder at 20 % (w/v). The dotted white rectangle indicates the analyzed area used to obtain the fluorescence intensity profiles shown in the right. Scale bars are 5 µm in panels **A-C)** and 10 µm in panel **D)**. Experiments were performed in triplicate with very similar results. Data in **C)** adapted with permission from David Polanco.

Considering that ΔN_t-Tau is unable to undergo LLPS in the absence of αS, we chose this Tau variant as a model for αS/Tau LLPS characterization, taking into consideration that in the LLPS system with full-length Tau both simple (Tau441/Tau441) and complex (αS/Tau441) coacervation processes occur simultaneously. We compared the extent of αS condensation (as fraction of the protein in the condensed phase, $f_{\alpha S,c}$) in αS/Tau and αS/ΔN_t-Tau system by centrifugation and SDS-PAGE analysis of the disperse phase (**see Fig. 2.4D**), and we found very similar values being all the proteins at the same concentrations. More specifically, we obtained a $f_{\alpha S,c}$ of 89 ± 13 % and 81 ± 6 % for αS/Tau and αS/ΔN_t-Tau, respectively, which indicates that heterotypic interactions between αS and Tau are preferred to the homotypic interactions between Tau molecules.
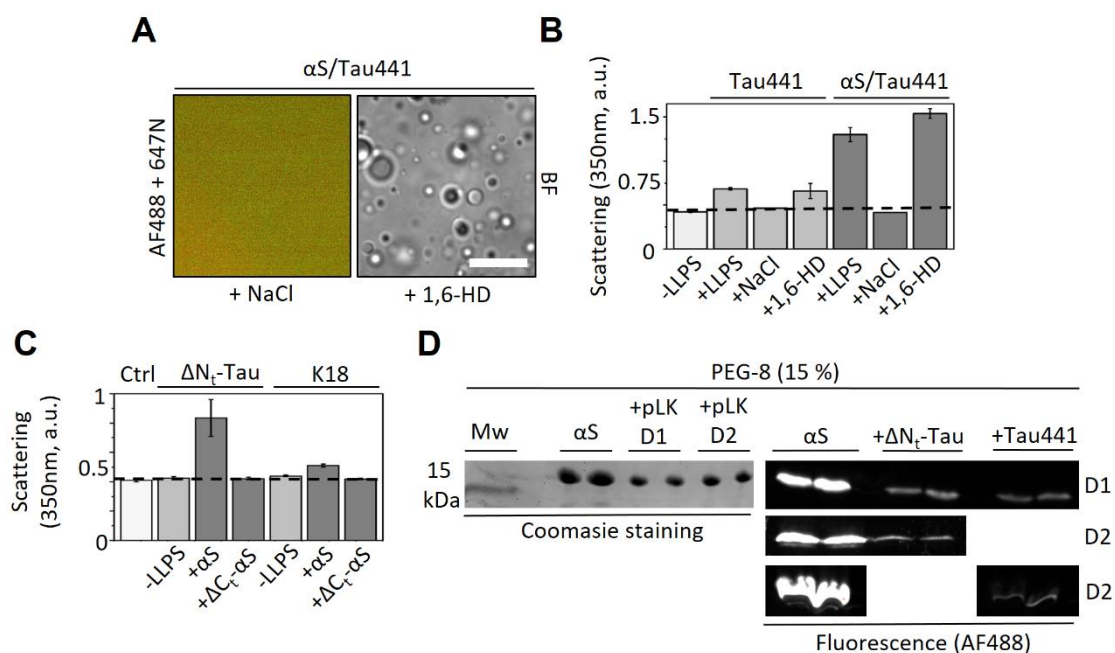
Figure 2.4. Role of electrostatic interactions and quantification of the coacervation of αS with the poly-cations. A) Representative WF (left) and BF (right) microscopy images of the effect of 1 M NaCl and 10 % (v/v) 1,6-Hexanediol (1,6-HD) on αS/Tau441 coacervates (10 µM each protein, 1 µM AF488-αS and Atto647N-Tau441 for WF microscopy). Scale bar = 20 µm. **B)** Light scattering (at 350 nm) of Tau441 and αS/Tau441 coacervate samples (10 µM each protein) in the absence or the presence of 1 M NaCl or 10 % 1,6-HD. **C)** Light scattering (at 350 nm) of αS or ΔC_t-αS coacervate samples with ΔN_t-Tau or K18 (50 µM each protein). LLPS buffer (15 % PEG) served as control. **D)** Quantification of the fraction of αS in the dispersed and condensed phases in the different LLPS systems: 100 µM αS with 1 mM pLK or 100 µM Tau441 or ΔN_t-Tau. The LLPS samples were centrifuged after 30 min incubation and the fraction of αS remaining in the disperse phase ($f_{\alpha S,d}$) was determined by SDS-PAGE gel

analysis. The protein bands were resolved by coomasie staining for the αS/pLK system and by fluorescence for the αS/Tau441 and αS/ΔN$_t$-Tau systems (for both αS and Tau variants quantification -1 μM of fluorescently-labelled proteins— although only αS quantification is shown). D1 and D2 indicate independent duplicate experiments. Data in **B)** and **C)** adapted with permission from Jorge Tarancón.

3. Characterization of αS dynamics in electrostatic complex coacervates

The influence of the interactions with the different poly-cations and of the coacervation processes on the dynamics of αS was first investigated by means of fluorescence recovery after photobleaching (FRAP). We conducted FRAP assays (**Fig. 2.5A-C**) on αS/Tau441, αS/ΔN$_t$-Tau and αS/pLK coacervates (100 μM αS, supplemented with 2 μM αS AF488-αS, with either 100 μM Tau441 or ΔN$_t$-Tau, or 1 mM pLK). Data were acquired within the first 30 minutes after mixing the components of the sample. As it can be seen from the representative FRAP images (**Fig. 2.5A**, αS/Tau441 coacervation) and their corresponding time-course curves (**Fig. 2.5B, Fig. 2.6A-C**), the dynamics of αS were almost identical in the coacervates with Tau441 and ΔN$_t$-Tau, while slightly faster with pLK. The diffusion coefficient of αS inside the coacervates estimated from the FRAP data (as described by Kang. M and co-workers [499] was $D = 0.013 \pm 0.009$ μm^2/s and $D = 0.026 \pm 0.009$ μm^2/s for αS/Tau441 and αS/ΔN$_t$-Tau, respectively, and $D = 0.17 \pm 0.04$ μm^2/s for αS/pLK systems (**Fig. 2.3C**). The diffusion coefficient of αS in the dispersed phase was determined by fluorescence correlation spectroscopy (FCS, *see* **Fig. 2.6**) under identical conditions (LLPS buffer) but in the absence of poly-cation, and we obtained $D = 8.14 \pm 4.33$ μm^2/s, more than 2 orders of magnitude higher than that of αS within the coacervates. αS translational dynamics are, thus, remarkably reduced within the coacervates as compared to the protein in the dispersed phase, due to a significant molecular crowding effect, although all the coacervates maintain a liquid-like nature within the first half an hour from their formation.

Complementary to this, we studied the dynamics of αS in the different coacervates by site-directed spin labeling (SDSL) continuous wave electron paramagnetic resonance (CW-EPR). This technique has proven useful to report on the flexibility and dynamic properties of IDPs with practically residue resolution [500–502]. To this end, we engineered cysteine residues in single-cys mutants and labeled them with a maleimide derivative of the spin probe 4-hydroxy-2,2,6,6-tetramethylpiperidine-N-oxyl (TEMPOL). More specifically, we introduced a TEMPOL probe at position 122 or at position 24 of αS (TEMPOL-122-αS and TEMPOL-24-αS). In the first case, we targeted the C-terminal region of the protein, which is involved in the interaction with the poly-cations. Conversely, position 24 could give us information on the overall dynamics of the protein inside the condensate. In both cases, the obtained EPR signal of the protein in the dispersed phase is consistent with a nitroxide radical in the fast motion regime. Upon phase-separation in presence of either Tau or pLK (100 μM TEMPOL-αS at a 1:1 ratio for Tau441 or ΔN$_t$-Tau, or 1:10 for pLK), the EPR spectra of αS show a loss of peak intensities associated to line broadening, which indicates a reduction of the αS reorientation dynamics in the liquid droplets as compared to the protein in the diluted phase (**Fig. 2.5D, Fig. 2.7A**).

These changes are more pronounced at position 122. While at position 24 the dynamics of the probe is not affected by the presence of pLK, at position 122 there is a significant change in the line shape of the spectrum. When we tried to simulate the spectra of position 122 for the two αS/poly-cation systems using the isotropic model (**Fig. 2.8B**),
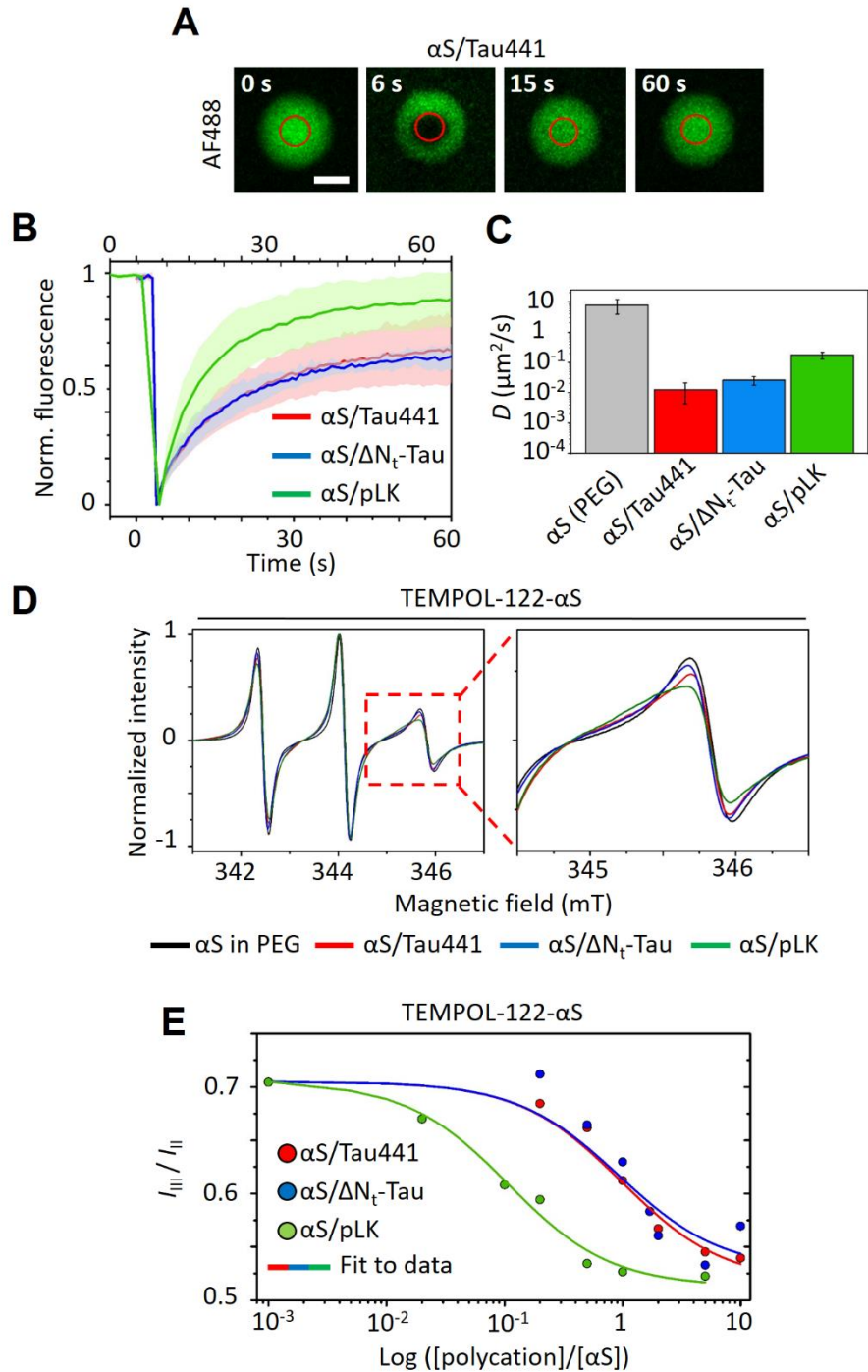
Figure 2.5. αS dynamics in electrostatic complex coacervates. A-C) FRAP analysis of αS dynamics (2 % AF488-labelled αS) within electrostatic coacervates. Representative images of a triplicate αS/Tau441 FRAP assay are shown in (**A**), where the red circle indicates the bleached area. Scale bar is 5 μm. **B**) Mean FRAP curves and (**C**) calculated diffusion coefficient (*D*) of 5 different droplets from a triplicate experiment with 100 μM αS and equimolar concentrations

of Tau441 (red) or ΔNt-Tau (blue) or 10-fold concentration of pLK (green) under LLPS conditions. The standard deviation of the FRAP curves is shown as shaded colors. Upper x-axis is for pLK while lower x-axis is for Tau441 and ΔNt-Tau. For comparison, the diffusion coefficient of αS in the dispersed phase was determined in triplicate by fluorescence correlation spectroscopy (FCS) (see **Fig. 2.6D** and methods for more information). **D**) CW X-Band EPR spectra of 100 μM TEMPOL-122-αS in 15 % PEG-8 without any poly-cation (black) or in the presence of a 100 μM Tau441 (red) or ΔNt-Tau (blue), or 1 mM pLK (green). The inset shows a zoom into the high-field line, where the most significant changes occur. **E**) Binding curves of 50 μM TEMPOL-122-αS to the different poly-cations in the absence of LLPS. The decrease in amplitude of band III relative to Band II (I_{III}/I_{II}) of normalized EPR spectra are shown for increasing molar ratios of Tau441 (red), ΔNt-Tau (blue) and pLK (green). Colored lines show the fit to data using an approximate binding model with n-identical and independent binding sites for each curve. EPR data adapted with permission from Ilenia Serra, Maruan A. Bracci and Dr. Inés García.
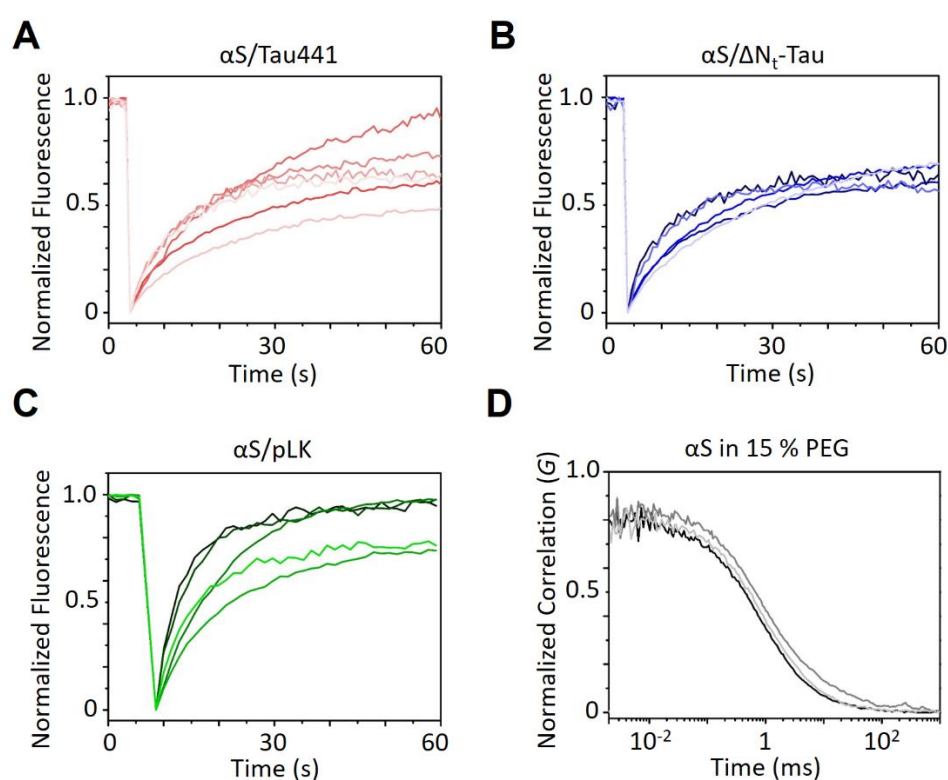
Figure 2.6. Dynamics of αS in electrostatic complex coacervates by Fluorescence Recovery After Photobleaching (FRAP) and Fluorescence Correlation Spectroscopy (FCS). A-C) Normalized FRAP curves of αS coacervates with Tau441 (**A**), ΔNt-Tau (**B**) or pLK (**C**). The kinetics of fluorescence recovery of 5 different droplets from 3 independent replicas are shown. **D**) Normalized FCS curves from a triplicate experiment with 1 nM AF488-αS using the same conditions as in **A-C** but without any poly-cation.

commonly used to describe the dynamics of spin-labelled IDPs [500, 502], we could not recover the experimental spectra, in contrast to the simulations of the spectra with the spin at position 24 (**Fig. 2.8A**). This suggests that there are preferred locations in the configurational space of the spin at the C-terminal region of the protein. When taking into account the fraction of αS in the condensed phase under the EPR experimental

conditions (89 ± 13 %, 81 ± 6 % and 54 ± 6 % for αS/Tau441, αS/ΔN$_t$-Tau and αS/pLK, respectively - *see* data analysis in **Fig. 2.4D**), it becomes evident that the spin dynamics changes detected by EPR reflect primarily the interaction of the C-terminal region of αS with the various poly-cations in the condensed phase, rather than the increased viscosity experienced by αS inside the coacervates. As expected, when adding 1 M NaCl to the mixture, the EPR spectrum of the protein in non-LLPS conditions is completely recovered (**Fig. 2.7B**).
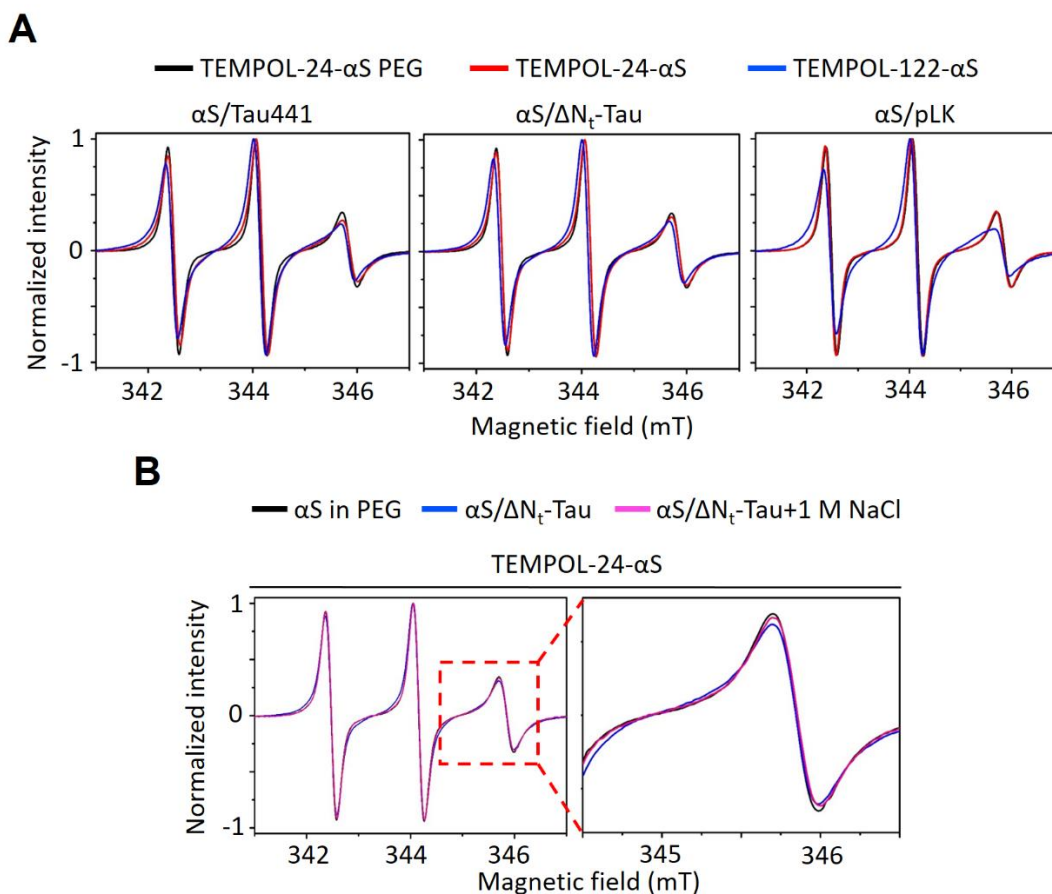
Figure 2.7. Dynamics of αS in electrostatic complex coacervates by EPR. A) Normalized CW X-Band EPR spectra of 100 μM TEMPOL-24-αS in 15 % PEG-8 (black) and TEMPOL-24-αS (red) or TEMPOL-122-αS (blue) in the presence of 100 μM Tau441 (left) or ΔN$_t$-Tau (center) or 1 mM pLK (right). **B**) Normalized CW X-Band EPR spectra of 100 μM TEMPOL-24-αS under LLPS conditions with ΔN$_t$-Tau before (blue) and after (pink) addition of 1 M NaCl. The spectrum of αS under LLPS conditions but without ΔN$_t$-Tau is shown in black for comparison. The inset shows a zoom into the high-field band, where the most significant changes occur. Data adapted with permission from Ilenia Serra, Maruan A. Bracci and Dr. Inés García.

To obtain more structural information of the protein inside the coacervates, we set out to study the LLPS system by solution state NMR. However, we could only detect the fraction of αS that remains in the dispersed phase, likely due to a combination of the reduced protein dynamics inside the coacervates and the deposition of the dense phase at the bottom of the solution within the experimental time required for the NMR analysis. When we analyzed the structure and dynamics of the protein that remains in

the dispersed phase in the LLPS samples by NMR (**Fig. 2.8C, D**), we observed that the protein behaves almost identically in the presence of pLK and ΔN$_t$-Tau, both in terms of secondary structure and protein backbone dynamics, as detected by secondary chemical shifts and $R_{1\rho}$ relaxation experiments. The NMR data corroborate the EPR results, showing that the C-terminus of αS undergoes the main loss of conformational flexibility, while maintaining the disordered nature as the rest of the protein sequence, under LLPS conditions with poly-cations.
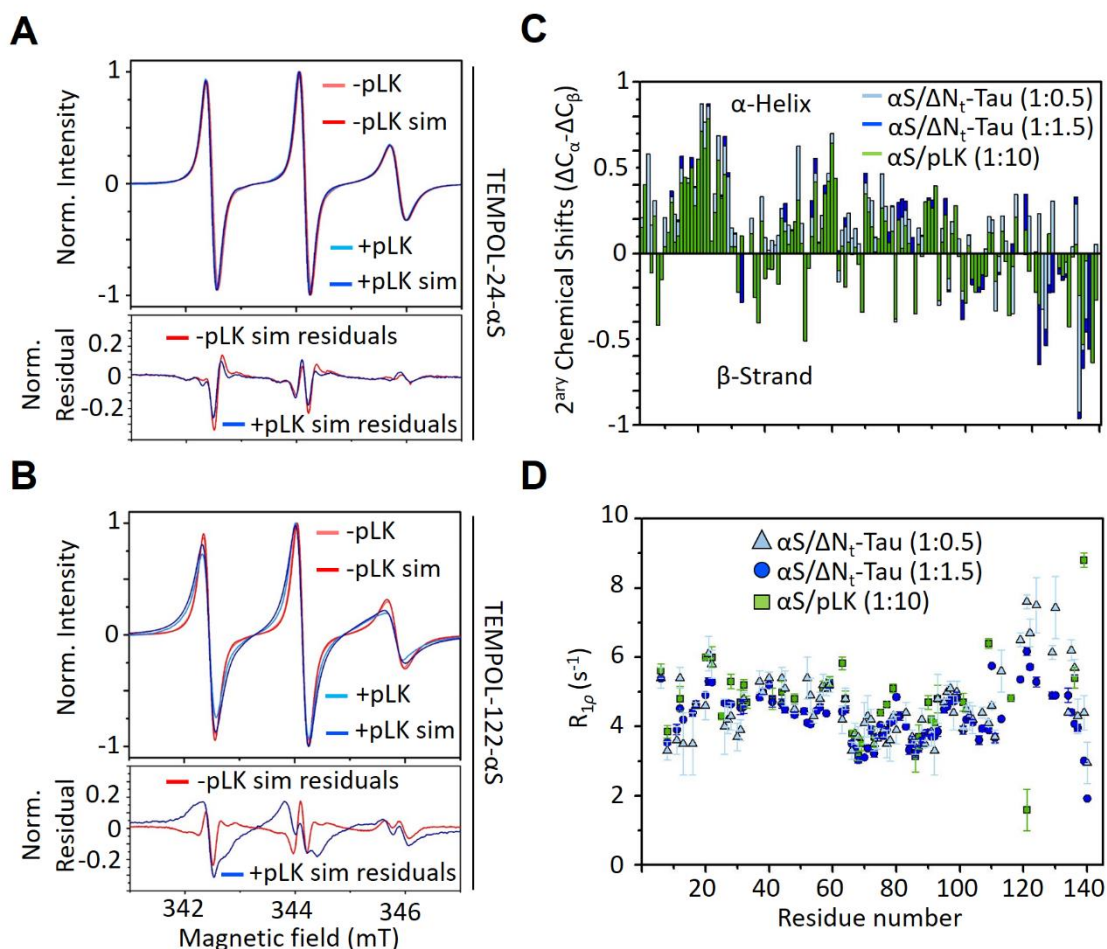
Figure 2.8. Restricted dynamics of the C-terminus of αS upon interaction with poly-cations in electrostatic complex coacervate samples by EPR and NMR. A-B) Normalized CW X-Band EPR spectra and simulations of TEMPOL-24-αS (**A**) and TEMPOL-122-αS (**B**) in 15 % PEG and in PEG with 10-molar equivalents of pLK. Spectra are shown in light red and blue for PEG and pLK, respectively. Simulations using a two-component isotropic model are shown in dark red and blue for PEG and pLK, respectively. The EPR signal of the protein in the dispersed phase is consistent with a nitroxide radical in the fast motion regime, characterized by g_{iso} = 2.0055 and axial hyperfine coupling (A = [20 20 104] MHz). Residuals were calculated as described in the "Materials and Methods" section and are shown for PEG (dark red) and pLK (dark blue). **C)** Secondary chemical shifts of HSQC spectra and (**D**) $R_{1\rho}$ relaxation analysis for 150 μM C^{13}/N^{15}-labeled αS in the presence of 1.5 mM pLK (green), 75 μM ΔN$_t$-Tau (light blue) or 225 μM ΔN$_t$-Tau (dark blue), respectively. The data shows the reduction of conformational flexibility in the C-terminal region of αS upon interacting with poly-cations in the LLPS context with both pLK and Tau. EPR data adapted with permission from Ilenia Serra, Maruan A. Bracci

and Dr. Inés García. NMR data adapted with permission from Dr. Javier Oroz and Dr. Douglas V. Laurents.

Since the broadening of the CW-EPR signal observed in TEMPOL-122-αS upon LLPS is indicative of the protein's interaction with the poly-cation, we performed EPR titrations to assess the binding affinity of αS for the different poly-cations in the absence of LLPS. The aim was to observe whether, despite the common liquid-like nature of all coacervates, they show any underlying differential behavior at a molecular scale. As expected, upon increasing the poly-cation concentration, the EPR spectrum broadens, reflecting a decrease in molecular flexibility due to molecular interactions up to a near-saturation regime for all interacting partners (**Fig. 2.5E, Fig. 2.9**). This saturation is achieved at a lower molar ratio (poly-cation:αS) for pLK, as compared to ΔNt-Tau and Tau441. Indeed, fitting the data with an approximated binding model assuming *n*-identical and independent binding sites revealed an apparent dissociation constant an order of magnitude smaller for pLK (~ 5 µM) than for Tau441 or ΔNt-Tau (~ 50 µM). Despite being a rough estimate, this indicates a higher affinity of αS for simpler poly-cations with an uninterrupted stretch of positive charges. Given such differences in affinities between αS and the various poly-cations, we hypothesized that their liquid properties might evolve differently over time.
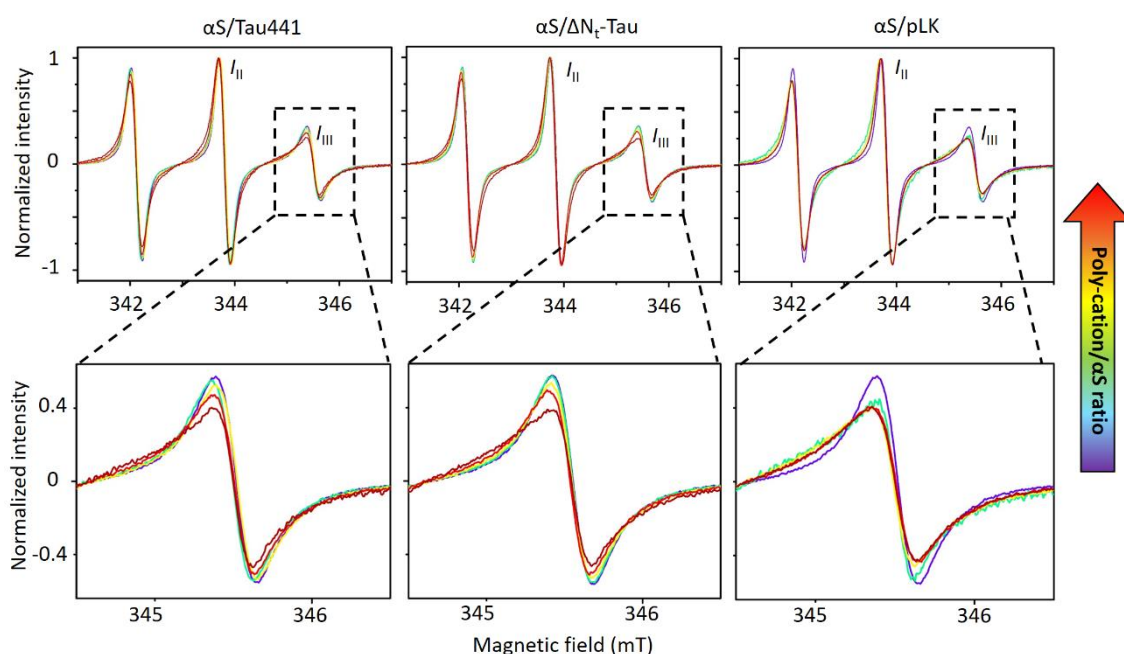
Figure 2.9. EPR binding titration of αS and different poly-cations. Normalized CW X-Band EPR spectra (top) and zooms (bottom) of 50 µM TEMPOL-122-αS in 15 % PEG-8 in the presence of increasing concentrations of Tau441 (left), ΔNt-Tau (center) or pLK (right). A cold-to-warm color code indicates increasing concentrations of the poly-cation. The second and third bands of the spin probe spectrum, used for the titration analysis (see **Fig. 2.5E** and methods for more information) are indicated as I_{II} and I_{III}, respectively, where I stands for intensity. Data adapted with permission from Ilenia Serra, Maruan A. Bracci and Dr. Inés García.

4. Rapid gelation or slow LSPT-driven amyloid aggregation in αS/pLK vs αS/Tau441 coacervates

Considering the highly crowded environment inside the protein coacervates and the amyloidogenic nature of the proteins, we monitored the behavior of the coacervates over time in order to detect possible LSPT processes. By using BF and CF microscopy (**Fig. 2.10**), we observed that αS/Tau441 coacervates undergo fusion to a great extent in solution forming large droplets, which get in contact to the surface of the bottom of the well/slide and wet the surface, as expected for totally liquid droplets (**Fig. 2.11D**); we termed these structures generated at the bottom "protein rafts". These structures remain liquid as they retain their fusion ability (**Fig. 2.11B**) and can be seen within a few hours after LLPS is triggered (**Fig. 2.10 and Fig. 2.11**C). We have observed that the wetting process is favored on the surface of hydrophilic materials, but not hydrophobic ones (**Fig. 2.11A**), as is expected for electrostatic coacervates with unbalanced charges and thus high electrostatic potential and surface tension. Remarkably, coalescence and raft formation are significantly reduced for αS/ΔNt-Tau and dramatically lower for αS/pLK condensates (**Fig. 2.10**). In this latter case, essentially only limited fusion events and wetting-incompetent droplets are observed at incubation times longer than 5h.
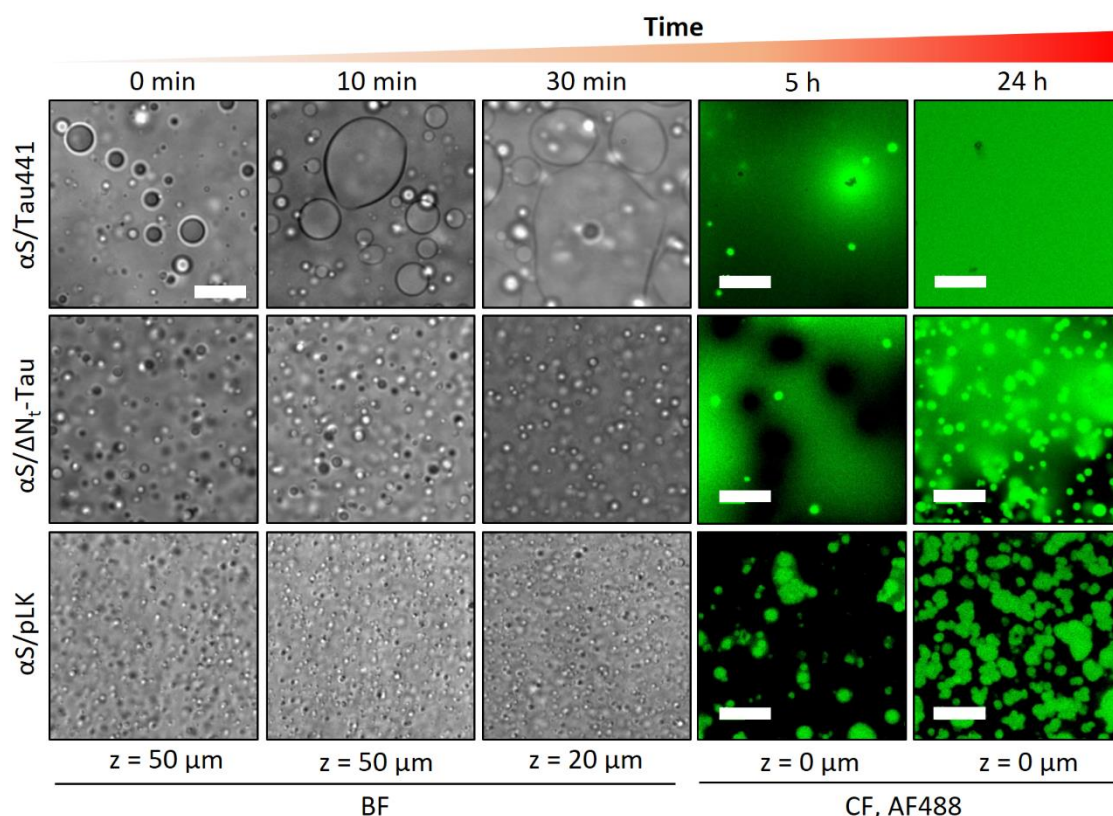
Figure 2.10. Coalescence and wetting properties of αS electrostatic complex coacervates. BF (grayscale panels) and CF (right, fluorescence of AF488-labelled αS in green) microscopy images of coacervate samples with 100 μM αS (1% fluorescently-labelled) in the presence of 100 μM Tau441 (top), ΔNt-Tau (middle) or 1 mM pLK (bottom) at different incubation times and focal heights (z, distance from the bottom of the plate well). αS/Tau441 coacervate wetting

after 24 h forms rafts larger than the image. Scale bar is 20 μm for all images. Data acquired in collaboration with David Polanco.

Next, we wondered whether the enormous liquid-like protein reservoirs generated in αS/Tau441 LLPS would lead to amyloid aggregation of any of the investigated proteins. We monitored the maturation of αS/Tau441 droplets over time by WF microscopy in the same conditions as described above but with 1 μM AF488-labelled αS and Atto647N-labelled Tau441 (**Fig. 2.12A**). As expected, we observed total co-localization of the proteins at all times of the maturation process. Interestingly, from ca. 5 h onwards, more intense, non-round structures which we termed "puncta" were observed inside the rafts, some co-localizing with αS and some enriched in Tau441 (**Fig. 2.12A** white arrowheads). These puncta were observed always inside the rafts and to a greater extent for αS/Tau441 than for αS/ΔNt-Tau. No puncta were evident in αS/pLK coacervates or in fusion-incompetent droplets of both pLK and Tau systems.
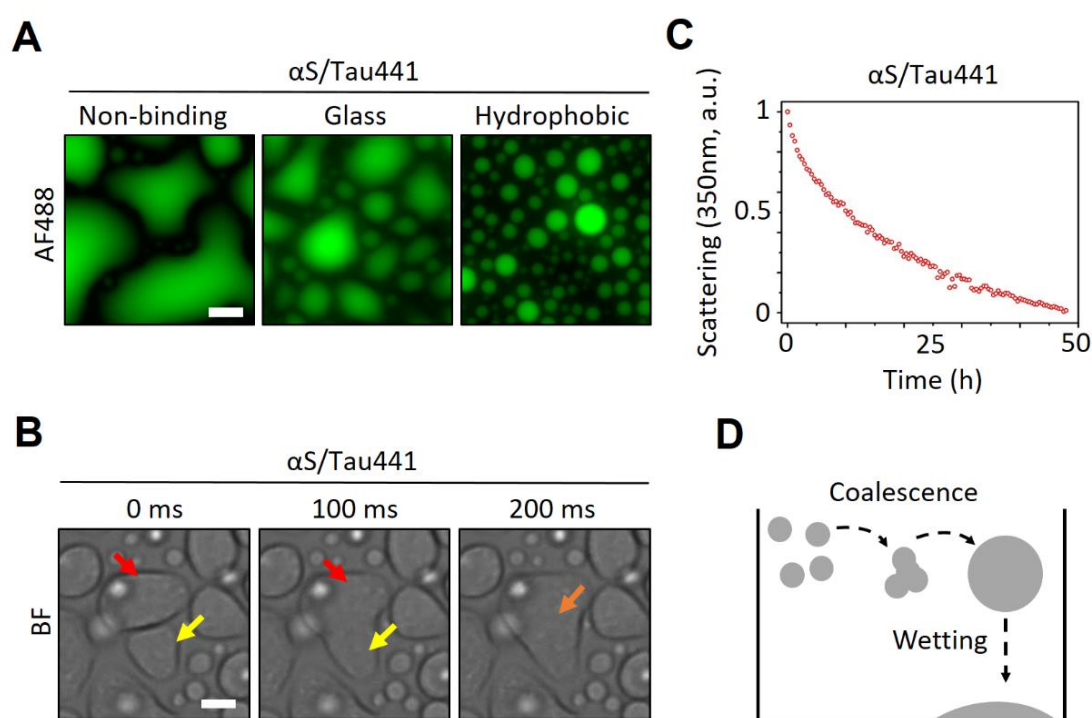
Figure 2.11. Coalescence and wetting properties of αS/Tau441 coacervates. A) Representative WF microscopy images of αS/Tau441 coacervates (25 μM each protein, 1 μM AF488-labeled αS) visualized at the bottom of the plate wells (z = 0 μm) after 24 h incubation using microwell plates with different material coatings as indicated. Both non-binding plates (PEG-based coated microwell plates typically used as non-binding plates for hydrophobic protein samples) and glass plates have hydrophilic coatings. As hydrophobic material, non-treated 96-well polystyrene microplates were used. **B**) A fusion event of two αS/Tau441 rafts as observed by BF microscopy is shown. Scale bars are 20 μm. **C**) Light scattering signal (at 350 nm) of an αS/Tau441 coacervate sample over time, indicating the time scale for the deposition and wetting of the droplets on the bottom of the sample. **D**) Schematic of the coalescence and

surface wetting of αS/Tau441 coacervates. Data in **A**) and **B)** adapted with permission of Jorge Tarancón and David Polanco.

To test whether these puncta containing αS and Tau441 were indeed amyloid aggregates, we conducted analogous experiments by CF microscopy where Tau441 was labeled with Atto647N and 12.5 µM thioflavin-T (ThT), an amyloid-specific dye, was added to the solution from the beginning. After 24 h, we observed ThT-positive structures, containing Atto647N-Tau441, that recapitulate the size, shape and localization of the previously described puncta within the protein rafts (**Fig. 2.12B** middle and bottom row), indicating amyloid aggregation inside the aged coacervates. However, no ThT staining of αS/Tau441 droplets or rafts, even after 24 h incubation, was observed (**Fig. 2.12B**, top row - remaining droplets above protein rafts).

To further prove the solid-like nature of the puncta, we treated stain-free 24 h-aged samples with high concentrations (1 M) of NaCl in order to dissolve the liquid coacervates (droplets and rafts) and isolate the puncta, as these structures are now salt resistant in contrast to the liquid coacervates (see **Fig. 2.2C** and **Fig. 2.4A, B**). Note that the fact that the puncta are salt resistant already suggest that these aggregates are not stabilized through charge-charge interactions, but by other type of interactions, in like to the hypothesis that they are amyloid-like aggregates. Once isolated, the puncta were incubated with ThT and a strong increase in ThT fluorescence signal was observed exclusively in the puncta, typical for amyloid-like aggregates (**Fig. 2.13**). When the same isolated puncta were incubated in 4 M guanidinium chloride (GdnHCl), they very rapidly disaggregated and the ThT signal is lost (**Fig. 2.13B**), as it is typically observed for amyloid fibrils [451]. Indeed, we compared samples or isolated puncta (LSPT-derived αS/Tau441 aggregates) with samples containing sonicated αS amyloid fibrils (treated with the same protocol as for the puncta isolation, *i. e.* incubation with 1M NaCl followed by ThT staining) and found that the particle size and ThT intensity between the two types of aggregates are indistinguishable (**Fig. 2.13A** and **C**)
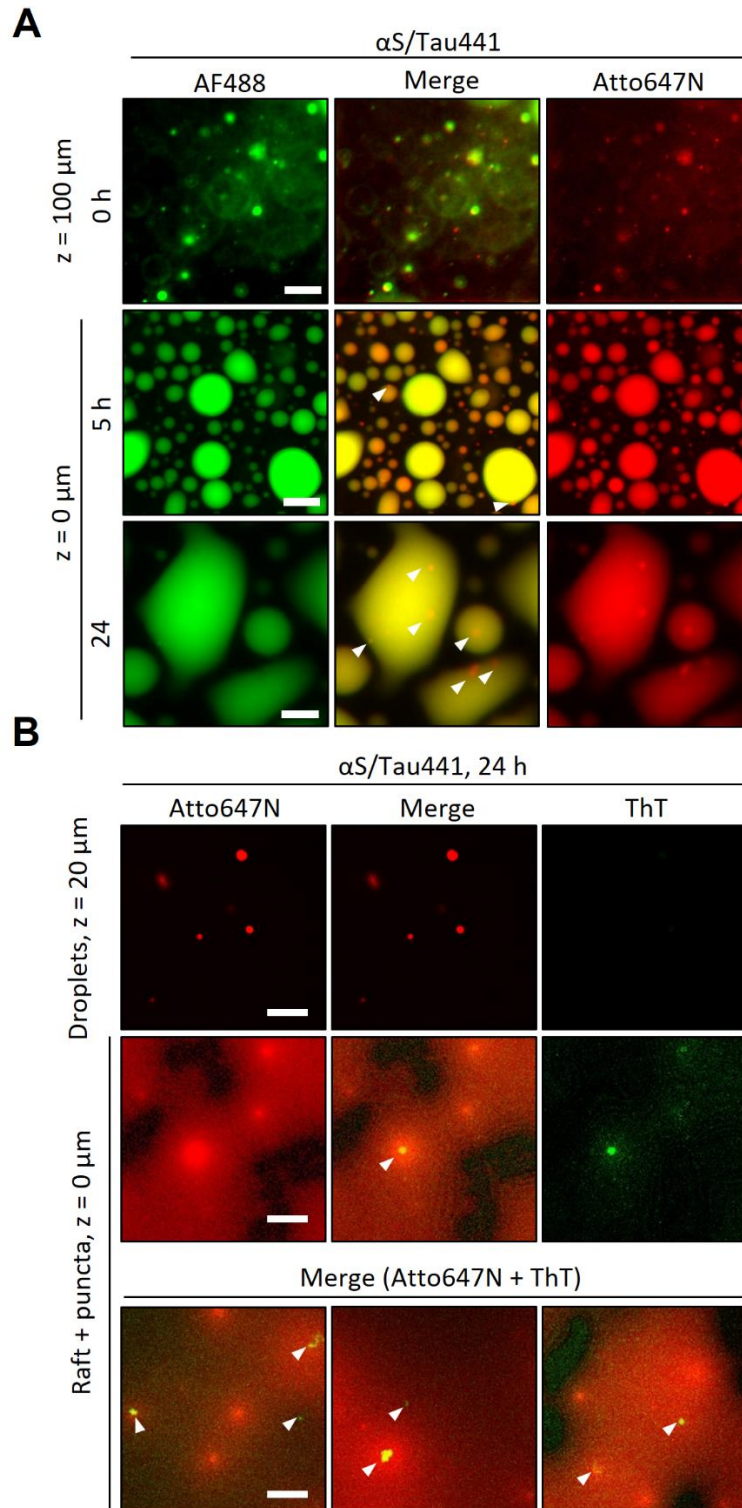
Figure 2.12. Liquid-to-solid phase transition and amyloid aggregation of αS/Tau441 coacervates. A) WF microscopy images of 25 μM αS in the presence of 25 μM Tau441 (1 μM AF488-labelled αS and Atto647N-labeled Tau441) at different incubation times and focal heights (z, distance from the bottom of the non-binding plate well). **B**) CF microscopy images of 25 μM αS in the presence of 25 μM Tau441 (1 μM Atto647N-labeled Tau441) and 12.5 μM thioflavin-T (ThT). Suspended protein droplets and deposited protein rafts and puncta are shown in the top and middle rows, respectively. The bottom row shows images of rafts and puncta from 3 independent replicate experiments. White arrowheads indicate ThT-positive

puncta in both panels. Scale bar is 20 μm for all images. Data in **B)** acquired in collaboration with David Polanco.
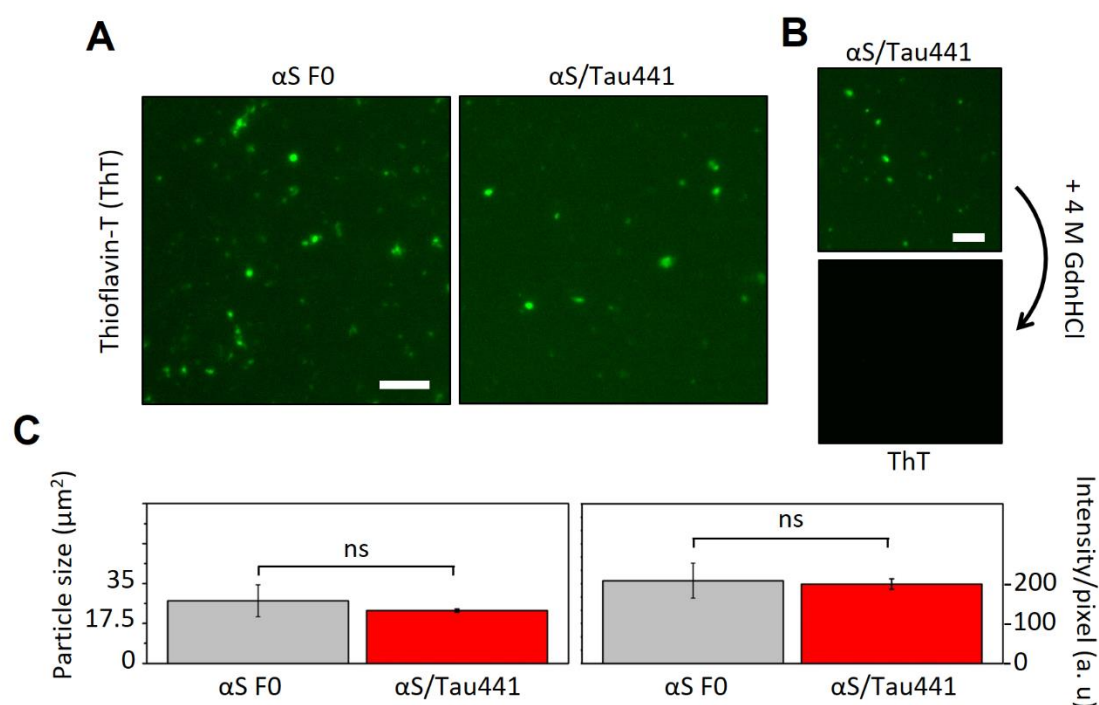
Figure 2.13. Thioflavin-T (ThT) analysis of the liquid-to-solid phase transition (LSPT) of αS/Tau441 coacervates. A) Representative WF microscopy images of a ThT stain (1:2 ThT:αS) of sonicated canonical αS fibrils (left) and αS/Tau441 (right) aggregates/puncta isolated in buffer without PEG but with 1 M NaCl, after LLPS and LSPT (25 μM each protein, unlabeled). The treatment with high salt concentration dissolves the rafts and any possible droplets that remained suspended in the solution. The puncta, however, are insensitive to this treatment, indicating a change of the main interactions that stabilize the protein structures. A control sample with sonicated αS fibrils treated in the same way as the puncta (fibrils were deposited on the bottom of the wells once formed and quantified and then resuspended in the same buffer with 1 M NaCl) is shown on the left panel. **B)** WF microscopy images of isolated αS/Tau441 aggregates before (top) and after (bottom) addition of 4 M GdnHCl. Scale bars are 40 μm. **C)** Statistical analysis of the particle size (left, N = 80-90) and mean particle intensity (right, N = 80-90) of the αS/Tau441 aggregates formed inside the protein liquid coacervates by LSPT (in red), as compared to the typical *in vitro*-generated αS fibrils (grey). The analysis was performed from data obtained from 3 independent samples with 3 analyzed fields per sample that contained at least 20 particles per field (**see Methods** for a detail description of the analysis). The mean and standard deviation are shown. The statistical significance between pairs of distributions was determined with a two sample t-test assuming unequal variances, but no significant (ns) difference was obtained for particle size and ThT-intensity per particle between LLPS-derived αS/Tau441 aggregates and the typical amyloid αS fibrils. Data adapted with permission of David Polanco.

After gaining insight into the molecular determinants that trigger αS/Tau441 LLPS and LSPT-driven amyloid aggregation of both proteins within the coacervates, we set out to investigate the changes in the protein networks during the liquid-to-solid transition in

more detail. To this end, we used fluorescence lifetime imaging (FLIM) and Förster resonance energy transfer (FRET) microscopy (**Fig. 2.14, 2.15 and 2.16**). We hypothesized that coacervate maturation into more condensed or even solid-like aggregated protein structures would bring proteins and, in turn, their attached fluorescent probes into closer contact, thus likely exerting a quenching effect manifested as a reduced fluorescence lifetime (τ) of the probes as described previously [503–505]. Likewise, this decrease in τ could also be concomitant, for doubly-labelled samples (AF488 and Atto647N as donor and acceptor FRET dyes), with an increase in FRET efficiency (E) upon condensation and LSPT of the coacervates. We monitored the raft and puncta formation of αS/Tau441 and αS/ΔN$_t$-Tau LLPS samples over time (at 25 μM each protein with 1 μM AF488-labelled αS and/or Atto647N-labelled Tau441 or ΔN$_t$-Tau in LLPS buffer). We observed a general trend consisting of a slight decrease in the fluorescence lifetimes of both AF488 (τ_{488}) and Atto647N (τ_{647N}) probes upon coacervate maturation (**Fig. 2.14** and **Fig. 2.15C**).

Interestingly, this change was dramatically enhanced for the puncta inside the rafts (**Fig. 2.14B-C**), suggesting that significant protein conformational rearrangements take place precisely upon LSPT rather than on coalescence and raft formation. In support of this, no significant change in fluorescence lifetime was observed for 24 h-aged droplets of αS/ΔN$_t$-Tau (**Fig. 2.15D**), suggesting that droplet gelation is a process distinct from raft and puncta formation and is not accompanied by a significant molecular reconfiguration within the coacervates. It needs to be mentioned that puncta had different sizes and heterogeneous morphologies, with variable content in αS, particularly for the αS/Tau441 system (**Fig. 2.15E**).

The reduced fluorescence lifetime in the puncta was concomitant with increased intensity, particularly for Atto647N-labelled Tau441 (**Fig. 2.15A**), and FRET efficiency (**Fig. 2.16**) for both αS/Tau441 and αS/ΔN$_t$-Tau systems, suggesting extensive condensation and LSPT of both proteins already at 5 h after LLPS was triggered. We observe lower τ_{647N} and slightly higher τ_{488} values, concomitant with lower and more heterogeneous FRET values, in αS/Tau441 puncta compared to αS/ΔN$_t$-Tau. Arguably, this might stem from the fact that in the αS/Tau441 system a more heterogeneous content of αS, typically sub-stoichiometric with respect to Tau, is observed and expected in the aggregates, as Tau441 can also undergo LLPS and aggregation by itself (**Fig. 2.15E**). The extent of droplet coalescence, raft formation and, importantly, protein aggregation inside liquid-like coacervates is, however, maximized when both Tau441 and αS are present.
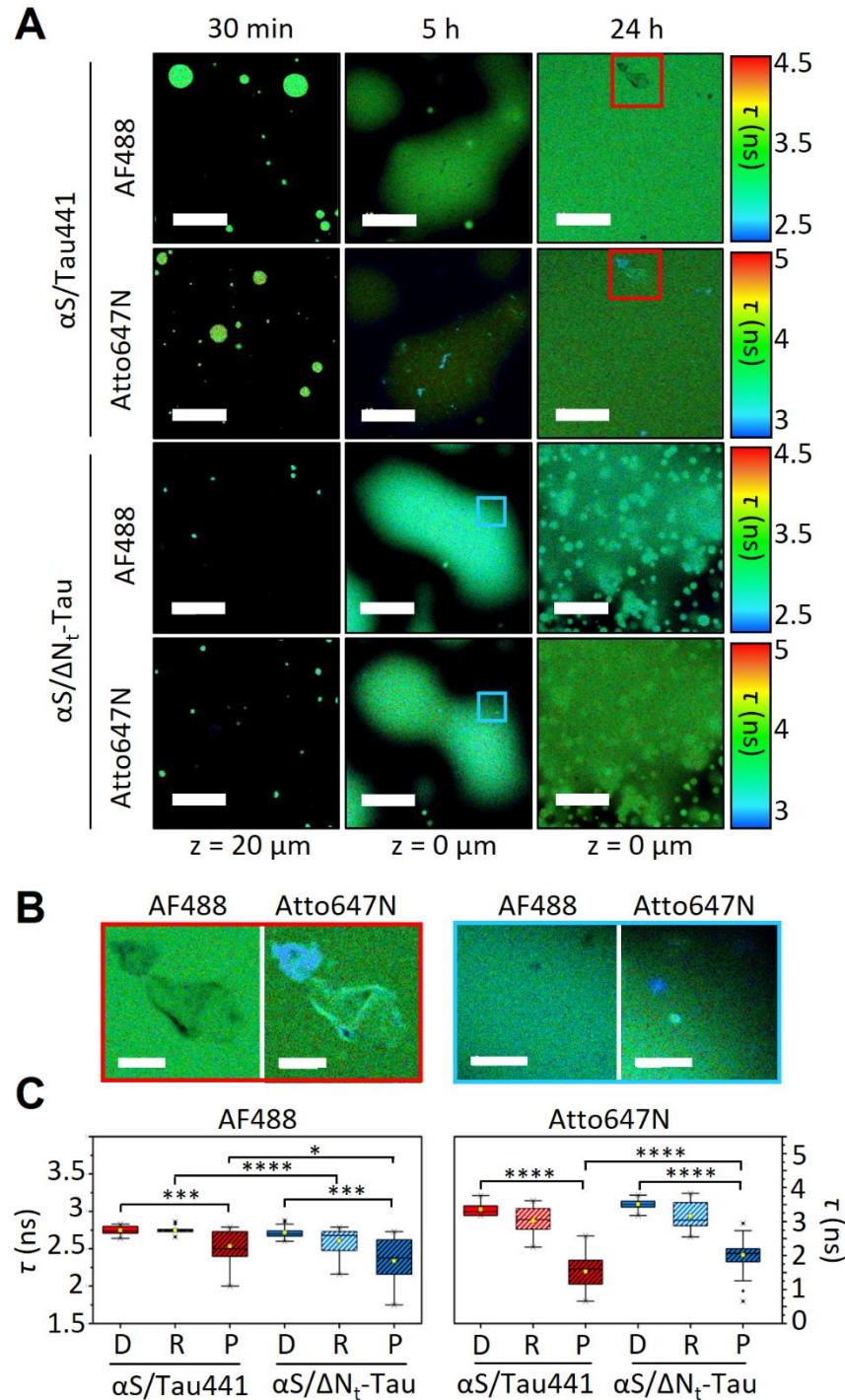
Figure 2.14. FLIM analysis of the liquid-to-solid phase transition of αS/Tau coacervates. A) Fluorescence lifetime imaging microscopy (FLIM) images of αS/Tau441 and αS/ΔNt-Tau with 25 μM of each protein (1 μM AF488-labelled αS and 1 μM Atto647N-labeled Tau441 or ΔNt-Tau). Columns show representative images of the LLPS samples at different maturation times (30 min, 5 h and 24 h). Red and blue boxes show regions containing puncta for αS/Tau441 and αS/ΔNt-Tau, respectively. Lifetime range shown as a color scale. **B)** Zoom-in FLIM images of the selected regions shown in red and blue boxes in panel **a**, showing αS/Tau441 (left panels) and αS/ΔNt-Tau (right panels) puncta. Lifetime range shown with the same color scale than in **A. C)** Box plots showing the lifetime distributions of AF488 (attached to αS) or Atto647N

(attached to Tau) for the different protein species (droplets -D-, rafts -R- and puncta -P-) identified in the FLIM images recorded for αS/Tau441 and αS/ΔNt-Tau coacervate samples. Mean and median values are shown as yellow squares and black lines within the boxes, respectively. Lower and upper box limits indicate the first and third quartile, respectively, while minimum and maximum values within 1.5 x interquartile range (IQR) are shown as whiskers. Outliers are shown as black diamonds. The statistical significance between pairs of distributions was determined with a two sample t-test assuming unequal variances. The *p*-value from a two-tailed t-test is shown as stars for each compared pair of data (* *p*-value > 0.01, ** *p*-value > 0.001, *** *p*-value > 0.0001, **** *p*-value > 0.00001, *ns* means not significant (*p*-value > 0.05). Scale bar = 20 μm for all images. Data acquired in collaboration with David Polanco and Dr. Nunilo Cremades.
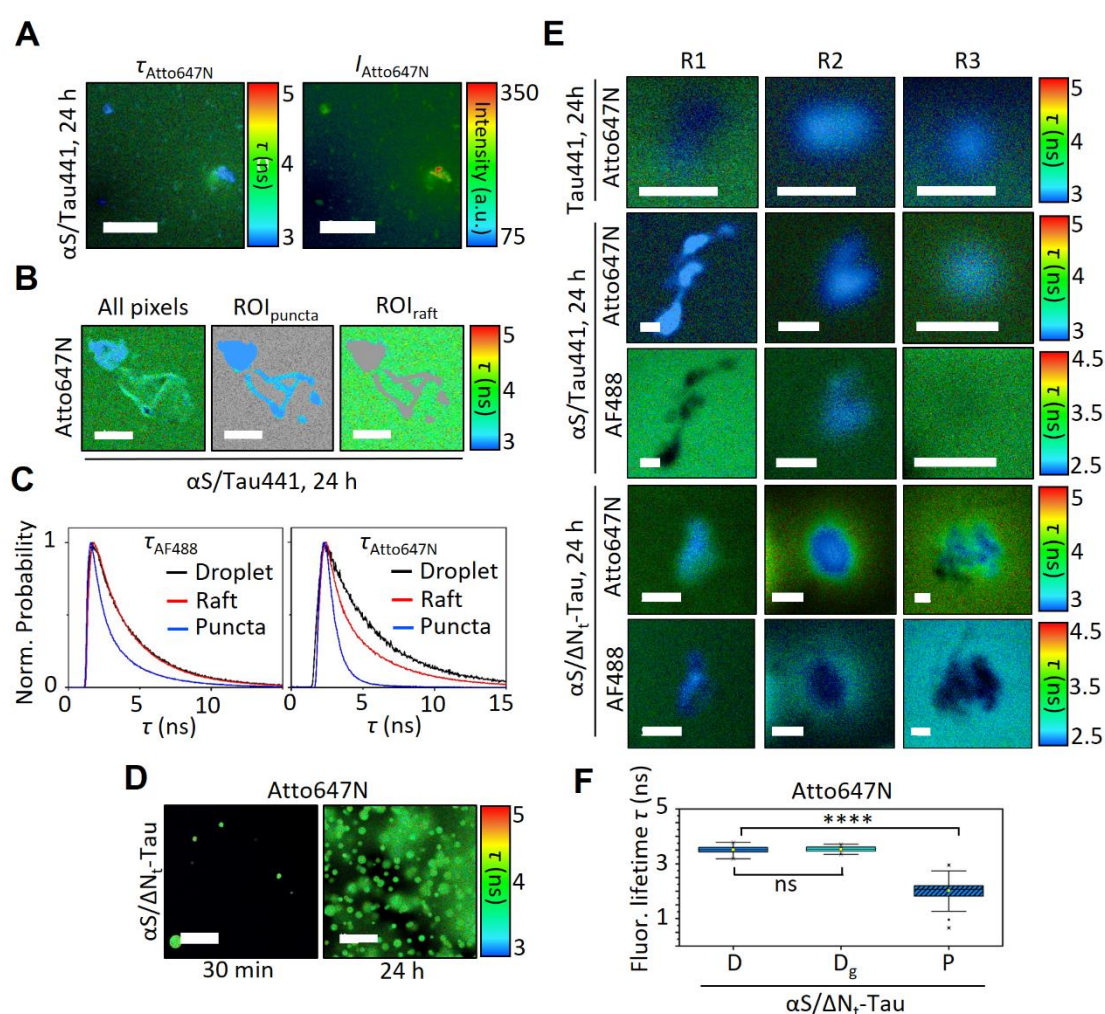
Figure 2.15. Fluorescence lifetime imaging microscopy (FLIM) analysis of the LSPT of αS/Tau441 coacervates. A) Representative lifetime (left) and intensity (right) color-coded FLIM images of αS/Tau441 coacervates after 24 h incubation and deposited on the bottom of the well (25 μM each protein, 1 μM AF488-αS and Atto647N-Tau441). The images show the same microscopy field with a large raft composed of both proteins occupying the entire field (shown in green in both images – note that the background intensity is ~ 30 counts) in which several puncta are visualized as a condensation of proteins (higher intensity values, visualized as brighter green-yellow-red spots). This correlates with lower fluorescence lifetimes (due to condensation-induced self-quenching) visualized as blue spots that coincide with the more

137

intense spots. Data is shown for the Atto647N channel. Scale bars = 10 μm. **B-C**) Analytical approach for species-specific lifetime analysis. A representative lifetime color-coded image of αS/Tau441 coacervates after 24 h incubation is shown in **B)**, and the selection of regions of interest (ROIs) containing species-specific lifetimes (ROI$_{puncta}$, ROI$_{raft}$) are selected from the overall image (ROI$_{all}$). Data is shown for the Atto647N channel. Scale bars are 5 μm. **C**) Representative normalized lifetime decays from species-specific ROIs for the AF488 (left) and Atto647N (right) channels. **D**) Representative lifetime color-coded FLIM images (left panels) of αS/ΔN$_t$-Tau droplets at initial times and after 24 h incubation and deposited on the bottom of the well (25 μM each protein, 1 μM AF488-αS and Atto647N-ΔN$_t$-Tau) and their pixel-wise lifetime analysis (right, box plot). 24-incubated gelated droplets (D$_g$) are shown in light turquoise blue. Early droplets (D) and puncta (P) are the same as in **Fig. 2.14C** but are shown here for comparison. Mean and median values are shown as yellow squares and black lines within the boxes, respectively. Lower and upper box limits indicate the first and third quartile, respectively, while minimum and maximum values within 1.5 x interquartile range (IQR) are shown as whiskers. Outliers are shown as black diamonds. The statistical significance between pairs of distributions was determined with a two sample t-test assuming unequal variances. No significant differences were found for droplets that gelated after 24-h incubation (D$_g$). The *p*-value from a two-tailed t-test is shown as stars for each compared pair of data (* *p*-value > 0.01, ** *p*-value > 0.001, *** *p*-value > 0.0001, **** *p*-value > 0.00001, *ns* means not significant (*p*-value > 0.05). Scale bar = 20 μm. **E**) Lifetime color-coded FLIM images showing the heterogeneity of size, shape and fluorescence lifetime in puncta from Tau441, αS/Tau441 and αS/ΔN$_t$-Tau. For αS/Tau441 and αS/ΔN$_t$-Tau puncta the variability in αS content is also evident. Scale bar = 1 μm. Data acquired in collaboration with David Polanco and Dr. Nunilo Cremades.
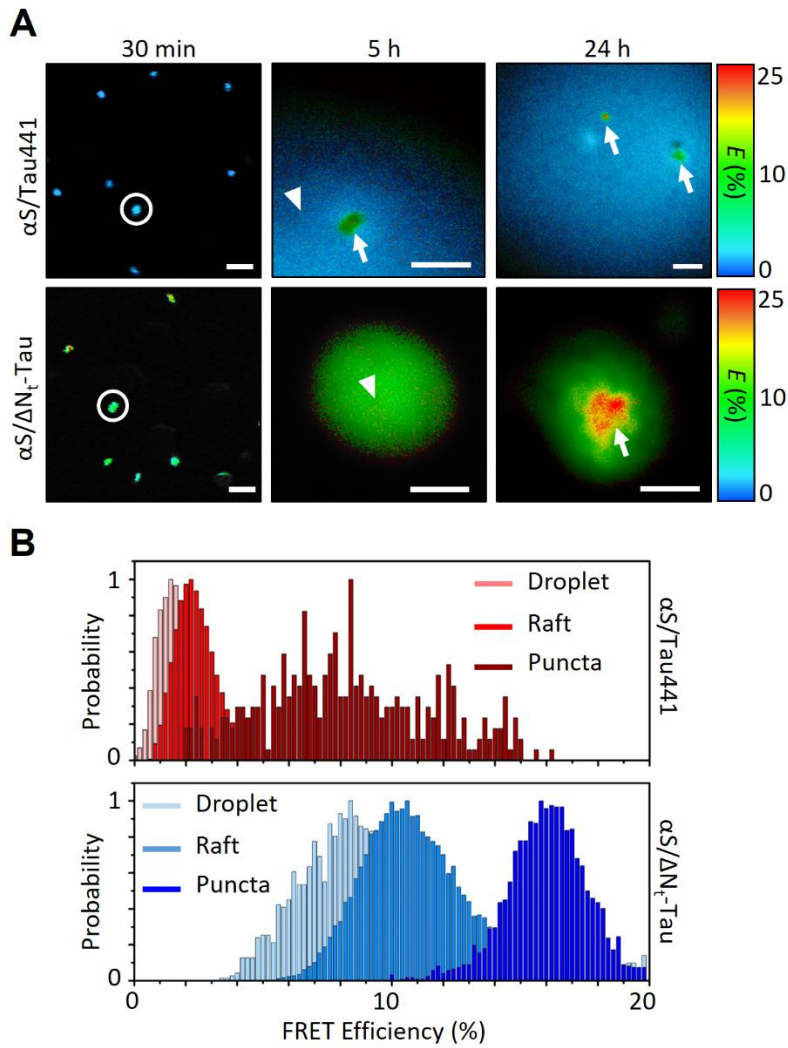
Figure 2.16. Förster Resonance Energy Transfer (FRET) analysis of the LSPT of αS electrostatic coacervates coacervates. A) Representative FRET efficiency (*E*) color-coded FRET images of αS/Tau441 (top) and αS/ΔN$_t$-Tau (bottom) coacervation at *t* = 30 min (left), 5 h (center) and 24 h (right). Higher, "red-shifted" *E* values in puncta (white arrows) respect to the droplets (white circles) and rafts (white arrowheads) indicate LSPT. Scale bars are 5 μm for the left images and 2 μm for the center and right images. **B**) Normalized FRET efficiency histograms for the different protein structures observed (droplets, rafts and puncta) in αS/Tau441 (top) and αS/ΔN$_t$-Tau (bottom) LLPS and LSPT processes. Each histogram is composed of a triplicate experiment with 2 analyzed fields per sample

Discussion

αS has been recently proposed by us and others to be able to phase separate from a solution by simple coacervation. The *in vitro* experiments reported required typically high protein concentrations (in the order of 200 μM) and specific experimental setups, and LLPS was typically observed after unusually long incubation times [436, 506]. Here, we present a detailed study of the phase-separating and LSPT behavior of αS in the presence of disordered poly-cations in a controlled environment at low micromolar concentrations and physiologically relevant conditions, following the typical thermodynamically-driven LLPS behavior. We have found that αS, containing a highly negatively charged C-terminal region at physiological pH, is able to trigger LLPS in the presence of highly cationic disordered polypeptides, such as pLK or Tau, by a process of electrostatic complex coacervation. In previous studies αS was described to be a client protein that partitions into pre-existing liquid droplets of Tau and polyU, given their electrostatic interaction [493]. Here, we prove that αS is indeed capable of co-driving the LLPS process with Tau through the same type of interactions but with an active role rather than being a simple client molecule. This might have relevant implications in a cellular context, where αS encounters a variety of poly-cationic molecules which have been related to its disease-linked aggregation both *in vitro* and *in vivo* [507–509].

Maturation or ageing of liquid protein condensates over time into gel-like or solid-like structures has been reported to be relevant for the functioning of certain physiological condensates [510], but also to disease, as an aberrant process that precedes amyloid aggregation [149, 151, 511]. In a number of studies, protein dynamics within liquid droplets has been suggested as one of the key factors dictating the maturation process [512, 513]. In the electrostatic coacervates of αS with poly-cations, however, αS dynamics play a minor role in their maturation, which, according to our results, is governed by the strength of the interaction with the poly-cation and, the valence and multiplicity of these interactions. Equilibrium theories establish that the equilibrium landscape of two liquid phase states would be the presence of one large droplet rich in the biopolymers that drive the LLPS [514, 515]. The growth of liquid droplets could be achieved by Ostwald ripening [516], coalescence [517] or by consumption of free monomers from the disperse phase [518]. In the case of αS and Tau441 or ΔNt-Tau, most of the protein is concentrated in the condensates under the conditions used in this study. However, while full-length Tau droplets rapidly undergo coalescence accompanied by surface wetting, droplet fusion is hindered for ΔNt-Tau and, to a dramatic extent, for pLK, indicative of a rapid loss of liquid properties in these two systems. According to our FLIM-FRET analysis, the aged pLK and ΔNt-Tau droplets show a similar degree of protein condensation as the initial droplets (similar fluorescence lifetimes), indicating that the initial protein network is preserved, although it becomes more rigid.

We have rationalized our experimental results in the following model (**Fig. 2.17**). A simple coacervate (with a reduced number of different components and valences), together with a higher affinity of the protein network, as in the case of the αS/pLK system, results in a rapid optimization of the coacervate charges (*i. e.* a rapid search of the polypeptide chains within the condensates to effectively engage and thus screen all the charges in the coacervate). This yields gel-like, fusion-incompetent droplets with low

surface energy and thus unable to wet surfaces. In contrast, a complex coacervate network, with multiple components or weak homotypic and heterotypic interactions occurring at the same time within individual coacervates, as in the αS/Tau441 case, would have more difficulties in screening all the charges. This results in droplets that keep a liquid-like behavior for longer times, and present high surface energy, which tends to be minimized by coalescing and growing (thus minimizing the droplets surface area/volume ratio), as well as by wetting hydrophilic surfaces. Interestingly, N terminally-truncated forms of Tau, including some natural isoforms [519], would show an intermediate behavior, with some coacervates with αS aging into long-lived, gel-like droplets, while others resulting in large liquid-like condensates. This duality in the maturation of the αS electrostatic coacervates is in line with recent theoretical and experimental LLPS studies that have highlighted the relevance of valence exhaustion and electrostatic screening within condensates as a key mechanism to control the size of the condensates and their liquid properties [515, 518].
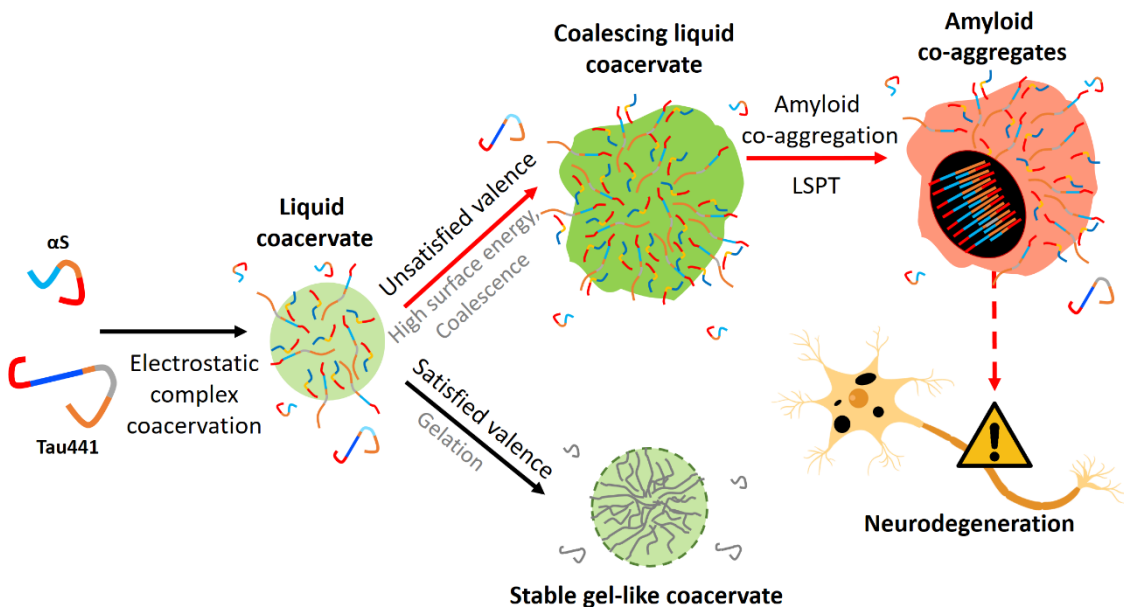
Figure 2.17. Model for the synchronized LLPS and LSPT-driven amyloid hetero-aggregation of αS and Tau441. The schematic shows the proposed amyloid aggregation pathway for αS and Tau441 through LLPS and LSPT. With complementary anion-rich (red) and cation-rich (blue) regions, αS and Tau electrostatic coacervates with satisfied valences have a lower surface energy and thus coalesce to a lesser extent, allowing the droplet to age rapidly reaching a stable, non-coalescing gel-like state. This situation is highly favorable in the case of αS/pLK coacervates owed to a higher affinity and simpler one-pair interaction protein network, which allows for a rapid gel-like transition. In contrast, droplets with unsatisfied valences and, thus, interaction-available protein charged regions, will make the coacervates more prone to coalesce and wet hydrophilic surfaces in order to reduce their high surface energy. This situation is preferred in αS/Tau441 coacervates, which have a multivalent complex network composed of Tau-Tau and αS-Tau interactions, and are thus more prone to remain with high surface tension. Larger coacervates, in turn, will be more susceptible to retain their liquid-like properties, allowing for other interactions to start taking place. Eventually, amyloid aggregates containing both proteins are formed within the liquid coacervates, potentially leading to neurodegeneration.

The resulting large, liquid-like structures, with a highly crowded and protein-concentrated environment, formed during the maturation of αS/Tau441 and, to a lesser degree, αS/ΔN$_t$-Tau coacervates, are ideal reservoirs for the nucleation of protein aggregation. We have indeed observed the formation of solid protein aggregates in such type of protein coacervates (rafts), which typically contain both αS and Tau. We have demonstrated that these hetero-aggregates are stabilized by non-electrostatic interactions, are able to bind the amyloid-specific ThT dye in the same way as canonical amyloid αS fibrils do and, indeed, share similar stabilities with respect to different treatments, suggesting that the αS/Tau aggregates formed inside electrostatic coacervates have an amyloid-like nature. These aggregates are only observed inside the coacervates that maintain liquid-like properties, and have never been observed if the coacervates/droplets have reached a gel-like state. In the latter case, the increase in strength of the electrostatic interactions and thus the concomitant rigidity of the protein network would impede the necessary protein conformational rearrangements for establishing the new type of protein interactions required for amyloid nucleation. This could be, however, achieved in a more flexible, liquid-like coacervate, which, in turn, is more likely to remain liquid upon increasing its size.

The fact that aggregate formation inside the condensed phase is largely favored in large αS/Tau condensates over small droplets, which can rapidly suffer gelation, highlights the relevance of identifying the factors that control droplet fusion. It is, therefore, not just the tendency to phase separate but also the size of the condensates that must be regulated for their proper functioning as well as for disease prevention [515, 518]. Our results also emphasize the importance of the balance between LLPS and LSPT for the αS/Tau system. While droplet formation might play a protective role regarding amyloid aggregation by reducing the amount of available protein monomers in saturation conditions, as it has been already proposed in other systems [115, 520], droplet coalescence of highly liquid droplets might lead to protein aggregation in the interior of the coacervates by a slow conformational rearrangement of the protein network facilitating sporadic nucleation.

Overall, our data strongly underlines the relevance of coacervate valence and satisfied/unsatisfied interactions in the context of LSPT. In particular, we show that only full length αS/Tau441 condensates are capable of effectively coalescing and nucleating to form amyloid-like hetero-aggregates involving both proteins, and propose a molecular mechanism based on our experimental results. The co-aggregation of both proteins inside the αS/Tau liquid coacervates that we report here could indeed be related to the co-localization of both proteins in disease-hallmark inclusions and might pave the way for understanding the link between LLPS and amyloid aggregation of IDPs in neurodegeneration. Furthermore, we believe the application of time-resolved fluorescence microscopy techniques such as FLIM and FRET microscopy allows us to better understand the molecular changes occurring upon liquid-to-solid phase transition of protein droplets and the subsequent amyloid co-aggregation of αS and Tau. Our data shows that combining such techniques with conventional ThT-based amyloid imaging enables a better interpretation of the data and paves the way for more accurate and quantitative descriptions of other ageing LLPS systems. Recently, Dr. Cremades and pre-doc student David Polanco have successfully employed dcFCCS/SPFS for

unambiguously demonstrating the LLPS and LSPT-mediante amyloid heteroaggregation of both proteins with single-particle resolution.

In this study, we show that αS can indeed phase-separate into liquid droplets in the presence of Tau by electrostatic complex coacervation, similarly as it does with other positively charged polypeptides like poly-L-lysine (pLK) and that, in this process, αS acts as scaffolding molecule. We have identified dramatic differences in the maturation processes of the αS electrostatic coacervates, which are related to the differences in the valences and interaction strengths of the proteins involved in the coacervate network. Interestingly, we have observed amyloid co-aggregation of αS and Tau inside the liquid coacervates and have determined some of the key factors that lead to aggregation of both proteins inside this type of coacervates. This process, which we have characterized here in detail, constitutes a possible molecular mechanism underlying the co-localization of both proteins in disease-hallmark inclusions.

Materials & methods

Protein expression, purification and labeling

Monomeric WT-αS, the cysteine mutants (Q24C-αS, N122C-αS) and the ΔC_t-αS variant ($\Delta 101$-140) were expressed in *E. coli* and purified as described before [292]. 5 mM DTT was included in all purification steps for the cysteine αS mutant variants to prevent disulfide bridge formation. Tau441 isoform (plasmid obtain from Addgene #16316) and the ΔN_t-Tau variant ($\Delta 1$-150, generated by IVA cloning with primers CTTTAAGAAGGAGATATACATATGATCGC CACACCGCGG, CATATGTATATCTCCTTCTTAAAGTTAAAC) were purified as described in[521] with the following modifications: *E. coli* cultures were grown at 37 °C and 180 rpm to an OD$_{600}$ = 0.6 - 0.7 and expression was induced with IPTG at 37 °C for 3 h. Cells were harvested at 11.500 x g for 15 min at 4 °C and washed with saline buffer containing NaCl 150 mM. The pellet was resuspended in lysis buffer (20 mL per 1 L of LB: MES 20 mM pH 6.8, NaCl 500 mM, EDTA 1 mM, MgCl$_2$ 0.2 mM, DTT 5 mM, PMSF 1 mM, benzamidine 50 μM, leupeptin 100 μM). The sonication step was performed on ice at 80 % amplitude with 10 pulses (1 min on, 1 min off). No more than 60 mL were sonicated at once. *E. coli* lysate was heated at 95 °C for 20 min and then cooled on ice and centrifuged for 40 min at 127.000 x g. The cleared supernatant was loaded into a 3.5 kDa membrane (Spectrum™ Thermo Fisher Scientific, UK) and dialyzed against 4 L of dialysis buffer (MES 20 mM pH 6.8, NaCl 50 mM, EDTA 1 mM, MgCl$_2$ 2 mM, DTT 2 mM, PMSF 0.1 mM) for 10 h. A 5 mL cationic exchange column (HiTrap SPFF, Cytiva, MA, USA) was equilibrated with equilibration buffer (MES 20 mM pH 6.8, NaCl 50 mM, EDTA 1 mM, MgCl$_2$ 2 mM, DTT 2 mM, PMSF 0.1 mM). Tau lysate was filtered through a 0.22 μm PVDF filter and injected into the column at a flow rate of 1 mL/min. Elution was performed gradually, and Tau was eluted at 15-30 % elution buffer (MES 20 mM pH 6.8, NaCl 1 M, EDTA 1 mM, MgCl$_2$ 2 mM, DTT 2 mM, PMSF 0.1 mM). Fractions were analyzed by SDS-PAGE, and all the fractions containing a single band at the expected M$_W$ of Tau were concentrated together with a 10 kDa centrifugal filter, changed to a buffer containing HEPES 10 mM, NaCl 100 mM to a final concentration of 100 μM, passed through a 0.22 μm PVDF filter, flash-frozen and stored at -80 °C. K18 protein was kindly provided by Prof. Alberto Boffi. Purity of the preparations was > 95 % as confirmed by SDS-PAGE and MALDI-TOF/TOF. Labelling of the different cysteine αS variants by maleimide chemistry with either AlexaFluor488-maleimide (AF488, ThermoFisher Scientific, Waltham, MA, USA) or TEMPOL-maleimide (Toronto Research Chemicals, Toronto, Canada) was performed as described before [292] and the degree of labelling was confirmed by absorbance and MALDI-TOF/TOF. Tau441, $\Delta 1$-150-Tau (αS/ΔN_t-Tau) and K18 were labelled with Atto647N-maleimide (ATTO-TEC GmbH, Siegen, Germany) using the natural cysteine residues at positions 191 and 322, following the same procedures. Tau441 and its variants were purified by David Polanco and Jorge Tarancón.

Liquid-liquid phase separation (LLPS) assays

Solid poly-L-lysine (pLK, Alamanda Polymers Inc, Huntsville, AL, USA) was dissolved in LLPS buffer (10 mM HEPES, 100 mM NaCl, pH 7.4) to a concentration of 10 mM, sonicated for 5 minutes in a bath sonicator and stored at -20 °C. PEG-8, dextran70 and

FITC-dextran-500 (Sigma-Aldrich, Sant Louis, MI, USA), as well as FITC-PEG-10 (Biochempeg, Watertown, MA, USA) were dissolved in water and dialyzed in LLPS buffer extensively to remove contaminant salts. They were further filtered by a 0.22 μm syringe filter and their concentration was calculated using a refractometer (Mettler Toledo, Columbus, OH, USA). LLPS samples were prepared at room temperature in the following order: Buffer and crowder were mixed and supplemented with 1 mM tris(2-carboxyethyl) phosphine (TCEP, Carbosynth, Compton, UK), 1 mM 2,2,2,2-(Ethane-1,2-diyldinitrilo) tetraacetic acid (EDTA, Carbosynth) and 1 % protease inhibitor cocktail (PMSF 100 mM, benzadimide 1 mM, leupeptin 5 μM). Then, αS and the coacervating poly-cation (pLK or Tau variants) were added. For thioflavin-T (ThT, Carbosynth, Compton, UK) time-series experiments, a total ThT concentration was used so that it was half of the concentration of αS. Samples were mixed gently but thoroughly to ensure their homogeneity. Concentrations of each component varied among experiments as described in the results section. No reducing agent was used in EPR assays to avoid nitroxide radical reduction. Azide was used at a 0.02 % (w/v) concentration whenever an experiment lasted longer than 4 h. For all assays with LLPS samples, mixtures were allowed to equilibrate for 5 minutes before assaying. These assays were performed in collaboration with David Polanco and Jorge Tarancón.

Light scattering

150 μL samples were spotted onto Non-Binding 96-Well Microplates (μClear®, Black, F-Bottom/Chimney Well, Greiner bio-one, Kremsmünster, Austria) and the plate was covered with an adhesive foil. LLPS was monitored by measuring the absorbance at 350 nm at the center of the solution in a CLARIOstar plate reader (BMG Labtech, Ortenberg, Germany). Experiments were performed at 25 °C in triplicate and errors were calculated as the standard deviation from the mean. These assays were performed in collaboration with David Polanco and Jorge Tarancón.

Brightfield (BF), Differential interference contrast (DIC) and widefield fluorescence (WF) microscopy

150 μL samples were typically spotted onto Non-Binding 96-Well Microplates and imaged on a Leica DMI6000B inverted microscope (Leica Microsystems, Wetzlar, Germany) at room temperature. For punctual experiments, μ-Slide Angiogenesis dishes (Ibidi GmbH, Gräfelfing, Germany) or 96-well polystyrene microplates (Corning Costar Corp., Acton, Massachusetts) were also used. A halogen lamp or a mercury metal halide bulb EL6000 (for BF/DIC and WF imaging, respectively) served as illumination sources. For WF microscopy, the light was focused on and collected from the sample using a 40x air objective lens (Leica Microsystems, Germany). For AF488- and ThT-labelled samples, the excitation and emission light was filtered with a standard GFP filter set with bandpass filters of 460-500 nm and 512-542 nm for excitation and emission, respectively, and a dichroic mirror of 495 nm. For Atto647N-labelled samples, a standard Cy5 filter set was used with 628-40 nm and 692-40 nm excitation and emission bandpass filters, respectively, and a dichroic mirror of 660 nm. For BF and DIC microscopy, the same objective was used to collect the reflected light. Collected light was detected on a Leica DFC7000 CCD camera (Leica Microsystems, Germany). Exposure times were 50 ms for BF and DIC microscopy imaging and 20 - 100 ms for WF microscopy imaging. For comparative purposes, exposure time was 100 ms for all ThT experiments. For droplet

fusion visualization, time-lapse experiments were performed, collecting images every 100 ms for several minutes. ImageJ (NIH, USA) was used for image analysis. Experiments were performed in triplicate with similar results. These assays were performed in collaboration with David Polanco and Jorge Tarancón.

Confocal fluorescence (CF) microscopy

For co-localization, FRAP and 3D-reconstruction experiments, images were acquired on a Zeiss LSM 880 inverted confocal microscope using ZEN 2 blue edition (Carl Zeiss AG, Oberkochen, Germany). 50 μL samples were spotted onto a μ-Slide Angiogenesis dish (Ibidi GmbH, Gräfelfing, Germany) treated with a hydrophilic polymer (ibiTreat) and placed on top of a 63x immersion oil objective lens (Plan-Apochromat 63x/N.A. 1.4 Oil DIC). Images were acquired with a resolution of 0.26 μm/pixel and a dwell time of 8 μs/pixel using 458 nm, 488 nm and 633 nm argon laser lines for excitation and emission detection windows of 470-600 nm, 493-628 nm and 638-755 nm for ThT, AF488 and Atto647N imaging, respectively. For FRAP experiments, time-lapses of each sample were recorded at 1 frame-per-second. Experiments were performed at room temperature in triplicate with similar results. All images were analyzed using the software Zen 2 blue edition (Carl Zeiss AG, Oberkochen, Germany). FRAP curves were normalized, plotted and fitted using OriginPro 9.1 from intensity/time data extracted from the images with Zen 2. Recovery curves were fitted to a mono-exponential model to account for molecular diffusion with an additional exponential term to account for acquisition bleaching effects. Then, we calculated D using the nominal bleaching radius and the recovery half-time previously determined, as in equation 5 of Kang M. et. al [499].

Electron paramagnetic resonance (EPR)

Single cysteine αS variants were spin-labelled with 4-hydroxy-2,2,6,6-tetramethylpiperidine-N-oxyl (TEMPOL) at positions 24 (TEMPOL-24-αS) and 122, respectively (TEMPOL-122-αS). For EPR experiments, αS concentration was set to 100 μM and the concentration of PEG was 15 % (w/v). For the different coacervation conditions, the αS:pLK ratio was of 1:10, while the ratios αS:ΔN$_t$-Tau and αS:Tau441 were kept to 1:1. For binding titration experiments in the absence of crowder, TEMPOL-122-αS was kept at 50 μM and the poly-cation was titrated in increasing concentrations, preparing each condition individually. CW-EPR measurements were performed with a Bruker ELEXSYS E580 X-band spectrometer equipped with a Bruker ER4118 SPT-N1 resonator operating at a microwave (MW) frequency of ~ 9.7 GHz. The temperature was set to 25 °C and controlled by a liquid nitrogen cryostat. Spectra were taken under non-saturating conditions with a MW power of 4 mW, a modulation amplitude of 0.1 mT and a modulation frequency of 100 kHz. Reported g-values were obtained from simulations of EPR spectra performed with the Easyspin software (v. 6.0.0-dev.34) implemented in Matlab® [522]. A two-component isotropic model was used for simulating the data. After normalizing all the signals, residuals were calculated by subtracting each simulation from the corresponding experimental spectrum. For binding titration assays, the relative intensity of the third band to the second band of the normalized EPR spectra (I_{III}/I_{II}) was used to monitor the binding of the poly-cation to αS. For estimating the dissociation constant (K_D), the resulting curves were fitted to an approximated model assuming n-identical and independent binding sites. EPR experiments were performed by Ilenia Serra, Maruan A. Bracci and Dr. Inés García.

Nuclear magnetic resonance (NMR)

NMR spectroscopy experiments were carried out utilizing a Bruker Neo 800 MHz (^{1}H) NMR spectrometer fitted with a cryoprobe and Z-gradients. All experiments used 130-207 uM αS and the corresponding equivalents of αS/ΔN$_t$-Tau and pLK in 10 mM Hepes, 100 mM NaCl, 10 % D$_2$O, pH 7.4, and were ran at 15 °C. To monitor LLPS by NMR, 10% PEG were added to the premixed samples. Chemical shift perturbation plots (**Fig. 2.1B**) show the averaged 1H and 15N chemical shifts. The αS 2D^{1}H-^{15}N HSQC spectrum was assigned based on previous assignments (BMRB entry #25227) and confirmed by recording and analysis of 3D HNCA, HNCO and CBCA(CO)NH spectra. ^{13}Cα and ^{13}Cβ chemical shifts were calculated in presence of αS/ΔN$_t$-Tau and pLK to measure possible changes in secondary structural trends upon comparison to the chemical shifts of αS in a pure statistical coil conformation [523] (**Fig. 2.8C**). $R_{1\rho}$ rates were measured by recording hsqctretf3gpsi experiments (obtained from the Bruker library) with delays of 8, 36, 76, 100, 156, 250, 400 & 800 ms and an exponential function was fit to the intensities of the peaks over the distinct time delays to determine the $R_{1\rho}$ rates and their experimental uncertainties. These experiments were performed by Dr. Javier Oroz and Dr. Douglas V. Laurents.

Phase separation quantification by centrifugation and SDS-PAGE

100 μL samples containing 1 μM AF488-labelled αS were prepared by thorough mixing and subsequently centrifuged for 30 minutes at 9600 x g upon which a pellet was visible in some samples. The upper 50 uL of supernatant were used for protein quantification by SDS-PAGE. The gel was scanned with an AF488 filter using a ChemiDoc Gel Imaging System (Bio-Rad Laboratories, Hercules, CA, USA) or stained with coomasie stain and imaged with the corresponding filter. The resulting bands were analyzed using ImageJ 1.53i version (NIH, USA). Experiments were performed in duplicate in two different experiments with similar results.

FCS, FLIM and FRET microscopy

Dual-color time-resolved fluorescence spectroscopy experiments were performed on a commercial MT200 (PicoQuant, Berlin, Germany) time-resolved fluorescence confocal microscope with a Time-Correlated Single Photon Counting (TCSPC) unit. Laser diode heads were used in Pulsed Interleaved Excitation (PIE) and the beams were coupled through a single-mode waveguide and adjusted to laser powers between 10 and 100 nW for both 481 nm and 637 nm laser lines measured after the dichroic mirror. This ensured optimal photon count rates while avoiding photon pile-up effects, photobleaching and saturation. The coverslip or μ-Slide Angiogenesis plate (Ibidi GmbH, Gräfelfing, Germany) was placed directly on the immersion water on top of a Super Apochromat 60x NA 1.2 objective with a correction collar (Olympus Life Sciences, Waltham, USA). A dichroic mirror of 488/640 nm (Semrock, Lake Forest, IL, USA) was used as the main beam splitter. Out-of-focus emission light was blocked by a 50 μm pinhole and the in-focus emission light was then split by a 50/50 beamsplitter into 2 detection paths. Bandpass emission filters (Semrock, Lake Forest, IL, USA) of 520/35 for the green dye (AF488) and 690/70 for the red dye (Atto647N) were used before the detectors. Single Photon Avalanche Diodes (SPADs) (Micro Photon Devices, Bolzano, Italy) served as

detectors. Both data acquisition and analysis were performed on the commercially available software SymphoTime64 (PicoQuant GmbH, Berlin, Germany).

For FCS and FRET experiments, only the 481 nm laser was used. For FCS, the effective focal volume of the green channel ($V_{eff, g}$) and its structural parameter (κ_g) in our microscope were determined using a 1 nM solution of Atto488 (ATTO-TEC GmbH, Siegen, Germany). For measuring the diffusion coefficient of αS, 50 µL of a freshly filtered (0.22 µm syringe filter) solution containing 5 nM AF488-labeled αS and 100 µM unlabeled αS in LLPS buffer (HEPES 10 mM pH 7.4, 100 mM NaCl, 15% PEG-8) were spotted into a µ-Slide Angiogenesis well plate. Intensity time traces for a triplicate experiment were acquired for 1 minute focusing the laser 20 µm above the well surface for optimal objective lens working distance. Auto-correlation curves ($G(t)$) were fitted with a 1 diffusion-component model with a blinking term accounting for the triplet state of the dye using the following equation:

$$G(t) = \left[1 + T\left[e^{\left(\frac{-t}{\tau_{Trip}}\right)} - 1\right]\right]\frac{1}{\left[1 + \frac{t}{\tau_D}\right]\left[1 + \frac{t}{\tau_D\,\kappa^2}\right]^{\frac{1}{2}}} \qquad \textbf{(Eq. 2.1)}$$

where $G(t)$ is the correlation amplitude, T denotes the amplitude of the triplet state, t is the correlation time, τ_D is the diffusion coefficient and κ is the structure parameter of the focal volume.

For FLIM and FRET microscopy experiments, 50 µL LLPS samples were spotted into a µ-Slide Angiogenesis well plate (Ibidi GmbH, Gräfelfing, Germany). Images were acquired focusing 20 µm above the well bottom for optimal objective lens working distance for suspended droplets and at ~1 µm for rafts and puncta, with an axial resolution of at least 0.25 µm/pixel and a dwell time of 400 µs/pixel. Data were selected by applying an intensity threshold based on the mean intensity of the background signal ($F_{BG,mean}$ + 2σ) to each channel in order to select only liquid protein droplets, rafts or puncta, filtering out any dim signal which could originate from the dispersed phase. For species-specific lifetime (τ) analysis of each channel (green, "g" for AF488 and red, "r" for Atto647N), we selected regions of interest (ROI) that contained either droplets, rafts or puncta (**Fig. 2.15C**), and obtained their mean τ by fitting their lifetime decays (τ_d, τ_r and τ_P for droplets, rafts or puncta, respectively, **Fig. 2.15C**) in each channel using the tail-fitting analysis and a 2-component decay model. ROIs that yielded too low photon counts for multi-exponential fitting (< 10^4 photons for rafts and puncta, and 10^3 for droplets - the threshold for the droplets was reduced since it was very difficult to obtain decay curves with higher intensity values because of the general small size and reduced number of droplets per image field) or too high photon counts above the photon pile-up limit (> 500 counts/pixel) were discarded for the analysis. Tail-fitting was performed on the ROI-derived intensity decay curves starting at a lifetime where intensity is 90 % of the maximum (slightly after the decay's maximum intensity) to ensure minimal IRF interference while maintaining the same relative time window for all intensity decay fittings. Between 25-50 ROIs for rafts and puncta and 15-25 ROIs for droplets, selected

from images obtained from more than 4 replicas recorded in at least 3 independent experiments were analyzed. Two-tailed t-tests were used for assessing statistical differences between the species or between coacervate systems. For pixel-wise lifetime (τ) analysis, the overall lifetime decay of the entire field was calculated for each channel and was tail-fitted to a 2/3-component exponential decay model. Then, the lifetime decay of each individual pixel was fitted using the previously calculated τ values, yielding a FLIM-fitted false color-coded image. The lifetime range for tail-fitting was the same throughout all images of the same channel and enabled a sufficient amount of photons per decay to allow for robust fits. For FRET analysis, pixels were selected by applying a lower intensity threshold of 100 photons, being the mean background signal (F_{BG}) 11 photons. The fluorescence intensity of each channel was corrected by the experimentally determined correction factors [409]: spectral cross-talk α was 0.004, direct excitation δ was 0.0305 and detection efficiency γ was 0.517. Pixel-wise FRET efficiency was then calculated as given by the following equation:

$$E = \frac{F_{DA} - \alpha F_{DD} - \delta F_{AA}}{F_{DA} - \alpha F_{DD} - \delta F_{AA} + \gamma F_{DD}} \qquad \textbf{(Eq. 2.2)},$$

where F_{DD} is the observed fluorescence intensity in the donor (green) channel, F_{DA} is the observed fluorescence intensity in the acceptor (red) channel through indirect excitation and F_{AA} is the observed fluorescence intensity in the acceptor (red) channel through direct excitation (PIE pulse). These experiments were performed in collaboration with David Polanco and Dr. Nunilo Cremades.

Liquid-to-solid phase transition (LSPT) puncta isolation and ThT staining

100 µL of an LLPS reaction containing 25 µM of unlabeled, monomeric Tau441 with or without 25 µM αS in LLPS buffer (supplemented as explained above) were spotted onto non-Binding 96-Well Microplates, covered with an adhesive foil, and droplet formation was verified after 10 min of equilibration by WF microscopy. After 48 h of incubation at room temperature, the presence of protein rafts and puncta was confirmed. Then, the liquid on top of the rafts was carefully removed from the well, and then 50 µL of isolation buffer (10 mM HEPES, pH 7.4, 1 M NaCl, 1 mM DTT) were added and incubated for 10 minutes. The high salt concentration ensured that no LLPS could re-occur due to residual PEG and that possible protein assemblies formed merely by electrostatically-driven interactions would be disassembled. The bottom of the well was then gently scraped using a micropipette tip and the resulting solution was transferred onto an empty well for visualization. The presence of isolated puncta was verified by WF microscopy after incubating the sample for 1 h with 50 µM ThT. Sonicated αS fibrils were prepared by incubating 300 µL of a 70 µM αS solution in PBS pH 7.4, sodium azide 0.01% for 7 days at 37 °C and 200 rpm in an orbital shaker. Then, the solution was centrifuged for 30 min at 9600 x g, the pellet was resuspended in PBS pH 7.4 and sonicated (1 min, 50 % cycles, 80 % amplitude in a Vibra-Cell VC130 Ultrasonic Processor, Sonics, Newton, USA) to generate fibrillar samples with a relatively homogeneous size distribution of small fibrils. These assays were performed by David Polanco.

Statistical analysis

After finding significant differences between variances via Levene's tests, two-sample t-tests assuming unequal variances were performed whenever the significance of differences between values were assessed using Excel (Excel 2000 9.0.3821 SR-1). All data were plotted using OriginPro 9.1. Statistical analyses were performed by David Polanco.

Chapter 3

Development of a Time-Resolved Single-Particle Fluorescence Spectroscopy Approach for Studying Multi Ligand-Multimeric Receptor Interactions: Unravelling the Detailed Molecular Mechanism of a Peptidic Inhibitor of α-Synuclein Amyloid Aggregation

Introduction

Amyloid aggregation of proteins stands at the core of a myriad of diseases in the human being, and is a hallmark of neurodegenerative disorders such as Alzheimer's and Parkinson's disease [11]. Even though there has been progress in developing strategies to tackle the toxicity of these amyloid aggregates *see* general introduction section 3 for more information and relevant bibliography), more specific and efficient tools are required for both therapeutic and diagnostic purposes. Among these, small molecules able to target the specific amyloid species responsible for the neurotoxicity hold the promise to become the drugs and early diagnostic agents of the future [201, 524]. However, the complex aggregation landscape together with the heterogeneity of the amyloid assemblies themselves imply a non-trivial "receptor-ligand" interaction scenario [203]. Here, the binding stoichiometry and affinity, key features defining the complexes, are elusive to most techniques and amyloid systems.

Furthermore, there are caveats regarding the current most typical methods for identifying potential amyloid interactors and assessing their activity. For instance, thioflavin-T (ThT) fluorescence-based studies, such as aggregation kinetic profiles, report on the overall inhibition potency of a molecule but is blind to the specificity, affinity and stoichiometry for each of the different amyloid assemblies that could be potentially involved in the process. Binding parameters can be obtained only assuming theoretical models [192]. Another example of a technique widely used for measuring interactions quantitatively is isothermal titration calorimetry (ITC), where the working concentration range, sample volume and possible artifacts arising from sample inhomogeneities are limiting factors [525]. These techniques, therefore, do not fulfill key requirements for becoming an optimal interaction assay for finding lead molecules: low sample consumption, coverage of a wide concentration range, minimum or absence of false positives and, most critically, offering direct access to both the affinity and the stoichiometry of the interaction. In a nutshell, the precise and comprehensive molecular mechanism of action of the candidate anti-amyloid molecules remains elusive for conventional experimental techniques.

In order to deal with this technical challenges, we hypothesized that single-particle techniques could be just what is needed. More specifically, dual-color time-resolved fluorescence intensity fluctuation methods have proven useful in monitoring molecular interactions in detail, provided that they monitor the diffusion of the involved species individually with high spatial (down to 2-10 nm) and time resolution (as fast as hundreds of picoseconds). Techniques such as dual-color fluorescence cross-correlation spectroscopy (dcFCCS) and dual-color single-particle fluorescence spectroscopy (dcSPFS) have already been used to dissect the binding between fluorescently labeled molecules [355, 401, 526, 527]. However, their potential to investigate the interaction between amyloid aggregates and potential interactors has not been explored.

Within the variety of amyloidogenic proteins involved in neurodegeneration, in our group we have been focusing on α-synuclein (αS) over the past 7 years. When it comes

154

to the species that are ultimately responsible for neural damage, it is increasingly established in the field that intermediate oligomers are the major pathogenic agents [20, 528–530], while these and also fibrils are involved in the cell-to-cell propagation of the disease, as well as through the brain tissue [531, 532]. In previous work from our group, we developed protocols for isolating toxic oligomers (Type B*) that share key features (β-sheet structure, proteinase-K resistance, cell toxicity) to those involved in disease [28], as well as benign, disordered oligomeric species (Type A*), which, together with the typical amyloid fibrils [533], consists on the main structural types of species generated during αS amyloid aggregation [20].

With this in hand, we decided to develop a combined dcFCCS and dcSPFS strategy to study the molecular interaction mechanism of potential inhibitory or diagnostic molecules to these isolated, concrete amyloid assemblies of αS. In order to do this, we collaborated with the laboratory of Prof. Salvador Ventura at the Institut de Biotecnología i Biomedicina (IBB) in the Universitat Autònoma de Barcelona (UAB). They used their expertise in protein and peptide engineering and design to contrive a small peptidic scaffold able to inhibit the amyloid aggregation of αS and to block the toxicity of type B* oligomers in cellular models. We tested the applicability of dcFCCS/dcSPFS to dissecting the details of this inhibition in terms of the stoichiometry, affinity and selectivity of binding of these peptides to the particular types of αS aggregated species. Our study validated the rational peptide design of our collaborators, as well as aided in the identification of a natural human inhibitory peptide, which holds great promise as a possible therapeutic target for PD.

Specific aims

- Implement dual-color fluorescence cross-correlation spectroscopy (dcFCCS) as a technique for the analysis of multi-ligand/multi-receptor interactions in our group.

- Develop a dual-color single-particle fluorescence spectroscopy-based (dcSPFS) experimental strategy for studying multi-ligand/multi-receptor interactions.

- Establish the combination of the former techniques as a combined, self-validating approach for multi-ligand/multi-receptor interactions at the single-particle level: dcFCCS/SPFS.

- Validate dcFCCS/dcSPFS with a peptide inhibitor of α-synuclein amyloid aggregation.

- Assess the specificity, affinity and avidity of the interaction of the inhibitor for distinct isolated α-synuclein aggregates by dcFCCS/SPFS.

- Aid in the validation of the rational design of the inhibitor peptide using dcFCCS/SPFS.

Results & discussion

1. A self-validated combination of dual-color time-resolved fluorescence spectroscopy techniques deciphers the details of multi-ligand/multi-receptor interactions at the single-particle level

Conventional, widely-used technique such as ThT fluorescence and ITC are technically challenged by the complexity of the interactions between small molecules and amyloid aggregates, as it has been explained above. We have published an experimental strategy (579) based on the combination of two time-resolved fluorescence spectroscopy techniques, dcFCCS and dcSPFS (**Fig. 3.1**), to circumvent these challenges. On the one hand, we take advantage of the unpaired ability of auto- and cross-correlation spectroscopy to quantitatively monitor the fraction of non-synchronized (free) and synchronized (bound) diffusion of two fluorescently labelled species and extract thereby the degree of binding [319, 338]. For that, we built on the theoretical framework by Krüger and co-workers [338]. On the other hand, by using dcSPFS we were able to monitor the stoichiometry and approximate proximity of the two labelled molecules in the complexes at the single particle level, thereby gaining access to the molecular mechanism of the interaction and cross-validating the information obtained by dcFCCS. This approach fulfills the aforementioned key requirements to become a remarkably powerful in the field of amyloid drug discovery: it requires no sample immobilization, is remarkably fast (up to a few seconds per sample if needed), virtually lacks false positive results and can be potentially used in any concentration range down to a few picomolar with sample volumes as small as 10 μL. Our experimental approach allows the monitoring of each interacting molecule individually and the two-way analytical approach makes the overall strategy robust and self-validated. Notably, this method enables studying multi-ligand/multi-receptor interactions in any macromolecular system provided the interacting partners are fluorescently labelled.

Figure 1 depicts, using a schematic, the workflow and fundamentals of dcFCCS/SPFS, adapted from our published experimental protocol (579). The species of interest need to be isolated and fluorescently labeled with a probe suitable for single-particle experiments: it should be small, photostable, with a high quantum yield and ready-to-react with a functional group of the protein. In our case, we used a thiol-maleimide chemistry reaction between the probe and an engineered single cysteine in αS as described in any other chapter of this thesis. Additionally, if FRET wants to be used, a sufficient spectral overlap between the donor (green, g) and the acceptor (red, r) probes is required. Basically, two scenarios can be found. One where the species of interest interact and co-diffuse (D_{gr}, where "g" and "r" stand for the two types of fluorophores, typically green and red fluorophores, respectively - *see* methods for more information -) through the dual laser focal volume (**Fig. 3.1A, B**). And another scenario where no interaction occurs and each fluorescent species diffuses independently (D_g and D_r, **Fig. 3.1B**). In the case where there is interaction, when a complex diffuses across the focal volume (generally $V_{eff, i}$, where "i" is a given detection channel, either "g" for green, "r"

for red, or "gr" for both), both fluorophores are excited and their emission is collected simultaneously, giving rise to a cross-correlated signal (**Fig. 3.1A,** top right graph).

On the one hand, analyzing intensity fluctuations of each channel (FCS) and the correlation between them (dcFCCS) enables us to obtain auto- (AC) and cross-correlation (CC) fluorescence curves such as those shown in **Fig. 3.1A,** bottom left graph. While AC curves report directly on the concentration and diffusion (and, thus, the size) of each labeled species, CC curves provide us with direct information on the degree of binding [338, 401, 526]. The amplitude of CC curves (referred to as G_{gr}) increases upon increasing the fraction of bound molecules until a threshold above which more and more ligand remains free in the solution, whereon the amplitude of the CC curve decreases. Applying
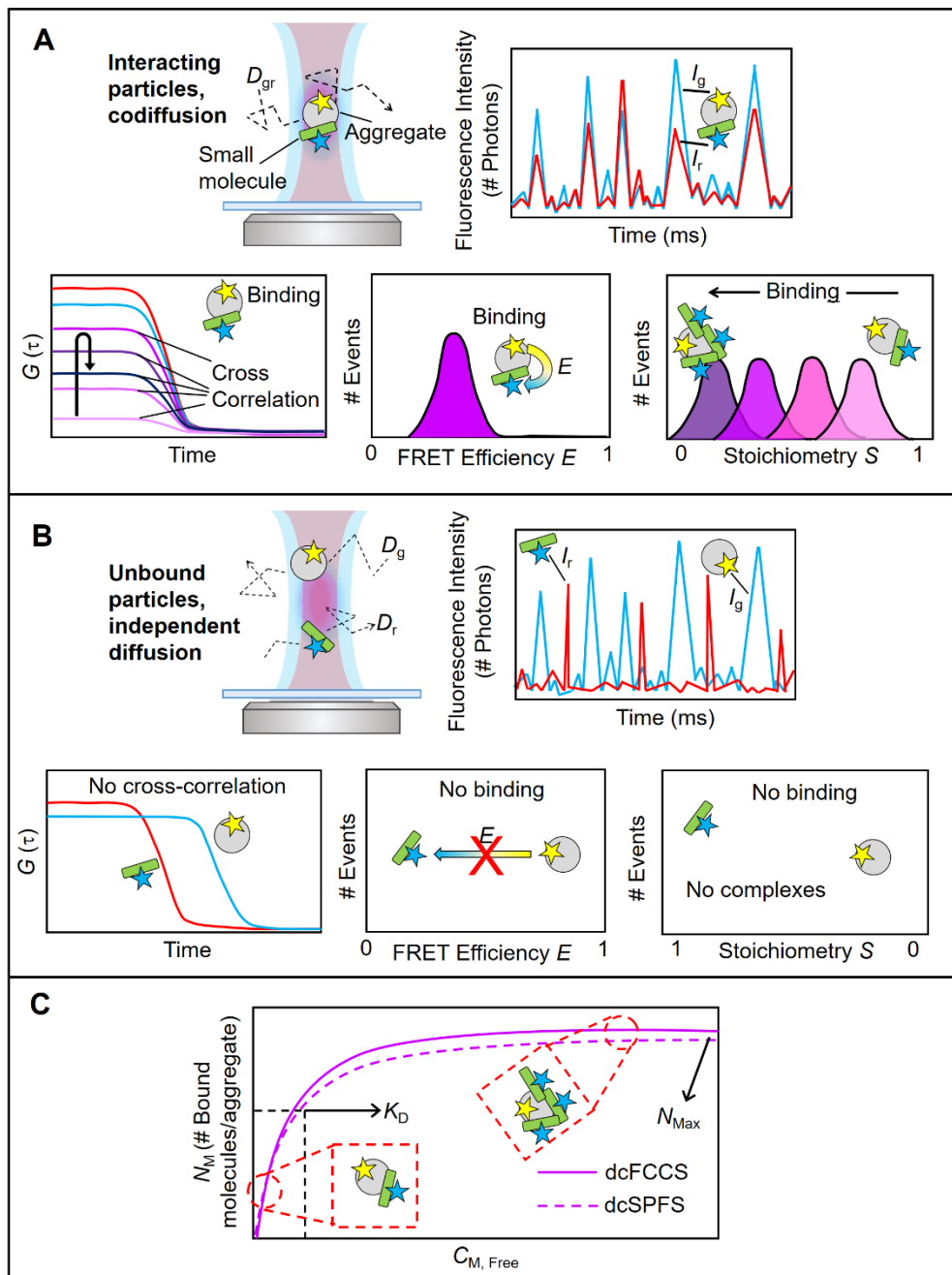
Fig. 3.1. Fundamentals and workflow of dcFCCS/SPFS. (**A**) Schematic of the principle of diffusion-based dual-color time-resolved fluorescence spectroscopy. Top: in the left side, two interacting labeled particles (grey particle with "green" dye as a yellow star and green particle with "red" dye as a blue star) co-diffuse (indicated by the diffusion coefficient D_{gr}) through a dual-laser focal volume ($V_{eff,gr}$) and their fluorescence intensity is detected. This gives rise to fluorescence intensity fluctuations in the form a time-trace (right) where the intensity bursts belong to either independent diffusion of the labeled particles (blue and red lines indicate the fluorescence intensity in the green (I_g) and red (I_r) channel, respectively) or a coincident burst arising from co-diffusing, interacting particles (magenta arrow). Bottom: this time trace is analyzed by an intensity fluctuation correlation (left) and a burst-wise single-particle intensity (center and right) method. Dual-color fluorescence cross-correlation spectroscopy (dcFCCS, left) analysis quantifies the amplitude changes of the cross-correlation curve (G_{gr}) arising from the binding between labeled particles and, through green and red auto-correlation analysis (blue and red curves, respectively), the concentration of particles in the focus (N_{Agg}, C_M). Dual-color single-particle fluorescence spectroscopy (dcSPFS) analysis calculates the ratio between the green and the red dye for each individual interacting event thus giving direct access to the binding stoichiometry (right). **B**) The same principles as in A are depicted for a non-interacting scenario. **C**) Both analytical approaches are used in a combined manner in order to calculate the binding curve of the interacting pair, yielding both the dissociation constant (K_D) and the maximum number of binding sites (N_{max}) per particle. This allows for a robust and detailed study of the interaction.

the theoretical model proposed by Krüger and co-workers to a classical binding titration experiment [338] (see methods for more detailed information), the number of bound ligands to each receptor can be calculated (N_M) as a function of the free ligand at any ligand concentration, which is obtained from the ligand's AC curve amplitude (G_g). From there, the maximum number of bound molecules (N_{max}) and the dissociation constant (K_D) of the complex can be extracted (**Fig. 3.1C**).

On the other hand, by assessing the intensity of each channel separately (the amount of photons detected in each channel, g and r, as a function of time) with a time resolution of a few microseconds, we can split the photon stream into bins small enough to capture the fluorescent bursts from each complex individually (dcSPFS). After that, the FRET efficiency (E) and the fluorescence stoichiometry (S) of the complexes can be directly calculated (see methods for more detailed information). For the former, the intensity ratio between the acceptor and the donor intensities is calculated, yielding a FRET efficiency distribution that will vary (between 0 and 1 or 0 % to 100 %) according to the relative proximity and orientation of donor and acceptor (**Fig. 3.1A** and **B,** bottom center graph). For the latter, the relative amount of green and red photons in the complexes is calculated for each point of the titration. As the number of interacting ligands increases across the titration, and thereby the relative amount of red photons, the complex stoichiometry is shifted to lower values between 1 and 0 (**Fig. 3.1A** and **B,** bottom right graph). From the photon stoichiometry of the complexes, the exact number of molecules in each complex (N_M) can be calculated, provided that we know the mean number of photons that each species contributes in the first place when they are found in the monomeric form. This needs to be calculated prior to the titration experiment using monomeric species with the same fluorescent probes that will be used for the multi-

ligand/multi-receptor assays. Ultimately, extracting N_M for each ligand concentration will yield a binding curve from which N_{max} and K_D can be calculated (**Fig. 3.1C**). Panel **B**) shows exactly the same aspects described in **A**) in a scenario where the species of interest do not interact with one another. No synchronized diffusion is expected and, therefore, there is a lack of dual-color fluorescent bursts, CC curve and no quantifiable single-particle fluorescence events. Thus, neither FRET nor stoichiometry analysis are possible. Comparing the binding parameters obtained by dcFCCS and dcSPFS, we will then determine whether the results are robust and whether, indeed, both analytical techniques can be used as a powerful tool for disentangling complex molecular interactions in multi-ligand/multi-receptor scenarios.
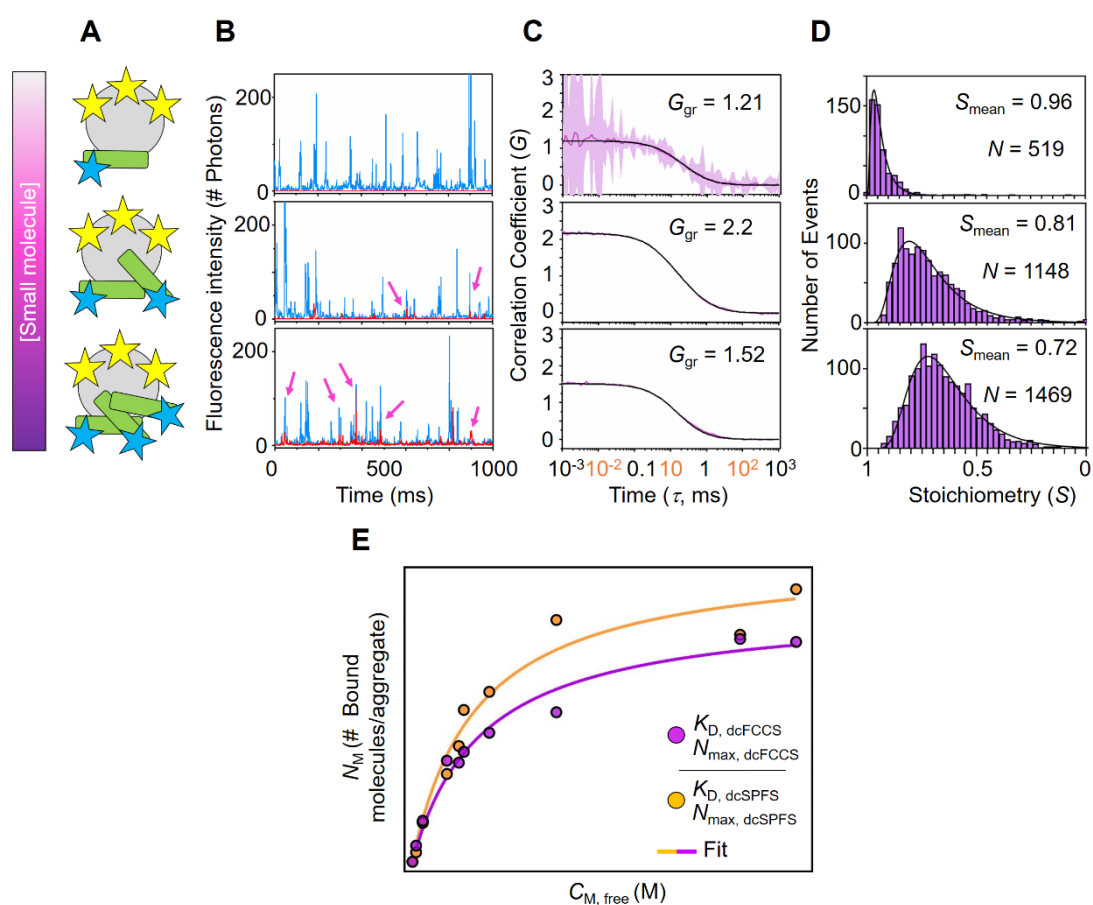
Fig. 3.2. Representative dcFCCS/dcSPFS results for a small molecule binding to αS oligomers. **A**) Schematic representations of the interaction scenarios for illustrative purposes. With increasing concentrations (top to bottom), the amount of small molecules (green, Atto647N dye in blue) bound to toxic αS oligomers (grey, AF488 dye in yellow) increases. **B**) Fluorescence intensity time traces of the binding scenarios depicted in **A**). Toxic αS oligomers and small binding molecule fluorescence traces are shown in blue and red, respectively. Dual-color coincident events are highlighted as magenta arrows. An increase in dual-color coincident events is observed with increasing small binding molecule concentrations. **C**) Cross-correlation analysis of the binding scenarios depicted in **A**). Cross-correlation amplitudes (G_{gr}) are shown as a purple line, their standard deviation is shown as faint colored area and the fitted

curves are shown as black lines. G_{gr} increases and then diminishes as it is expected with increasing free small binding molecule concentrations upon binding saturation. **D**) dcSPFS stoichiometry analysis of the binding scenarios depicted in **A**). Log-normal fits (black lines) to stoichiometry (S) distributions (magenta histograms) are shown. The stoichiometry (S) decreases with increasing small binding molecule concentrations, indicating binding. These results illustrate how to apply two fundamentally different analytical methods to the same data in a complex binding scenario in order to produce comparable and reliable results. **E**) By plotting the number of bound small molecules per oligomer (N_M) as a function of the free small molecule ($C_{M, free}$), the binding curves derived by either dcFCCS (purple circles) or dcSPFS spectroscopy (orange circles) are obtained. By fitting these curves to a specific binding model, in this particular case a model with n identical and independent binding sites (purple or orange line, respectively), the dissociation constant K_D and the maximum binding sites N_{max} is obtained for each analytical method. The results shown in the figure illustrate the good match between both methods, indicating their suitability as complementary approaches for studying binding of small molecules to protein aggregates in great detail.

In order to test our method, we studied the interaction of αS type B* oligomers (OB) with one small ligand molecule. OB and the ligand were 100 % labelled with AF488 and Atto647N, respectively, as explained in the Materials and Methods section and in our published protocol in Methods in Molecular Biology (579). In particular, we performed a binding titration experiment and analyzed it by dcFCCS/dcSPFS (**Fig. 3.2**, adapted from (579)) as it has been outlined above. We observed that, at low concentrations of the ligand (**Fig. 3.2A**), almost no intensity is observed for the red channel (**Fig. 3.2B**) and, as a consequence, a noisy CC amplitude (G_{gr}) and a stoichiometry (S) value near to 1 are observed (**Fig. 3.2C, D**), reflecting the absence of low fraction of ligands bound to OB. CC might lead to confusion if it is taken as a measure of binding alone, since the concentration of free ligand ($C_{M, free}$) also needs to be obtained and considered for calculating the number of bound particles N_P (see methods for more details and equations). On the one hand, the cross- correlation amplitude is relative to the proportion between complexed and free ligand.

Therefore, the increment of $C_{M, free}$ as we approach the binding saturation regime will dramatically reduce G_{gr} in this part of the titration. However, since N_P is directly related to $C_{M, free}$ (see methods for more detailed information and equations), the reduced G_{gr} is balanced by the free ligand. In other words, G_{gr} and $C_{M, free}$ usually dominate the exponential part and the saturation plateau of the binding curve, respectively.

As the ligand concentration increases, more coincident bursts are detected, concomitantly with an increase in the CC amplitude and a lowering of the fluorescent stoichiometry S, indicating a higher fraction of bound small molecules to the type B* oligomers. Notably, this is accompanied by an increase in the total number of coincident events (N) as observed in dcSPFS analysis, further confirming the trend of the titration. Finally, when the ligand concentration is even higher, more coincident events are seen,

as expected, and the stoichiometry drops to lower values. However, as explained before, G_{gr} decreases again as a consequence of having reached binding saturation whereon the free ligand dominates the signal over the CC amplitude. As it is expected, N was also incremented. When we plotted the binding curves obtained by both techniques (**Fig. 3.2D**), we observe that, indeed, both were able to monitor the increment of the interaction of the small molecule to OB across the titration. Remarkably, both dcFCCS and dcSPFS yield very similar binding curves and validate each other. More details on these and related experiments are found in the Materials and Methods section and below in the following sections of this chapter.

Based on our results, we believe the combination of these techniques is a promising tool for more extensive studies of amyloid-small molecule interactions. Regarding selectivity, it is noteworthy that dcFCCS can resolve specific interactions of one molecule of interest to different aggregates based on their diffusion coefficient [534], so our strategy could be used in heterogeneous mixtures of different amyloid species with distinct properties and toxicities, something that cannot be achieved, to the best of our knowledge, with any other experimental approach. Overall, our methodology paves the way for finding new drugs and early diagnostic molecules to a variety of amyloidogenic proteins and, in turn, help fight a number of amyloid disorders. Recently, Dr. Cremades and pre-doc student David Polanco have successfully employed dcFCCS/SPFS for demonstrating the LLPS and LSPT-mediante amyloid heteroaggregation, further reinforcing the applicability of this experimental approach.

2. An α-helical peptidic scaffold inhibits the aggregation and cytotoxicity of toxic species of αS

All the results in the following sections of this chapter were published in Nature Communications [174] as a result of a collaboration between our group and Prof. Ventura's lab at the UAB as previously mentioned. In order to design the inhibitor peptide and test its interaction with different species (monomeric of aggregated) of αS, they took into consideration a number of critical features of the latter. In particular, the size in number of monomers (aggregation number), the charge at neutral pH, hydrophobicity and secondary structure were considered (**Fig. 3.3**).

	Monomer	Oligomer type A*	Oligomer type B*	Fibrils
Number of monomers	1	~19[†]	~33[†]	>100[†]
Anionic character	-9	~ -271[†]	~ -297[†]	>-900
Relative hydrophobicity	Low	Low	High	Medium
Secondary structure	Disordered	Disordered	β-sheet	β-sheet

Fig. 3.3. Rational identification of a peptide ligand for αS toxic species. Main molecular features of the four isolated αS species. Values with a dagger (†) represent extrapolations based on the average number of monomers in each species. In the upper schemes of αS oligomeric and fibrillar species, the acidic C-terminal region is not depicted since it has been described to be in a disordered and conformationally flexible state [528, 535]. Figure adapted with permission from Jaime Santos.

Since all species, especially those which are cytotoxic (OB and fibrils), are highly anionic at neutral pH (the negatively charge C-terminal regions of the protein molecules decorate the core of the aggregates), a cationic nature of the peptide was envisioned. Next, attending to the relative hydrophobicity (the density of hydrophobic patches within the total particle surface), it seemed well-suited that the peptide should be able to target those and, therefore, it should feature a hydrophobic region. To unite these two characteristics, an amphipathic molecule was desirable and, therefore, a short α-helical peptide with a cationic and a hydrophobic face seemed to offer sufficient structural stability to hold both virtues together and bind to the toxic species of αS efficiently. A computational search identified one promising candidate: the bacterial peptide PSMα3 (**Fig. 3.4**), which became the proof of principle of the inhibition mechanism study. Indeed, circular dichroism (CD) confirmed its α-helical structure in solution (**Fig. 3.4A**) and its ability to inhibit, even sub-stoichiometrically, the *in vitro* aggregation of αS was verified by ThT kinetics (**Fig. 3.4B**). It does so, as a matter of fact, with even higher efficacy than a recent drug candidate developed previously by Prof. Ventura and Prof. Sancho from the University of Zaragoza [183]. Furthermore, treating SH-SY5Y neuroblastoma cells with a stoichiometric amount of the peptide PMS3α with respect to OB totally reverted the dramatic increase of radical oxygen species induced by OB (**Fig. 3.4C and D**), indicating the cell-protective role of the peptide towards the toxic amyloid assemblies of αS. Overall, this confirmed the therapeutic potential of PSM3α and validated the design of the physico-chemical features of the peptide.
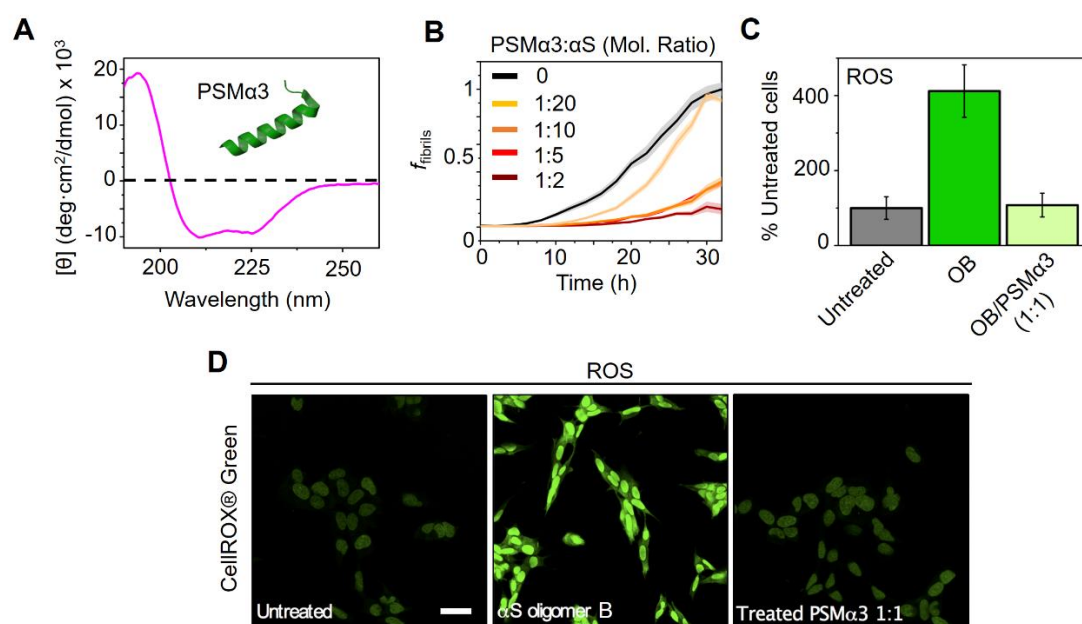
Fig. 3.4. Biochemical and cellular characterization of the inhibitory activity of PSMα3. A) Far-UV circular dichroism spectra of PSMα3. **B**) Aggregation kinetics of 70 μM αS and titration of the inhibitory activity of PSMα3 at different concentrations: 35 μM (green), 14 μM (orange), 7 μM (blue), 3.5 μM (gray) and in the absence of PSMα3 (black). Mean values are shown as solid lines and faint bands represent the standard deviation (n = 9 independent experiments). **C**) Quantification of the levels of intracellular ROS shown in **D**) SH-SY5Y cells were incubated with 10 μM of type B* oligomers preincubated with different concentrations of PSMα3. 233, 230 and 240 cells, (respectively, for untreated, αS oligomers and PSMα3) were analyzed from two independent experiments **D**) Representative confocal images of the analysis of panel **C**). Scale bar represents 30 μM. Data adapted with permission from Jaime Santos.

3. The dcFCCS/dcSPFS approach gives direct access to the molecular binding mechanism of a peptidic inhibitor of αS amyloid aggregation

In order to characterize the binding mechanism of PSMα3 by dcFCCS/dcSPFS, we first produced and isolated four different species of αS using protocols published by our group [528, 533]), *see* methods for more detailed information). Specifically, we were able to obtain pure samples of type A* (OA) and type B* (OB) oligomers, sonicated fibrils (SF) and monomeric (M) αS. We characterized the different protein samples we produced to prove their homogeneity and the key structural properties of each type of aggregate in order to better rationalize the following binding results (**Fig. 3.5**). Atomic fore microscopy (AFM) experiments performed by Dr. José Camino, from our lab, confirmed the globular morphology and small size (~ 20 nm) of the oligomeric assemblies, while sonicated fibrils showed an elongated shape and monomeric αS was hardly visible by this technique (**Fig. 3.5A**). In all cases, sample homogeneity was remarkable. The size of the different protein preparations was confirmed by either SDS-PAGE (M and SF) or SDS-less native PAGE (OA and OB) as shown in **Fig. 3.5B**, where aggregated species did not enter the separating gel as expected. Dynamic light scattering (DLS) further reinforced these results (**Fig. 3.5C**) even though the data for SF are not shown since the rod-like shape of this species did not allow for a reliable estimation of their size. **Fig. 3.5D** and **E** show the infrared (IR) and 8-anilino-1-naphthalenesulfonic acid (ANS) fluorescence spectra of all four species, respectively. The β-sheet content is clearly visible in OB and SF by IR, while a full random-coil conformation is seen for the other species. ANS binding and a blue-shifted ANS emission spectrum shows that the β-sheet structure of these amyloid species is concomitant with an exposure of hydrophobic patches to the solvent, as reported elsewhere [533, 536, 537] and depicted in **Fig. 3.3**, while OA and M give rise to a much lower signal, indicating the absence of exposed hydrophobic regions. All our results were in agreement with what was previously published by our group and others [528, 533, 536].
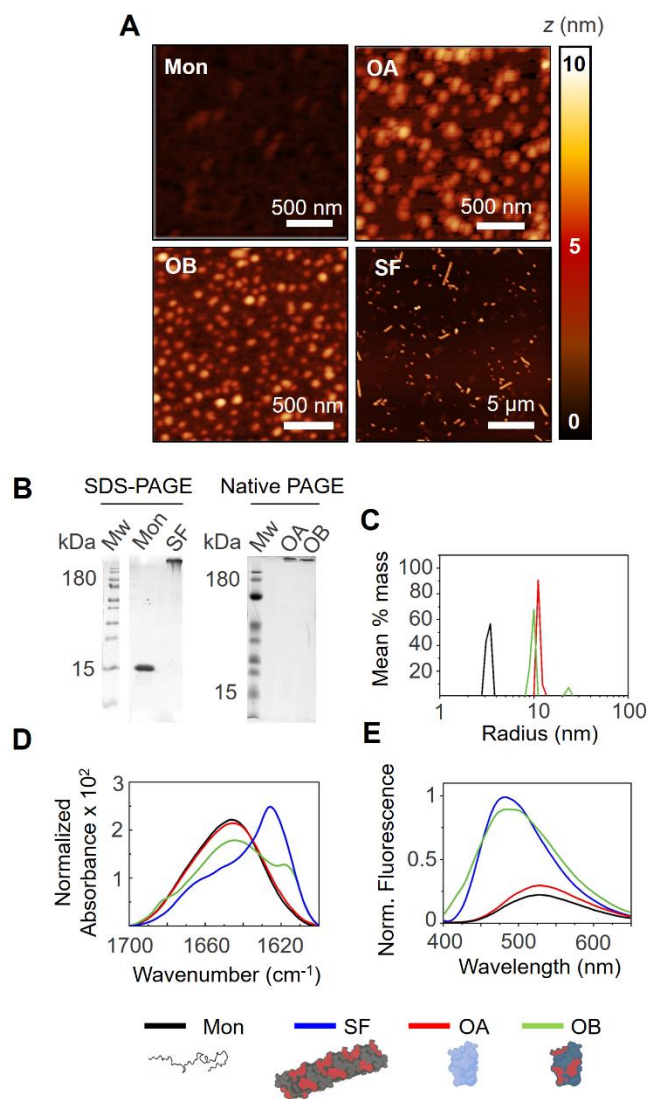
Fig. 3.5. Characterization of αS species. The size, morphology, purity, structure and hydrophobicity of the αS species used in this study (bottom figure legend) were analyzed in order to provide a molecular basis for further result interpretation. **A**) AFM analysis of monomeric αS (top left), type A* (top right) and type B* (bottom left) oligomers and sonicated fibrils (bottom right) are shown. Statistical size distribution analysis yielded a 5.1 ± 0.4 nm height and 28 ± 6 nm diameter for type A* oligomers, 4.4 ± 0.9 nm height and 32 ± 5 nm diameter for type B* oligomers, and a 6.3 ± 0.3 nm height, 95 ± 14 nm width and 300 ± 140 nm length for sonicated fibrils. Scale bar and height color code are shown for every image. These data are in good agreement with the diffusive behavior of the αS species as mentioned in the article and also in agreement with previously published data [538]. **B**) Electrophoretic behavior and purity of the αS species in denaturing (left) or native PAGE (right). No fragments or other contamination are visible in the sample. Importantly, no monomeric αS (referred to as "Mon" in the figure) is visible in the oligomeric (in both type A* and type B* oligomers, referred to as "OA" and "OB", respectively, in the figure) or fibrillar protein preparations (referred to as "SF" in the figure). Aggregated species are larger than 180 kDa and thus do not enter the wells, in agreement with previously published data [538]. **C**) DLS analysis of αS species. A fairly homogeneous size distribution is visible for monomeric αS (black) as well as type A* (red) and type B* (green) oligomers. The fibrillar αS samples showed a very large polydispersity index preventing their analysis by this technique. Size distributions are given in % mass. **D**)

Normalized infrared (IR) spectra of monomeric αS (black), type A* oligomers (red), type B* oligomers (green) and fibrils (blue). A clearly disordered conformation can be seen for the monomer and type A* oligomers while substantial β-sheet structure is observed in the type B* oligomers, if less than in the fibrils, as expected and reported previously [528, 538]. In particular, deconvolution analysis yielded a β-sheet content of 0 % for monomer and type A* oligomers, 35 % for type B* and 56.4 % for fibrils, also in good agreement with previously published data [528, 538]. **E)** ANS binding analysis of αS species. The normalized fluorescent spectra of the different samples show a higher hydrophobicity, seen as an enhanced fluorescence emission and a spectral blue-shift of type B* oligomers (green) and fibrils (blue) compared with monomeric (black) αS and type A* oligomers (red), which show a similarly low intensity and are not blue-shifted. This is in good agreement with previously published data [528, 538].

Next, we wanted to verify the ability of our concrete microscope configuration, especially the dual-laser alignment and its resulting dual-color focal volume ($V_{eff, gr}$), for detecting co-diffusing molecules in the time-resolved fluorescence spectroscopy experiments. For that, we designed a dsDNA molecule that we termed a DNA ruler which has one AF488 and one Atto647N dye on each strand (as described in our publication in MiMB (579)), the same dyes that would be used for labelling αS and PSMα3, respectively. More details on this can be found in the Materials and Methods section. We measured the auto- and cross-correlation of freely-diffusing rulers in PBS buffer (**Fig. 3.6A**) and confirmed that, indeed, a significant CC amplitude was obtained, thus validating our setup for subsequent experiments. A dsDNA concentration of ~ 10 nM solution was used owing to the fact that, due to product flaws, there was an excess of Atto647N-DNA strand so more molecules than usual (~ 1 nM) were needed to obtain a good CC curve. To further ensure there would be no false positives in CC due to chance coincidence of AF488- and Atto647N-labelled molecules in the focal volume, we performed additional control experiments. We measured the CC curve of a sample containing αS monomers labelled with either dye at a total fluorescent dye concentration of 30 nM (15 nM each dye), which was envisioned as the higher range of concentrations to be used in the PSMα3/αS titrations. As is shown in **Fig. 3.6A**, no CC amplitude was apparent, indicating that, with our experimental setup, no false negatives were expected at concentrations as high as 30 nM. Remarkably, this implies that the working concentration range for the dcFCCS/dcSPFS binding assays can range from ~ 100 pM to a few tens of nM.
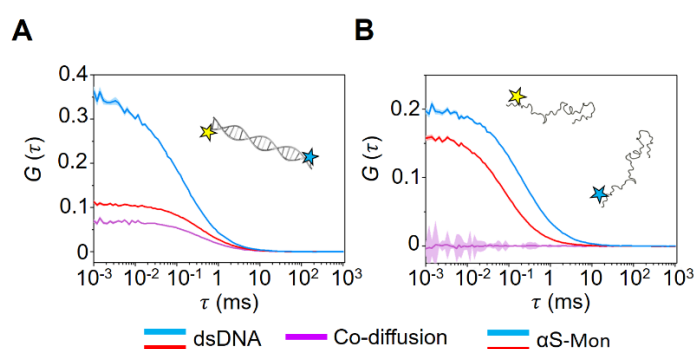
Fig. 3.6. Fluorescence cross-correlation spectroscopy positive and negative control. Auto-correlation curves of AF488 (blue) and Atto647N (red) and cross-correlation curves (purple) of samples containing (A) 10 nM of doubly-labelled dsDNA molecule or (B) 15 nM of non-interacting AF488-αS and Atto647N-αS (15 nM each). The amplitude (G) error is shown as faint colored area for the corresponding correlation curves.

With this in hand, we proceeded to setup the binding titration assays. For that, we used 100 % fluorescently-labelled molecules; in particular, AF488 and Atto647N were used for labelling αS and PSMα3, respectively, via maleimide chemistry on single engineered cysteins as described elsewhere in this thesis and in our publications. By doing this, we were able to produce 100 % labelled αS species. As a first proof of principle test, we mixed OB and PSMα3 at 1 nM each and recorded the intensity fluctuations in the green and red channel over several minutes. All dcFCCS/dcSPFS experiments were performed in phosphate buffered saline (PBS, phosphate 10 mM, NaCl 150 mM) pH 7.4 at room temperature (RT). We observed coincident events (**Fig. 3.7**) in the form of two-color intensity bursts ($I_g + I_r$), already indicating the interaction between the toxic oligomers and the inhibitory peptide.

We did the same for OA, SF and monomeric αS (M) with the exception that, for the latter, 15 nM αS and 15 nM PSMα3 were used. As it can be seen in **Fig. 3.8**, dcFCCS shows no cross-correlation and, thus, no interaction between M and PSMα3 even at total mass concentrations as high as 30 nM (**Fig. 3.8A**). Interestingly, OA seems to interact only slightly with the peptide telling from a very weak CC signal (**Fig. 3.8B**) while OB (**Fig. 3.8C**) and SF (**Fig. 3.8D**) exhibit very significant co-diffusion. This is a strong indicator of the specific interaction between the toxic αS aggregated amyloid species and the inhibitory α-helical peptide PSMα3, already pointing towards an explanation for the potent anti-amyloid activity described before. Another feature of the dcFCCS data worth considering are the auto-correlation curves which, as explained at the beginning of this chapter, report on the diffusive behavior of each species separately. In this case, the signal of PSMα3 (G_r) decays in a synchronized manner to the signal of OB (G_r) and the two-color signal (G_{gr}) following the same behavior over time. This is a hallmark of co-

diffusing species, where the correlation functions of the individual species and the cross-correlated signal arising from the complexed particles show the same behavior, *i. e.*, they diffuse together. The same is true for SF but not for OA and monomeric αS, further confirming the poor or null binding of PSMα3 to these species. Remarkably, when the same experiment of OB/PSMα3 was repeated in the presence of monomeric αS up to a 500x molar excess (500 monomer:OB 1), neither the AC nor the CC amplitudes were modified (**Fig. 3.8E**). This suggests a very strong binding of the peptide to the toxic oligomers and, again, confirms that the physiologically functional monomer remains free in solution and unaffected by the presence of PSMα3, which is critical in order to ensure a proper functioning of the soluble, monomeric αS in potential therapeutic applications with this small molecule.
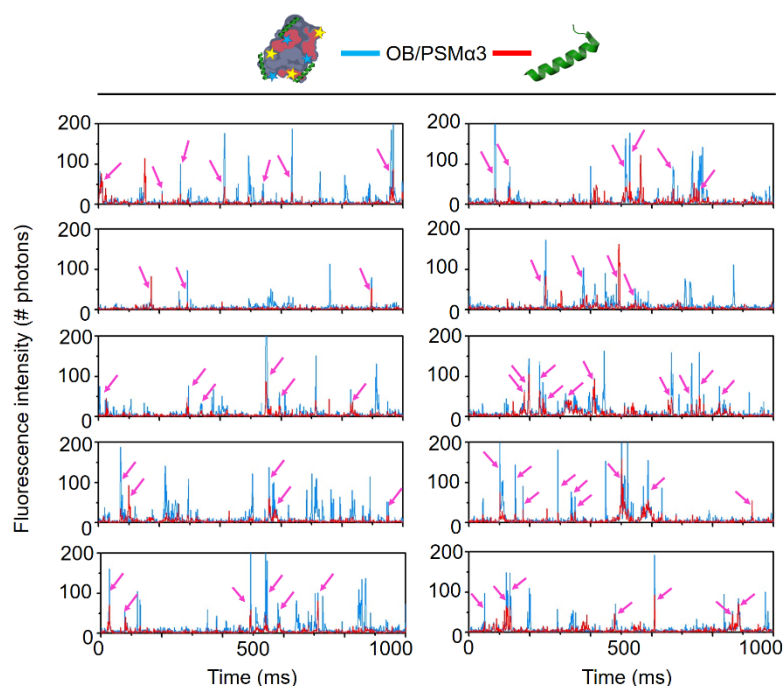
Fig. 3.7. Single-particle conditions in time-resolved fluorescence spectroscopy experiments. 10 representative 1-second intensity time traces (raw data) from a binding experiment with ~1 nM type B* oligomers (blue) and ~10 nM PSMα3 (red) are shown (note that concentrations are given as protein/peptide mass concentrations and that particle concentrations are significantly lower). Two-color coincident events that were intensity threshold-selected for fluorescence stoichiometry analysis are shown with pink arrows. The aggregate/complex-event frequency allows for optimal single-event selection and further burst-wise FRET and stoichiometry analysis, in full agreement with the aggregate mean volume occupancy <*N*> far below 1.

In order to gain further insights into the molecular mechanism of action of PSMα3, in particular the binding affinity and avidity to the αS species of interest, we performed analogous experiments with increasing concentrations of PSMα3 at a fixed αS concentration range of 1 – 5 nM, where the latter is expressed in mass. This implies that, considering that αS aggregates are formed by several tens of monomers, the species concentration for these species were in the range of pM, therefore ensuring single-

particle conditions throughout the titration series. The concentrations of each species were not assumed by serially-diluting the stock solutions but actually calculated experimentally from each measurement by FCS auto-correlation, providing an *in situ* adjustment and precise measurement of the sample concentration at each titration point.
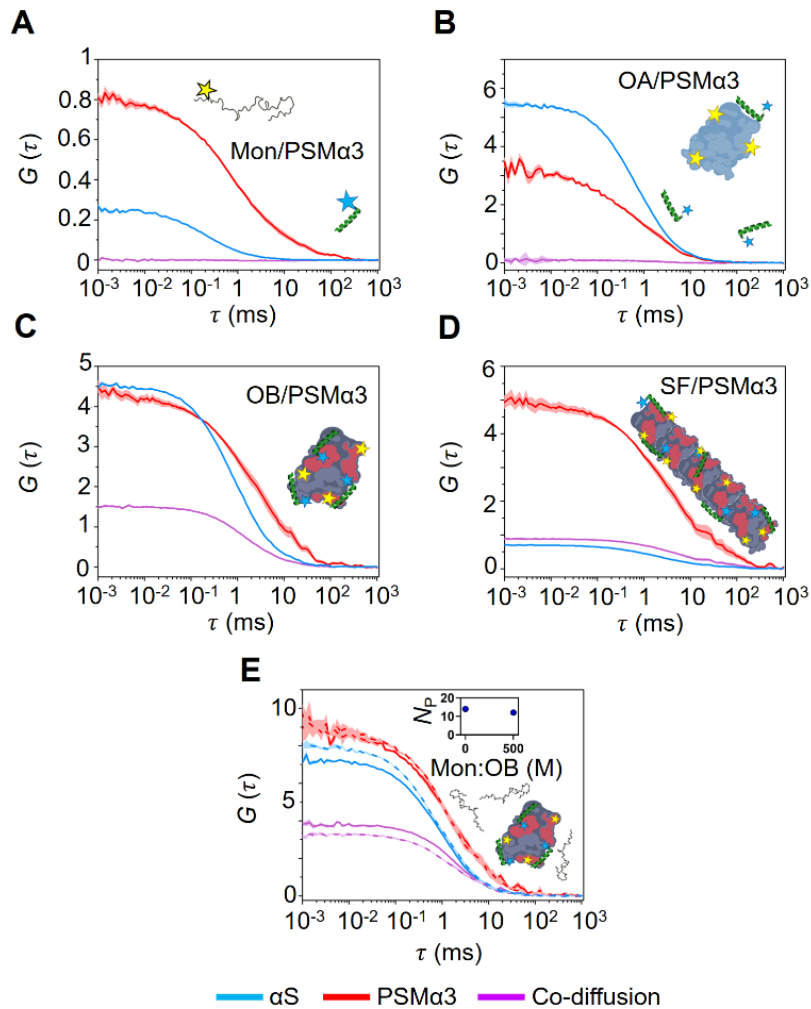
Fig. 3.8. Interaction of PSMα3 with different αS species by dcFCCS. A-E) Representative auto-correlation curves for α-synuclein (αS) (blue line) and PSMα3 (red line) and cross-correlation curves for interacting molecules (purple line). The amplitude (*G*) error is shown as faint colored area for the corresponding correlation curves. Samples contained ~15 nM αS monomer and ~15 nM PSMα3 (**A**), 1 nM type A* and ~5 nM PSMα3 (**B**), 1 nM type B* oligomers and ~5 nM PSMα3 (**C**) or ~5 nM sonicated fibrils and ~5 nM PSMα3 (**D**). E) Auto-correlation curves (αS in blue, PSMα3 peptide in red) and cross-correlation curve for the interacting molecules (in purple) obtained in samples containing ~1 nM αS type B* oligomers and ~2 nM PSMα3 in the absence (solid lines) or presence (dashed lines) of a 500 molar excess of unlabeled monomer with respect to the particle concentration of oligomers. The inset shows the number of bound peptides (N_P) per aggregate in both conditions. For αS aggregated species, each consisting of several tens of monomers, the species concentrations are in the picomolar range and, as further explained before, single-particle conditions are ensured throughout the experiments.

We first performed a dcFCCS analysis. For obtaining either the initial amplitude of the correlation curves (G_0) or the diffusion coefficient of each species (τ_D), the G_g and G_r were fit to a two-component three-dimensional diffusion model, where the second component (τ_{D_2}) accounted for the remaining monomeric αS and unbound PSMα3 (Fig. XY). G_{gr} was

fit with a one-component model owing to the fact that only one species is expected for αS/PSMα3 complexes.
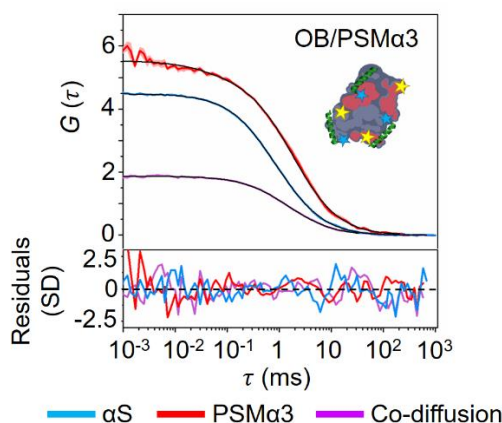
Fig. 3.9. Fitting of fluorescence correlation and cross-correlation data. Representative auto-correlation and cross-correlation curves of a sample of 1 nM type B* oligomers and 5 nM LL-37 peptide are shown in blue, red and purple lines, respectively. The amplitude (G) error is shown as faint colored area for the corresponding correlation curves. Best fits to 1-diffusion component (cross-correlation) or 2-diffusion component (auto-correlations) simple diffusion models are shown as black lines. The residual analysis of the best fits is also shown as standard deviation in colored lines for each correlation curve fit.

This allowed us to calculate the number of bound peptides per aggregate (N_P) from the cross-correlation amplitude ($G_{gr,0}$) and the concentration of free PSMα3 ($C_{P,free}$) from $G_{r,0}$. By doing this for each point of the titration we obtained binding curves for OA, OB and SF (**Fig. 3.10**). Using a simplistic Langmuir isotherm model, we estimated the single-state dissociation constant (K_D) of the interactions and the average maximum number of peptide binding sites (N_{max}) in each type of αS species. This revealed a dramatically higher degree of binding for OB and SF compared to OA ($N_{max} = 3$), as expected from the preliminary dcFCCS measurement where no cross-correlation was found for this pair at 1 nM concentration each. Interestingly, both OB and SF show N_{max} values (31 and 120, respectively) very similar to the average number of monomers per aggregate (33 and 107) which was calculated from the same experiments by comparing the molecular brightness of the aggregates to that of the monomeric protein (see methods for more information). In terms of binding affinity, we found that all αS aggregated species had a similar K_D, namely 3.07 nM, 6.67 nM, and 7.8 nM for OA, OB and SF, respectively.

It should be emphasized that this affinity is comparable to what can be found for most anti-amiloyd antibodies [539–541] endorsing PSMα3 as a promising candidate for targeting very low-populated species in aggregation reactions just like the toxic type B* oligomers of αS. Together, our results suggest that the binding avidity in terms of N_{max}, rather than the individual affinity for the interaction, is the key feature governing the amyloid-inhibitory effect exerted by the peptide. Moreover, the binding of PSMα3 to the toxic species follows a nearly-perfect 1:1 stoichiometric behavior, which could aid in the design of new molecules. Overall, to the best of our knowledge this was the first time

that the molecular mechanism of an anti-amyloid molecule was described in this level of detail and at the single-particle resolution.
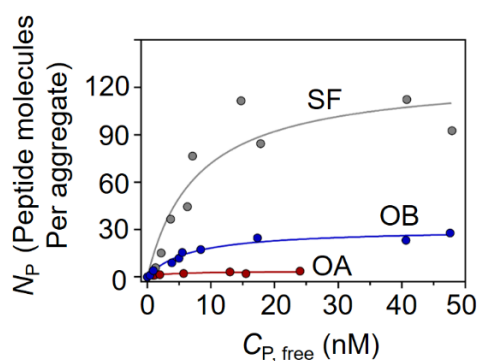
Fig. 3.10. Quantification of the Interaction of PSMα3 with different αS species by dcFCCS. Titration binding curves for the interaction of PSMα3 with type A* oligomers (red circles), type B* oligomers (blue circles) or sonicated fibrils (gray circles) obtained by dcFCCS (data from **Fig. 3.8B-D**), showing their corresponding analysis assuming a model of n identical and independent binding sites (referred to in **Eq. 3.7** as N_{max}) per αS aggregated species (solid lines). N_P represents the number of bound peptides per aggregate.

In order to put the suitability of our combined strategy to the test on this system, we next analyzed the same data for the OB/PSMα3 binding titration at single-particle resolution by dcSPFS. Here, a burst-wise ratiometric intensity analysis was performed (see methods for more information), instead of a correlation analysis, so that both the FRET efficiency (E) and the fluorescence stoichiometry (S) were obtained. The data shown in **Fig. 3.11.** is the same as in **Fig. 3.2** since these data were used to illustrate the method and its wider applicability in our experimental protocol. As it can be seen, the number of two-color coincident bursts (**Fig. 3.11B** and N in **Fig. 3.12C**) increase upon increasing the concentration of PSMα3 at a fixed OB concentration. This is accompanied by a step-wise decrease in S, arising from the fact that the fluorescent intensity from OB (I_g) becomes less and less dominant as the relative contribution of the bound PSMα3 (I_r) grows.

When we looked at the binding specificity of the peptide to the different aggregated species of αS through the lens of dcSPFS, we again were able to confirm what was observed by dcFCCS (**Fig. 3.12**). While a great number of two-color coincident events were found for OB and SF (**Fig. 3.12B** and N in **Fig. 3.12C**), almost none were detected for OA, pinpointing the very low avidity of the peptide for the disordered, benign oligomers. The FRET analysis revealed a different transfer efficiency for OB and SF. However, the complexity of the interactions and the multiple combinations and orientations of FRET pairs including possible antenna effects [542, 543] made it impossible to extract structural information from the data. Nevertheless, considering the high spatial resolution of FRET in terms of molecular binding (see general introduction section 6 for more details and relevant bibliography) and the extremely low probability of false positives when studying interaction by this technique, we can say that it can be

used as a complementary analysis to verify the interactions between the inhibitor and the aggregates.
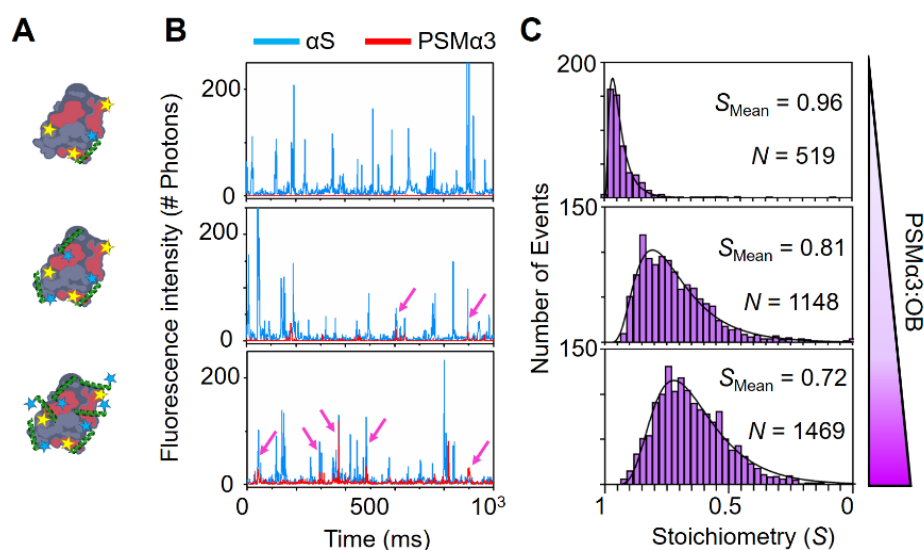
Fig. 3.11. Quantification of the Interaction of PSMα3 with different αS species by dcSPFS. Data is provided to illustrate the experimental approach leading to a burst-wise fluorescence stoichiometry analysis which complements the dcFCCS analysis to obtain the binding curves shown in this work. **A)** Schematic representations of type B* oligomers bound to increasing (top to bottom) concentrations of PSMα3. **B)** Intensity-based raw data corresponding to 1-second time frames (intensity time traces) of binding experiments with ~1 nM type B* oligomers (blue) and ~0.1 nM (top), ~2 nM (middle) and ~10 nM (bottom) PSMα3 (red). Note that the concentrations are given as protein/peptide mass concentrations and that particle concentrations are significantly lower, always under single-particle regime (for example in the case of type B* oligomers, 1 nM of mass concentration corresponds to ~30 pM oligomer particle concentration). Two-color coincident events that were intensity threshold-selected for stoichiometry analysis are shown with pink arrows in the figure panels. **C)** Fluorescence stoichiometry distributions from the experiments shown in **B)**. Increasing PSMα3 concentrations yield lower stoichiometry values as more peptide molecules can be bound to one oligomer. The log normal-fitted mean stoichiometry value (S_{Mean}) is shown. The total number of events (N), which increases with increasing PSMα3 concentrations, is also shown. Acquisition times were the same for all data shown.
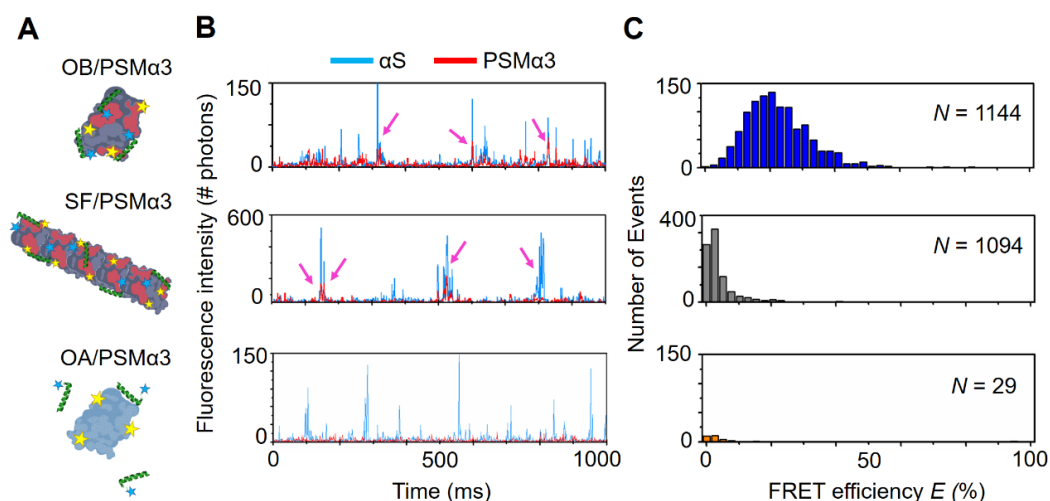
Fig. 3.12. αS/PSMα3 binding analyzed by Fluorescent single-particle spectroscopy. The binding scenarios are shown as schematics in **A**). Representative intensity time traces (**B**) and intensity-calculated FRET efficiency histograms (**C**) for samples containing ~1 nM αS type B* oligomers and ~5 nM PSMα3 (top), ~5 nM αS fibrils and ~5 nM PSMα3 (center) and 1 nM αS type A* oligomers and ~5 nM PSMα3 (bottom). The concentrations expressed as protein/peptide mass concentrations; particle concentrations in the range of pM. In the intensity traces, events displaying both donor and acceptor intensities above αS monomer threshold (see materials and methods) are shown in purple dashed boxes. These events were then used to calculate the intensity-based FRET efficiency E histograms. The total number of FRET events, N, used to calculate each histogram is shown in each panel. These results show, directly from the intensity raw data, the high avidity of both PSMα3 for either type B* oligomers or fibrils and the low ability to bind non-toxic aggregated species like the type A* oligomers. Acquisition times were the same for all data shown.
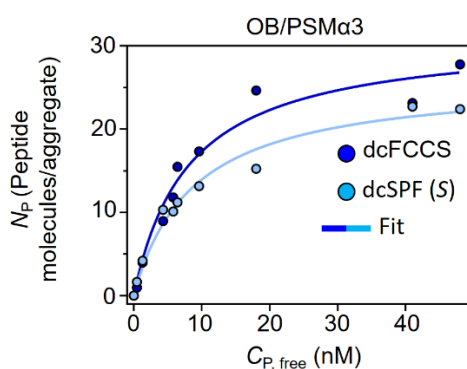
Fig. 3.13. Comparison of the titration binding curves of αS type B* oligomers with PSMα3 obtained by dcFCCS and dcSPFS analysis. The number of peptide molecules bound to one oligomer (N_P) at increasing peptide concentrations was calculated independently by dcFCCS (dark blue circles) or fluorescence stoichiometry analysis in dcSPFS (light blue circles), yielding very similar binding curves that resulted in very similar binding parameters (see **Table 3.1** below) when analyzed using a model of n identical and independent binding sites per αS aggregated species (solid lines). The fitted parameters K_D and N_{max} are also shown for each analytical approach. These results show how two different analytical methods, one which correlates fluorescence fluctuations over whole time traces and another one which analyzes

single fluorescent bursts, can be applied to obtain very similar binding parameters, thus validating our strategy.

Lastly, we calculated N_P from S as described above (**see** methods for more information) and compared the binding curves for OB/PSMα3 obtained by either dcFCCS or dcSPFS (**Fig. 3.13**). As described in the first section of this chapter, both independent methods yielded remarkably similar results. Both K_D as well as N_{max} were almost identical as it is shown in **Table 3.1**.

	K_D **(M)**	N_{max} **(peptides/aggregate)**
dcFCCS	8.11 x 10-9	31.34
dcSPFS	8.73 x 10-9	26.11

Table 3.1. Comparison of the binding parameters of αS type B* oligomers with PSMα3 obtained by dcFCCS and dcSPFS analysis. The binding affinity in terms of K_D and the maximum number of PSMα3 binding sites per oligomer (N_{max}) are shown for the analysis performed by dcFCCS and dcSPFS.

4. Validation of the rational design of the amyloid-inhibitory peptidic scaffold by the dcFCCS/dcSPFS approach

The results obtained for the specific interaction between PSMα3 and the toxic amyloid assemblies of αS, SF and OB, strongly suggests that Ventura lab's initial conception of the peptide based on the properties of these aggregates was correct. In order to gain more understanding on this and to verify what are the key features of the peptidic inhibitor, they designed a variant of PSMα3 where a proline residue disrupted the helix rendering the peptide in a random-coil conformation, as was confirmed by CD spectroscopy (**Fig. 3.14A**. This would, in turn, abolish the amphipathic character imprinted on the PSMα3 peptide. We termed this peptide dPSMα3 where "d" stands for disrupted. Under the hypothesis that without these properties, dPSMα3 would fail to bind to the toxic oligomers OB and, therefore, would not be able to exert a protective effect on cells, ROS assays were performed in SH-SY5Y neuroblastoma cells (**Fig. 3.14B, C**). We observed that, indeed, the membrane damage and ROS signal detected upon treatment with OB was not rescued at all by pre-incubating the oligomers with a stoichiometric amount of the dPSMα3. Remarkably, this confirmed that the amphipatic nature in the form of an α-helix was paramount for PSMα3 peptide to bind and inhibit toxic αS aggregates. Further peptide designs were tested by Jaime Santos (from Ventura's lab) which underpinned the requirement of a cationic face of the peptide together with the amphipatic signature, but the results on this part are not shown because they are out of the scope of this doctoral thesis. They were, however, published in our joint article in Nature Communications [174].
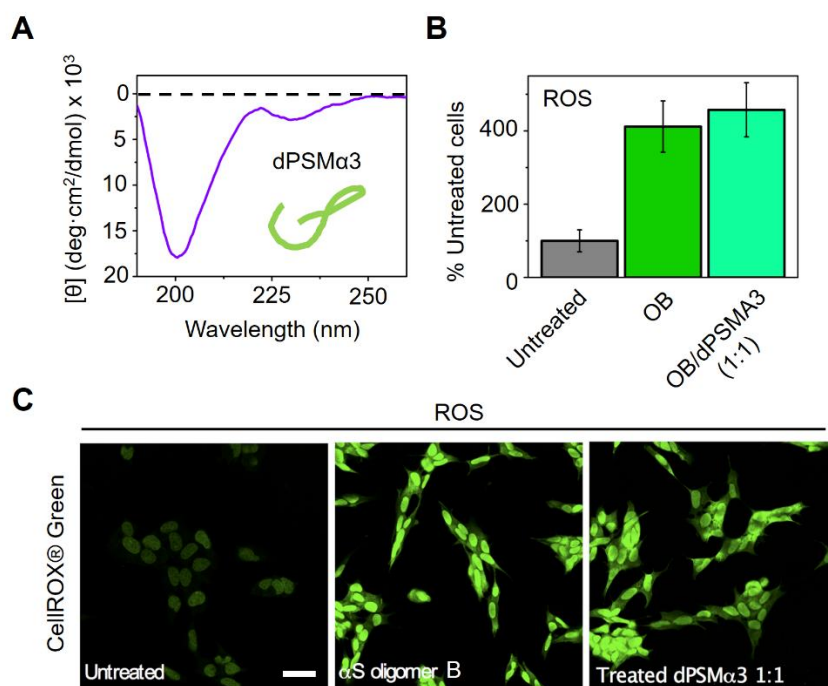
Fig. 3.14. Biochemical and cellular characterization of the inhibitory activity of dPSMα3. A) Far-UV circular dichroism spectra of dPSMα3. **B)** Quantification of the levels of intracellular ROS shown in **D)** SH-SY5Y cells were incubated with 10 μM of type B* oligomers preincubated with different concentrations of dPSMα3. 233, 230 and 100 cells, (respectively, for untreated, αS oligomers and dPSMα3) were analyzed from two independent experiments. **C)** Representative confocal images of the analysis of panel **B)**. Scale bar represents 30 μM. Data adapted with permission from Jaime Santos.

With this in hand, we used dcFCCS/dcSPFS to assess the binding of dPSMα3 to the different species of αS, as we did before with PSMα3 (**Fig. 3.15**). Here, no cross-correlation (**Fig. 3.15A-D**) and virtually no two-color coincident fluorescent bursts (**Fig. 3.15E, F**) were found for any of the interaction pairs, confirming the expected inability of the disrupted peptide for targeting the toxic amyloid assemblies. This highlights the key role of the amphipathicity of the peptide from a single-particle perspective and further endorses the application of dcFCCS/dcSPFS to disentangling complex binding mechanisms and aiding in the design of small molecules for amyloid blocking or detection.

5. Assessment of the binding mechanism of a natural human peptide which inhibits αS amyloid aggregation with great potency

After having established the molecular determinants of the binding and inhibitory potency of the peptide, the group from Prof. Ventura set out to identify natural molecules that shared physico-chemical features with PSMα3 and could, potentially, exhibit an anti-amyloid activity similar to PSMα3. They found a peptide named LL-37 which is constitutively expressed in the brain and the gastrointestinal tract; its presence

in both tissues is engaging, as the brain-gut axis connection is gaining momentum in Parkinson's Disease [544–546]. After having verified the α-helical conformation of LL-37 by CD spectroscopy (not shown), we set out to assess the binding ability of this drug candidate towards αS following the same strategy as we presented above for PSMα3.
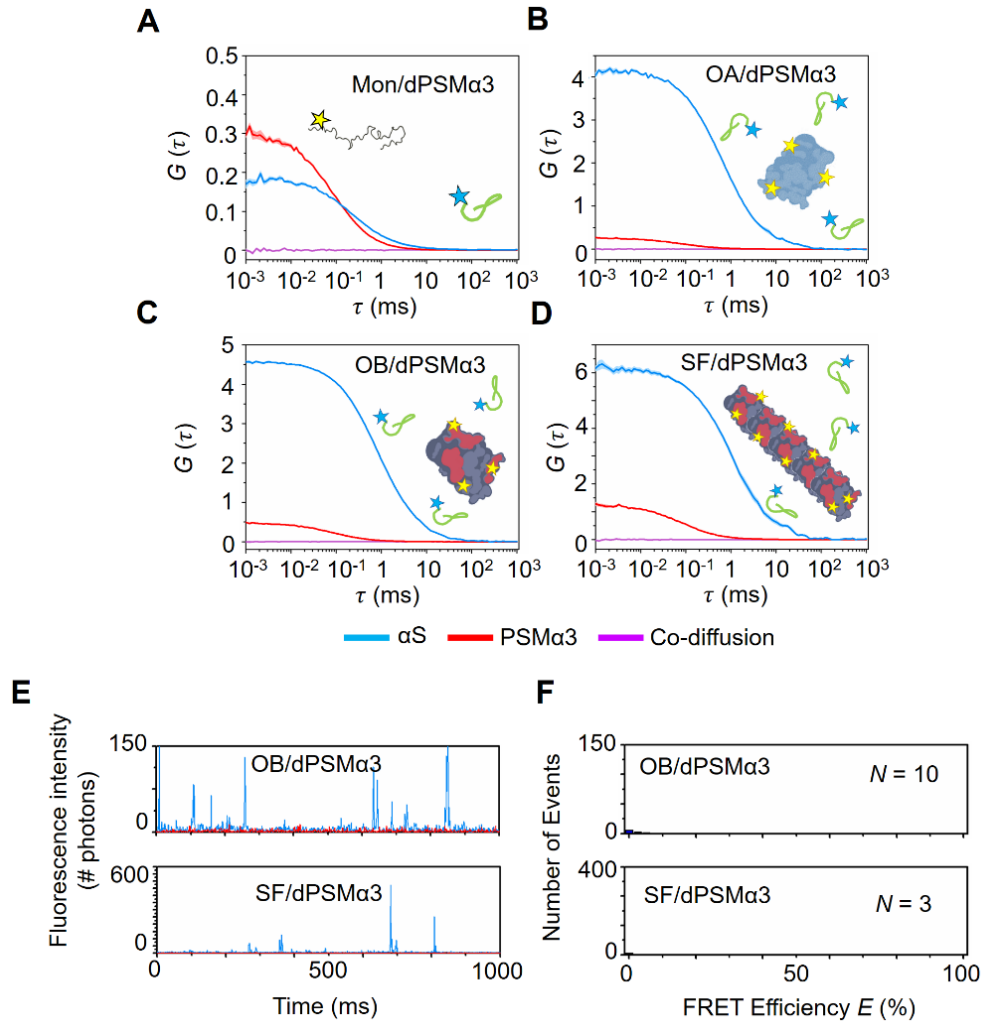
Fig. 3.15. Interaction of dPSMα3 with the different αS species. A-D) Auto-correlation curves for αS and dPSMα3 and cross-correlation curves for interacting molecules are shown in blue, red and purple lines, respectively. The amplitude (*G*) error is shown in faint blue, red and purple, respectively. ~15 nM αS monomer (**A**), ~1 nM type A* (**B**), type B* (**C**) oligomers and sonicated fibrils (**D**) were allowed to interact with ~15 nM dPSMα3. No cross-correlation is observed in any case. **E, F**) αS-dPSMα3 binding analyzed by dual-color single-particle fluorescent spectroscopy. Representative intensity time traces (**E**) and intensity-calculated FRET efficiency histograms (**F**) for samples containing ~1 nM αS type B* oligomers (top) and ~5 nM dPSMα3 or ~5 nM αS fibrils and ~5 nM dPSMα3 (bottom). FRET single-particle fluorescence data directly show the inability of dPSMα3 to interact with either type B* oligomers or fibrils as just few, if any, events were observfed in comparison to the experiments with the PSMα3 peptide. Acquisition times were the same for all data shown.
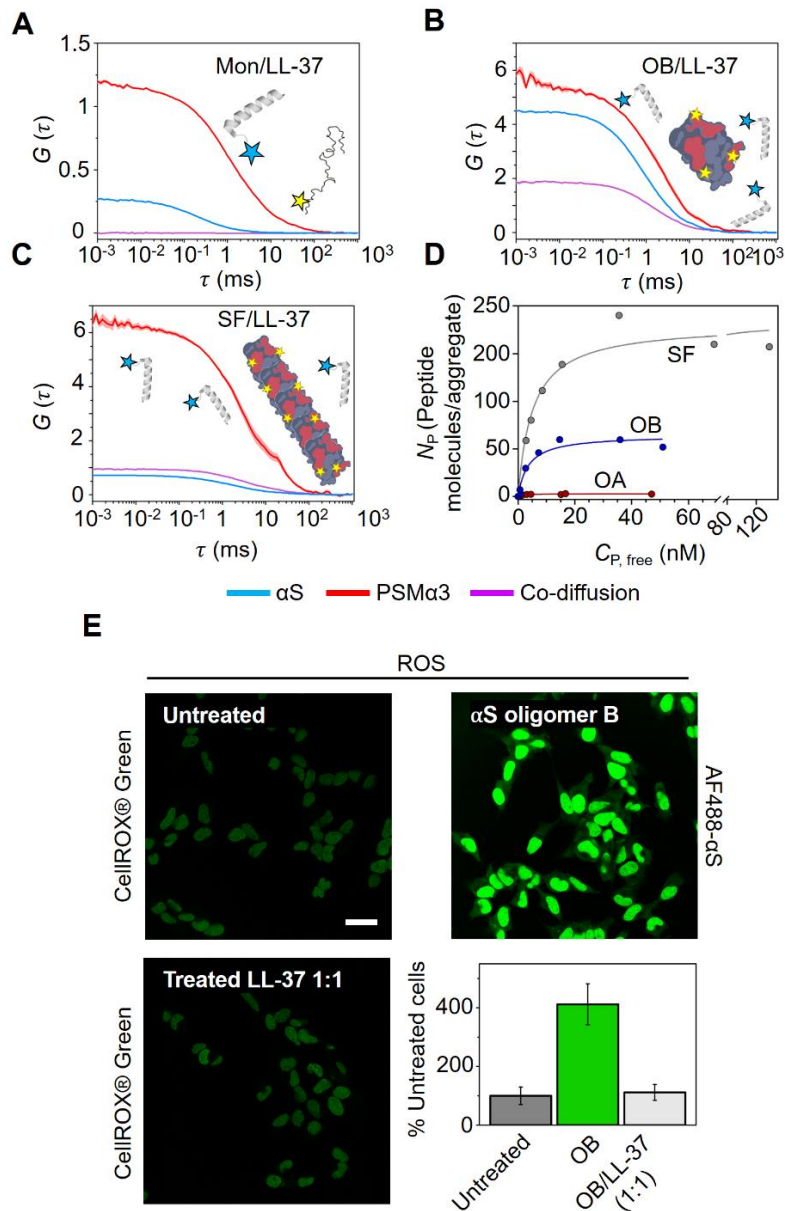
Fig. 3.16. Characterization of the interaction of LL-37 with the αS toxic species. A-C)
Representative auto-correlation curves for αS and LL- 37 peptide and cross-correlation curves
for interacting molecules are shown in blue, red and purple lines, respectively. The amplitude
(*G*) error is shown as faint colored area for the corresponding correlation curves. Samples
contained (**A**) ~15 nM αS monomers and ~15 nM LL-37, (**B**) 1 nM type B* oligomers and ~5
nM LL-37 or (**C**) ~5 nM sonicated fibrils and ~5 nM PSMα3. **D**) Titration binding curves for
the interaction of LL-37 with type A* oligomers (red circles), type B* oligomers (blue circles) or
sonicated fibrils (gray circles) obtained by dcFCCS, showing their corresponding analysis
assuming a model of *n* independent binding sites per αS aggregated species (solid lines). NP
represents the number of bound peptides per aggregate. **E**) Representative confocal images of
SH-SY5Y cells treated with 10 μM of type B* oligomers in the presence of an equimolar
concentration of LL-37. Scale bar represents 30 μM. The bottom left panel shows the
quantification of the intracellular ROS of the experiment A total of 233, 230, and 199 cells,
(respectively, for untreated αS oligomer and LL-37 1:1) were analyzed from two independent
experiments. For αS aggregated species, consisting of several tens of monomers, the species

concentrations in **A-C**) are in the picomolar range and, as further explained above, single-particle conditions are ensured throughout the experiments. ROS data adapted with permission of Jaime Santos.

First, we used dcFCCS to interrogate LL-37 about its capacity to bind to the different species (**Fig. 3.16**) and found that, indeed, it very efficiently targeted OB and SF (**Fig. 3.16A, B**), while no cross-correlation was found for monomeric αS (**Fig. 3.16C**) and only very faint binding was seen for OA (**Fig. 3.17A, B**).
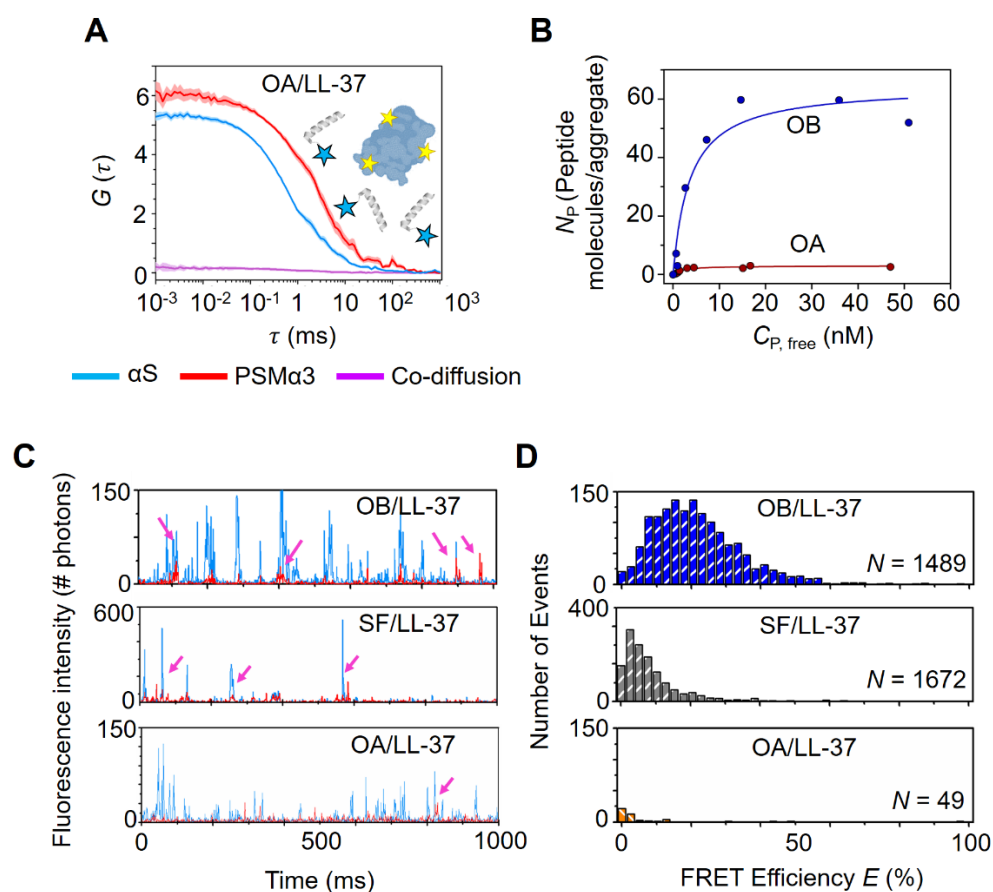
Fig. 3.17. Interaction of LL-37 with αS aggregates by dcFCCS and dcSPFS. A) Auto-correlation curves for αS (blue) and LL-37 (red) and cross-correlation curve for the interacting molecules (purple) in samples containing ~1 nM type A* oligomers and ~5 nM LL-37 peptide. The amplitude (G) error is shown as faint colored area for the corresponding correlation curves. (**B**) Titration binding curves for the interaction of LL-37 with type A* oligomers (red circles) or type B* oligomers (blue circles) obtained by dcFCCS, showing their corresponding analysis assuming a model of n independent binding sites per αS aggregated species (solid lines). C, D) αS-LL-37 binding analyzed by dcSPFS. Representative intensity time traces (A) and intensity-calculated FRET efficiency histograms (B) for samples containing (**c**) ~1 nM αS type B* oligomers and ~5 nM LL-37 (top), ~5 nM αS fibrils and ~5 nM LL-37 (middle) and ~1 nM αS type A* oligomers and ~5 nM LL-37 (bottom). Acquisition times were the same for all data shown.

We then performed binding titration experiments and analyzed them as explained above (**Fig. 3.16D**). We observed that LL-37 displays slightly higher affinities than PSMα3 (K_D = 3.62 nM for type B* oligomers, K_D = 5.14 nM for sonicated fibrils and K_D = 1.92 nM for type A* oligomers), and a significantly higher number of binding sites in type B* oligomers (N_{max} = 64) and sonicated fibrils (N_{max} = 181), while remain the same as PSMα3 for the number of binding sites in the type A* oligomers, which was in any case marginal (N_{max} = 3). This already indicates a remarkable affinity of this human natural peptide, making it a promising candidate for therapeutic purposes. These binding properties we accompanied by a protective effect towards the production of ROS in neuroblastoma cells upon exposure to OB, where the ROS levels dramatically increased by the oligomer-derived damage were totally restored by pre-incubation with LL-37 (**Fig. 3.16E**). When we analyzed the binding by dcSPFS at single-particle resolution we found that, indeed, the amount of two-color coincident events was similar for OB and SF (**Fig. 3.17C, D**) while it was extremely low for OA. This, again, indicates a very good agreement between dcFCCS and dcSPFS.

LL-37 is not related in sequence to PSMα3, but both peptides share the same structural and physicochemical traits. This confirms that a linear combination of these properties suffices to identify, and potentially design, potent inhibitors of αS aggregation. Whether LL-37 is actually involved or not in the pathogenesis of PD remains unexplored. However, it is tempting to speculate that small peptides able to interact actively with αS aggregated species might cohabitate with this protein in tissues relevant to the disease. These human peptides may open an unexplored avenue for PD treatment, *i. e.*, by stimulating their endogenous expression.

In this work in collaboration with the group of Prof. Ventura, we have exploited our recent advances in the understanding of the structural determinants of toxicity of αS oligomers to rationally identify novel molecules able to target the pathogenic species of αS. By using a time-resolved single-particle fluorescence approach we demonstrate that short, amphipathic and cationic α-helical peptides bind toxic oligomers and fibrils with unprecedented specificity and affinity, resulting in the substoichiometric inhibition of αS aggregation and abrogation of oligomer toxicity in neuronal cell models. We then used a protein engineering approach to dissect the molecular determinants accounting for this interaction, which has allowed us to identify a human peptide, constitutively expressed in the brain and gastrointestinal tract, that binds with low nanomolar affinity and high specificity to αS pathogenic species, thus suppressing the aggregation cascade and its associated neurotoxicity. In fact, we patented the identified inhibitory peptide scaffolds (Ventura, S.; Pallarés, I.; Santos, J.; Cremades, N.; **Gracia, P (2020)**. *Inhibitors of α-synuclein aggregation and uses thereof*. (Spain EP20382658). Oficina Española de Patentes y Marcas). This discovery opens previously unexplored avenues for the diagnosis and/or therapeutics of PD and related disorders. Furthermore, we have established a robust, self-validated methodology based on cutting-edge single-particle fluorescence techniques with exquisite spatial and time-resolution. This combined approach has proven extremely useful in our effort to characterize complex multi-ligand/multi-

receptor complexes in an amyloid scenario and we believe its application could be extended to any other binding mechanisms. From our point of view, the methodology and results we present here are on an unprecedented level of detail and shed new light on the molecular determinants of amyloid inhibition. This opens new avenues for aiding in the rational design and testing new small molecules for therapeutic and diagnostic purposes in the field.

Materials & methods

αS expression and purification. Human αS was expressed and purified as previously described [183, 547]. *Escherichia coli* BL21 (DE3) cells containing a pET21a plasmid encoding the αS gene were grown in LB medium supplemented with 100 μM/mL ampicillin. Protein expression was induced at an optical density of 0.8 (600 nm) with 1 mM isopropyl β-D-thiogalactopyranoside (IPTG) for 4 h. Cells were harvested by centrifugation and washed up by resuspension and centrifugation in PBS pH 7.4. Next, pellets were resuspended in 50 mL per culture liter in lysis buffer (50 mM Tris pH 8, 150 mM NaCl, 1μg/mL pepstatin, 20 μg/mL aprotinin, 1 mM benzamidine, 1 mM PMSF, 1 mM EDTA and 0.25 mg/mL lysozyme) and sonicated using a LabSonic®U sonicator (B. Braun Biotech International, Melsungen, Germany). Samples were boiled during 10 minutes at 95 °C and centrifugated at 20,000g at 4 °C for 40 minutes. The soluble fraction was treated with 136 μL/mL of 10 % w/v streptomycin sulfate and 228 μL/mL of pure acetic acid. Upon centrifugation, soluble extracts were fractionated by adding 1:1 of saturated ammonium sulfate and resuspending the insoluble fraction with 50 % ammonium sulfate. The pellet was resuspended in 100 mM pH 8 ammonium acetate (5 mL per culture liter) and pure EtOH 1:1 (v/v) and harvested by centrifugation. The insoluble fraction was resuspended in Tris 20 mM pH 8, filtered with a 0.22 μm filter and loaded into an anion exchange column HiTrap Q HP (GE Healthcare, Chicago, USA) coupled to an ÄKTA purifier high performance liquid chromatography system (GE Healthcare, Chicago, USA). Tris 20 mM pH 8 and Tris 20 mM pH 8, NaCl 1 M were used as buffer A and buffer B. αS was eluted using a using a step gradient: Step 1: 0 %–20 % buffer B, 5 column volumes (cv); Step 2: 20 %–45 % buffer B, 11 cv; Step 3: 100 % buffer B, 5 cv. Purified αS was dialyzed against 5 L ammonium acetate 50 mM in two steps; 4 h and overnight. Finally, protein purity was addressed using 15 % SDS-PAGE. The purest fractions were lyophilized and stored at -80 °C. For the experiments, αS lyophilized aliquots were resuspended to a final concentration of 210 μM using PBS pH 7.4 and filtered using 0.22 μm filters. αS concentration was determined measuring the absorbance at 280 nm and using 5,960 M^{-1} cm^{-1} as extinction coefficient. WT αS was produced by Jaime Santos, Jordi Pujols and Samuel Peña-Díaz.

Peptide preparation. PSMα3, dPSMα3 and LL-37 were purchased from Synpeptide (Shanghai, China) with a purity > 95 %. Single cysteine containing variants were purchased from Genscript (Piscataway, USA) with a purity > 95 %. LL-37 was diluted in Milli-Q sterilized water, divided into aliquots and lyophilized. Cysteine containing peptides were resuspended in PBS pH 7.4, 5 mM TCEP and subsequently labeled with the corresponding fluorophore. PSMα3 and dPSMα3 were dissolved in a 1:1 mixture of trifluoroacetic acid and hexafluoroisopropanol and sonicated for 10 minutes. Stock solutions were divided into aliquots and vacuum dried with a SpeedVac (Thermo Fisher Scientific, Waltham, USA) and stored at - 80 °C until assayed. Peptide aliquots were resuspended in pure Milli-Q water prior their use. Peptide samples were prepared by Jaime Santos, Jordi Pujols and Samuel Peña-Díaz.

αS and peptide labeling. Site-specific labeling of αS was performed in an αS variant with a single engineered cysteine at position 122 (αS N122C). This variant was expressed and purified as previously described [20, 292]. The protein was labeled with maleimide-

modified Alexa Fluor 488 (AF488) (Invitrogen, Carlsbad, USA) for 15-20 h at 4 °C in the dark. After quenching the reaction with 10 mM DTT, free unreacted dye in the protein solution was subsequently separated using a PD10 desalting column (GE Healthcare, Waukesha, USA), and the labeled protein solution was flash frozen with liquid nitrogen and stored at -80 °C. The different peptides, PSMα3, dPSMα3 and LL-37, were labeled at a single engineered cysteine at the N-terminus with maleimide-modified Atto647N (ATTO-TEC, Siegen, Germany). The same labeling and purification strategy were followed as for αS, although in this case the unreacted free dye was removed from the protein solution using a polyacrylamide desalting column (Thermo Fisher Scientific, Waltham, USA). Two cleaning steps were required to remove completely the free dye from the labeled peptide solution. PSMα3, dPSMα3 and LL-37 were labelled by Jaime Santos.

Preparation of the different isolated αS aggregates samples. Oligomeric samples were prepared as previously described [528, 533]. For the isolation of type B* oligomers purified αS was dialyzed against Milli-Q water and lyophilized for 48 h in aliquots of 6 mg. The aliquots were resuspended in 500 µL of PBS pH 7.4 to a final concentration of ca. 800 µM, filtered through 0.22 µm filters and incubated at 37 °C without agitation for 20-24 h. The sample was then ultracentrifuged at 288,000g in a SW55Ti Beckman rotor, in order to remove any possible fibrillar species formed during the incubation, and later filtered by four consecutive cycles of filtration through 100 kDa centrifuge filters (Merck, Darmstadt, Germany) in order to remove the great excess of monomeric protein from the oligomeric solution. Type A* oligomers were generated by incubating 210 µM of αS in PBS pH 7.4 with ten molar equivalents of epigallocatechin-3-gallate (EGCG) (Merck, Darmstadt, Germany) for 48 h at 37 °C. The excess of compound and unreacted monomeric protein were then removed by six consecutive cycles of filtration through 100 kDa centrifuge filters (Merck, Darmstadt, Germany). The concentration of the final oligomeric solutions was determined measuring the absorbance at 280 nm and using an extinction coefficient of 5,960 M^{-1} cm^{-1} or absorbance at 495 nM and an extinction coefficient of 72,000 M^{-1} cm^{-1} for AF488-labeled oligomers. In all cases, the oligomers were kept at room temperature and were used within 3 days after their production. The fibrillar samples were produced as explained in the aggregation kinetics methodology section. The non-reacted protein and small non-fibrillar species that could be formed during the aggregation reaction were removed from the sample by 3 consecutive steps of centrifugation and resuspension of the precipitated fraction in PBS buffer at pH 7.4. Fibrils were then sonicated (1 min, 50 % cycles, 80 % amplitude in a Vibra-Cell VC130 Ultrasonic Processor (Sonics, Newton, USA) to generate fibrillar samples with a relatively homogeneous size distribution of small fibrils. The concentration of the AF488-labeled fibrillar samples was determined by subtracting the absorbance of the monomer after centrifugation at 495 nm using an extinction coefficient of 72,000 M^{-1} cm^{-1}, with respect to the total soluble protein at time 0. For type A* oligomers, the concentration was adjusted *in situ* for each experiment so that a suitable and consistent burst-rate was reached. Thus, an interference of EGCG in quantifying the sample was avoided.

Far-ultraviolet circular dichroism analysis. Far-UV CD spectra of the different peptide solutions were recorded on a Jasco J-815 CD spectrometer (Halifax, Canada) at 25 °C using samples of 15 µM peptide final concentration in Milli-Q water. CD signal was

measured from 260 nm to 190 nm at 0.2 nm intervals, 1 nm bandwidth, 1 second of response time and a scan speed of 100 nm/min on a 0.1 cm quartz cell. 10 accumulations were recorded and averaged for each measurement. For LL-37 peptide samples, CD spectra were recorded in PBS pH 7.4, because of structural differences of this peptide in water and saline solvents. These experiments were performed by Jaime Santos, Jordi Pujols and Samuel Peña-Díaz.

Time-Resolved Fluorescence Spectroscopy. Dual-Color Time-Resolved Fluorescence Spectroscopy experiments were performed on a commercial MT200 (PicoQuant, Berlin, Germany) time-resolved fluorescence confocal microscope with a Time-Correlated Single Photon Counting (TCSPC) unit. Laser diode heads were used in Pulsed Interleaved Excitation (PIE), and the beams were coupled through a single-mode waveguide and adjusted to laser powers of 6 μW (481 nm) and 5 μW (637 nm) measured after the dichroic mirror for optimal count rates while avoiding photobleaching and saturation. The coverslip was placed directly on the immersion water on top of a Super Apochromat 60x NA 1.2 objective with a correction collar (Olympus Life Sciences, Waltham, USA). A dichroic mirror of 488/640 nm (Semrock, Lake Forest, IL, USA) was used as the main beam splitter. Out-of-focus emission light was blocked by a 50 μm pinhole and the in-focus emission light was then split by a 50/50 beamsplitter into 2 detection paths. Bandpass emission filters (Semrock, Lake Forest, IL, USA) of 520/35 for the green dye (AF488) and 690/70 for the red dye (Atto647N) were used before the detectors. Single Photon Avalanche Diodes (SPADs) (Micro Photon Devices, Bolzano, Italy) served as detectors. Each measurement had an acquisition time of 1 to 3 minutes.

For FCS experiments, the effective focal volume of the green channel and its structural parameters in our system were determined using a 1 nM solution of Atto488 (ATTO-TEC GmbH, Siegen, Germany) yielding $V_{eff, g}$ = 0.51 fL and κ_g = 3.97. Positive and negative cross-correlation controls were performed with a dual-labeled dsDNA (10 nM) and an equimolar mixture (15 nM each) of AF488- and Atto647N-labelled monomeric αS (**Fig. 3.6A**). The positive control was also used for the determination of the red and dual-color effective focal volume and their structural parameter, yielding $V_{eff,r}$ = 0.1 fL, $V_{eff,gr}$ = 0.091 fL, κ_r = 2.78 and κ_{gr} = 2.67, respectively.

AF488-labeled aggregated αS samples were diluted in PBS pH 7.4 to a final protein concentration of ~1-5 nM in a 50 μL droplet and spotted directly onto a cover glass (Corning, Corning, USA) previously coated with a 1 mg/mL BSA solution. Atto 647N-labeled peptides were titrated into the droplet and the peptide concentration was measured individually for each experiment by auto-correlation analysis of the red dye. No significant changes in correlation amplitudes were observed over time after equilibrating the samples for 2 minutes. Experiments were performed at 20 °C and samples were covered to avoid evaporation. It is important to note that, for αS aggregated species, consisting of several tens of monomers, the species concentrations are in the picomolar range and, as further explained below, single-particle conditions are ensured throughout the experiments. The aggregated species coexist with a certain amount of monomeric αS due to the stark sample dilution employed in the experiments and, therefore, the donor auto-correlation curves in **Figures 8, 9, 15-17**, show both the diffusion component of the monomer and the aggregate. A similar behavior is observed

for peptides PSMα3 and LL-37, which can exist as oligomerized species. For obtaining the diffusion coefficients of the different aggregates the diffusion component of the monomeric species in the samples was filtered out by intensity-filtered dcFCCS analysis as explained below. The diffusion coefficient (D_g or D_r) fitted to data for αS species are 103 ± 16 μm^2 s^{-1}, 4 ± 0.9 μm^2 s^{-1}, 3.46 ± 1.2 μm^2 s^{-1} and 0.81 ± 0.12 μm^2 s^{-1} for the monomer, type A*oligomers, type B* oligomers and fibrils, respectively, in very good agreement with the diffusion coefficients expected according to their corresponding sizes as determined by AFM and DLS (**see Fig. 3.5)** and as reported before [528, 538]. Additionally, such intensity thresholds yield a confocal volume mean occupancy (N) well below 1 for all fluorescent species involved, with $N = 0.019$, $N = 0.043$ and $N = 0.053$ for type A*oligomers, type B* oligomers and fibrils, respectively. Therefore, in terms of burst selection for the PIE-FRET and fluorescence stoichiometry analysis, where the same intensity threshold is applied, the experiments were conducted under single-particle conditions. This becomes even more evident when looking at the raw data in the form of intensity time traces of, for instance, the PSMα3 - type B* oligomer interaction experiments (**Fig. 3.7**). D_g values of 14.6 ± 3.6, 19.2 ± 4.2 μm^2 s^{-1} and 108 ± 18 μm^2 s^{-1} were calculated for PSMα3, LL-37 and dPSMα3, respectively, with $N = 0.053$ and $N = 0.11$, for PSMα3 and LL-37, respectively. These data indicate that PSMα3 and LL-37 exhibit a certain degree of oligomerization, despite no aggregates were detected in TEM images of peptides alone (not shown), and the data indicates that they bind to their targets in the monomeric form (**Fig. 3.10** and **3.16D**).

Both data acquisition and analysis were performed on the commercially available software SymphoTime64 (PicoQuant, Berlin, Germany). For the oligomeric and fibrillar samples, a lower intensity threshold of 27 photons in the green dye auto correlation analysis was applied to filter out the low intensity signal arising from the monomeric αS events generated upon dilution-induced disaggregation of the aggregated samples. This threshold was calculated as 3 times the mean intensity of monomeric αS obtained from the analysis of a sample of pure αS monomers. Additionally, an upper intensity threshold was applied to auto-correlation and cross-correlation analysis to filter out any possible artifacts such as dust particles or aggregate clusters (anyway these events were very scarce): 500 photons for monomer, type A* and type B* oligomers and 1500 photons for sonicated fibrils. Data on the red channel corresponding to the peptide fluorescence signal was intensity-filtered with a lower intensity threshold in analogy to the green channel owing to the fact that the peptide can also exist as self-assembled species. The reference signal was that of the monomer-only dPSMα3 sample. The PIE excitation scheme together with the TSCPC acquisition enabled the application of a lifetime-weighted filter which allowed for removal of background and spectral cross-talk. The corrected auto-correlations of the green and the red channel (G_i) were given by

$$G_i(\tau) = \frac{\langle F_i(t) \cdot F_i(t + \tau) \rangle}{F_i^2} - 1 \qquad \textbf{(Eq. 3.1)}$$

where $F_i(t)$ denotes the fluorescence intensity either the green or the red channel, τ is the correlation time and the angled brackets indicate a time average over the acquisition time. The cross-correlation (G_{gr}) between the green and the red channel was given by

$$G_{\mathrm{gr}}(\tau) = \frac{\langle F_{\mathrm{g}}(t) \cdot F_{\mathrm{r}}(t+\tau)\rangle}{\langle F_{\mathrm{g}}\rangle\langle F_{\mathrm{r}}\rangle} - 1 \qquad \textbf{(Eq. 3.2)}$$

Auto-correlation curves for both the green and red channel were fitted with a 2 diffusion-component model accounting for residual monomeric αS and bound and unbound peptide, respectively, using the following equation:

$$G_{\mathrm{i}}(\tau) = G_{\mathrm{i}}^{0} \frac{f_{\mathrm{i},1}}{\left(1 + \dfrac{\tau}{\tau_{\mathrm{D_{i,1}}}}\right)\sqrt{1 + \dfrac{\tau}{\kappa^2\,\tau_{\mathrm{D_{i,1}}}}}} + \frac{f_{\mathrm{i},2}}{\left(1 + \dfrac{\tau}{\tau_{\mathrm{D_{i,2}}}}\right)\sqrt{1 + \dfrac{\tau}{\kappa^2\,\tau_{\mathrm{D_{i,2}}}}}}, \qquad \textbf{(Eq. 3.3)}$$

where G_{i}^{0} is the correlation amplitude at correlation time 0, $f_{\mathrm{i},1}$ and $f_{\mathrm{i},2}$ denote the fractional amplitudes of the monomeric and aggregated αS for the green channel (where i = g) and the bound and unbound peptide for the red channel (where i = r) and κ^2 is the structure parameter of the focal volume. The same applies for the diffusion terms $\tau_{\mathrm{D_{i,1}}}$ and $\tau_{\mathrm{D_{i,2}}}$. No correlated blinking is expected when multiple dyes are present on one particle as it is our case and therefore a blinking term was not included.

Cross-correlation amplitudes were fitted with a 1-component simple diffusion model since only one diffusion coefficient is expected for the interacting species (**Fig. 3.9**) using the following equation:

$$G_{\mathrm{gr}}(\tau) = G_{\mathrm{gr}}^{0} \frac{1}{\left(1 + \dfrac{\tau}{\tau_{\mathrm{D,gr}}}\right)\sqrt{1 + \dfrac{\tau}{\kappa^2\,\tau_{\mathrm{D,gr}}}}}. \qquad \textbf{(Eq. 3.4)}$$

With the corrected green dye auto-correlation function and the mean intensity of monomeric αS, the average aggregate particle number (N_{Ag}) for each αS aggregated sample was estimated as $N_{\mathrm{Ag}} = \frac{1}{G_{\mathrm{g}}^{0}}$. The average particle number for the peptide was calculated in analogy to that of αS. The peptide concentration was calculated as $C_{\mathrm{P}} = \frac{N_{\mathrm{r}}}{V_{\mathrm{eff,r}}\,N_{\mathrm{A}}}$, where N_{r} is the average number of particles in the red confocal volume, $V_{\mathrm{eff,r}}$ is the red focal volume and N_{A} is the Avogadro number. The cross-correlation amplitudes, N_{Ag}, dual-laser focal volume, $V_{\mathrm{eff,gr}}$, and peptide concentrations, C_{P}, were used for calculating the number of peptides bound to each αS species (N_{P}) and the free peptide concentration ($C_{\mathrm{P, Free}}$) as described by Kruger and coworkers [338].

For single-burst FRET and stoichiometry analysis, an acceptor (red dye) direct excitation lower threshold based on the mean intensity of the time trace ($I_{\mathrm{A,mean}} + 2\sigma$) was used to filter out those events without an active acceptor molecule. To further select those events arising from αS aggregates, a burst selection intensity threshold of 100 photons was used. In the FRET analysis, experimentally determined correction factors were applied: spectral bleed-through α was 0.004, direct excitation (spectral cross-talk) δ was 0.0305 and detection efficiency γ was 0.517. Burst-wise FRET efficiency and stoichiometry were calculated as given by

$$E = \frac{F_{A,IE}}{F_D + F_{A,SE}} \qquad \textbf{(Eq. 3. 5)}$$

$$S = \frac{F_D + F_{A,IE}}{F_D + F_{A,IE} + F_{A,DE}} \qquad \textbf{(Eq. 3. 6)}$$

where F_D is the fluorescence intensity in the donor (green) channel, $F_{A,IE}$ is the fluorescence intensity in the acceptor (red) channel through indirect excitation and $F_{A,DE}$ is the fluorescence intensity in the acceptor (red) channel after direct excitation by PIE pulse.

Stoichiometry values were corrected for the difference in mean intensity between the monomeric αS and peptide bursts, obtained from monomeric αS-only and peptide-only measurements; the obtained mean intensity ratio $I_{mean,\alpha S}:I_{mean,peptide}$ was found to be 0.77. Alternatively, the differences in the molecular brightness between the αS monomer ($\eta_{B,mon}$) and the small binding molecule ($\eta_{B,M}$) can be calculated by fitting the auto-correlation curves to a suitable diffusion model. Under our experimental conditions, correlated blinking from single emitters was observed and therefore a 1-diffusion component and a blinking term (τ_T) should be used for the fitting the data as with the following equation:

$$G_i(\tau) = G_i^0 \left(1 + \frac{T\, e^{-\frac{\tau}{\tau_T}}}{1-T} \right) \frac{1}{\left(1 + \frac{\tau}{\tau_{D,i}}\right)\sqrt{1 + \frac{\tau}{\kappa^2 \tau_{D,i}}}}, \qquad \textbf{(Eq. 3. 7)}$$

Where i denotes either the green or the red channel, T is the average fraction of dye in the dark state and τ_T is the blinking relaxation time. The molecular brightness is given by $\eta_B = \frac{cps}{N}$.

Stoichiometry distributions were fitted to a log-normal distribution to obtain the mean stoichiometry value for each measurement. The number of bound peptides per aggregate (N_P) was then estimated by multiplying the mean stoichiometry value previously obtained by the mean number of αS monomers present on each aggregate as calculated empirically from the molecular brightness in FCCS experiments. The free peptide concentration ($C_{P,\ Free}$) and N_P obtained by either FCCS or single-burst stoichiometry analysis were used for calculating the binding curves as described by Kruger and coworkers [338]. To obtain the dissociation constant K_D and the maximum specific binding sites N_{max}, the resulting binding curves were fitted to the following specific binding model with n identical and independent binding sites:

$$Y = \frac{N_{max}\, X}{(K_D + X)} \qquad \textbf{(Eq. 3.8)}$$

The binding curves and binding parameters obtained from either dcFCCS or dcSPFS analysis were compared (**Fig. 3.13**) and found to be remarkably similar, which validates the analysis.

Aggregation kinetics. αS amyloid aggregation was monitored in a 96 wells plate (non-treated) (Sarstedt, Germany) containing Teflon polyballs (1/8″ diameter) (Polysciences Europe GmbH, Eppelheim, Germany) as described by Pujols and coworkers [548]. Each well contained 150 µL solutions of 70 µM αS in PBS buffer with 40 µM thioflavin-T and the corresponding concentration of peptide. Plates were incubated at 37 °C, 100 rpm in an orbital culture shaker Max-Q 4000 (Thermo Fisher Scientific, Waltham, USA). Aggregation was analyzed every 2 h using a Victor3.0 Multilabel Reader (PerkinElmer, Waltham, USA). End-point measurements were performed after 32 h of incubation. Fluorescence intensity was measured in triplicate by exciting with a 430–450 nm filter and collecting the emission with a 480–510 nm filter. The resulting kinetics were normalized to the maximum fluorescence of the αS control (untreated). These experiments were performed by Jaime Santos, Jordi Pujols and Samuel Peña-Díaz.

Atomic force microscopy. αS samples were diluted to a protein concentration of 0.1 - 0.5 µM and deposited on cleaved Muscovite Mica V-5 (Electron Microscopy Sciences; Hatfield, Pensilvania, USA). Slides were washed with double distilled water and allowed to dry before imaging acquisition on a Bruker Multimode 8 (Bruker; Billerica, USA) using a FMG01 gold probe (NT-MDT Spectrum Instruments Ltd., Russia) in intermittent-contact mode in air. Images were processed using Gwyddion and the width measurements were corrected for the tip shape and size (10 nm). These experiments were performed by José Camino.

Polyacrylamide gel electrophoresis. For monomeric and fibrillar αS species, 5 µg protein in denaturing loading buffer were loaded onto a 15 % acrylamide SDS-PAGE. For type A* and type B*, 2 µg protein in non-denaturing buffer were loaded onto a 15 % native-PAGE. The only difference between the denaturing and non-denaturing gel electrophoresis was the absence of SDS in the sample, gel and buffer of the native PAGE. No boiling step was included in either case.

Dynamic light scattering. Estimations of the hydrodynamic radius of αS species were made on a DynaPro NanoStar (Wyatt, USA) equipped with a Peltier temperature control. Protein samples were prepared at a 25 µM concentration in filtered PBS (0.22 µm cellulose acetate syringe filters). DLS measurements were performed at 25 °C at a fixed angle of 90 °. 20 acquisitions per measurement were collected using a 2 s acquisition time. An average of 10 measurements were performed for the statistical size analysis. Data was analyzed using the Dynamics software (version 6.12.03).

Fourier-Transform infrared (FT-IR) spectroscopy. αS aggregates species were transferred to deuterated buffer, by either centrifugation/resuspension or filtering cycles, to a final protein concentration of ca. 4 mg/ml. Samples were then deposited between two CaF2 polished windows separated by a PTFE Spacer (Harrick Scientific Products Inc., USA). Spectra were collected in transmission mode at room temperature

using a VERTEX 70 FTIR Spectrometer (Bruker, USA) equipped with a cryogenic MCT detector cooled in liquid nitrogen. IR spectra were processed and analyzed using standard routines in OPUS (Bruker, USA), RAMOPN (NRC, National Research Council of Canada) and Spectra-Calc-Arithmetic© (Galactic Inc., USA). These experiments were performed by José Camino.

ANS fluorescence spectroscopy. 10 µM of each αS sample was incubated with 500 µM 8-anilo-1-naphtalene-sulfonic acid (ANS) in PBS for 45 min before recording the spectra. The extinction coefficient of ANS at 350 nm was assumed to be 5000 cm^{-1}.M^{-1}. In order to monitor ANS binding to the each αS species, samples were excited at 350 nm and their emission spectra were recorded from 400 to 650 nm in 1-nm steps. Spectra were collected at room temperature in a Cary Eclipse Fluorescence Spectrophotometer (Varian, Palo Alto, California, United States) with slit-widths of 5/5 nm. An averaging time of 100 ms was used.

Transmission electron microscopy. For electron microscopy analyses, end-point aggregated samples were sonicated for 5 min at minimum intensity in an ultrasonic bath (VWR ultrasonic cleaner) and placed onto carbon-coated copper grids and allowed to adsorb for 5 min. The grids were then washed with distilled water and negative stained with 2 % (w/v) uranyl acetate for 1 minute. Finally, the excess of uranyl acetate was absorbed using ashless filter paper and the grids were left to air-dry for 15 minutes. A TEM JEM-1400 (JEOL, Peabody, USA) microscope was used operating at an accelerating voltage of 120 kV. The more representative images of each grid were selected. These experiments were performed by Jaime Santos, Jordi Pujols and Samuel Peña-Díaz.

Isolation of low molecular weight aggregates generated during αS *in vitro* aggregation. αS aggregation was performed as previously described in absence and presence of PSMα3. Aliquots at the analyzed time point were taken and flash frozen in liquid nitrogen and stored at -80 ºC until assayed. To fractionate our sample into insoluble species, low-molecular weight aggregates and monomers, we adapted the centrifugation based protocol developed by Kumar and coworkers [549]. Briefly, αS preparations were subjected to ultracentrifugation at 100,000g for 30 min at 20 °C in a SW55Ti Beckman rotor in order to isolate larger fibrillar species. The soluble fraction (100 µl) containing low molecular weight aggregates and monomeric αS was then filtrated through 100 kDa centrifuge filters (Merck, Darmstadt, Germany) in order to fractionate these two species. The filtrated samples contain monomeric or -theoretically- dimeric αS. The excess of monomeric species retained in the filter were then washed by filtrating 400 µl of PBS. Finally, aggregated species retained in the filter were recovered by adding 100 µl of PBS to the membrane and carefully pipetting. This fraction containing low molecular weight aggregates was subsequently analyzed by transmission electron microscopy as previously described. These experiments were performed by Jaime Santos, Jordi Pujols and Samuel Peña-Díaz.

Neuroblastoma culture. Human SH-SY5Y neuroblastoma cells (ATCC) were cultured in DMEM/F12 medium supplemented with 15 % FBS and 1xNEAA. Cells were grown at

37 °C in a 5 % CO_2 humidified atmosphere until an 80 % confluence for a maximum of 20 passages. Jaime Santos and Susanna Navarro performed these experiments.

Analysis of intracellular ROS. SH-SY5Y cells were seeded onto glass coverslips (Ibidi, Gräfelfing, Germany) at 0.5×10^6 cells/mL and treated for 15 minutes with 10 μM of type B* oligomers or type B* pretreated for 15 minutes with the tested peptide (PSMα3, dPSMα3 and LL-37). Then, CellROX® Green (Invitrogen, Carlsbad, USA) at a final concentration of 5 μM was added and incubated for 30 minutes at 37 °C. Cells were washed with PBS and fixed with 3.7 % paraformaldehyde (PFA) for 15 min. The intracellular fluorescence of the SH-SY5Y cells was analyzed on a Leica TCS SP5 (Leica Microsystems, Wetzlar, Germany) with a HCX PL APO 63 × 1.4 oil immersion objective, under UV light by using a 488 nm excitation laser for CellROX and collecting the emission with a 515-560 nm filter range. Jaime Santos and Susanna Navarro performed this analysis.

Redesign of PSMα3 variants. To guide and assist the design of PSMα3 peptide variants some computational tools were employed. Briefly, AGADIR was used to predict the helical propensity of the peptide variants based on the helix/coil transition theory [550]. FoldX allows a rapid evaluation of the effect of mutations on the stability, folding and dynamics of proteins [551]. We exploited it to evaluate if the designed mutations may compromise the stability of the α-helix specially regarding extensive redesign or those involving electrostatic repulsions. The peptides mean hydrophobicity (*H*), and their helical hydrophobic moment (μ_H), a measure of the amphiphilicity of a helix, were calculated according to Eisenberg and coworkers [552]. Peptide redesign was done by Salvador Ventura, Irantzu Pallarés and Jaime Santos.

Chapter 4

Pyrene and Fluorescence Dequenching Spectroscopy for Monitoring Amyloid Dissaggregation: Insights into the Molecular Mechanism of the Chaperone Machinery Hsc70 over α-Synuclein Toxic Amyloid Species

Introduction

Currently, there are two main species of α-synuclein (αS) in the spotlight when it comes to relating amyloid aggregation and neurodegeneration in diseases such as Parkinson's disease (PD), dementia with Lewy Bodies (DLB) or multiple system atrophy (MSA) [553–555]. On the one hand, small, transient oligomers are known for their ability to disrupt cellular membranes and induce a variety of cellular insults such as oxidative stress, calcium homeostasis deregulation or mitochondrial dysfunction [536]. In addition to this, recent studies have pointed them out as possible disease spreading agents and propagators of neural damage [556, 557]. Along these lines, small amyloid fibrils have likewise been directly linked to propagation of neurodegeneration and cell-to-cell amyloid transmission [77, 532, 558]. However, in contrast to these two amyloid assemblies, large fibrils are considered less toxic and less involved in amyloid spreading towards cells [559]. Their tight and highly ordered molecular packing and slow diffusion are believed to be the underlying features that reduce the undesired interaction of these species with cellular components.

One of the molecular machineries that cells have evolved ever since to tackle the toxic effect of protein aggregates are chaperones and cochaperones. Although the functioning of these molecules and their orchestrated action with the proteasome and autophagy systems remains largely obscure, some advances have been made in understanding this complex cellular toolbox. In particular, the constitutive human chaperone Hsc70 has been previously shown to disassemble αS fibrils [236], working together with the Hsp40 family cochaperone DnaJB1. This otherwise slow disaggregation process was significantly accelerated in the presence of the nucleotide exchange factor (NEF) Apg2, a Hsp110 family member. Indeed, previous studies suggested that the sole combination of members of these three families was enough to efficiently fragment and depolymerize αS fibrils resulting in the release of a variety of species: small fibrils, oligomers and, finally, monomeric αS. However, despite the importance of this emerging chaperone disaggregase functionality, its mechanism of action remains largely unknown. Currently, the two most widely accepted models propose that the human disaggregase depolymerizes fibrils extracting monomers from their ends [236], whereas one of them also puts forward that chaperones can extract monomers from the center of the fibrils, therefore breaking them into smaller fragments [224]. Recently, this very same chaperone combination was proven able to clear tau and Htt aggregates [560, 561], suggesting that this Hsp70-based machinery could, indeed, represent a human disaggregase specifically evolved for dealing with amyloid assemblies.

From an experimental point of view, monitoring the disaggregation activity of the chaperone machinery over amyloid assemblies poses a technical challenge. Typically, thioflavin-T (ThT) is the golden standard for monitoring the presence of amyloid structures over time, both for studying aggregation and amyloid inhibition by small molecules or chaperones, owing to its generally accepted binding specificity to cross-β amyloid structures. Mainly, this is due to its cost efficiency and adaptability to high-throughput screening (HTS) assays. Nevertheless, using ThT as an extrinsic probe for

directly measuring the fraction of amyloid aggregates in a protein sample has certain caveats. While it is well-suited for the test tube, *in vivo* studies are not yet a reality in the field, thereby often preventing ThT from accessing physiologically relevant information as a standalone method. Another pitfall when using ThT for studying heterogeneous system with a large diversity of protein variants, aggregate sizes and protein conformations, is the inability of ThT to distinguish different types of amyloid assemblies. This makes it challenging to establish a quantitative comparison between the aggregation or disaggregation of different amyloid structures. Of particular relevance is the fact that ThT barely binds to intermediate amyloid species likely related to neurodegeneration. Therefore, ThT is limited to mature amyloid aggregates. The low degree of binding for some amyloid aggregates, together with the differences between distinct amyloid structures, often yield noisy chaperone-mediated disaggregation curves that do not allow for a quantitative modelling of the data. Lastly, ThT has been reported to interact non-specifically with other non-amyloid protein structures, including some chaperones, as well as with small molecules in drug screening studies, thereby requiring exquisite control of the experimental conditions and caution when interpreting the data. Besides, our collaborators from Prof. Arturo Muga's lab at the University of the Basque Country have found that ThT also interferes with the functioning of the Hsc70 machinery, rendering ThT time-course data unreliable when analyzing disaggregation of αS amyloid fibrils. For more detailed information and relevant bibliography on this topic, *see* general introduction section 4 and 5.

To overcome these technical challenges when studying amyloid disaggagregation, we considered using other fluorescence-based techniques that could also be used in a straightforward, cost-efficient, high throughput platform. For that, we hypothesized pyrene fluorescence and fluorescence dequenching could be suitable provided the protein is covalently-bound to the appropriate fluorescence probes. On the one hand, pyrene has a double spectral readout, as it has been explained before in this thesis (see introduction and chapter 1), providing a richer data output than ThT that may inform with more detail on the conformational properties of the aggregates requiring only a plate reader. On the other hand, monitoring the pyrene excimer formation is limited to β-sheet parallel amyloid assemblies. Monitoring the fluorescence dequenching of an intrinsic probe has been successfully used previously for quantifying amyloid disaggregation [224] and, in particular, using the probe AlexaFluor488 (AF488), has been increasingly used for *in vivo* studies of αS aggregation [20, 414], indicating its suitability for disaggregation studies in cells. These assays are easily performed in a plate-reader and do not depend on the structural particularities of amyloid aggregates as long as the fluorophore is placed in a position in the protein sequence where it suffers stronger quenching events in the amyloid state. Furthermore, AF488 is a photophysical- and photochemically very powerful dye that is widely used for advanced fluorescence techniques including fluorescence anisotropy, lifetime imaging and spectroscopy and single-particle techniques such as fluorescence correlation spectroscopy (FCS) and Förster resonance energy transfer (FRET) spectroscopy (see general introduction section 5 and 6). This could open new avenues for disaggregation studies in the future.

Considering all this, we asked ourselves whether pyrene fluorescence and AF488-dequenching (AF488-Deq) could be used for obtaining reliable, high quality kinetic data on the disaggregation process of αS amyloid assemblies induced by the Hsc70 system. In combination with structural information of the system obtained by real-time atomic force microscopy, this would allow us to come up with a model for its molecular mechanism. Further, we hypothesized that, upon characterizing the clearance of large and short fibrils as well as toxic oligomers, we would be able to describe the disaggregase function of the Hsc70 machinery in terms of structural specificity and efficiency. This would shed new light on the relationship between distinct αS amyloid assemblies, their toxicity and the evolutionary response of the cell via the chaperone system.

Specific aims

- Implement pyrene spectroscopy as an alternative tool to thioflavin-T for monitoring amyloid disaggregation

- Establish fluorescence dequenching as an independent method to thioflavin-T for studying amyloid disaggregation

- Using fluorescence dequenching to aid deciphering the detailed molecular mechanism of amyloid disaggregation of the chaperone machinery Hsc70 over αS fibrils

- Describing the relationship between biologically relevant αS amyloids with distinct features and the efficacy and velocity of their disaggregation by Hsc70 using fluorescence dequenching

Results

1. Establishing pyrene spectroscopy and fluorescence dequenching as alternative methods to ThT for monitoring the disassembly of amyloid α-synuclein fibrils over time

In chapter 1 of this thesis we have described how we established pyrene fluorescence as a powerful tool for monitoring amyloid aggregation and aggregate topology with end-point ratiometric analysis of the spectra. From there, we envisioned extending this approach onto kinetic measurements of αS aggregation in different conditions and, later, disaggregation. For this we based our first experiments on the work by Jovin *et. al.* [443]. First, we tested how the amyloid self-assembly of αS monomers labelled with a pyrene molecule (see methods for more information) was indeed visible by real-time ratiometric pyrene fluorescence. We did this for parallel β-sheet aggregates formed by heterogeneous nucleation (reaction triggered in the presence of 10 % MeOH under quiescent conditions) and antiparallel β-sheet aggregates formed by homogeneous nucleation (reaction triggered in the presence of 35 % MeOH under quiescent conditions) (see chapter 1 of this thesis for more details). We did this by labelling αS at position 24 of its primary sequence (Pyr24-αS). We observed that for parallel (**Fig. 4.1A**) and antiparallel (**Fig. 4.1B**) aggregates, both the inter-pyrene proximity-related excimer/monomer (E/M) ratio and the polarity-reporting band I/band III (I_I/I_{III}) ratio showed a time-response that could be described by sigmoidal functions, as expected for the typical profile of amyloid aggregation.
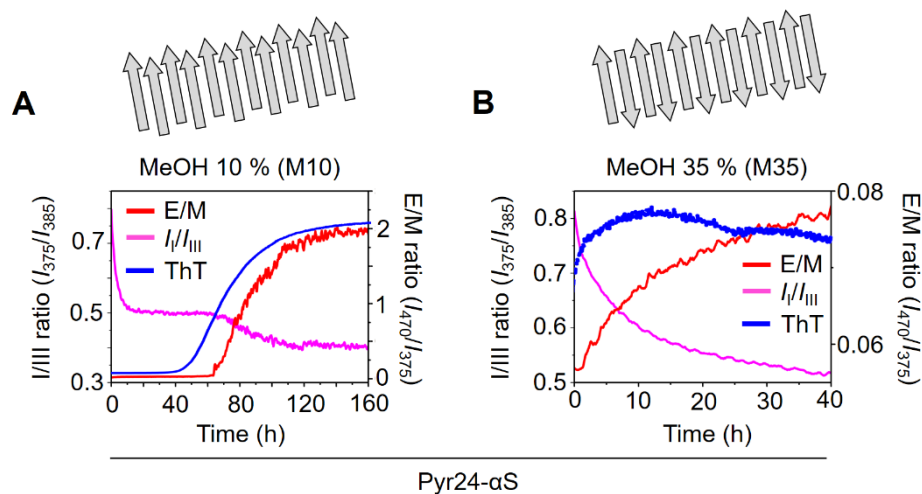
Fig. 4.1. Pyrene spectroscopy monitors the aggregation kinetics of αS under different conditions. Time course of aggregation assays with 50 μM Pyr24-αS (100 % labelled) in PBS (pH 7.4) in the presence of 10 % MeOH (**A**) and 35 % MeOH (**B**). The E/M and I_I/I_{III} ratios are shown in red and pink, respectively, and the ThT signal of an equivalent experiment using WT-αS is shown in blue. Sketches (top) illustrate the parallel (**A**) and antiparallel (**B**) nature of each aggregate as described in chapter 1 of this thesis.

For parallel β-sheet aggregates (**Fig. 4.1A**), the pyrene moiety shows an increase of the E/M ratio with a sigmoidal curve that is comparable to that of the ThT signal used as a control experiment, while a reduction in the polarity of the microenvironment of the pyrene moiety during the lag phase of the ThT curve is observed. One possible explanation for the biphasic curve of the I_I/I_{III} ratio is that the first decay reports on the nucleation events while the second reflects the subsequent interactions that give rise to the amyloid core.

When we did the same on antiparallel β-sheet aggregates (**Fig. 4.1B**), the I_I/I_{III} ratio nicely reproduced the time-behavior of the ThT signal, without showing any lag-phase. This observation falls in line with what we proposed in our published results on homogeneous nucleation and antiparallel aggregation of αS, where amyloid nucleation occur at the same rate or faster than elongation. On the other hand, owing to the antiparallel nature of this polymorph, monitoring the E/M ratio was not as informative as for the heterogeneous aggregation scenario. The amplitude changes were too small to allow a reliable analysis and, thus, this particular ratiometric analysis was discarded for assessing antiparallel amyloid aggregation pathways.

Our results underline the power of site-specific pyrene fluorescence for dissecting the role of different regions of a protein along the complex amyloid nucleation and aggregation process. It needs to be pointed out that pyrene fluorescence, specially the I_I/I_{III} ratio, reveals changes at time-points in the self-assembly process where ThT is insensitive, highlighting the scope of this technique. However, the study of antiparallel aggregates poses a severe challenge to this technique and, therefore, complementary approaches need to be implemented.

In order to test the suitability of pyrene fluorescence and AF488-Deq for studying the disaggregation of αS amyloid species, we collaborated with the lab of Prof. Arturo Muga from the Biofisika Institute at the University of the Basque Country (UPV), who are experts in the field of chaperone systems and amyloid disaggregation. In particular, we set out to decipher the molecular mechanism of the human disaggregase machinery (Hsc70/DnaJB1/Apg2) over αS amyloid fibrils. The chaperones and the how-to knowledge on disaggregation assays were contributed by Prof. Muga, Dr. Adelina Prado and Dr. Aitor Franco. The results presented in this chapter contributed to the publication of a research article in PNAS USA [562]. For these assays, we used the Pyr85-αS variant owing to the fact that it yields the largest contrast from the aggregate pyrene signal to the free monomer. We used this variant for extensive aggregation studies as described in chapter 1 of this thesis with good results and no hints of artifacts regarding aggregate stability or aggregation efficiency, in line with what Jovin *et. al.* reported [443]. Unless indicated otherwise, 2 μM αS (concentration given in mass) and a chaperone mixture containing 2 μM Hsc70, 1 μM DnaJB1 and 0.2 μM Apg2 (Hsc70:αS ratio 1:1, chaperone ratio Hsc70:DnaJB1:Apg2 1:0.5:0.1) in disaggregation buffer (see methods for more information) with 2 mM ATP and ATP-regeneration system (8 mM PEP, 20 ng/μL pyruvate kinase) were used for disaggregation assays.

As an unspecific binding control we mixed monomeric αS (100 % pyr-labelled) and the chaperone mixture and observed no change in the spectrum (**Fig. 4.2A** left panel), which showed the typical properties of monomeric pyrene. In particular, we observed no excimer formation (I_{470} nm) and a dominant vibrational peak at 375 nm (Band I or I_I) over the 385 nm peak (Band III or III_I), indicating the pyrene molecules were exposed to the solvent and thus in a polar environment. Then, we prepared αS (100 % pyr-labelled) fibrils (F) in an air/water interface with agitation as described by our group and others [506, 533] and sonicated them to generate a more homogeneous sample (SF1) in terms of size and morphology [533, 563]. When we incubated SF1 with the chaperone mixture over 18 h (**Fig. 4.2A** right panel), we performed an end-point spectral measurement and observed that the excimer peak that is present in the control (without chaperones) mostly disappeared as a consequence of the disaggregase activity. Then, we aimed at reducing the fraction of pyr-labelled αS in the assays. Although unlikely, possible artifacts could exist considering the rather hydrophobic nature of the probe. When we performed a time-course experiment with Hsc70:αS ratio of 1:1, we observed a small difference in the kinetic profile (**Fig. 4.2B**), where the soluble fraction of αS decayed faster when 100 % pyrene was used compared to 20 % pyrene. Also, the 100 %-pyr decay showed some non-ideal behavior visible as a bump along its exponential part. This could indicate that an excess of pyrene molecules within the assemblies could slightly destabilize them or artificially enhance the chaperone binding or disaggregase activity. Therefore, we established 20 % pyr85-αS as a reasonable compromise hereon between low pyrene concentration and good contrast, while obtaining good quality disaggregation curves. Adding no chaperones to the reaction resulted in no disaggregation as expected, confirming the fibrils did not spontaneously dissociate over our experimental observation time. Also, the spectra did not change around the polarity-reporting bands I and III upon chaperone binding, indicating that the interaction of the disaggregase with the fibrils alone is not responsible for any of the changes observed upon the reaction.
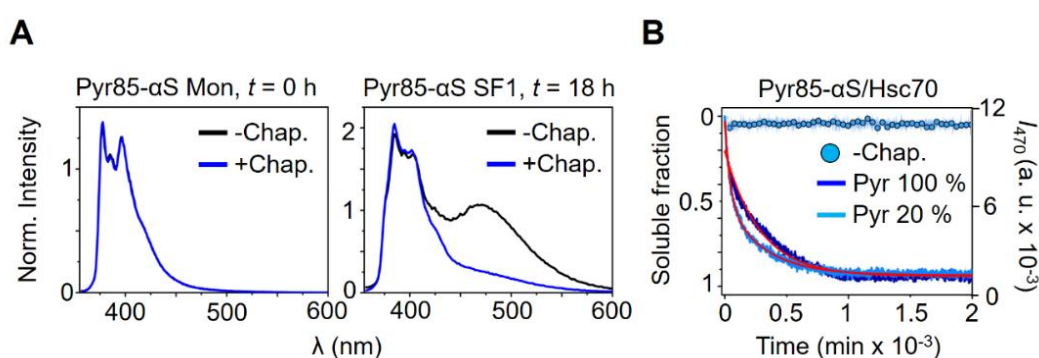
Fig. 4.2. Pyrene spectroscopy monitors the dissagregation of αS amyloid fibrils by the Hsc70 machinery. A) Pyrene spectra of 2 μM Pyr85-αS (100 % labelled) monomer (left) or sonicated fibrils (SF1, right) in the presence (blue) or absence (black) of chaperones (2 μM Hsc70) in disaggregation buffer (pH 7.4). The left and right panel show the spectra at initial times and after 18 h, respectively. Spectra are normalized to I_{375}. **B**) Time-course of the disaggregation of 2 μM SF1 by the chaperone mixture (2 μM Hsc70) for fibrils containing 20 % (cyan) or 100 % (dark blue) Pyr85-αS. The negative control of 20 % Pyr85-αS SF1 without chaperones is shown

as cyan circles. The pyrene excimer (I_{470}) intensity was monitored. The curves in the presence of chaperones are normalized from 0 to 1, being 1 the maximum soluble fraction. This normalization was guided by fluorescent PAGE assays by Dr. Aitor Franco (not shown). The blue-shaded bands around the data represent the standard deviation from a triplicate experiment. Red lines show fits to data.

Next, we decided to test whether pyrene fluorescence was able to follow differences in the disaggregation kinetics of SF1 as a function of the Hsc70:αS ratio, which would in turn yield relevant information into the molecular mechanism of the disaggregase machinery. For this, we performed homologous experiments as those described in the paragraphs above but varying Hsc70:αS ratio (**Fig. 4.3**), always keeping the ratio between the chaperones and co-chaperones the same, as described earlier. We acquired time-course data as well as time-point fluorescent spectra at 3 h and 18 h (**Fig. 4.3** left and center graphs), without chaperones, as a control, and at Hsc70:αS molar ratios of 0.2, 0.5, 1, 2.5 and 5. The comparison between pyrene spectra at the different ratios tested at 3 h and at 18 h, as compared to the control (without chaperones), clearly show that at 3h most of the sonicated fibrils were already solubilized into monomers. When looking into the kinetic traces of fibril disaggregation as a function of Hsc70:αS ratio, a clear dependency both in terms of fluorescence intensity change (amplitude) and speed of the decay (rate) was observed.

After having established the fundamental methodology for assessing the disaggregase activity on sonicated canonical fibrils, we wondered whether the same experimental approach could be applied to novel amyloid polymorphs of αS. In particular, we decided to put to the test the potential of pyrene fluorescence to distinguish the aggregation efficiency and kinetics of the human disaggregase on parallel β-sheet amyloids formed in 10 MeOH % (M10) and 2 M NaCl (N2) under quiescent conditions. These exhibit different sizes, morphologies and β-sheet content than the typical fibrils generated under strong shaking conditions, building from the results we described in chapter 1 of this thesis. We hypothesized chaperones should be able to disaggregate these assemblies too, considering they share the key amyloid features with the canonical fibrils, but perhaps at different rates or yields, being able to discriminate distinct types of structural arrangements between αS amyloid polymorphs. For more details on the preparation of the polymorphs, *see* the materials & methods section.

When we mixed SF1, M10 and N2 aggregates with the chaperone mixture (Hsc70 1:1 αS) we observed the disaggregase was able to work on all three different assemblies with very similar efficacy (**Fig. 4.4**), reaching identical end-point I_{470} values. No disaggregation occurred in the absence of chaperones, confirming the intrinsic stability of all aggregates over time. However, the kinetics of disaggregation differed dramatically from SF1 to the other two polymorphs, where the former follow the expected single-exponential behavior and the latter share an irregular, non-ideal exponential shape and exhibit clearly slower rates. Interestingly, this difference could be explained considering the morphology of the aggregates: while the sonicated fibrils are elongated as it has been characterized by our group and others with high structural resolution [506, 533], M10

and N2 polymorphs show a rather globular shape, especially MeOH-induced aggregates (see chapter 1 of our thesis and our publication in Chemical Science [506].
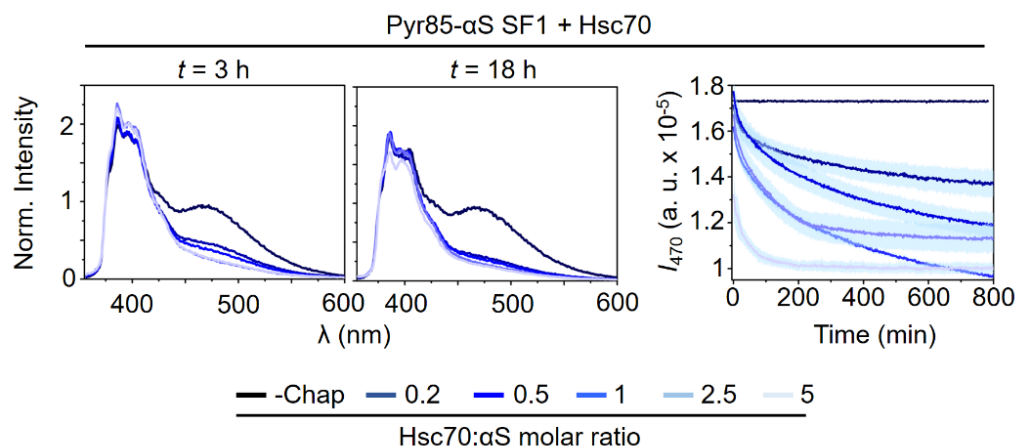
Fig. 4.3. Effect of the Hsc70:αS ratio in amyloid fibrils disaggregation observed by steady-state and real-time pyrene spectroscopy. Pyrene spectra of 2 μM αS (20 % Pyr85-αS) sonicated fibrils (SF1) in the presence of increasing Hsc70:αS ratios after 3 h (left) and 18 h (center). The molar ratio is represented as a color-scale as indicated in the figure legend. Spectra are normalized to I_{375}. The right panel shows the disaggregation time-course of the conditions in the left and center panels. The pyrene excimer (I_{470}) intensity was monitored. The blue-shaded bands around the data represent the standard deviation from a triplicate experiment.

Our data suggest that the disaggregase machinery has evolved to process long-shaped amyloid structures more efficiently even if, eventually, can also solubilize non-fibrillar assemblies. One reason behind the slower kinetics seen for M10 and N2 could be that, given their apparent globular arrangement, more interactions could be found between adjacent protomers as compared with SF1, where each protomer only interacts with two neighbors. We address this topology questions and the possible role of lateral associations within amyloid structures later in this chapter. In terms of β-sheet structure, it may be worth mentioning that SF have around 54 % β-content as seen by IR [506], which is about 10 % richer than M10 (roughly 41 %) and N2 (roughly 43 %) (data obtained by Dr. José D. Camino from our group). Still, the difference between M10 and N2 in curve shape and apparent speed cannot be explained by such β-sheet difference, which is within experimental error. Therefore, the impact of the secondary structure and overall morphology of αS polymorphs on the disaggregase activity required further research. The M10 and N2 polymorphs find their antiparallel counterparts in M35 and N3.5 aggregates (**see** chapter 1 of this thesis), *i. e.*, the amyloid aggregates obtained by aggregating monomeric αS in the presence of 35 % MeOH and 3.5 M NaCl, respectively. However, as we pointed out earlier, the lack of excimer formation in these structures prevents pyrene fluorescence to address their disaggregation by the Hsc70 machinery.

Overall, these preliminary data confirmed the ability of pyrene fluorescence spectroscopy to monitor the Hsc70 machinery disaggregation of αS parallel β-sheet aggregates by end-point and kinetic analysis. As outlook, we believe it would be

interesting to establish a relationship between the structural features of these parallel and antiparallel β-sheet polymorphs, their potential cellular toxicity and the ability of the human disaggregase system to break them apart into monomeric αS. Further studies will be required in order to do this but, from our viewpoint, they would widen the understanding of structure-toxicity relationship in the amyloid field as well as add new detail to the exact way in which the Hsc70 chaperone machinery remodels distinct amyloid assemblies.
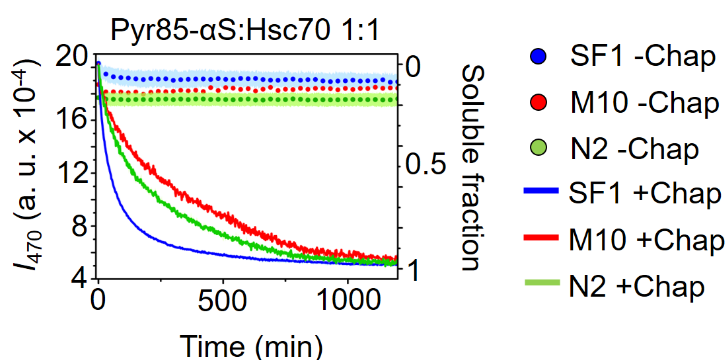
Fig. 4.4. Disaggregation kinetics of distinct αS amyloid assemblies by the Hsc70 machinery analyzed by real-time pyrene fluorescence spectroscopy. Disaggregation time-course of 2 μM (20 % Pyr85-αS) sonicated fibrils (SF1) and aggregates formed in the presence of 10 % MeOH and 2 M NaCl are shown in blue, red and green solid lines, respectively. Control experiments in the absence of chaperones are shown as circles. The pyrene excimer (I_{470}) intensity was monitored. The curves in the presence of chaperones are normalized from 0 to 1, being 1 the maximum soluble fraction. This normalization was guided by fluorescent PAGE assays by Dr. Aitor Franco (not shown). The blue, red and green-shaded bands around the data represent the standard deviation from a triplicate experiment.

Next, we wanted to compare the disaggregase behavior on sonicated fibrils with large, unsonicated and, most critically, cytotoxic αS oligomers. For this, we took advantage of protocols established by our group previously [533] which allow to produce and isolate a pure protein sample consisting what are termed as type B* oligomers (OB). These are small, globular-like, amyloid structures which recapitulate the properties of the transient oligomers generated along the pathway of amyloid fibril formation [20, 533, 536], and thus capable of inducing membrane disruption, calcium leakage, ROS production and, ultimately, cell death [531, 538, 564]. Owing to these, they have become a key species to study αS amyloid-induced neurodegeneration and are currently widely used *in vitro* [536, 565] and *in vivo* [531, 563] where they typically show the highest levels of cell damage, followed by the sonicated fibrils (SF1). Type B* oligomers exhibit an antiparallel intermolecular β-sheet topology and are, therefore, not amenable by pyrene fluorescence nor conventional ThT fluorescence. To the end of circumventing this issue we took advantage of fluorescence dequenching using AF488-labelled αS (AF488-Deq). The fluorescent probe was covalently linked to the protein by site-directed maleimide chemistry (see methods and other chapters of this thesis for more information).

Essentially, for monomeric αS, AF488 finds itself in a freely rotating, sterically undisturbed environment and its fluorescence quantum yield and, in general, fluorescence emission, is maximum. However, in amyloid aggregates, the tight molecular packing between protomers induces a dramatic reduction of the probe's accessible configurational space, thereby quenching its fluorescence emission greatly [503, 566]. We chose a variant of αS labelled with AF488 in its N-terminus, particularly at position 24 (AF488-24-αS), owing to its large monomer-aggregate dequenching contrast. This region is not part of the amyloid core and it has been used by us and others successfully using multiple techniques [292, 567]. Besides, we tested disaggregation with an αS variant labelled with AF488 at the C-terminus (AF488-122-αS) with similar results, suggesting that this degree of labelling with this specific probe had little or no effect on the disaggregation by the Hsc70 machinery. We hypothesized that we could use this property to study the solubilization of αS aggregates into monomers, by monitoring the dequenching of AF488 as a function of time.
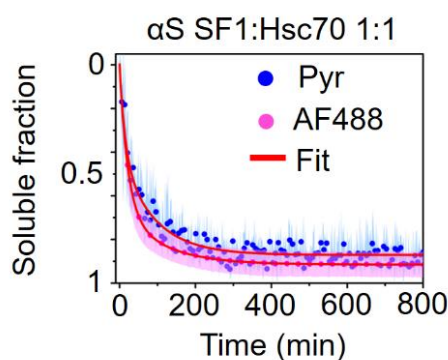
Fig. 4.5. Comparison between pyrene fluorescence and AF488-dequenching for monitoring disaggregation of αS fibrils by the Hsc70 machinery. Disaggregation time-course of 2 μM (20 % Pyr85-αS in blue or ~ 20 % AF488-24-αS in pink) sonicated fibrils (SF1) by the chaperone mixture (2 μM Hsc70). The pyrene excimer intensity (I_{470}) or the fluorescence intensity at 520 nm for AF488 were monitored. The curves are normalized from 0 to 1, being 1 the maximum soluble fraction. This normalization was guided by fluorescent PAGE assays by Dr. Aitor Franco (not shown). The blue and pink-shaded bands around the data represent the standard deviation from a triplicate experiment. Red lines show fits to data.

Indeed, when we mixed sonicated fibrils (~ 20 % AF488) with the chaperone system (Hsc70 1:1 αS) using the same conditions as described above and followed the fluorescence of AF488 in a time-course experiment, we obtained an exponential increase of fluorescence (not shown) that we represented as soluble fraction over time (**Fig. 4.5**). The data obtained were fitted using the aggregated mass decay expression (**see** methods and **Eq. 4.1** of this chapter), and the model described the data with exquisite accuracy. The disaggregation rates obtained are 0.039 and 0.038 min^{-1} for pyrene- and AF488-labeled fibrils, respectively (**Table 4.1**). These values are virtually identical and endorse the application of AF488-Deq as a means to quantitatively characterize the disaggregation mechanism of the Hsc70 machinery. Importantly, given that AF488-Deq does not depend on the relative orientation of the protomers within the amyloid

structures, it could be used to tackle disaggregation on antiparallel β-sheets species such as Type B* oligomers.

	r_{max} (min^{-1})	$f_{soluble}$
Pyr-Ex	0.039	0.86
AF488-Deq	0.038	0.90

Table 4.1. Disaggregation parameters obtained by pyrene fluorescence and AF488-dequenching for disaggregation of αS fibrils by the Hsc70 machinery. The saturation rate (K_{max}) and the soluble fraction ($f_{soluble}$) at the end of the disaggregation reaction are shown for the data in **Fig. 4.5**.

2. Detailed molecular mechanism for the all-or-none unzipping and solubilization of amyloid αS fibrils and cytotoxic oligomers: exploiting fluorescence dequenching

After having set up AF488-Deq as a strategy for monitoring disaggregation of an amyloid structure in real-time, we set out to apply the technique to better understanding the molecular mechanism of the human disaggregase over αS assemblies. As introduced before, our aim was to compare the degree and speed of processing from amyloid structures to monomer and, potentially, to establish a structure-toxicity-disaggregation relationship for large unsonicated (F) vs sonicated fibrils (SF) and cytotoxic type B* oligomers (OB). This work was part of a collaboration with Prof. Arturo Muga's lab and the results obtained have been published in PNAS [568], and the AF488-Deq approach has contributed to other publications [569] by Arturo Muga's lab.

Figure 4.6 shows a summary of the biochemical, biophysical and kinetic characterization of the disaggregation process performed by our collaborators. They used the same conditions we described before for the pyrene fluorescence and AF488-Deq experiments. Sedimentation and SDS-PAGE (**Figure 4.6A, B**) were used to quantify preliminarily the solubilization efficiency and revealed that sonication is key for increasing the ability of the chaperones to process the aggregates. These results are reminiscent of those we described when comparing the disaggregation of SF1 and the M10 and N2 polymorphs. Here, a very low soluble fraction is found for the F1 sample, where multiple fibrils are commonly found as clumps and lateral associations can significantly increase the overall aggregate stability [570, 571]. Besides, it would be reasonable to argue that the mesh-like network formed between fibrils in these clumps would hinder the binding of chaperones required for to the disaggregase activity. Furthermore, shorter fibrils would have a greatly increased number of chaperone-accessible ends (fibril tips), which could also increase the disaggregation efficiency compared to unsonicated fibrils. The effect of aggregate size and heterogeneity is shown in **Figure 4.6C**, where an MTS assay showed that cell death increased vastly upon fibril sonication and that the small fibrils remaining in the supernatant after aggregate centrifugation were more toxic than the larger ones deposited in the pellet. Importantly, type B* oligomers revealed themselves as the most cytotoxic amyloid species, in agreement with what we explained above.

With this, it was clear to us that probing the Hsc70 machinery of OB was essential to gain a more realistic and physiologically relevant picture of the disaggregation process and its implications in nature. Interestingly, these and other data from our article demonstrates that, during the disaggregation process, only monomeric αS, and no oligomeric species is released. This is key provided that the current view of the conformational landscape of the protein and the associated toxicity of each species proposes the type B* oligomers as the main neurotoxic agent. In contrast to what has been suggested before [572], we show that Hsc70-mediated clearance of fibrils has no expectable side effects regarding toxic oligomer release. In fact, our collaborators have observed that incubating SF1 and OB with the chaperone mixture before exposing the cells to these amyloid species greatly prevented cell death (unpublished data).
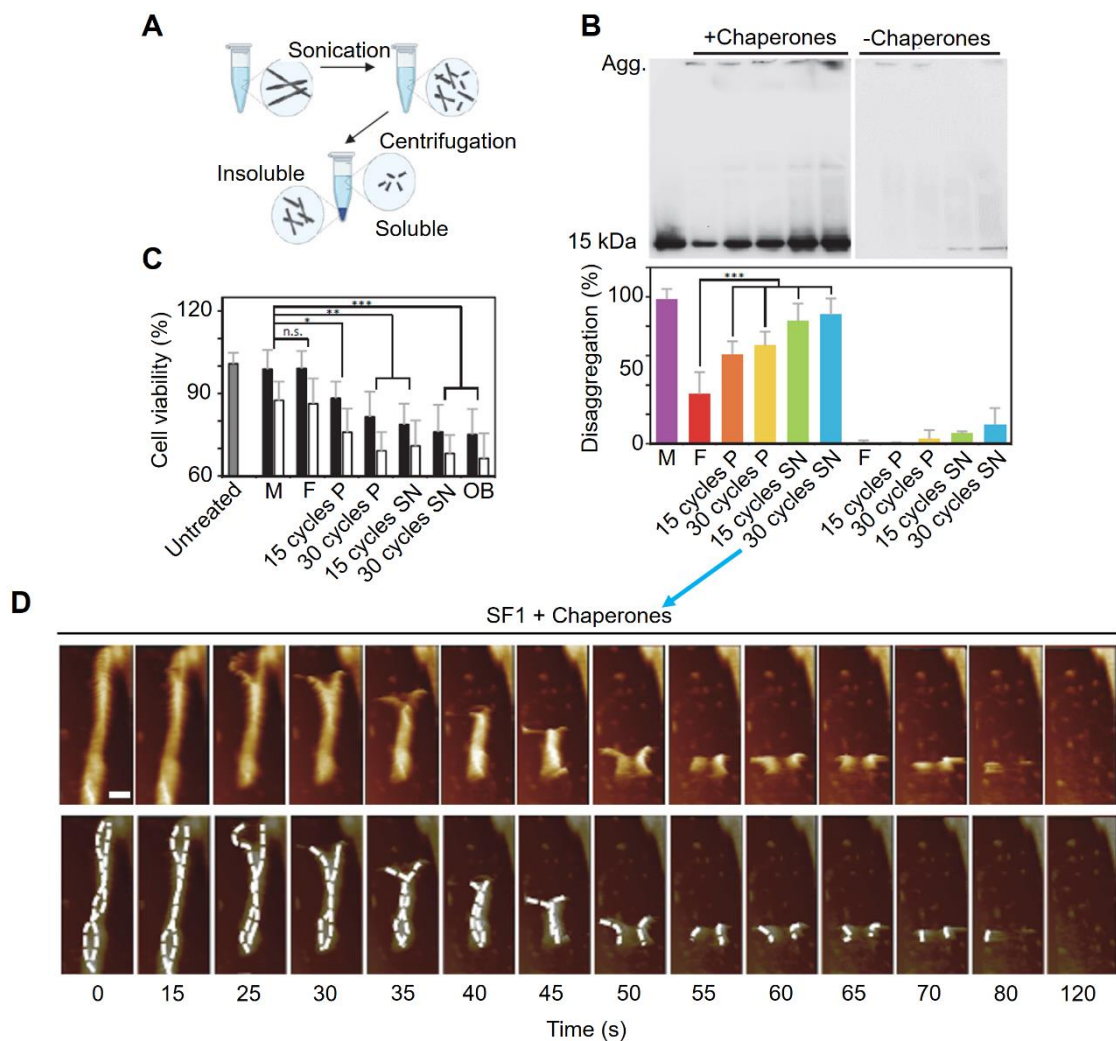
Fig. 4.6. Biochemical and mechanistic characterization of the molecular mechanism of the human disaggregase over αS amyloid aggregates. A) Schematic representation of the procedure used to obtain fibril populations of different sizes. Fibrils were either not sonicated (unsonicated) or sonicated using 15 or 30 cycles (1s ON; 1s OFF). After sonication, samples were centrifuged at 16,000 g for 30 min to separate the soluble (SN) and insoluble (P) fractions. **B)** 2 μM of α-syn fibrils of different lengths were incubated with 10 μM Hsc70, 5 μM DnaJB1 and 1 μM Apg2 in the presence of ATP and an ATP-regeneration system. Disaggregation

reactions after 2 h incubation at 30 °C were analyzed by Native-PAGE and immunoblotting. The same concentration of monomeric and fibril samples in the absence of chaperones were used as controls. Disaggregation (%) was calculated as the amount of monomeric αS relative to the monomer. Data are shown as mean ± SD of n = 4 independent experiments. **C)** Cell toxicity of different αS aggregates. Each aggregation state (0.3 or 0.6 µM αS) was added to SH-SY5Y cells and after 24 h incubation cell viability was measured monitoring mitochondrial activity by the reduction of MTS. Control cells in the absence of αS (untreated) are shown in grey. M and OB stand for monomeric αS and type B* oligomers, respectively. Error bars, SD ($n = 5$) (n.s.: not significant; * P < 0.05; ** P < 0.01; *** P < 0.001). **D)** High-speed AFM movie frames of the chaperone-mediated disaggregation of αS sonicated fibrils (SF1) immediately after addition –time 0- of chaperones, ATP and an ATP-regeneration system to the chamber. The time-resolved disassembly of an individual fibril is shown. White dashed lines follow each individual protofilament during unzipping for visual aid. Data adapted with permission of Dr. Aitor Franco.

Our collaborators performed cutting-edge high-speed AFM to further characterize the disaggregation of SF1 in real time with nanometer resolution (**Figure 4.6D**). Strikingly, this revealed a fibril dissolution process that started from the tips of one fibril and proceeded straight to the further end, creating a so-called "ram's horns" motif along the depolymerization axis. This was the first time, to our knowledge, that αS disaggregation was visualized in this level of detail (see [568] for more details and AFM videos). The images unambiguously showed an all-or-none depolymerization mechanism, where one fibril could remain whole for a long period of time but come apart very quickly in a burst behavior. This implies that the minutes-to-hours kinetic curves typically obtained in this experimental conditions actually do not arise from a very slow but synchronized processing of the amyloid fibrils. Instead, it suggests that each fibril can be depolymerized independently and in a sudden manner, with the aggregated form having a long dwell-time.
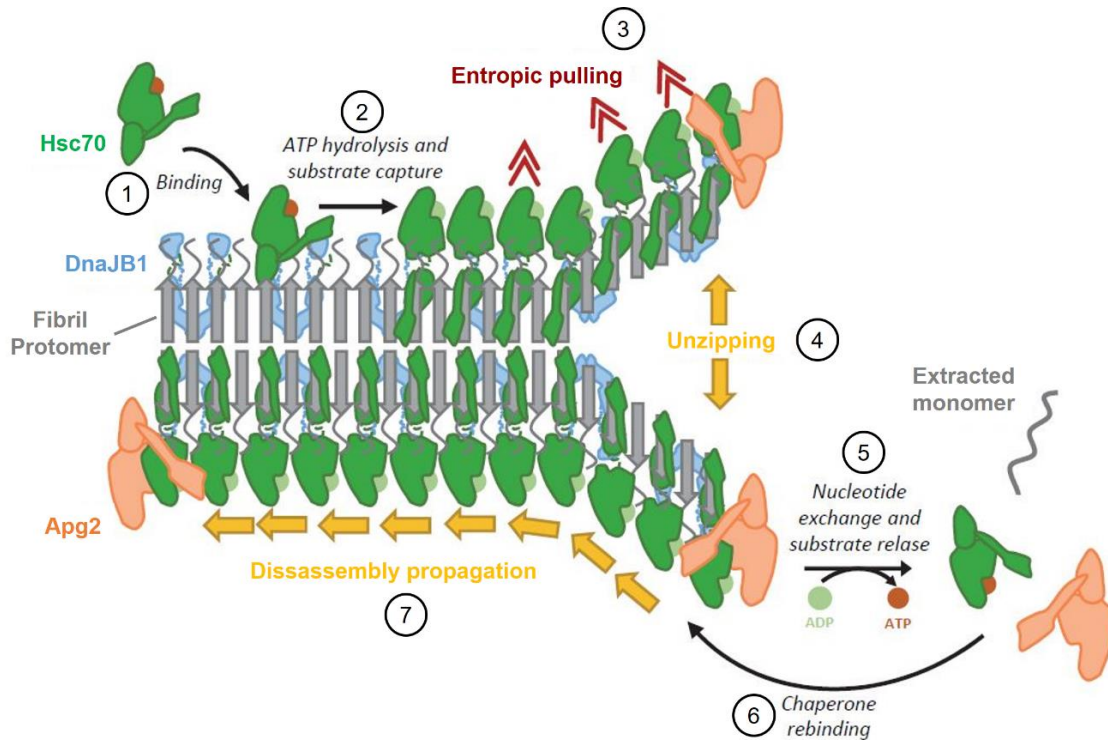
Fig. 4.7. Model proposed for the disassembly of αS fibrils by the human disaggregase. DnaJB1 recruits Hsc70 to the fibril surface, where it can reach a binding stoichiometry of 1:0.5 (α-syn:Hsc70). The high Hsc70 density on the fibril surface induces an exclusion volume effect on Apg2, a necessary factor for fibril disassembly, which is displaced to the fibril ends to interact with the chaperone. Destabilization of the tips as a consequence of the joint chaperone action is followed by fast protofilament unzipping and monomer extraction, which could be facilitated by the entropic pulling forces generated by Hsc70 crowding that facilitate complete disaggregation. Illustration adapted with permission of Dr. Aitor Franco.

These observations led to the model which is shown in **Figure 4.7**. The DnaJB1-induced increase in the affinity of Hsc70 for the amyloid substrate provides the energy required to load the chaperone in this dense arrangement [242]. Crowding of Hsc70 at the fibril surface provokes steric clashes between neighboring Hsc70 molecules, an energetically unfavorable situation that exerts entropic pulling forces on Hsc70-bound αS molecules [242]. Furthermore, the high molecular mass of Apg2 could impede the shuffling of crowded Hsc70 molecules, biasing NEF activity to those chaperone molecules that are not densely packed on the fibrils [242]. Therefore, we rationalize that Apg2 preferentially interacts with the fibril ends or nearby regions, where the excluded volume effect of Hsc70 molecules is the lowest, explaining why fibril unzipping and depolymerization starts at this location. Depolymerization starts by fibril unzipping at the fibril tips and propagates fast through the fibril axis. This could be due to the unfavorable dense packing of Hsc70 molecules along the protofilaments, which would destabilize them exerting the pulling force required to extract monomers as Hsc70 molecules become accessible to Apg2 due to progressive depolymerization. The "ram´s horns" motif observed during depolymerization suggests unzipping of the twisted filaments that form the fibril, which could be necessary for monomer extraction. We believe this model

sheds light onto the ongoing debate in the field and offers an unprecedented direct and detailed observation of the human disaggregase orchestra at work.

To the end of finding out possible differences between large, clumped fibrils, sonicated short fibrils and type B* oligomers in terms of disaggregation, we performed analogous AF488-Deq experiments with the chaperone mixture as described earlier. While maintaining the chaperone mixture ratio and the mass concentration of αS at 2 µM, we titrated the Hsc70:αS ratio from 0 to 5 (**Fig 4.8**). While F1 were solubilized only to a small extent (**Fig 4.8A**), SF1 were processed in a much more efficient way, and almost all the protein mass turned into monomer after 13h (**Fig 4.8B**).
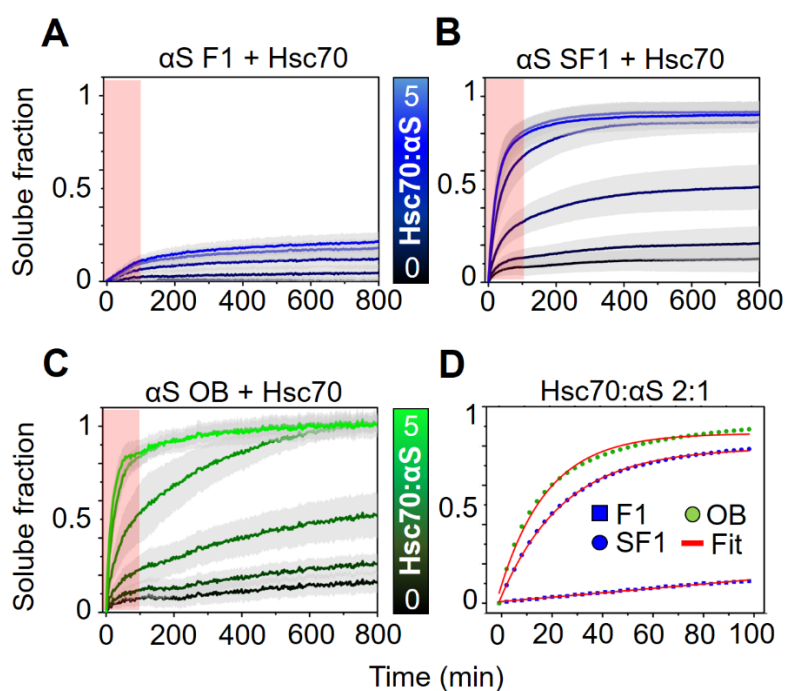
Fig. 4.8. Disaggregation kinetics of αS aggregates monitored by AF488-Deq. Unsonicated αS fibrils (F1, **A**), sonicated fibrils (SF1, **B**) and type B* oligomers (OB, **C**) labeled with AlexaFluor488 (~ 20 % AF488-24-αS) were disaggregated at αS mass concentration of 2 µM with different chaperone concentrations with a molar ratio of Hsc70:DnaJB1:Apg2 constant at 1:0.5:0.1. Disaggregation was followed as a fluorescence dequenching process. The grey-shaded bands correspond to the standard deviation of several independent replicate experiments ($5 < n < 10$). **D**) The first 100 minutes (red-shaded boxes) from the aggregated mass time courses in **A-C** were fitted (red line) to the aggregated mass decay expression (**Eq. 1**).

This is in full agreement with the biochemical data presented above and the dequenching curves totally overlapped with what Dr. Franco observed by fluorescence SDS-PAGE gel analysis [568], further validating our experimental approach. Remarkably, type B* oligomers were disaggregated even slightly more efficiently than SF1 (**Fig 4.8C**), suggesting that the aggregate size and morphology might not be exactly the key feature governing disaggregation but, instead, chaperones have evolved to attack specifically those species that are cytotoxic. It must be mentioned that our data, together with the fluorescence SDS-PAGE gel analysis performed by Dr. Franco, showed

that, as it was the case for SF1, monomeric αS was the only product of the disaggregation reaction. Again, this points towards am evolutionarily refined chaperone action which yields only benign, physiological protein without the side effect of producing even smaller and more toxic oligomers though incomplete aggregate breakage. The good quality and reproducibility of the data, especially compared to pyrene and ThT fluorescence, allowed to fit the kinetic curves with the aggregated mass decay expression (see **Eq.** 4.1 in the methods section) to obtain saturation rates (r_{max}), apparent dissociation constants (K_D) and the cooperativity (n) of the chaperone/αS complex (**Fig 4.9** and **Table 4.2**). This emphasizes the relevance of AF488-Deq to obtain detailed information from the disaggregation reaction.
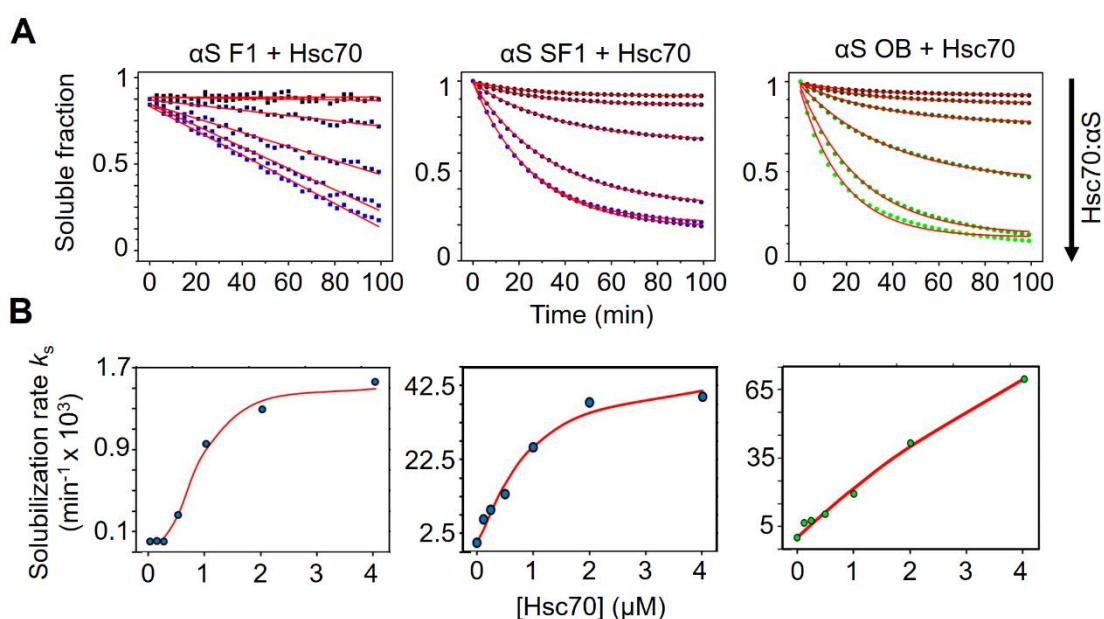
Fig. 4.9. Modelling the kinetics of αS aggregates monitored by AF488-Deq. A) The first 100 minutes from the aggregated mass time courses of F1, SF1 and OB shown in **Fig. 4.7 A-C** were fitted (red lines) to the aggregated mass decay expression (**Eq. 1**). **B**) The average disaggregation rates (circles) for F1, SF1 and OB at each chaperone concentration were calculated from the inferred dynamic parameters and the results fitted (red lines) to a concentration dependent rate (**Eq. 2**). Modelling adapted with permission of Dr. Aitor Franco.

The model accurately described the time-dependent loss of aggregated αS at increasing chaperone concentrations (**Fig 4.9A**). The disaggregation rate of both types of fibrillary samples reached saturation at about equimolar αS:Hsc70 concentrations, while it showed an almost linear dependence within the same chaperone concentration range for oligomers (**Fig 4.9B** and **Table 4.2**). This difference could be explained considering the lower affinity of chaperones for oligomers as compared with fibrils. Whereas the K_D values obtained for unsonicated and sonicated fibrils were identical (0.86 and 0.84 μM, respectively), the K_D estimated for oligomers was 65.22 μM. The values of r_{max} inferred through the model showed that a major effect of fibril sonication is to induce a remarkable 30-fold increase in the maximum disaggregation rate. It is important to note

that in the case of the oligomers, the disaggregation rate does not show any clear indication of saturation in the range of chaperone concentrations analyzed.

	r_{max} (min^{-1})	K_D (µM)	n
Fibrils (F)	0.0015	0.86	2.75
Sonicated fibrils (SF1)	0.047	0.84	1.29
Type B* oligomers (OB)	0.89	65.22	0.88

Table 4.2. Disaggregation parameters obtained by AF488-dequenching for disaggregation of different αS amyloids by the Hsc70 machinery. The saturation rate (r_{max}), the apparent dissociation constant (K_d) and the cooperativity (n) the disaggregation reaction are shown for the data in **Fig. 4.7** and **4.8**.

Namely, the rate is largely proportional to the chaperone concentration with a proportionality coefficient given approximately by r_{max}/K_D. Therefore, only the ratio r_{max}/K_D is identifiable. From our data, it is clear that the apparent dissociation constant K_d is substantially larger than 4 µM and that r_{max} is substantially larger for oligomers than for fibrils but it is not possible to reliably infer their precise individual values. Additionally, the cooperativity parameter n was around 1 for sonicated fibrils and oligomers, indicating that the disaggregation rate is essentially proportional to the binding of chaperones to the aggregate, and slightly lower than 3 for unsonicated fibrils, suggesting that in the latter case chaperone cooperation is needed for disaggregation to occur. The higher number of chaperones required to trigger solubilization at much lower rates with the same affinity for chaperones suggests that although unsonicated fibrils are efficiently targeted by the chaperone system, they could be mechanically more stable than sonicated fibrils or oligomers and therefore it would be more difficult to engage them in a productive disassembly process.

These observations are summarized and rationalized in the diagram shown in **Fig. 4.10**. Elongated fibrils, both large and clumpled, and sonicated, short ones, have a higher affinity for the chaperone machinery. This is due to a fibril surface which is arranged in a manner that is better-suited for the chaperones to land and cluster, whereas type B* oligomers, with a lower content in β-sheet (approximately 35 %), expose a less extended chaperone-accessible surface. It could be that, besides this, the relative parallel orientation of the protomers in the fibrils was preferred for accommodating other partners, in this case chaperones, as it has been proposed for other small molecules [259, 573]. On the other hand, the fact that SF1 and OB are shorter and present an increased number of free ends make these structures far more accessible for the chaperones, especially the NEF Apg2, which have been described by us and others to bind preferentially at the tips of the fibrils, thereby enhancing chaperone clustering and subsequent disaggregase activity. The shorter size of the sonicated fibrils and, especially, the toxic type B* oligomers (around 30-mers according to single-particle fluorescence studies performed by us [174], would decrease the total number of inter-protomer interactions compared to clumpled, large aggregates, thus making the former less stable.

In the case of the oligomers, a hypothetical scenario is that they might spontaneously disassemble below a certain number of protomers, making them particularly unstable. Short fibrils and oligomers, produced in our work by sonication and liophylization, respectively, also occur naturally by fibril fragmentation and other processes [424, 574], making them particularly interesting amyloid assemblies to understand in terms of disaggregation. On the other side, we find unsonicated fibrils, where the lateral associations between different fibrils would boost the stability of the aggregates making them much more resilient to the human disaggregase. Lastly, the overall capacity of the Hsc70 machinery to process and totally disassemble αS amyloid structures seem to correlate with the toxic effect these assemblies have on cells, as we have explained above.

Our data provide molecular insights into the selective processing of toxic amyloids which is critical to identify potential therapeutic targets against increasingly prevalent neurodegenerative disorders. Besides, we strongly believe that AF488-Deq has yielded unprecendeted high quality, reproducible kinetic data on such a complex scenario as amyloid/chaperone interaction and disaggregation. Also, it has enabled us to study the disaggregation of antiparallel β-sheet, highly cytotoxic oligomers, which are not addressable by conventional techniques such as ThT fluorescence. Finally, it has helped in understanding the role of lateral associations between αS fibrils in their overall stability and Hsc70-mediated disassembly [569]. We endorse AF488-Deq as a cost-efficient, straight-forward, plate reader-based assay, which could be applied to any other amyloid disaggregation studies and help unveil key aspects of chaperone molecular mechanism as well as small molecule-based therapies based on amyloid depolymerization.
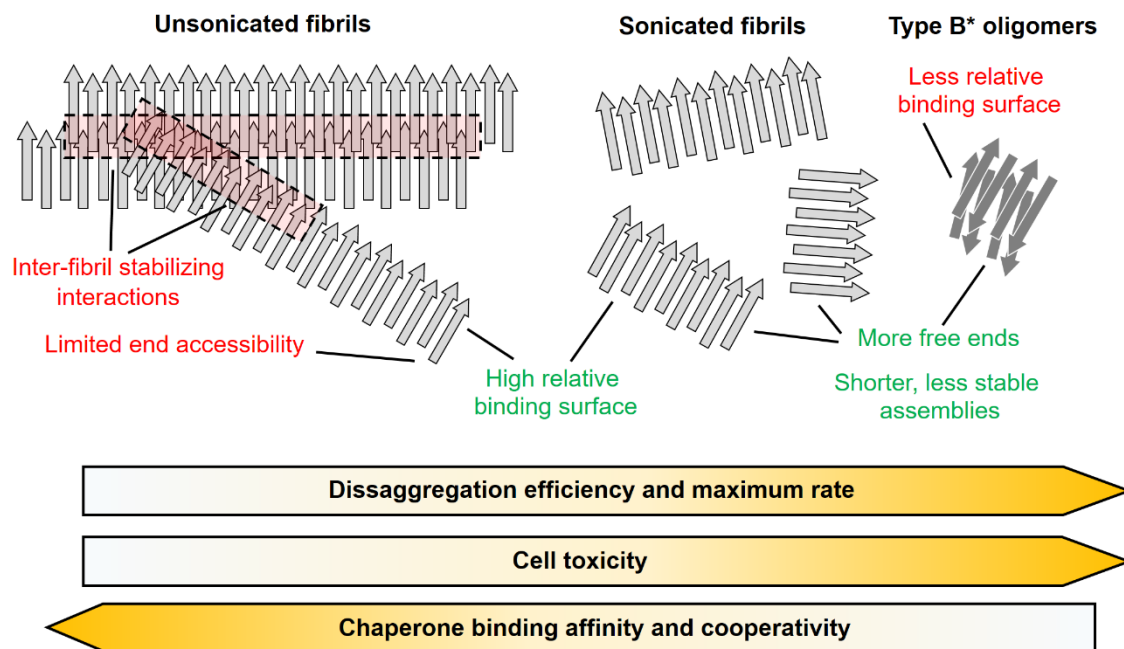
Fig. 4.10. Model proposed for the differential disassembly of αS toxic aggregates by the human disaggregase. Schematic illustrating the different features among αS toxic assemblies and and how these might be linked to the efficiency of the human disaggregase to process them. Unsonicated fibrils show less accessible fibril ends as well as an increased stability owing to the inter-fibril lateral associations which, in turn, might hinder the disaggregase activity despite showing a high affinity likely arising from the large relative binding surface. The more toxic short fibrils and oligomers have a higher number of accessible fibril ends and are intrinsically less stable, making the depolymerization process more favorable. However, while fibrils maintain a well-defined, largely accessible surface, small, non-fibrillar oligomers present a less-optimal binding structure, reducing the affinity of the human disaggregase for this species. All in all, our model propounds that the human disaggregase machinery has indeed evolved to target and disassemble more efficiently those αS aggregates that are more heavily involved in neurodegeneration, be it by inducing neural damage or by causing the spread of the disease.

Materials & methods

Protein overexpression and purification. Chaperones were produced as previously reported ([238]. αS was cloned in a pT7-7 vector and expressed in *E. coli* BL21 (DE3) cells. αS was purified from the periplasm by performing an osmotic shock followed by an anion exchange chromatography as described previously (Protein Expr. Purif. 42, 173–177 (2005)). The cysteine-containing αS mutants were expressed and purified as the WT protein but including 2 mM DTT in all purification steps. Chaperones were produced by Aitor Franco.

Labeling of proteins. Alexa Fluor488-24-αS (AF488-24-αS), pyrene-24-αS and pyrene-85-αS (Pyr-24-αS, Pyr-85-αS) were obtained following the protocol previously described [292] to label cysteine-containing variants with maleimide-derivatized fluorophores (see methods section in chapter 1 of this thesis for details). Labeling efficiency (85 - 100 %) was estimated spectrophotometrically, using absorption at 494 nm for Alexa Fluor 488 concentration (ε_{494} = 72,000 M^{-1} cm^{-1}), at 344 nm for pyrene (ε_{344} = 22,000 M^{-1} cm^{-1}) and at 280 nm for protein concentration (ε_{280} = 5,960 M^{-1} cm^{-1}), after subtracting the contribution of the absorption of the dye at that wavelength.

αS aggregates preparation. αS type B* oligomers, which have been related to the toxic transient oligomeric species formed during fibril formation, were obtained by lyophilization as previously described [533, 538]. This experimental procedure gave reproducible oligomer populations with size distribution of 10-40 nm. To prepare αS fibrils, a 100 μM protein solution was incubated at 37 °C under orbital agitation (1000 rpm) for 7 days in 50 mM Tris, 100 mM NaCl and 0.05% NaN₃, pH 7.4. Afterwards, fibrils were purified by centrifugation for 30 min at 16,000 g and 4 °C. Pelleted fibrils were resuspended, unless otherwise stated, in Disaggregation Buffer (40 mM HEPES-KaOH pH 7.6, 50 mM KCl, 5 mM MgCl₂ and 2 mM DTT). Aggregates labeled with fluorescent dyes contained 8–20 % labeled αS molecules, a concentration range that did not significantly change the kinetics of the chaperone-mediated disassembly reaction. The final protein concentration (monomer equivalents) was determined by disassembling an aliquot of the preparation into monomers in 4 M GdnHCl and measuring its absorption at 280 nm. Sonicated fibrils were obtained using a Branson 450 Digital Sonifier equipped with a tapered microtip of 3 mm diameter at 10% power. Bursting was carried out in cycles of 1 s on; 1 s off with the sample set on ice-cold water. To obtain αS fibrils of different sizes, soluble and insoluble fractions of samples sonicated for 15 or 30 cycles were separated by centrifugation (30 min at 16,000 g and 4 °C). Pellets were resuspended in Disaggregation Buffer and supernatants were passed through 100 K Amicon® Ultra - 0.5 mL filters to remove any possible monomer released during sonication. This procedure consisted in 7 washing steps (4 min at 10,000 g and 20 °C) with 400 μL of Disaggregation Buffer. For the kinetic analysis, preparation of sonicated fibril samples was done with a total of 90 sonication cycles. This protocol yielded reproducible fibril samples with a size distribution centered at around 90 nm. When labeled fibrils were prepared, a monomeric αS solution that contained 15 - 20 % of AF488-24-αS or Pyr-85-αS, was seeded with 5 % (mol/mol) of preformed sonicated fibrils and incubated at 37 °C under quiescent conditions for 1-4 days. Labeled fibrils were purified as explained above. Labeled type B* oligomers were prepared as unlabeled ones but with 25% of

AF488-24-αS. M10 and N2 aggregates containing 20 % pyrene-24-αS) were prepared as described in the section below and in chapter 1 of this thesis.

αS aggregation kinetics. For M10 and N2 aggregates, 50 μM monomeric Pyr24-αS (~ 100 % pyrene-labelled) was incubated in PBS buffer pH 7.4, 50 μM ThT, 0.01 % azide, in the presence of given concentrations co-solvents or salts at 37 °C until reaction was complete. Non-Binding 96-Well Microplate (μClear®, Black, F-Bottom/Chimney Well) (Greiner bio-one North America Inc., USA) were used and the plates were covered with adhesive foil to prevent evaporation. All buffer samples and additive stock solutions were pre-filtered with 0.22 mm filters and both the multi-well plates and microfluidic devices were thoroughly cleaned before use. Kinetic reads were recorded in a FLUOstar plate reader (BMG Labtech, Germany); excitation at 450 ± 5 nm and emission at 485 ± 5 nm for ThT and excitation at 340 nm and emission at 375 nm (band I), 385 nm (band III) or 470 nm (excimer) for pyrene. For pyrene-labeled αS, aggregation assays were performed in the presence of 200 μM TCEP to prevent disulfide bridge formation between the free cysteines of marginal unlabeled protein during the aggregation.

Steady-state pyrene fluorescence spectroscopy. The emission spectra of the aggregated Pyr-85-αS excited at 343 nm were collected at room temperature in a Cary Eclipse Fluorescence Spectrophotometer (Varian, Palo Alto, California, United States) with slit-widths of 5/5 nm. An averaging time of 100 ms was used. The fluorescence spectra were normalized to the intensity at 375 nm (I_{375}).

Disaggregation kinetics. Disaggregation was carried out in 96-Well Half Area Black plates (Non-binding surface; Corning®) at a final αS concentration of 2 μM. 20 μL of aggregates were mixed with 25 μL of increasing chaperone concentrations. No disaggregation (0 %) and complete (100 %) disaggregation controls were obtained with aggregates alone or monomers in the presence of chaperones, respectively. Before starting the reaction, samples were stabilized for 30 min at 30 °C in the plate reader. The reaction was initiated with the addition of 5 μL of a mixture of ATP and ATP-regeneration system, and afterwards plates were sealed with HD Clear Duct tape and measured. In AF488-Deq experiments, fluorescence readings were collected every 3 min from the top, using excitation and emission filters of 485/20 and 528/20 nm and a gain of 60-75. For pyrene-labeled fibrils (20 % pyr-85-αS), fluorescence was monitored using excitation and emission wavelengths of 337 and 470 nm, respectively, under the same experimental conditions.

Quantitative disaggregation modeling and analysis. To model quantitatively the disaggregation process, we need to restrict the range of potential pathways to solubilization by considering the experimental observations. The most straightforward source of insight is high-speed AFM visualization because it provides a direct picture of how the process progresses over time. Explicitly, it shows that sonicated fibrils do not shorten their length progressively in the time scales of disaggregation. Instead, each fibril remains largely intact until it suddenly disappears. Therefore, the mechanism of disaggregation observed through high-speed AFM visualization of sonicated fibrils is consistent with the results obtained with other methodologies such as AF488-Deq and with the results of AF488-Deq for unsonicated fibrils and type B* oligomers.

Such a major time-scale separation indicates that we cannot use the established continuous disaggregation models [575]. These types of processes, instead, are typically modelled in terms of dwell-time distributions [576, 577]. Here, dwell time refers to the time the fibril survives disaggregation in a meta-stable state. Because there is disaggregation as soon as chaperones are added, we consider that the survival probability P_a of an aggregate a follows an exponential decay $P_a(t) = e^{-k_a t}$ with rate k_a. If all the aggregates were identical, the total aggregated mass over time, $m(t)$, would follow an exponential decay, $m(0)e^{-k_a t}$. However, DLS and EM analyses (not shown) revealed that there is high heterogeneity in aggregate size. At the same time, the extent of disaggregation is higher for smaller fibrils (**Fig 4.6, 4.8 and 4.9**, which indicates that the decay rate depends at least on the size of the aggregate.

Therefore, we need to consider heterogeneity in the individual aggregate mass and decay rate. Explicitly, the expected total aggregated mass as a function of time for an ensemble of aggregates with individual masses, m_a, and rates, k_a, is given by $m(t) = \sum_a m_a P_a(t) = \sum_a m_a e^{-k_a t}$. Taking the time derivative of $m(t)$ results in $\frac{dm(t)}{dt} = \sum_a m_a P_a(t) = -\sum_a k_a m_a e^{-k_a t}$, which can be rewritten in terms of a disaggregation kinetics as $\frac{dm(t)}{dt} = -r(t)m(t)$ with a time-dependent disaggregation rate $r(t) = \frac{\sum_a k_a m_a e^{-k_a t}}{\sum_a m_a e^{-k_a t}}$.

To describe the effects of aggregate heterogeneity, firstly, we consider the sum over the aggregates as an integral so that $\sum_a m_a e^{-k_a t} = m(0) \int f(k_a) e^{-k_a t} dk_a$, where $f(k_a) dk_a$ is the initial mass fraction of aggregates with rates between k_a and $k_a + dk_a$. Secondly, we obtained an estimation of $f(k_a)$ using a gamma distribution as a functional form. This choice is motivated by the proven versatility of the gamma distribution to model distributions of positive quantities [578]. It includes as particular cases the exponential and chi-square distributions, and it can adapt to multiple distribution shapes, including Gaussian distributions centered dominantly around positive values. Explicitly, we consider $f(k_a) = \frac{\beta^\alpha}{\Gamma(\alpha)} k_a^{\alpha-1} e^{-\beta k_a}$, with shape α and rate β parameters.

The characterization in terms of the gamma distribution leads to an overall aggregated mass decay

$$m(t) = \frac{m(0)}{\left(1 + \frac{t}{\beta}\right)^\alpha} \tag{Eq. 4.1}$$

that closely mimics the observed kinetics of disaggregation. Therefore, a major prediction of the model is the lack of a plateau in the dynamics. Instead of reaching a plateau, the disaggregation speed becomes increasingly slow, but noticeable, as time progresses as indicated by the mathematical expression of the disaggregation rate, given explicitly by $r(t) = \frac{\alpha}{\beta}\left(1 + \frac{t}{\beta}\right)^{-1}$. The lack of plateau can, indeed, be observed for all types of aggregates and chaperone concentrations shown in **Fig 4.9**.

To characterize the disaggregation rate under different conditions, we obtained the parameters α and β for each case by fitting the expected dynamics to fluorescence dequenching time courses over the first 100 minutes of the disaggregation process. The

results (**Fig 4.9**) show that the effects of the chaperone concentration $[c]$ on the resulting initial average disaggregation rates can generally by described by a general functional form given by

$$r(0) = r_{max} \frac{([c]/K_\mathrm{D})^n}{1 + ([c]/K_\mathrm{D})^n}, \qquad (\textbf{Eq. 4.2})$$

where n is a cooperativity parameter; K_D is the apparent dissociation constant of the chaperone's binding to the aggregate; and r_max is the saturation rate.

The dissociation constant of Hsc70 for fibrils has been estimated following other approaches [242]. The results of the fitting show that the apparent dissociation constant is the same for both unsonicated and sonicated fibrils and that it is similar with its previously estimated value for Hsc70. Our results also show that the apparent dissociation constant for type B* oligomers is much higher than for fibrils, consistently with fibrils providing better substrate for binding to chaperones than oligomers.

The values obtained for r_max are also consistent with larger aggregates being more stable than smaller ones because the values of r_max increase from unsonicated fibrils, through sonicated fibrils, to type B* oligomers. It is also important to note that, in the case of the oligomers, the disaggregation rate does not show any clear indication of saturation in the range of chaperone concentrations analyzed. Namely, the rate is largely proportional to the chaperone concentration with a proportionality coefficient given approximately by $r_\mathrm{max}/K_\mathrm{D}$. Therefore, only the ratio $r_\mathrm{max}/K_\mathrm{D}$ is identifiable. From the data, it is clear that the apparent dissociation constant K_D is substantially larger than 4 µM and that r_max is substantially larger for oligomers than for fibrils but it is not possible to reliably infer their precise individual values.

The value of n around 1, as observed for sonicated fibrils and type B* oligomers, indicates that the disaggregation rate is essentially proportional to the binding of chaperones to the aggregate. In contrast, a value of n substantially higher than 1, such as n close to 3 as observed for unsonicated fibrils, indicates the presence of cooperative effects. In the case of unsonicated fibrils, cooperativity could arise from chaperones required to both open the tips of the fibrils and weaken the two-strand association in order to trigger the unzipping process. The model was developed by José M.G. Vilar and Leonor Saiz based on the experimental kinetic and mechanistic evidence of disaggregation by HS-AFM and AF488-Deq.

MTS assay. SH-SY5Y cells were seeded at 20.000 cells/well in 96-well plates and incubated overnight in in Dulbecco's modified Eagle's medium (DMEM) low glucose with 1 g/L L-glutamine supplemented with 10% heat-inactivated Fetal Bovine Serum (FBS), penicillin and streptomycin (50 U/mL and 50 µg/mL, respectively) and MycoZap™ Prophylactic (Lonza, 1/1000 dilution). The next day, the medium was replaced by 100 µL of fresh medium containing 0.15 or 0.3 µM of αS and cells were incubated for 24 h. Freshly prepared MTS/PES mixture was directly added (20 µL) to culture wells and incubated for 1-4 hours. Formazan formation was measured by recording the absorbance at 490 nm in a Synergy HTX plate reader (Biotek). Control values of cells without αS and culture medium without cells were taken as 100 % and 0

% cell viability, respectively. These experiments were performed by Aitor Franco and José Ángel Fernández-Higuero.

AFM and HS-AFM images. Bare mica was covered with 100 µL Poly-L-lysine solution (Sigma, P8920) for 5 min for the AFM (JPK, Nanowizard 3 UltraSpeed2) images or 10 µL Poly-L-Ornithine (Sigma, P4957) for the HS-AFM (Bruker, NanoRacer) measurements and rinsed 3 times with Disaggregation Buffer. Fibrils were deposited onto the surface, incubated for 15 min and gently rinsed three times with 500 µL or 10 µL of disaggregation buffer for the AFM or HS-AFM experiments, respectively. Finally, 18k00/800 µL of this buffer were added to the chambers for AFM/HS-AFM experiments and after the identification of interesting spots, 100/50 (AFM/HS-AFM) µL of the chaperone mixture were incorporated into the samples. Finally, a solution containing ATP and ATP-RS was added to the imaging chamber resulting in final sample volumes of 2000 µL and 900 µL. The AFM equipment was operated in QI mode with MSNL-10 cantilevers (Bruker). For fast imaging with HS-AFM, tapping mode and USC-F1.2 (NanoWorld) cantilevers were used. Images and movies were analyzed with JPKSPM Data Processing, ImageJ and WSxM software. These experiments were performed by Adai Colom and Alexander Dulebo.

Statistical analysis. All measurements were done at least three times and levels of significance were determined by a two-tailed Student´s t-test. A value of $P < 0.05$ was considered statistically significant (n.s.: not significant; * $P < 0.05$; ** $P < 0.01$; *** $P < 0.001$). Statistical analyses were performed by Dr. Aitor Franco.

Conclusions

Conclusions

- Pyrene fluorescence spectroscopy was successfully implemented for discerning the intermolecular topology of amyloid aggregates of αS and holds the potential to extend its application to the study of amyloid topology in a general context. Pyrene fluorescence and IR results remarkably overlapped, thus endorsing the combination of both techniques for such studies.

- Limited hydration conditions tune the aggregation energy landscape of αS and leads to homogeneous amyloid nucleation, resulting in the formation of antiparallel β-sheet amyloid polymorphs with distinct structural and thermodynamic properties.

- Homotypic LLPS of αS leads to the formation of poorly hydrated protein condensates where antiparallel amyloid aggregation is favored, possibly through homogeneous nucleation. This suggests that LLPS might indeed be relevant for the *in vivo* aggregation of αS by reducing the hydration shell of the protein and promoting its amyloid aggregation.

- We have established a physiologically relevant model for studying the electrostatic complex coacervation of αS with polycations and provided a quantitative description of the system, including the propensity of the proteins to undergo LLPS, the forces governing the process and the dynamics of αS within the condensates over time. In particular, we have proposed a molecular mechanism by which αS and Tau may potentially undergo amyloid co-aggregation in the cell through LSPT.

- Polypeptide dynamics plays a minor role in determining the time-evolution of αS/polycation coacervates. Instead, the valency occupancy and strength of the interactions between the oppositely charged molecules governs the ageing of the droplets, being strong interactions in simple coacervates (low number of different types of valencies) in favor of droplet gelation while weaker, multi-valent associations promote coalescence, slow ageing and, finally, amyloid aggregation inside the droplets.

- We successfully applied FLIM to tackle the ambiguity of ThT fluorescence when probing amyloid aggregation in LLPS-LSPT systems. By looking at each of the αS and Tau separately, we have been able to observe amyloid-compatible fluorescence lifetime changes that correlate with ThT-positive staining.

- Time-resolved dcFCCS/dcSPFS was successfully implemented to directly access the binding parameters of multi-ligand and multi-receptor systems, concretely the inter-molecular interactions between a small molecule and αS aggregates.

- dcFCCS/dcSPFS is robust and self-validated, offers single-particle resolution, monitors each of the binding partners separately and requires very small amounts of sample, making it a promising experimental approach for disentangling complex molecular interactions.

- The peptidic inhibitor of αS amyloid aggregation PSMα3 is able to selectively bind the toxic assemblies of αS with low nanomolar affinity and lays out generic properties for future rational peptide design: an amphipatic helical scaffold with a both a cationic and a hydrophobic side to target, respectively, the highly negatively charged regions and solvent-exposed hydrophobic patches of αS toxic amyloid structures.

- dcFCCS/dcSPFS has helped validate the rational design of other αS amyloid aggregation inhibitors and find a human peptide with high therapeutic potential.

- Pyrene fluorescence and fluorescence dequenching of AF488 (AF488-Deq) were implemented as alternative methods to study amyloid aggregation and disaggregation, circumventing some of the caveats of ThT-based fluorescence assays.

- AF488-Deq was successfully applied to obtain reliable kinetic data of the disaggregation of αS amyloid fibrils by the human disaggregase, leading to a detailed model for its molecular mechanism. In combination with biophysical and structural studies by our collaborators, we proved an all-or-none disassembly mechamism for the Hsp70 chaperomne system with unprecedented detail.

- AF488-Deq was successfully applied to ascertaining the relationship between cellular toxicity, morphology, structure and size of different relevant αS amyloid aggregates and the efficacy and rate of their disassembly by the human disaggregase.

Conclusiones

Conclusiones

- La espectroscopia de fluorescencia de pireno ha sido implementada con éxito para distinjir la topología intermolecular de agregados amiloides de αS y posee el potencial de ser aplicada al estudio de la topología amiloide en un contexto general. La fluorescencia de pireno y la espectroscopia de IR ofrecen resultados destacablemente semejantes, de manera que proponemos su uso combinado para tales estudios.

- Las condiciones de hidratación limitada modulan el paisaje energético de la agregación amiloide de αS y propician la nucleación amiloide homogénea, la cual da lugar a la formación de polimorfos amiloides con lámina β antiparalela y propiedades termodinámicas y estructurales características.

- La LLPS homotípica de αS resulta en la formación de condensados de proteína con bajo nivel de hidratación donde la agregación amiloide antiparalela se ve favorecida, probablemente a través de nucleación homogénea. Esto sugiere que la LLPS podría ser relevante como escenario de agregación in vivo de αS reduciendo la capa de hidratación de la proteína y, como consecuencia, promoviendo su agregación amiloide.

- Hemos establecido un modelo fisiológicamente relevante para el estudio de la coacervación electrostática compleja de αS con policationes y hemos realizado una descripción cuantitativa del sistema, incluyendo la propensión de las proteínas a sufrir LLPS, las fuerzas que regulan el proceso y la dinámica de αS dentro de los condensados a lo largo del tiempo. Concretamente, hemos propuesto un mecanismo molecular mediante el cual αS y Tau podrían formar co-agregados amiloides en las células por medio de una LSPT.

- La dinámica de las cadenas polipeptídicas juega un papel menor en cuanto a la evolución temporal de los coacervados αS/policatión. Por el contrario, la ocupación de la valencia de las interacciones entre moléculas opuestamente cargadas, así como la fuerza de esas interacciones, determina el comportamiento de maduración de los condensados. En coacervados simples, con un bajo número de diferentes tipos de valencia, las interacciones son fuertes y propician la gelificación de los coacervados mientras que, en asociaciones débiles y multivalentes, la coalescencia entre condensados se ve favorecida, dando lugar a una maduración lenta y, en última instancia, a la agregación amiloide dentro de los coacervados.

- Hemos aplicado FLIM con éxito para abordar la ambigüedad asociada a la fluorescencia de ThT a la hora de estudiar la agregación amiloide en un sistema de LLPS-LSPT. Gracias a la observación por separado de αS y Tau hemos logrado

observar cambios en el tiempo de vida fluorescente compatibles con agregación amiloide y que se correlacionan con una tinción positiva en ThT.

- Hemos implementado la estrategia dcFCCS/dcSPFS resuelta en el tiempo con éxito y obtenido de manera directa los parámetros de unión en sistemas multi-ligando/receptor multimérico, en particular para resolver las interacciones intermoleculares entre pequeñas moléculas y agregados de αS.

- dcFCCS/dcSPFS es una estrategia robusta y se auto valida, proporciona resolución de partícula individual, es capaz de seguir a cada una de las moléculas interactuantes por separado y requiere muy poca cantidad de muestra, haciendo de ella una herramienta experimental prometedora para desentrañar los detalles de interacciones molecular complejas.

- El inhibidor peptídico de la agregación amiloide de αS, PSMα3, es capaz de unirse de manera selectiva a las estructuras tóxicas de αS con afinidad nanomolar y encapsula las propiedades genéricas para el diseño racional futuro de péptidos con actividad semejante: un armazón de hélice anfipática con un lado catiónico y otro hidrofóbico para dirigirse, respectivamente, a las regiones altamente aniónicas y las hidrofóbicas y expuestas al solvente de las estructuras amiloides tóxicas de αS.

- dcFCCS/dcSPFS ha contribuido a la validación del diseño racional de otros inhibidores de la agregación amiloide de αS y a encontrar un péptido humano con elevado potencial terapéutico.

- La fluorescencia de pireno y la desextinción de fluorescencia de AF488 (AF488-Deq) han sido implementados como métodos alternativos para el estudio de la agregación y desagregación amiloide, resolviendo algunas de las carencias de los ensayos basados en fluorescencia de ThT.

- Se ha aplicado AF488-Deq para obtener datos cinéticos fiables de la desagregación de fibras amiloides por parte de la desagregasa humana, propiciando la creación de un modelo detallado de su mecanismo molecular. En combinación con técnicas biofísicas y estructurales empleadas por nuestros colaboradores, hemos demostrado un mecanismo de desensamblado de "todo o nada" del sistema de chaperonas Hsc70 con un nivel de detalle sin precedentes.

- Se ha empleado AF488-Deq con éxito para esclarecer la relación entre toxicidad celular, morfología, estructura y tamaño de diferentes agregados amiloides de αS relevantes y la eficacia y velocidad de su desensamblado por la desagregasa humana.

References

References

1. C. M. Dobson, Protein misfolding, evolution and disease. *Trends Biochem. Sci.* **24**, 329–332 (1999).

2. C. M. Dobson, Protein folding and misfolding. *Nature* **426**, 884–890 (2003).

3. L. Luo, *et al.*, Ten years of Nature Reviews Neuroscience: insights from the highly cited. *Nat. Rev. Neurosci.* **11**, 718–726 (2010).

4. G. G. Glenner, C. W. Wong, Alzheimer's disease: initial report of the purification and characterization of a novel cerebrovascular amyloid protein. *Biochem. Biophys. Res. Commun.* **120**, 885–890 (1984).

5. I. Grundke-Iqbal, *et al.*, Microtubule-associated protein tau. A component of Alzheimer paired helical filaments. *J. Biol. Chem.* **261**, 6084–6089 (1986).

6. M. G. Spillantini, *et al.*, α-Synuclein in Lewy bodies. *Nature* **388**, 839–840 (1997).

7. M. DiFiglia, *et al.*, Aggregation of huntingtin in neuronal intranuclear inclusions and dystrophic neurites in brain. *Science* **277**, 1990–1993 (1997).

8. L. I. Bruijn, *et al.*, Aggregation and motor neuron toxicity of an ALS-linked SOD1 mutant independent from wild-type SOD1. *Science* **281**, 1851–1854 (1998).

9. D. C. Bolton, M. P. McKinley, S. B. Prusiner, Identification of a protein that purifies with the scrapie prion. *Science* **218**, 1309–1311 (1982).

10. M. G. Iadanza, M. P. Jackson, E. W. Hewitt, N. A. Ranson, S. E. Radford, A new era for understanding amyloid structures and disease. *Nat. Rev. Mol. Cell Biol.* **19**, 755–773 (2018).

11. F. Chiti, C. M. Dobson, Protein Misfolding, Amyloid Formation, and Human Disease: A Summary of Progress Over the Last Decade. *Annu. Rev. Biochem.* **86**, 27–68 (2017).

12. Z. L. Almeida, R. M. M. Brito, Structure and Aggregation Mechanisms in Amyloids. *Molecules* **25** (2020).

13. K. Bhasne, S. Sebastian, N. Jain, S. Mukhopadhyay, Synergistic Amyloid Switch Triggered by Early Heterotypic Oligomerization of Intrinsically Disordered α-Synuclein and Tau. *J. Mol. Biol.* **430**, 2508–2520 (2018).

14. J. Luo, S. K. T. S. Wärmländer, A. Gräslund, J. P. Abrahams, Cross-interactions between the Alzheimer Disease Amyloid-β Peptide and Other Amyloid Proteins: A Further Aspect of the Amyloid Cascade Hypothesis. *J. Biol. Chem.* **291**, 16485–16493 (2016).

15. I. Horvath, *et al.*, Co-aggregation of pro-inflammatory S100A9 with α-synuclein in Parkinson's disease: ex vivo and in vitro studies. *J. Neuroinflammation* **15**, 172 (2018).

16. D. Eisenberg, M. Jucker, The amyloid state of proteins in human diseases. *Cell* **148**, 1188–1203 (2012).

17. M. Sunde, *et al.*, Common core structure of amyloid fibrils by synchrotron X-ray diffraction. *J. Mol. Biol.* **273**, 729–739 (1997).

18. A. W. P. Fitzpatrick, *et al.*, Atomic structure and hierarchical assembly of a cross-β amyloid fibril. *Proc. Natl. Acad. Sci. U. S. A.* **110**, 5468–5473 (2013).

19. S. I. A. Cohen, M. Vendruscolo, C. M. Dobson, T. P. J. Knowles, From macroscopic measurements to microscopic mechanisms of protein aggregation. *J. Mol. Biol.* **421**, 160–171 (2012).

20. N. Cremades, *et al.*, Direct Observation of the Interconversion of Normal and Toxic Forms of α-Synuclein. *Cell* **149**, 1048–1059 (2012).

21. T. Knowles, *et al.*, An analytical solution to the kinetics of breakable filament assembly. *Science* **326**, 1533–37 (2009).

22. M. Bucciantini, *et al.*, Inherent toxicity of aggregates implies a common mechanism for protein misfolding diseases. *Nature* **416**, 507–511 (2002).

23. K. C. Luk, *et al.*, Pathological α-synuclein transmission initiates Parkinson-like neurodegeneration in non-transgenic mice. *Science* **338**, 949–953 (2012).

24. L. A. Volpicelli-Daley, *et al.*, Exogenous α-synuclein fibrils induce Lewy body pathology leading to synaptic dysfunction and neuron death. *Neuron* **72**, 57–71 (2011).

25. I. Benilova, E. Karran, B. De Strooper, The toxic Aβ oligomer and Alzheimer's disease: An emperor in need of clothes. *Nat. Neurosci.* **15**, 349–357 (2012).

26. B. Winner, *et al.*, In vivo demonstration that α-synuclein oligomers are toxic. *Proc. Natl. Acad. Sci. U. S. A.* **108**, 4194–4199 (2011).

27. G. B. Irvine, O. M. El-Agnaf, G. M. Shankar, D. M. Walsh, Protein aggregation in the brain: the molecular basis for Alzheimer's and Parkinson's diseases. *Mol. Med.* **14**, 451–464 (2008).

28. E. Deas, *et al.*, A-Synuclein Oligomers Interact with Metal Ions to Induce Oxidative Stress and Neuronal Death in Parkinson's Disease. *Antioxid. Redox Signal.* **24**, 376–391 (2016).

29. M. Stefani, C. M. Dobson, Protein aggregation and aggregate toxicity: new insights into protein folding, misfolding diseases and biological evolution. *J. Mol. Med. (Berl).* **81**, 678–699 (2003).

30. C. A. Ross, C. M. Pickart, The ubiquitin-proteasome pathway in Parkinson's disease and other neurodegenerative diseases. *Trends Cell Biol.* **14**, 703–711 (2004).

31. J. T. Pedersen, *et al.*, Amyloid-β and α-Synuclein Decrease the Level of Metal-Catalyzed Reactive Oxygen Species by Radical Scavenging and Redox Silencing. *J. Am. Chem. Soc.* **138**, 3966–3969 (2016).

32. K. Taguchi, Y. Watanabe, A. Tsujimura, M. Tanaka, Brain region-dependent differential expression of α-synuclein. *J. Comp. Neurol.* **524**, 1236–1258 (2016).

33. T. Bartels, *et al.*, The N-terminus of the intrinsically disordered protein α-synuclein triggers membrane binding and helix folding. *Biophys. J.* **99**, 2116–2124 (2010).

34. E. R. Georgieva, T. F. Ramlall, P. P. Borbat, J. H. Freed, D. Eliezer, Membrane-Bound α-Synuclein Forms an Extended Helix: Long-Distance Pulsed ESR Measurements Using Vesicles, Bicelles, and Rodlike Micelles. *J. Am. Chem. Soc.* **130**, 12856–12857 (2008).

35. J. M. George, H. Jin, W. S. Woods, D. F. Clayton, Characterization of a novel protein regulated during the critical period for song learning in the zebra finch. *Neuron* **15**, 361–372 (1995).

36. K. Uéda, *et al.*, Molecular cloning of cDNA encoding an unrecognized component of amyloid in Alzheimer disease. *Proc. Natl. Acad. Sci. U. S. A.* **90**, 11282–11286 (1993).

37. A. R. Braun, M. M. Lacy, V. C. Ducas, E. Rhoades, J. N. Sachs, α-Synuclein's Uniquely Long Amphipathic Helix Enhances its Membrane Binding and Remodeling Capacity. *J. Membr. Biol.* **250**, 183–193 (2017).

38. T. Viennet, *et al.*, Structural insights from lipid-bilayer nanodiscs link α-Synuclein membrane-binding modes to amyloid fibril formation. *Commun. Biol.* **1**, 44 (2018).

39. L. C. Serpell, J. Berriman, R. Jakes, M. Goedert, R. A. Crowther, Fiber diffraction of synthetic α-synuclein filaments shows amyloid-like cross-beta conformation. *Proc. Natl. Acad. Sci. U. S. A.* **97**, 4897–4902 (2000).

40. D. E. Mor, S. E. Ugras, M. J. Daniels, H. Ischiropoulos, Dynamic structural flexibility of α-synuclein. *Neurobiol. Dis.* **88**, 66–74 (2016).

41. C. A. Waudby, *et al.*, In-Cell NMR Characterization of the Secondary Structure Populations of a Disordered Conformation of α-Synuclein within E. coli Cells. *PLoS One* **8** (2013).

42. B. Fauvet, *et al.*, α-Synuclein in central nervous system and from erythrocytes, mammalian cells, and Escherichia coli exists predominantly as disordered monomer. *J. Biol. Chem.* **287**, 15345–15364 (2012).

43. M. M. Dedmon, K. Lindorff-Larsen, J. Christodoulou, M. Vendruscolo, C. M. Dobson, Mapping long-range interactions in α-synuclein using spin-label NMR and ensemble molecular dynamics simulations. *J. Am. Chem. Soc.* **127**, 476–477 (2005).

44. C. W. Bertoncini, *et al.*, Release of long-range tertiary interactions potentiates aggregation of natively unstructured α-synuclein. *Proc. Natl. Acad. Sci. U. S. A.* **102**, 1430–1435 (2005).

45. H.-J. Lee, S. Patel, S.-J. Lee, Intravesicular localization and exocytosis of α-synuclein and its aggregates. *J. Neurosci.* **25**, 6016–6024 (2005).

46. R. M. Meade, D. P. Fairlie, J. M. Mason, A-synuclein structure and Parkinson's disease - lessons and emerging principles. *Mol. Neurodegener.* **14**, 29 (2019).

47. M. Grazia Spillantini, *et al.*, Filamentous α-synuclein inclusions link multiple system atrophy with Parkinson's disease and dementia with Lewy bodies. *Neurosci. Lett.* **251**, 205–208 (1998).

48. H. McCann, C. H. Stevens, H. Cartwright, G. M. Halliday, α-Synucleinopathy phenotypes. *Parkinsonism Relat. Disord.* **20**, S62–S67 (2014).

49. L. V Kalia, A. E. Lang, Parkinson's disease. *Lancet (London, England)* **386**, 896–912 (2015).

50. F. Chiti, C. M. Dobson, Protein misfolding, functional amyloid, and human disease. *Annu. Rev. Biochem.* **75**, 333–366 (2006).

51. N. Cremades, C. M. Dobson, The contribution of biophysical and structural studies of protein self-assembly to the design of therapeutic strategies for amyloid diseases. *Neurobiol. Dis.* **109**, 178–190 (2018).

52. J. Zhang, X. Li, J.-D. Li, The Roles of Post-translational Modifications on α-Synuclein in the Pathogenesis of Parkinson's Diseases. *Front. Neurosci.* **13**, 381 (2019).

53. M. Kasten, C. Klein, The many faces of α-synuclein mutations. *Mov. Disord.* **28**, 697–701 (2013).

54. D. Hoffman-Zacharska, *et al.*, Novel A18T and pA29S substitutions in α-synuclein may be associated with sporadic Parkinson's disease. *Parkinsonism Relat. Disord.* **19**, 1057–1060 (2013).

55. R. Krüger, *et al.*, Familial parkinsonism with synuclein pathology: clinical and PET studies of A30P mutation carriers. *Neurology* **56**, 1355–1362 (2001).

56. P. Pasanen, *et al.*, Novel α-synuclein mutation A53E associated with atypical

multiple system atrophy and Parkinson's disease-type pathology. *Neurobiol. Aging* **35**, 2180.e1–5 (2014).

57. C. Proukakis, H. Houlden, A. H. Schapira, Somatic α-synuclein mutations in Parkinson's disease: hypothesis and preliminary data. *Mov. Disord.* **28**, 705–712 (2013).

58. A. P. Kiely, *et al.*, α-Synucleinopathy associated with G51D SNCA mutation: a link between Parkinson's disease and multiple system atrophy? *Acta Neuropathol.* **125**, 753–769 (2013).

59. S. Lesage, *et al.*, G51D α-synuclein mutation causes a novel parkinsonian-pyramidal syndrome. *Ann. Neurol.* **73**, 459–471 (2013).

60. S. Appel-Cresswell, *et al.*, A-synuclein p.H50Q, a novel pathogenic mutation for Parkinson's disease. *Mov. Disord.* **28**, 811–813 (2013).

61. J. J. Zarranz, *et al.*, The new mutation, E46K, of α-synuclein causes Parkinson and Lewy body dementia. *Ann. Neurol.* **55**, 164–173 (2004).

62. D. W. Miller, *et al.*, A-synuclein in blood and brain from familial Parkinson disease with SNCA locus triplication. *Neurology* **62**, 1835–1838 (2004).

63. E. M. Valente, *et al.*, Hereditary early-onset Parkinson's disease caused by mutations in PINK1. *Science* **304**, 1158–1160 (2004).

64. A. Zimprich, *et al.*, Mutations in LRRK2 cause autosomal-dominant parkinsonism with pleomorphic pathology. *Neuron* **44**, 601–607 (2004).

65. G. Bieri, *et al.*, LRRK2 modifies α-syn pathology and spread in mouse models and human neurons. *Acta Neuropathol.* **137**, 961–980 (2019).

66. L. A. Volpicelli-Daley, *et al.*, G2019S-LRRK2 Expression Augments α-Synuclein Sequestration into Inclusions in Neurons. *J. Neurosci.* **36**, 7415–7427 (2016).

67. E. Ryan, G. Seehra, P. Sharma, E. Sidransky, GBA1-associated parkinsonism: new insights and therapeutic opportunities. *Curr. Opin. Neurol.* **32**, 589–596 (2019).

68. M. X. Henderson, *et al.*, Spread of α-synuclein pathology through the brain connectome is modulated by selective vulnerability and predicted by network analysis. *Nat. Neurosci.* **22**, 1248–1257 (2019).

69. P. Ibáñez, *et al.*, Causal relation between α-synuclein gene duplication and familial Parkinson's disease. *Lancet (London, England)* **364**, 1169–1171 (2004).

70. J. T. Jarrett, P. T. Lansbury, Amyloid fibril formation requires a chemically discriminating nucleation event: studies of an amyloidogenic sequence from the bacterial protein OsmB. *Biochemistry* **31**, 12345–12352 (1992).

71. T. R. Serio, *et al.*, Nucleated conformational conversion and the replication of conformational information by a prion determinant. *Science* **289**, 1317–1321 (2000).

72. G. A. Garcia, S. I. A. Cohen, C. M. Dobson, T. P. J. Knowles, Nucleation-conversion-polymerization reactions of biological macromolecules with prenucleation clusters. *Phys. Rev. E* **89**, 32712 (2014).

73. T. P. J. Knowles, *et al.*, An Analytical Solution to the Kinetics of Breakable Filament Assembly. *Science* **326**, 1533–1537 (2009).

74. S. Campioni, *et al.*, The presence of an air-water interface affects formation and elongation of α-Synuclein fibrils. *J. Am. Chem. Soc.* **136**, 2866–2875 (2014).

75. R. Gaspar, *et al.*, Secondary nucleation of monomers on fibril surface dominates α-synuclein aggregation and provides autocatalytic amyloid amplification. *Q. Rev. Biophys.* **50**, e6 (2017).

76. T. C. T. Michaels, *et al.*, Chemical Kinetics for Bridging Molecular Mechanisms

and Macroscopic Measurements of Amyloid Fibril Formation. *Annu. Rev. Phys. Chem.* **69**, 273–298 (2018).

77. L. a Volpicelli-daley, *et al.*, A Syn Fibrils. *Neuron* **72**, 57–71 (2011).

78. A. B. Singleton, *et al.*, α-Synuclein locus triplication causes Parkinson's disease. *Science* **302**, 841 (2003).

79. E. M. Rocha, B. De Miranda, L. H. Sanders, A-synuclein: Pathology, mitochondrial dysfunction and neuroinflammation in Parkinson's disease. *Neurobiol. Dis.* **109**, 249–257 (2018).

80. G. J. Masilamoni, Y. Smith, Chronic MPTP administration regimen in monkeys: a model of dopaminergic and non-dopaminergic cell loss in Parkinson's disease. *J. Neural Transm.* **125**, 337–363 (2018).

81. T. B. Sherer, *et al.*, An in vitro model of Parkinson's disease: linking mitochondrial impairment to altered α-synuclein metabolism and oxidative damage. *J. Neurosci. Off. J. Soc. Neurosci.* **22**, 7006–7015 (2002).

82. J. Burré, M. Sharma, T. C. Südhof, Definition of a molecular pathway mediating α-synuclein neurotoxicity. *J. Neurosci. Off. J. Soc. Neurosci.* **35**, 5221–5232 (2015).

83. L. Giehm, N. Lorenzen, D. E. Otzen, Assays for α-synuclein aggregation. *Methods* **53**, 295–305 (2011).

84. J. D. Camino, *et al.*, The extent of protein hydration dictates the preference for heterogeneous or homogeneous nucleation generating either parallel or antiparallel β-sheet α-synuclein aggregates. *Chem. Sci.* **11**, 11902–11914 (2020).

85. K. A. Conway, J. D. Harper, P. T. Lansbury, Accelerated in vitro fibril formation by a mutant α-synuclein linked to early-onset Parkinson disease. *Nat. Med.* **4**, 1318–1320 (1998).

86. J. Pronchik, X. He, J. T. Giurleo, D. S. Talaga, In vitro formation of amyloid from α-synuclein is dominated by reactions at hydrophobic interfaces. *J. Am. Chem. Soc.* **132**, 9797–9803 (2010).

87. E. J. Castillo, J. L. Koenig, J. M. Anderson, Characterization of protein adsorption on soft contact lenses. IV. Comparison of in vivo spoilage with the in vitro adsorption of tear proteins. *Biomaterials* **7**, 89–96 (1986).

88. C. Wang, N. Shah, G. Thakur, F. Zhou, R. M. Leblanc, A-synuclein in α-helical conformation at air-water interface: implication of conformation and orientation changes during its accumulation/aggregation. *Chem. Commun. (Camb).* **46**, 6702–6704 (2010).

89. A. K. Srivastava, *et al.*, β-Amyloid aggregation and heterogeneous nucleation. *Protein Sci.* **28**, 1567–1581 (2019).

90. R. Zuzak, *et al.*, Nonacene Generated by On-Surface Dehydrogenation. *ACS Nano* **11**, 9321–9329 (2017).

91. S. Mukherjee, P. Chowdhury, F. Gai, Infrared Study of the Effect of Hydration on the Amide I Band and Aggregation Properties of Helical Peptides. *J. Phys. Chem. B* **111**, 4596–4602 (2007).

92. S. Mukherjee, P. Chowdhury, F. Gai, Effect of dehydration on the aggregation kinetics of two amyloid peptides. *J. Phys. Chem. B* **113**, 531–535 (2009).

93. M. S. Celej, *et al.*, Toxic prefibrillar α-synuclein amyloid oligomers adopt a distinctive antiparallel β-sheet structure. *Biochem. J.* **443**, 719–726 (2012).

94. S. J. Prestrelski, N. Tedeschi, T. Arakawa, J. F. Carpenter, Dehydration-induced conformational transitions in proteins and their inhibition by stabilizers. *Biophys.*

J. **65**, 661–671 (1993).

95. K. Griebenow, A. M. Klibanov, Lyophilization-induced reversible changes in the secondary structure of proteins. *Proc. Natl. Acad. Sci. U. S. A.* **92**, 10969–10976 (1995).

96. S. Ray, *et al.*, α-Synuclein aggregation nucleates through liquid–liquid phase separation. *Nat. Chem.* **12**, 705–716 (2020).

97. M. C. Hardenberg, *et al.*, Observation of an α-synuclein liquid droplet state and its maturation into Lewy body-like assemblies. *J. Mol. Cell Biol.* **13**(4), 282-294 (2021).

98. S. Huang, B. Xu, Y. Liu, Calcium promotes α-synuclein liquid-liquid phase separation to accelerate amyloid aggregation. *Biochem. Biophys. Res. Commun.* **603**, 13–20 (2022).

99. A. Agarwal, L. Arora, S. K. Rai, A. Avni, S. Mukhopadhyay, Spatiotemporal modulations in heterotypic condensates of prion and α-synuclein control phase transitions and amyloid conversion. *Nat. Commun.* **13**, 1154 (2022).

100. A. A. Hyman, C. A. Weber, F. Jülicher, Liquid-Liquid Phase Separation in Biology. *Annu. Rev. Cell Dev. Biol.* **30**, 39–58 (2014).

101. J. A. Ditlev, L. B. Case, M. K. Rosen, Who's In and Who's Out-Compositional Control of Biomolecular Condensates. *J. Mol. Biol.* **430**, 4666–4684 (2018).

102. A. S. Lyon, W. B. Peeples, M. K. Rosen, A framework for understanding the functions of biomolecular condensates across scales. *Nat. Rev. Mol. Cell Biol.* **22**, 215–235 (2021).

103. C. So, *et al.*, A liquid-like spindle domain promotes acentrosomal spindle assembly in mammalian oocytes. *Science* **364** (2019).

104. O. Beutel, R. Maraspini, K. Pombo-García, C. Martin-Lemaitre, A. Honigmann, Phase Separation of Zonula Occludens Proteins Drives Formation of Tight Junctions. *Cell* **179**, 923-936.e11 (2019).

105. J. B. Woodruff, *et al.*, The Centrosome Is a Selective Condensate that Nucleates Microtubules by Concentrating Tubulin. *Cell* **169**, 1066-1077.e10 (2017).

106. E. S. Freeman Rosenzweig, *et al.*, The Eukaryotic CO(2)-Concentrating Organelle Is Liquid-like and Exhibits Dynamic Reorganization. *Cell* **171**, 148-162.e19 (2017).

107. S. K. Powers, *et al.*, Nucleo-cytoplasmic Partitioning of ARF Proteins Controls Auxin Responses in Arabidopsis thaliana. *Mol. Cell* **76**, 177-190.e5 (2019).

108. T. Hirose, *et al.*, NEAT1 long noncoding RNA regulates transcription via protein sequestration within subnuclear bodies. *Mol. Biol. Cell* **25**, 169–183 (2014).

109. M. Zeng, *et al.*, Reconstituted Postsynaptic Density as a Molecular Platform for Understanding Synapse Formation and Plasticity. *Cell* **174**, 1172-1187.e16 (2018).

110. X. Su, *et al.*, Phase separation of signaling molecules promotes T cell receptor signal transduction. *Science* **352**, 595–599 (2016).

111. G. Wan, *et al.*, Spatiotemporal regulation of liquid-like condensates in epigenetic inheritance. *Nature* **557**, 679–683 (2018).

112. M. Feric, *et al.*, Coexisting Liquid Phases Underlie Nucleolar Subcompartments. *Cell* **165**, 1686–1697 (2016).

113. T. J. Nott, T. D. Craggs, A. J. Baldwin, Membraneless organelles can melt nucleic acid duplexes and act as biomolecular filters. *Nat. Chem.* **8**, 569–575 (2016).

114. P. Yang, *et al.*, G3BP1 Is a Tunable Switch that Triggers Phase Separation to Assemble Stress Granules. *Cell* **181**, 325-345.e28 (2020).

115. F. Frottin, *et al.*, The nucleolus functions as a phase-separated protein quality control compartment. *Science* **365**, 342–347 (2019).

116. M. Zeng, *et al.*, Phase Transition in Postsynaptic Densities Underlies Formation of Synaptic Complexes and Synaptic Plasticity. *Cell* **166**, 1163-1175.e12 (2016).

117. M. W. Parker, *et al.*, A new class of disordered elements controls DNA replication through initiator self-assembly. *Elife* **8** (2019).

118. A. Yamasaki, *et al.*, Liquidity Is a Critical Determinant for Selective Autophagy of Protein Condensates. *Mol. Cell* **77**, 1163-1175.e9 (2020).

119. D. Sun, R. Wu, J. Zheng, P. Li, L. Yu, Polyubiquitin chain-induced p62 phase separation drives autophagic cargo segregation. *Cell Res.* **28**, 405–415 (2018).

120. A. K. Chakravarty, T. Smejkal, A. K. Itakura, D. M. Garcia, D. F. Jarosz, A Non-amyloid Prion Particle that Activates a Heritable Gene Expression Program. *Mol. Cell* **77**, 251-265.e9 (2020).

121. X. Liu, *et al.*, Mitotic Implantation of the Transcription Factor Prospero via Phase Separation Drives Terminal Neuronal Differentiation. *Dev. Cell* **52**, 277-293.e8 (2020).

122. C. M. Phillips, T. A. Montgomery, P. C. Breen, G. Ruvkun, MUT-16 promotes formation of perinuclear mutator foci required for RNA silencing in the C. elegans germline. *Genes Dev.* **26**, 1433–1444 (2012).

123. S. Mehta, J. Zhang, Liquid-liquid phase separation drives cellular function and dysfunction in cancer. *Nat. Rev. Cancer* **22**, 239–252 (2022).

124. C. E. Sing, S. L. Perry, Recent progress in the science of complex coacervation. *Soft Matter* **16**, 2885–2914 (2020).

125. S. F. Banani, H. O. Lee, A. A. Hyman, M. K. Rosen, Biomolecular condensates: organizers of cellular biochemistry. *Nat. Rev. Mol. Cell Biol.* **18**, 285–298 (2017).

126. Y. Shin, C. P. Brangwynne, Liquid phase condensation in cell physiology and disease. *Science* **357** (2017).

127. M. Kato, *et al.*, Cell-free formation of RNA granules: low complexity sequence domains form dynamic fibers within hydrogels. *Cell* **149**, 753–767 (2012).

128. J. T. Wang, *et al.*, Regulation of RNA granule dynamics by phosphorylation of serine-rich, intrinsically disordered proteins in C. elegans. *Elife* **3**, e04591 (2014).

129. A. C. Murthy, *et al.*, Molecular interactions underlying liquid-liquid phase separation of the FUS low-complexity domain. *Nat. Struct. Mol. Biol.* **26**, 637–648 (2019).

130. S. Kim, *et al.*, Complexation and coacervation of like-charged polyelectrolytes inspired by mussels. *Proc. Natl. Acad. Sci. U. S. A.* **113**, E847-53 (2016).

131. C. W. Pak, *et al.*, Sequence Determinants of Intracellular Phase Separation by Complex Coacervation of a Disordered Protein. *Mol. Cell* **63**, 72–85 (2016).

132. T. K. Lytle, L.-W. Chang, N. Markiewicz, S. L. Perry, C. E. Sing, Designing Electrostatic Interactions via Polyelectrolyte Monomer Sequence. *ACS Cent. Sci.* **5**, 709–718 (2019).

133. J. H. Ortony, D. S. Hwang, J. M. Franck, J. H. Waite, S. Han, Asymmetric collapse in biomimetic complex coacervates revealed by local polymer and water dynamics. *Biomacromolecules* **14**, 1395–1402 (2013).

134. D. Priftis, N. Laugel, M. Tirrell, Thermodynamic characterization of polypeptide complex coacervation. *Langmuir* **28**, 15947–15957 (2012).

135. S. L. Perry, *et al.*, Chirality-selected phase behaviour in ionic polypeptide

complexes. *Nat. Commun.* **6** (2015).

136.   X. Li, P. Erni, J. van der Gucht, R. de Vries, Encapsulation Using Plant Proteins: Thermodynamics and Kinetics of Wetting for Simple Zein Coacervates. *ACS Appl. Mater. Interfaces* **12**, 15802–15809 (2020).

137.   X.-L. Gu, X. Zhu, X.-Z. Kong, Y. Tan, Comparisons of simple and complex coacervations for preparation of sprayable insect sex pheromone microcapsules and release control of the encapsulated pheromone molecule. *J. Microencapsul.* **27**, 355–364 (2010).

138.   T. Haggerty, *et al.*, Hyperphosphorylated Tau in an α-synuclein-overexpressing transgenic model of Parkinson's disease. *Eur. J. Neurosci.* **33**, 1598–1610 (2011).

139.   S. F. Banani, *et al.*, Compositional Control of Phase-Separated Cellular Bodies. *Cell* **166**, 651–663 (2016).

140.   P. Welch, M. Muthukumar, Dendrimer−Polyelectrolyte Complexation: A Model Guest−Host System. *Macromolecules* **33**, 6159–6167 (2000).

141.   J. van der Gucht, E. Spruijt, M. Lemmers, M. A. Cohen Stuart, Polyelectrolyte complexes: bulk phases and colloidal systems. *J. Colloid Interface Sci.* **361**, 407–422 (2011).

142.   J.-M. Choi, A. S. Holehouse, R. V. Pappu, Physical Principles Underlying the Complex Biology of Intracellular Phase Transitions. *Annu. Rev. Biophys.* **49**, 107–133 (2020).

143.   H. Y. J. Fung, M. Birol, E. Rhoades, IDPs in macromolecular complexes: the roles of multivalent interactions in diverse assemblies. *Curr. Opin. Struct. Biol.* **49**, 36–43 (2018).

144.   T. J. Nott, *et al.*, Phase transition of a disordered nuage protein generates environmentally responsive membraneless organelles. *Mol. Cell* **57**, 936–947 (2015).

145.   S. Elbaum-Garfinkle, *et al.*, The disordered P granule protein LAF-1 drives phase separation into droplets with tunable viscosity and dynamics. *Proc. Natl. Acad. Sci. U. S. A.* **112**, 7189–7194 (2015).

146.   Z. Monahan, *et al.*, Phosphorylation of the FUS low-complexity domain disrupts phase separation, aggregation, and toxicity. *EMBO J.* **36**, 2951–2967 (2017).

147.   H.-R. Li, W.-C. Chiang, P.-C. Chou, W.-J. Wang, J.-R. Huang, TAR DNA-binding protein 43 (TDP-43) liquid-liquid phase separation is mediated by just a few aromatic residues. *J. Biol. Chem.* **293**, 6090–6098 (2018).

148.   H. J. Kim, *et al.*, Mutations in prion-like domains in hnRNPA2B1 and hnRNPA1 cause multisystem proteinopathy and ALS. *Nature* **495**, 467–473 (2013).

149.   A. Molliex, *et al.*, Phase Separation by Low Complexity Domains Promotes Stress Granule Assembly and Drives Pathological Fibrillization. *Cell* **163**, 123–133 (2015).

150.   Y. R. Li, O. D. King, J. Shorter, A. D. Gitler, Stress granules as crucibles of ALS pathogenesis. *J. Cell Biol.* **201**, 361–372 (2013).

151.   A. Patel, *et al.*, A Liquid-to-Solid Phase Transition of the ALS Protein FUS Accelerated by Disease Mutation. *Cell* **162**, 1066–1077 (2015).

152.   S. Wegmann, *et al.*, Tau protein liquid–liquid phase separation can initiate tau aggregation. *EMBO J.* **37** (2018).

153.   S. Ambadipudi, J. Biernat, D. Riedel, E. Mandelkow, M. Zweckstetter, Liquid–liquid phase separation of the microtubule-binding repeats of the Alzheimer-related protein Tau. *Nat. Commun.* **8**, 275 (2017).

154. A. E. Conicella, G. H. Zerze, J. Mittal, N. L. Fawzi, ALS Mutations Disrupt Phase Separation Mediated by α-Helical Structure in the TDP-43 Low-Complexity C-Terminal Domain. *Structure* **24**, 1537–1549 (2016).

155. Y. Lin, D. S. W. Protter, M. K. Rosen, R. Parker, Formation and Maturation of Phase-Separated Liquid Droplets by RNA-Binding Proteins. *Mol. Cell* **60**, 208–219 (2015).

156. W. M. Babinchak, *et al.*, The role of liquid-liquid phase separation in aggregation of the TDP-43 low-complexity domain. *J. Biol. Chem.* **294**, 6306–6317 (2019).

157. J. Yang, *et al.*, Highly specific detection of Aβ oligomers in early Alzheimer's disease by a near-infrared fluorescent probe with a "V-shaped" spatial conformation. *Chem. Commun. (Camb).* **56**, 583–586 (2020).

158. Y. Zhang, C. Ding, C. Li, X. Wang, Advances in fluorescent probes for detection and imaging of amyloid-β peptides in Alzheimer's disease. *Adv. Clin. Chem.* **103**, 135–190 (2021).

159. C. Ding, *et al.*, A label-free fluorescent probe for dynamic in situ visualization of amyloid-β peptides aggregation. *Sensors Actuators B Chem.* **347**, 130607 (2021).

160. V. Sharma, K. S. Ghosh, Inhibition of Amyloid Fibrillation by Small Molecules and Nanomaterials: Strategic Development of Pharmaceuticals Against Amyloidosis. *Protein Pept. Lett.* **26**, 315–323 (2019).

161. P. Velander, *et al.*, Natural product-based amyloid inhibitors. *Biochem. Pharmacol.* **139**, 40–55 (2017).

162. A. Mitra, N. Sarkar, Sequence and structure-based peptides as potent amyloid inhibitors: A review. *Arch. Biochem. Biophys.* **695**, 108614 (2020).

163. J. T. Jarrett, P. T. J. Lansbury, Seeding "one-dimensional crystallization" of amyloid: a pathogenic mechanism in Alzheimer's disease and scrapie? *Cell* **73**, 1055–1058 (1993).

164. S. L. Shammas, *et al.*, Binding of the molecular chaperone αB-crystallin to Aβ amyloid fibrils inhibits fibril elongation. *Biophys. J.* **101**, 1681–1689 (2011).

165. C. A. Waudby, *et al.*, The interaction of αB-crystallin with mature α-synuclein amyloid fibrils inhibits their elongation. *Biophys. J.* **98**, 843–851 (2010).

166. T. P. J. Knowles, *et al.*, Kinetics and thermodynamics of amyloid formation from direct measurements of fluctuations in fibril mass. *Proc. Natl. Acad. Sci. U. S. A.* **104**, 10016–10021 (2007).

167. C. Lendel, *et al.*, On the mechanism of nonspecific inhibitors of protein aggregation: dissecting the interactions of α-synuclein with Congo red and lacmoid. *Biochemistry* **48**, 8322–8334 (2009).

168. B. Y. Feng, *et al.*, Small-molecule aggregates inhibit amyloid polymerization. *Nat. Chem. Biol.* **4**, 197–199 (2008).

169. R. Limbocker, *et al.*, Squalamine and Its Derivatives Modulate the Aggregation of Amyloid-β and α-Synuclein and Suppress the Toxicity of Their Oligomers. *Front. Neurosci.* **15**, 680026 (2021).

170. Y. Porat, A. Abramowitz, E. Gazit, Inhibition of amyloid fibril formation by polyphenols: structural similarity and aromatic interactions as a common inhibition mechanism. *Chem. Biol. Drug Des.* **67**, 27–37 (2006).

171. H. Kobayashi, M. Murata, S. Kawanishi, S. Oikawa, Polyphenols with Anti-Amyloid β Aggregation Show Potential Risk of Toxicity Via Pro-Oxidant Properties. *Int. J. Mol. Sci.* **21** (2020).

172. L. Fernandes, T. R. Cardim-Pires, D. Foguel, F. L. Palhano, Green Tea Polyphenol Epigallocatechin-Gallate in Amyloid Aggregation and Neurodegenerative Diseases. *Front. Neurosci.* **15**, 718188 (2021).

173. D. Goyal, S. Shuaib, S. Mann, B. Goyal, Rationally Designed Peptides and Peptidomimetics as Inhibitors of Amyloid-β (Aβ) Aggregation: Potential Therapeutics of Alzheimer's Disease. *ACS Comb. Sci.* **19**, 55–80 (2017).

174. J. Santos, *et al.*, α-Helical peptidic scaffolds to target α-synuclein toxic species with nanomolar affinity. *Nat. Commun.* **12**, 3752 (2021).

175. S. Bieler, C. Soto, Beta-sheet breakers for Alzheimer's disease therapy. *Curr. Drug Targets* **5**, 553–558 (2004).

176. C. Soto, L. Estrada, Amyloid inhibitors and beta-sheet breakers. *Subcell. Biochem.* **38**, 351–364 (2005).

177. L. K. Cuddy, C. Seah, S. H. Pasternak, R. J. Rylett, Amino-Terminal β-Amyloid Antibody Blocks β-Amyloid-Mediated Inhibition of the High-Affinity Choline Transporter CHT. *Front. Mol. Neurosci.* **10**, 361 (2017).

178. L. Pradier, *et al.*, SAR228810: an antibody for protofibrillar amyloid β peptide designed to reduce the risk of amyloid-related imaging abnormalities (ARIA). *Alzheimers. Res. Ther.* **10**, 117 (2018).

179. Z.-T. Sun, *et al.*, Application of Antibody Fragments Against Aβ With Emphasis on Combined Application With Nanoparticles in Alzheimer's Disease. *Front. Pharmacol.* **12**, 654611 (2021).

180. S. S. Ghanem, *et al.*, Natural Alkaloid Compounds as Inhibitors for A-Synuclein Seeded Fibril Formation and Toxicity. *Molecules* **26**, 3736 (2021).

181. P. Michele, *et al.*, A natural product inhibits the initiation of α-synuclein aggregation and suppresses its toxicity. *Proc. Natl. Acad. Sci.* **114**, E1009–E1017 (2017).

182. S. Pena-DIaz, S. Ventura, One ring is sufficient to inhibit α-synuclein aggregation. *Neural Regen. Res.* **17**, 508–511 (2022).

183. J. Pujols, *et al.*, Small molecule inhibits α-synuclein aggregation, disrupts amyloid fibrils, and prevents degeneration of dopaminergic neurons. *Proc. Natl. Acad. Sci. U. S. A.* **115**, 10481–10486 (2018).

184. D. L. Price, *et al.*, The small molecule α-synuclein misfolding inhibitor, NPT200-11, produces multiple benefits in an animal model of Parkinson's disease. *Sci. Rep.* **8**, 16165 (2018).

185. M. Necula, R. Kayed, S. Milton, C. G. Glabe, Small molecule inhibitors of aggregation indicate that amyloid beta oligomerization and fibrillization pathways are independent and distinct. *J. Biol. Chem.* **282**, 10311–10324 (2007).

186. P. T. Lansbury, H. A. Lashuel, A century-old debate on protein aggregation and neurodegeneration enters the clinic. *Nature* **443**, 774–779 (2006).

187. J. Chen, A. H. Armstrong, A. N. Koehler, M. H. Hecht, Small molecule microarrays enable the discovery of compounds that bind the Alzheimer's Aβ peptide and reduce its cytotoxicity. *J. Am. Chem. Soc.* **132**, 17015–17022 (2010).

188. J. Bieschke, Natural compounds may open new routes to treatment of amyloid diseases. *Neurother. J. Am. Soc. Exp. Neurother.* **10**, 429–439 (2013).

189. J. L. Cummings, T. Morstorf, K. Zhong, Alzheimer's disease drug-development pipeline: few candidates, frequent failures. *Alzheimers. Res. Ther.* **6**, 37 (2014).

190. E. Karran, J. Hardy, A critique of the drug discovery and phase 3 clinical programs

targeting the amyloid hypothesis for Alzheimer disease. *Ann. Neurol.* **76**, 185–205 (2014).

191. B. De Strooper, E. Karran, The Cellular Phase of Alzheimer's Disease. *Cell* **164**, 603–615 (2016).

192. P. Arosio, M. Vendruscolo, C. M. Dobson, T. P. J. Knowles, Chemical kinetics for drug discovery to combat protein aggregation diseases. *Trends Pharmacol. Sci.* **35**, 127–135 (2014).

193. J. Habchi, *et al.*, An anticancer drug suppresses the primary nucleation reaction that initiates the production of the toxic Aβ42 aggregates linked with Alzheimer's disease. *Sci. Adv.* **2**, e1501244 (2016).

194. S. I. A. Cohen, *et al.*, A molecular chaperone breaks the catalytic cycle that generates toxic Aβ oligomers. *Nat. Struct. Mol. Biol.* **22**, 207–213 (2015).

195. S. I. A. Cohen, *et al.*, Proliferation of amyloid-β42 aggregates occurs through a secondary nucleation mechanism. *Proc. Natl. Acad. Sci. U. S. A.* **110**, 9758–9763 (2013).

196. Y. C. Wong, D. Krainc, α-synuclein toxicity in neurodegeneration: mechanism and therapeutic strategies. *Nat. Med.* **23**, 1–13 (2017).

197. B. Dehay, *et al.*, Targeting α-synuclein for treatment of Parkinson's disease: mechanistic and therapeutic considerations. *Lancet. Neurol.* **14**, 855–866 (2015).

198. J. Wagner, *et al.*, Anle138b: a novel oligomer modulator for disease-modifying therapy of neurodegenerative diseases such as prion and Parkinson's disease. *Acta Neuropathol.* **125**, 795–813 (2013).

199. M. Kurnik, *et al.*, Potent α-Synuclein Aggregation Inhibitors, Identified by High-Throughput Screening, Mainly Target the Monomeric State. *Cell Chem. Biol.* **25**, 1389-1402.e9 (2018).

200. M. Perni, *et al.*, Multistep Inhibition of α-Synuclein Aggregation and Toxicity in Vitro and in Vivo by Trodusquemine. *ACS Chem. Biol.* **13**, 2308–2319 (2018).

201. L. Parnetti, *et al.*, Cerebrospinal fluid biomarkers in Parkinson disease. *Nat. Rev. Neurol.* **9**, 131–140 (2013).

202. S. Giorgetti, C. Greco, P. Tortora, F. Aprile, Targeting Amyloid Aggregation: An Overview of Strategies and Mechanisms. *Int. J. Mol. Sci.* **19**, 2677 (2018).

203. S. Giorgetti, C. Greco, P. Tortora, F. A. Aprile, Targeting Amyloid Aggregation: An Overview of Strategies and Mechanisms. *Int. J. Mol. Sci.* **19** (2018).

204. F. U. Hartl, M. Hayer-Hartl, Molecular chaperones in the cytosol: from nascent chain to folded protein. *Science* **295**, 1852–1858 (2002).

205. A. L. Goldberg, Protein degradation and protection against misfolded or damaged proteins. *Nature* **426**, 895–899 (2003).

206. C. Soto, S. Pritzkow, Protein misfolding, aggregation, and conformational strains in neurodegenerative diseases. *Nat. Neurosci.* **21**, 1332–1340 (2018).

207. C. Campanella, *et al.*, Heat Shock Proteins in Alzheimer's Disease: Role and Targeting. *Int. J. Mol. Sci.* **19** (2018).

208. L. Galluzzi, *et al.*, Molecular definitions of autophagy and related processes. *EMBO J.* **36**, 1811–1836 (2017).

209. A. B. Meriin, *et al.*, Hsp70-Bag3 complex is a hub for proteotoxicity-induced signaling that controls protein aggregation. *Proc. Natl. Acad. Sci. U. S. A.* **115**, E7043–E7052 (2018).

210. K. C. Walls, *et al.*, Swedish Alzheimer mutation induces mitochondrial

dysfunction mediated by HSP60 mislocalization of amyloid precursor protein (APP) and beta-amyloid. *J. Biol. Chem.* **287**, 30317–30327 (2012).

211. S. Kuzuhara, H. Mori, N. Izumiyama, M. Yoshimura, Y. Ihara, Lewy bodies are ubiquitinated. A light and electron microscopic immunocytochemical study. *Acta Neuropathol.* **75**, 345–353 (1988).

212. P. J. McLean, *et al.*, TorsinA and heat shock proteins act as molecular chaperones: suppression of α-synuclein aggregation. *J. Neurochem.* **83**, 846–854 (2002).

213. N. L. Wankhede, *et al.*, Involvement of molecular chaperone in protein-misfolding brain diseases. *Biomed. Pharmacother.* **147**, 112647 (2022).

214. S. Parakh, J. D. Atkin, Protein folding alterations in amyotrophic lateral sclerosis. *Brain Res.* **1648**, 633–649 (2016).

215. P. J. Muchowski, *et al.*, Hsp70 and hsp40 chaperones can inhibit self-assembly of polyglutamine proteins into amyloid-like fibrils. *Proc. Natl. Acad. Sci. U. S. A.* **97**, 7841–7846 (2000).

216. P. Kazemi-Esfarjani, S. Benzer, Genetic suppression of polyglutamine toxicity in Drosophila. *Science* **287**, 1837–1840 (2000).

217. M. S. Hipp, P. Kasturi, F. U. Hartl, The proteostasis network and its decline in ageing. *Nat. Rev. Mol. Cell Biol.* **20**, 421–435 (2019).

218. M. Brehme, *et al.*, A chaperome subnetwork safeguards proteostasis in aging and neurodegenerative disease. *Cell Rep.* **9**, 1135–1150 (2014).

219. A. Mogk, E. Kummer, B. Bukau, Cooperation of Hsp70 and Hsp100 chaperone machines in protein disaggregation. *Front. Mol. Biosci.* **2**, 22 (2015).

220. S. Kaushik, A. M. Cuervo, Chaperone-mediated autophagy: a unique way to enter the lysosome world. *Trends Cell Biol.* **22**, 407–417 (2012).

221. D. Balchin, M. Hayer-Hartl, F. U. Hartl, In vivo aspects of protein folding and quality control. *Science* **353**, aac4354 (2016).

222. J. Labbadia, R. I. Morimoto, The biology of proteostasis in aging and disease. *Annu. Rev. Biochem.* **84**, 435–464 (2015).

223. N. B. Nillegoda, *et al.*, Crucial HSP70 co-chaperone complex unlocks metazoan protein disaggregation. *Nature* **524**, 247–251 (2015).

224. X. Gao, *et al.*, Human Hsp70 Disaggregase Reverses Parkinson's-Linked α-Synuclein Amyloid Fibrils. *Mol. Cell* **59**, 781–793 (2015).

225. J. Shorter, The mammalian disaggregase machinery: Hsp110 synergizes with Hsp70 and Hsp40 to catalyze protein disaggregation and reactivation in a cell-free system. *PLoS One* **6**, e26319 (2011).

226. J. Kirstein, *et al.*, In vivo properties of the disaggregase function of J-proteins and Hsc70 in Caenorhabditis elegans stress and aging. *Aging Cell* **16**, 1414–1424 (2017).

227. H. Rampelt, *et al.*, Metazoan Hsp70 machines use Hsp110 to power protein disaggregation. *EMBO J.* **31**, 4221–4235 (2012).

228. A. Mogk, *et al.*, Identification of thermolabile Escherichia coli proteins: prevention and reversion of aggregation by DnaK and ClpB. *EMBO J.* **18**, 6934–6949 (1999).

229. J. R. Glover, S. Lindquist, Hsp104, Hsp70, and Hsp40: a novel chaperone system that rescues previously aggregated proteins. *Cell* **94**, 73–82 (1998).

230. S. Zietkiewicz, J. Krzewska, K. Liberek, Successive and synergistic action of the Hsp70 and Hsp100 chaperones in protein disaggregation. *J. Biol. Chem.* **279**, 44376–44383 (2004).

231. J. Weibezahn, B. Bukau, A. Mogk, Unscrambling an egg: protein disaggregation

by AAA+ proteins. *Microb. Cell Fact.* **3**, 1 (2004).

232. M. P. Mayer, B. Bukau, Hsp70 chaperones: cellular functions and molecular mechanism. *Cell. Mol. Life Sci.* **62**, 670–684 (2005).

233. R. W. Walters, R. Parker, Coupling of Ribostasis and Proteostasis: Hsp70 Proteins in mRNA Metabolism. *Trends Biochem. Sci.* **40**, 552–559 (2015).

234. J. Winkler, J. Tyedmers, B. Bukau, A. Mogk, Hsp70 targets Hsp100 chaperones to substrates for protein disaggregation and prion fragmentation. *J. Cell Biol.* **198**, 387–404 (2012).

235. S. P. Acebrón, I. Martín, U. del Castillo, F. Moro, A. Muga, DnaK-mediated association of ClpB to protein aggregates. A bichaperone network at the aggregate surface. *FEBS Lett.* **583**, 2991–2996 (2009).

236. M. L. Duennwald, A. Echeverria, J. Shorter, Small Heat Shock Proteins Potentiate Amyloid Dissolution by Protein Disaggregases from Yeast and Humans. *PLoS Biol* **10** (2012).

237. H. H. Kampinga, E. A. Craig, The HSP70 chaperone machinery: J proteins as drivers of functional specificity. *Nat. Rev. Mol. Cell Biol.* **11**, 579–592 (2010).

238. Y. Cabrera, *et al.*, Regulation of Human Hsc70 ATPase and Chaperone Activities by Apg2: Role of the Acidic Subdomain. *J. Mol. Biol.* **431**, 444–461 (2019).

239. R. Kityk, M. Vogel, R. Schlecht, B. Bukau, M. P. Mayer, Pathways of allosteric regulation in Hsp70 chaperones. *Nat. Commun.* **6**, 8308 (2015).

240. A. Zhuravleva, E. M. Clerico, L. M. Gierasch, An interdomain energetic tug-of-war creates the allosterically active state in Hsp70 molecular chaperones. *Cell* **151**, 1296–1307 (2012).

241. O. Faust, *et al.*, HSP40 proteins use class-specific regulation to drive HSP70 functional diversity. *Nature* **587**, 489–494 (2020).

242. A. S. Wentink, *et al.*, Molecular dissection of amyloid disaggregation by human HSP70. *Nature* **587**, 483-488 (2020).

243. R. Sousa, *et al.*, Clathrin-coat disassembly illuminates the mechanisms of Hsp70 force generation. *Nat. Struct. Mol. Biol.* **23**, 821–829 (2016).

244. P. De Los Rios, A. Ben-Zvi, O. Slutsky, A. Azem, P. Goloubinoff, Hsp70 chaperones accelerate protein translocation and the unfolding of stable protein aggregates by entropic pulling. *Proc. Natl. Acad. Sci. U. S. A.* **103**, 6166–6171 (2006).

245. A. Bracher, J. Verghese, The nucleotide exchange factors of Hsp70 molecular chaperones. *Front. Mol. Biosci.* **2**, 10 (2015).

246. R. Tycko, Amyloid Polymorphism: Structural Basis and Neurobiological Relevance. *Neuron* **86**, 632–645 (2015).

247. R. Guerrero-Ferreira, *et al.*, Two new polymorphic structures of human full-length α-synuclein fibrils solved by cryo-electron microscopy. *Elife* **8**, 1–24 (2019).

248. M. Fändrich, J. Meinhardt, N. Grigorieff, Structural polymorphism of Alzheimer Abeta and other amyloid fibrils. *Prion* **3**, 89–93 (2009).

249. J. R. Brender, *et al.*, Probing the sources of the apparent irreproducibility of amyloid formation: drastic changes in kinetics and a switch in mechanism due to micellelike oligomer formation at critical concentrations of IAPP. *J. Phys. Chem. B* **119**, 2886–2896 (2015).

250. A. K. Buell, C. M. Dobson, T. P. J. Knowles, The physical chemistry of the amyloid phenomenon: thermodynamics and kinetics of filamentous protein aggregation. *Essays Biochem.* **56**, 11–39 (2014).

251. R. Wetzel, Kinetics and thermodynamics of amyloid fibril assembly. *Acc. Chem. Res.* **39**, 671–679 (2006).

252. A. Hawe, M. Sutter, W. Jiskoot, Extrinsic Fluorescent Dyes as Tools for Protein Characterization. *Pharm. Res.* **25**, 1487–1499 (2008).

253. C. W. Bertoncini, M. S. Celej, Small molecule fluorescent probes for the detection of amyloid self-assembly in vitro and in vivo. *Curr. Protein Pept. Sci.* **12**, 205–220 (2011).

254. M. A. Leissring, *et al.*, Kinetics of amyloid beta-protein degradation determined by novel fluorescence- and fluorescence polarization-based assays. *J. Biol. Chem.* **278**, 37314–37320 (2003).

255. F. Gorka, *et al.*, A Comparative Study of High-Contrast Fluorescence Lifetime Probes for Imaging Amyloid in Tissue. *J. Phys. Chem. B* **125**, 13710–13717 (2021).

256. K. Gade Malmos, *et al.*, ThT 101: a primer on the use of thioflavin T to investigate amyloid formation. *Amyloid* **24**, 1–16 (2017).

257. P. S. VASSAR, C. F. CULLING, Fluorescent stains, with special reference to amyloid and connective tissues. *Arch. Pathol.* **68**, 487–498 (1959).

258. H. Naiki, K. Higuchi, M. Hosokawa, T. Takeda, Fluorometric determination of amyloid fibrils in vitro using the fluorescent dye, thioflavin T1. *Anal. Biochem.* **177**, 244–249 (1989).

259. M. Biancalana, S. Koide, Molecular mechanism of Thioflavin-T binding to amyloid fibrils. *Biochim. Biophys. Acta* **1804**, 1405–1412 (2010).

260. H. Naiki, *et al.*, Fluorometric examination of tissue amyloid fibrils in murine senile amyloidosis: use of the fluorescent indicator, thioflavine T. *Anal Biochem* **62**, 768–73 (1989).

261. H. LeVine 3rd, Quantification of beta-sheet amyloid fibril structures with thioflavin T. *Methods Enzymol.* **309**, 274–284 (1999).

262. C. Wu, M. Biancalana, S. Koide, J.-E. Shea, Binding modes of thioflavin-T to the single-layer beta-sheet of the peptide self-assembly mimics. *J. Mol. Biol.* **394**, 627–633 (2009).

263. M. Biancalana, K. Makabe, A. Koide, S. Koide, Molecular mechanism of thioflavin-T binding to the surface of beta-rich peptide self-assemblies. *J. Mol. Biol.* **385**, 1052–1063 (2009).

264. P. K. Singh, M. Kumbhakar, H. Pal, S. Nath, Ultrafast bond twisting dynamics in amyloid fibril sensor. *J. Phys. Chem. B* **114**, 2541–2546 (2010).

265. G. Habicht, *et al.*, Directed selection of a conformational antibody domain that prevents mature amyloid fibril formation by stabilizing Abeta protofibrils. *Proc. Natl. Acad. Sci. U. S. A.* **104**, 19232–19237 (2007).

266. D. M. Walsh, *et al.*, Amyloid beta-protein fibrillogenesis. Structure and biological activity of protofibrillar intermediates. *J. Biol. Chem.* **274**, 25945–25952 (1999).

267. C. S. Goldsbury, *et al.*, Studies on the in vitro assembly of a beta 1-40: implications for the search for a beta fibril formation inhibitors. *J. Struct. Biol.* **130**, 217–231 (2000).

268. E. N. Cline, M. A. Bicca, K. L. Viola, W. L. Klein, The Amyloid-β Oligomer Hypothesis: Beginning of the Third Decade. *J. Alzheimers. Dis.* **64**, S567–S610 (2018).

269. P. Misra, R. Kodali, S. Chemuru, K. Kar, R. Wetzel, Rapid α-oligomer formation mediated by the Aβ C terminus initiates an amyloid assembly pathway. *Nat.*

Commun. **7**, 12419 (2016).

270. M. Groenning, *et al.*, Study on the binding of Thioflavin T to β-sheet-rich and non-β-sheet cavities. *J. Struct. Biol.* **158**, 358–369 (2007).

271. I. M. Kuznetsova, A. I. Sulatskaya, V. N. Uversky, K. K. Turoverov, Analyzing thioflavin T binding to amyloid fibrils by an equilibrium microdialysis-based technique. *PLoS One* **7**, e30724 (2012).

272. R. Carrotta, R. Bauer, R. Waninge, C. Rischel, Conformational characterization of oligomeric intermediates and aggregates in beta-lactoglobulin heat aggregation. *Protein Sci.* **10**, 1312–1318 (2001).

273. L. Halabelian, *et al.*, A covalent homodimer probing early oligomers along amyloid aggregation. *Sci. Rep.* **5**, 14651 (2015).

274. G. V De Ferrari, W. D. Mallender, N. C. Inestrosa, T. L. Rosenberry, Thioflavin T is a fluorescent probe of the acetylcholinesterase peripheral site that reveals conformational interactions between the peripheral and acylation sites. *J. Biol. Chem.* **276**, 23282–23287 (2001).

275. S. Grudzielanek, V. Smirnovas, R. Winter, Solvation-assisted pressure tuning of insulin fibrillation: from novel aggregation pathways to biotechnological applications. *J. Mol. Biol.* **356**, 497–509 (2006).

276. H. 3rd LeVine, Thioflavine T interaction with synthetic Alzheimer's disease beta-amyloid peptides: detection of amyloid aggregation in solution. *Protein Sci.* **2**, 404–410 (1993).

277. M. Groenning, *et al.*, Study on the binding of Thioflavin T to beta-sheet-rich and non-beta-sheet cavities. *J. Struct. Biol.* **158**, 358–369 (2007).

278. M. Ilanchelian, R. Ramaraj, Emission of thioflavin T and its control in the presence of DNA. *J. Photochem. Photobiol. A Chem.* **162**, 129–137 (2004).

279. L. P. Jameson, N. W. Smith, S. V Dzyuba, Dye-binding assays for evaluation of the effects of small molecule inhibitors on amyloid (aβ) self-assembly. *ACS Chem. Neurosci.* **3**, 807–819 (2012).

280. J. Zhang, *et al.*, Epigallocatechin-3-gallate (EGCG)-stabilized selenium nanoparticles coated with Tet-1 peptide to reduce amyloid-β aggregation and cytotoxicity. *ACS Appl. Mater. Interfaces* **6**, 8475–8487 (2014).

281. S. Roy, R. Bhat, Suppression, disaggregation, and modulation of γ-Synuclein fibrillation pathway by green tea polyphenol EGCG. *Protein Sci.* **28**, 382–402 (2019).

282. A. Kroes-Nijboer, Y. S. Lubbersen, P. Venema, E. van der Linden, Thioflavin T fluorescence assay for beta-lactoglobulin fibrils hindered by DAPH. *J. Struct. Biol.* **165**, 140–145 (2009).

283. D. C. Dong, M. A. Winnik, The Py scale of solvent polarities. *Can. J. Chem.* **62**, 2560–2565 (1984).

284. K. Hara, W. R. Ware, Influence of solvent perturbation on the radiative transition probability from the 1B1u state of pyrene. *Chem. Phys.* **51**, 61–68 (1980).

285. T. Förster, Excimers. *Angew. Chemie Int. Ed. English* **8**, 333–343 (1969).

286. S. S. Lehrer, Intramolecular pyrene excimer fluorescence: a probe of proximity and protein conformational change. *Methods Enzymol.* **278**, 286–295 (1997).

287. G. Bains, A. B. Patel, V. Narayanaswami, Pyrene: a probe to study protein conformation and conformational changes. *Molecules* **16**, 7909–7935 (2011).

288. J. Liang, H.-B. Liu, J. Wang, Pyrene-based ratiometric and fluorescent sensor for

selective Al3+ detection. *Inorganica Chim. Acta* **489**, 61–66 (2019).

289. H. J. Pownall, L. C. Smith, Pyrene-labeled lipids: versatile probes of membrane dynamics in vitro and in living cells. *Chem. Phys. Lipids* **50**, 191–211 (1989).

290. P. Conlon, *et al.*, Pyrene excimer signaling molecular beacons for probing nucleic acids. *J. Am. Chem. Soc.* **130**, 336–342 (2008).

291. S. Tamamizu-Kato, *et al.*, Calcium-triggered membrane interaction of the α-synuclein acidic tail. *Biochemistry* **45**, 10947–10956 (2006).

292. J. D. Camino, *et al.*, The extent of protein hydration dictates the preference for heterogeneous or homogeneous nucleation generating either parallel or antiparallel β-sheet α-synuclein aggregates. Chem. Sci. **11**, 11902–11914 (2020)

293. V. Gupta, *et al.*, Lipid-induced extension of apolipoprotein E helix 4 correlates with low density lipoprotein receptor binding ability. *J. Biol. Chem.* **281**, 39294–39299 (2006).

294. J. M. West, H. Tsuruta, E. R. Kantrowitz, A fluorescent probe-labeled Escherichia coli aspartate transcarbamoylase that monitors the allosteric conformational state. *J. Biol. Chem.* **279**, 945–951 (2004).

295. E. Folgado, *et al.*, π-Stacking Interactions of Graphene-Coated Cobalt Magnetic Nanoparticles with Pyrene-Tagged Dendritic Poly(Vinylidene Fluoride). *Chempluschem* **84**, 78–84 (2019).

296. D. S. Karpovich, G. J. Blanchard, Relating the polarity-dependent fluorescence response of pyrene to vibronic coupling. Achieving a fundamental understanding of the py polarity scale. *J. Phys. Chem.* **99**, 3951–3958 (1995).

297. K. Kalyanasundaram, J. K. Thomas, Environmental effects on vibronic band intensities in pyrene monomer fluorescence and their application in studies of micellar systems. *J. Am. Chem. Soc.* **99**, 2039–2044 (1977).

298. C. Tedeschi, H. Möhwald, S. Kirstein, Polarity of Layer-by-Layer Deposited Polyelectrolyte Films As Determined by Pyrene Fluorescence. *J. Am. Chem. Soc.* **123**, 954–960 (2001).

299. S. L. Betcher-Lange, S. S. Lehrer, Pyrene excimer fluorescence in rabbit skeletal $\alpha\alpha$tropomyosin labeled with N-(1-pyrene)maleimide. A probe of sulfhydryl proximity and local chain separation. *J. Biol. Chem.* **253**, 3757–3760 (1978).

300. A. Nakajima, Effects of isomeric solvents on vibronic band intensities in fluorescence spectrum of pyrene. *J. Mol. Spectrosc.* **61**, 467–469 (1976).

301. V. Raussens, V. Narayanaswami, E. Goormaghtigh, R. O. Ryan, J. M. Ruysschaert, Alignment of the apolipophorin-III α-helices in complex with dimyristoylphosphatidylcholine. A unique spatial orientation. *J. Biol. Chem.* **270**, 12542–12547 (1995).

302. D. Sahoo, P. M. M. Weers, R. O. Ryan, V. Narayanaswami, Lipid-triggered conformational switch of apolipophorin III helix bundle to an extended helix organization. *J. Mol. Biol.* **321**, 201–214 (2002).

303. G. M. Strasburg, P. C. Leavis, J. Gergely, Troponin-C-mediated calcium-sensitive changes in the conformation of troponin I detected by pyrene excimer fluorescence. *J. Biol. Chem.* **260**, 366–370 (1985).

304. T. I. Lin, Excimer fluorescence of pyrene-tropomyosin adducts. *Biophys. Chem.* **15**, 277–288 (1982).

305. A. B. Patel, P. Khumsupan, V. Narayanaswami, Pyrene fluorescence analysis offers new insights into the conformation of the lipoprotein-binding domain of

human apolipoprotein E. *Biochemistry* **49**, 1766–1775 (2010).

306. J. I. Gallea, M. S. Celej, Structural insights into amyloid oligomers of the Parkinson disease-related protein α-synuclein. *J. Biol. Chem.* **289**, 26733–26742 (2014).

307. R. D. Astumian, Thermodynamics and kinetics of molecular motors. *Biophys. J.* **98**, 2401–2409 (2010).

308. G. Metcalfe, M. F. M. Speetjens, D. R. Lester, H. J. H. Clercx, Beyond Passive: Chaotic Transport in Stirred Fluids in Advances in Applied Mechanics (Eds. E. van der Giessen, H. Aref), Elsevier (Amsterdam, Netherlands) **45**, 109-188 (2012).

309. T. Yanagida, Y. Ishii, Single molecule detection, thermal fluctuation and life. *Proc. Jpn. Acad. Ser. B. Phys. Biol. Sci.* **93**, 51–63 (2017).

310. J. Zlatanova, K. van Holde, Single-molecule biology: what is it and how does it work? *Mol. Cell* **24**, 317–329 (2006).

311. E. Barkai, Y. Jung, R. Silbey, Theory of single-molecule spectroscopy: beyond the ensemble average. *Annu. Rev. Phys. Chem.* **55**, 457–507 (2004).

312. S. S. Mandal, Force Spectroscopy on Single Molecules of Life. *ACS omega* **5**, 11271–11278 (2020).

313. A. N. Kapanidis, T. Strick, Biology, one molecule at a time. *Trends Biochem. Sci.* **34**, 234–243 (2009).

314. J. Sankaran, *et al.*, Simultaneous spatiotemporal super-resolution and multi-parametric fluorescence microscopy. *Nat. Commun.* **12**, 1748 (2021).

315. T. Sungkaworn, F. Rieken, M. J. Lohse, D. Calebiro, High-resolution spatiotemporal analysis of receptor dynamics by single-molecule fluorescence microscopy. *J. Vis. Exp.*, e51784 (2014).

316. Y.-H. Lee, R. G. Maus, B. W. Smith, J. D. Winefordner, Laser-Induced Fluorescence Detection of a Single Molecule in a Capillary. *Anal. Chem.* **66**, 4142–4149 (1994).

317. B. Schuler, Single-molecule FRET of protein structure and dynamics - a primer. *J. Nanobiotechnology* **11 Suppl 1**, S2 (2013).

318. T. Förster, Zwischenmolekulare Energiewanderung und Fluoreszenz. *Ann. Phys.* **437**, 55–75 (1948).

319. L. Yu, *et al.*, A Comprehensive Review of Fluorescence Correlation Spectroscopy. *Front. Phys.* **9** (2021).

320. J. Ries, P. Schwille, Fluorescence correlation spectroscopy. *Bioessays* **34**, 361–368 (2012).

321. D. Magde, E. L. Elson, W. W. Webb, Fluorescence correlation spectroscopy. II. An experimental realization. *Biopolymers* **13**, 29–61 (1974).

322. E. L. Elson, D. Magde, Fluorescence correlation spectroscopy. I. Conceptual basis and theory. *Biopolym. Orig. Res. Biomol.* **13**, 1–27 (1974).

323. R. Datta, T. M. Heaster, J. T. Sharick, A. A. Gillette, M. C. Skala, Fluorescence lifetime imaging microscopy: fundamentals and advances in instrumentation, analysis, and applications. *J. Biomed. Opt.* **25**, 1–43 (2020).

324. B. D. Venetta, Microscope Phase Fluorometer for Determining the Fluorescence Lifetimes of Fluorochromes. *Rev. Sci. Instrum.* **30**, 450–457 (1959).

325. E. Gaviola, Ein Fluorometer. Apparat zur Messung von Fluoreszenzabklingungszeiten. *Zeitschrift für Phys.* **42**, 853–861 (1927).

326. R. Kühnemuth, C. A. M. Seidel, Principles of Single Molecule Multiparameter Fluorescence Spectroscopy. *Single Mol.* **2**, 251–254 (2001).

327. I. König, *et al.*, Single-molecule spectroscopy of protein conformational dynamics

in live eukaryotic cells. *Nat. Methods* **12**, 773–779 (2015).

328. Z. Liu, L. D. Lavis, E. Betzig, Imaging live-cell dynamics and structure at the single-molecule level. *Mol. Cell* **58**, 644–659 (2015).

329. P. Schwille, Fluorescence correlation spectroscopy and its potential for intracellular applications. *Cell Biochem. Biophys.* **34**, 383–408 (2001).

330. S. Mukhopadhyay, R. Krishnan, E. A. Lemke, S. Lindquist, A. A. Deniz, A natively unfolded yeast prion monomer adopts an ensemble of collapsed and rapidly fluctuating structures. *Proc. Natl. Acad. Sci. U. S. A.* **104**, 2649–2654 (2007).

331. G. Krainer, *et al.*, Slow Interconversion in a Heterogeneous Unfolded-State Ensemble of Outer-Membrane Phospholipase A. *Biophys. J.* **113**, 1280–1289 (2017).

332. E. Shaw, P. St-Pierre, K. McCluskey, D. A. Lafontaine, J. C. Penedo, Using sm-FRET and denaturants to reveal folding landscapes. *Methods Enzymol.* **549**, 313–341 (2014).

333. B. Schuler, W. A. Eaton, Protein folding studied by single-molecule FRET. *Curr. Opin. Struct. Biol.* **18**, 16–26 (2008).

334. J. Langowski, Protein-protein interactions determined by fluorescence correlation spectroscopy. *Methods Cell Biol.* **85**, 471–484 (2008).

335. A. Margineanu, *et al.*, Screening for protein-protein interactions using Förster resonance energy transfer (FRET) and fluorescence lifetime imaging microscopy (FLIM). *Sci. Rep.* **6**, 28186 (2016).

336. S. Farooq, C. Fijen, J. Hohlbein, Studying DNA-protein interactions with single-molecule Förster resonance energy transfer. *Protoplasma* **251**, 317–332 (2014).

337. T. Kobayashi, N. Okamoto, T. Sawasaki, Y. Endo, Detection of protein-DNA interactions in crude cellular extracts by fluorescence correlation spectroscopy. *Anal. Biochem.* **332**, 58–66 (2004).

338. D. Krüger, J. Ebenhan, S. Werner, K. Bacia, Measuring Protein Binding to Lipid Vesicles by Fluorescence Cross-Correlation Spectroscopy. *Biophys. J.* **113**, 1311–1320 (2017).

339. G. Krainer, *et al.*, A minimal helical-hairpin motif provides molecular-level insights into misfolding and pharmacological rescue of CFTR. *Commun. Biol.* **1**, 154 (2018).

340. Z. Zhang, D. Yomo, C. Gradinaru, Choosing the right fluorophore for single-molecule fluorescence studies in a lipid environment. *Biochim. Biophys. acta. Biomembr.* **1859**, 1242–1253 (2017).

341. W. E. Moerner, D. P. Fromm, Methods of single-molecule fluorescence spectroscopy and microscopy. *Rev. Sci. Instrum.* **74**, 3597–3619 (2003).

342. H. S. Chung, *et al.*, Extracting rate coefficients from single-molecule photon trajectories and FRET efficiency histograms for a fast-folding protein. *J. Phys. Chem. A* **115**, 3642–3656 (2011).

343. W. L. Klein, G. A. Krafft, C. E. Finch, Targeting small Aβ oligomers: the solution to an Alzheimer's disease conundrum? *Trends Neurosci.* **24**, 219–224 (2001).

344. R. D. Johnson, D. G. Steel, A. Gafni, Structural evolution and membrane interactions of Alzheimer's amyloid-beta peptide oligomers: new knowledge from single-molecule fluorescence studies. *Protein Sci.* **23**, 869–883 (2014).

345. J. K. Hannestad, *et al.*, Single-vesicle imaging reveals lipid-selective and stepwise membrane disruption by monomeric α-synuclein. *Proc. Natl. Acad. Sci. U. S. A.* **117**, 14178–14186 (2020).

346. B. Mollenhauer, *et al.*, Direct quantification of CSF α-synuclein by ELISA and first cross-sectional study in patients with neurodegeneration. *Exp. Neurol.* **213**, 315–325 (2008).

347. L. F. Lue, *et al.*, Soluble amyloid beta peptide concentration as a predictor of synaptic change in Alzheimer's disease. *Am. J. Pathol.* **155**, 853–862 (1999).

348. C. A. McLean, *et al.*, Soluble pool of Abeta amyloid as a determinant of severity of neurodegeneration in Alzheimer's disease. *Ann. Neurol.* **46**, 860–866 (1999).

349. A. Tiiman, J. Jarvet, A. Gräslund, V. Vukojević, Heterogeneity and Turnover of Intermediates during Amyloid-β (Aβ) Peptide Aggregation Studied by Fluorescence Correlation Spectroscopy. *Biochemistry* **54**, 7203–7211 (2015).

350. Y. Guan, *et al.*, Real-Time Monitoring of Alzheimer's-Related Amyloid Aggregation via Probe Enhancement-Fluorescence Correlation Spectroscopy. *ACS Chem. Neurosci.* **6**, 1503–1508 (2015).

351. J. J. Mittag, S. Milani, D. M. Walsh, J. O. Rädler, J. J. McManus, Simultaneous measurement of a range of particle sizes during Aβ1-42 fibrillogenesis quantified using fluorescence correlation spectroscopy. *Biochem. Biophys. Res. Commun.* **448**, 195–199 (2014).

352. E. R. Middleton, E. Rhoades, Effects of curvature and composition on α-synuclein binding to lipid vesicles. *Biophys. J.* **99**, 2279–2288 (2010).

353. E. Rhoades, T. F. Ramlall, W. W. Webb, D. Eliezer, Quantification of α-synuclein binding to lipid vesicles using fluorescence correlation spectroscopy. *Biophys. J.* **90**, 4692–4700 (2006).

354. A. Orte, R. Clarke, D. Klenerman, Single-molecule two-colour coincidence detection to probe biomolecular associations. *Biochem. Soc. Trans.* **38**, 914–918 (2010).

355. A. Orte, R. Clarke, S. Balasubramanian, D. Klenerman, Determination of the fraction and stoichiometry of femtomolar levels of biomolecular complexes in an excess of monomer using single-molecule, two-color coincidence detection. *Anal. Chem.* **78**, 7707–7715 (2006).

356. M. H. Horrocks, *et al.*, Fast flow microfluidics and single-molecule fluorescence for the rapid characterization of α-synuclein oligomers. *Anal. Chem.* **87**, 8818–8826 (2015).

357. D. V O'connor, D. Phillips, Time-correlated single photon counting. Academic Press: London; 1984.

358. J. R. Lakowicz, Instrumentation for Fluorescence Spectroscopy in *Principles of fluorescence spectroscopy* (Ed. J. R. Lakowicz), Springer (Boston, MA), 27–61 (2006).

359. M. Wahl, "Modern TCSPC Electronics: Principles and Acquisition Modes BT - Advanced Photon Counting: Applications, Methods, Instrumentation" in P. Kapusta, M. Wahl, R. Erdmann, Eds. (Springer International Publishing, 2015), pp. 1–21.

360. C. C. Gradinaru, D. O. Marushchak, M. Samim, U. J. Krull, Fluorescence anisotropy: from single molecules to live cells. *Analyst* **135**, 452–459 (2010).

361. B. Bowen, N. Woodbury, Single-molecule Fluorescence Lifetime and Anisotropy Measurements of the Red Fluorescent Protein, DsRed, in Solution. *Photochem. Photobiol.* **77**, 362–369 (2003).

362. D. V O'Connor, W. R. Ware, J. C. Andre, Deconvolution of fluorescence decay curves. A critical comparison of techniques. *J. Phys. Chem.* **83**, 1333–1343 (1979).

363. A. Periasamy, N. Mazumder, Y. Sun, K. G. Christopher, R. N. Day, "FRET microscopy: basics, issues and advantages of FLIM-FRET imaging" in *Advanced Time-Correlated Single Photon Counting Applications*, (Springer, 2015), pp. 249–276.

364. I. V Gopich, A. Szabo, Theory of the energy transfer efficiency and fluorescence lifetime distribution in single-molecule FRET. *Proc. Natl. Acad. Sci.* **109**, 7747–7752 (2012).

365. B. Sarkar, K. Ishii, T. Tahara, Microsecond conformational dynamics of biopolymers revealed by dynamic-quenching two-dimensional fluorescence lifetime correlation spectroscopy with single dye labeling. *J. Phys. Chem. Lett.* **10**, 5536–5541 (2019).

366. L. K. Fraiji, D. M. Hayes, T. C. Werner, Static and dynamic fluorescence quenching experiments for the physical chemistry laboratory. *J. Chem. Educ.* **69**, 424 (1992).

367. M. Wahl, *et al.*, Integrated multichannel photon timing instrument with very short dead time and high throughput. *Rev. Sci. Instrum.* **84**, 43102 (2013).

368. J. Kalisz, Review of methods for time interval measurements with picosecond resolution. *Metrologia* **41**, 17 (2003).

369. X. F. Wang, T. Uchida, D. M. Coleman, S. Minami, A two-dimensional fluorescence lifetime imaging system using a gated image intensifier. *Appl. Spectrosc.* **45**, 360–366 (1991).

370. P. Kapusta, M. Wahl, R. Erdmann, Advanced photon counting. *Springer Ser. Fluoresc.* **15** (2015).

371. N.-T. Chen, *et al.*, Probing the dynamics of doxorubicin-DNA intercalation during the initial activation of apoptosis by fluorescence lifetime imaging microscopy (FLIM) (2012).

372. A. C. Sparavigna, Poissonian Distributions in Physics: Counting Electrons and Photons (2021).

373. Q. Zhao, I. T. Young, J. G. S. de Jong, Photon budget analysis for fluorescence lifetime imaging microscopy. *J. Biomed. Opt.* **16**, 86007 (2011).

374. L. Ritsma, B. Ponsioen, J. van Rheenen, Intravital imaging of cell signaling in mice. *IntraVital* **1**, 2–10 (2012).

375. I. Georgakoudi, K. P. Quinn, Optical imaging using endogenous contrast to assess metabolic state. *Annu. Rev. Biomed. Eng.* **14**, 351–367 (2012).

376. Y. H. Sun, *et al.*, Fluorescence lifetime imaging microscopy for brain tumor image-guided surgery. *J. Biomed. Opt.* **15**, 56022 (2010).

377. C. Stringari, *et al.*, In vivo single-cell detection of metabolic oscillations in stem cells. *Cell Rep.* **10**, 1–7 (2015).

378. K. Suhling, *et al.*, Fluorescence lifetime imaging for viscosity and diffusion measurements in *Multiphoton Microscopy in the Biomedical Sciences XIX*, (International Society for Optics and Photonics, p. 1088210 (2019)

379. S. Ogikubo, *et al.*, Intracellular pH sensing using autofluorescence lifetime microscopy. *J. Phys. Chem. B* **115**, 10385–10390 (2011).

380. K. Okabe, *et al.*, Intracellular temperature mapping with a fluorescent polymeric thermometer and fluorescence lifetime imaging microscopy. *Nat. Commun.* **3**, 1–9 (2012).

381. L. Loura, M. J. Prieto, FRET in membrane biophysics: An overview. *Front. Physiol.* **2**, 82 (2011).

382. B. T. Bajar, E. S. Wang, S. Zhang, M. Z. Lin, J. Chu, A guide to fluorescent protein

FRET pairs. *Sensors* **16**, 1488 (2016).

383. D. W. Piston, G.-J. Kremers, Fluorescent protein FRET: the good, the bad and the ugly. *Trends Biochem. Sci.* **32**, 407–414 (2007).

384. A. Pliss, L. Zhao, T. Y. Ohulchanskyy, J. Qu, P. N. Prasad, Fluorescence lifetime of fluorescent proteins as an intracellular environment probe sensing the cell cycle progression. *Acs Chem. Biol.* **7**, 1385–1392 (2012).

385. J. B. Grimm, L. D. Lavis, Caveat fluorophore: an insiders' guide to small-molecule fluorescent labels. *Nat. Methods* **19**, 149–158 (2022).

386. Y. Chen, J. D. Müller, K. M. Berland, E. Gratton, Fluorescence fluctuation spectroscopy. *Methods* **19**, 234–252 (1999).

387. S. Nie, D. T. Chiu, R. N. Zare, Real-time detection of single molecules in solution by confocal fluorescence microscopy. *Anal. Chem.* **67**, 2849–2857 (1995).

388. J. Enderlein, I. Gregor, D. Patra, T. Dertinger, U. B. Kaupp, Performance of fluorescence correlation spectroscopy for measuring diffusion and concentration. *ChemPhysChem* **6**, 2324–2336 (2005).

389. A. Połatyńska, *et al.*, Temperature dependent FCS studies using a long working distance objective: viscosities of supercooled liquids and particle size. *J. Chem. Phys.* **146**, 84506 (2017).

390. E. Sherman, *et al.*, Using fluorescence correlation spectroscopy to study conformational changes in denatured proteins. *Biophys. J.* **94**, 4819–4827 (2008).

391. M. A. Medina, P. Schwille, Fluorescence correlation spectroscopy for the detection and study of single molecules in biology. *Bioessays* **24**, 758–764 (2002).

392. X. W. Ng, N. Bag, T. Wohland, Characterization of lipid and cell membrane organization by the fluorescence correlation spectroscopy diffusion law. *Chim. Int. J. Chem.* **69**, 112–119 (2015).

393. J.-P. Günther, M. Börsch, P. Fischer, Diffusion Measurements of Swimming Enzymes with Fluorescence Correlation Spectroscopy. *Acc. Chem. Res.* **51**, 1911–1920 (2018).

394. R. F. Wissner, A. Steinauer, S. L. Knox, A. D. Thompson, A. Schepartz, Fluorescence Correlation Spectroscopy Reveals Efficient Cytosolic Delivery of Protein Cargo by Cell-Permeant Miniature Proteins. *ACS Cent. Sci.* **4**, 1379–1393 (2018).

395. J. Chojnacki, *et al.*, Envelope glycoprotein mobility on HIV-1 particles depends on the virus maturation state. *Nat. Commun.* **8**, 1–10 (2017).

396. P. Schwille, F.-J. Meyer-Almes, R. Rigler, Dual-color fluorescence cross-correlation spectroscopy for multicomponent diffusional analysis in solution. *Biophys. J.* **72**, 1878–1886 (1997).

397. M. Eigen, R. Rigler, Sorting single molecules: application to diagnostics and evolutionary biotechnology. *Proc. Natl. Acad. Sci.* **91**, 5740–5747 (1994).

398. B. K. Müller, E. Zaychikov, C. Bräuchle, D. C. Lamb, Pulsed interleaved excitation. *Biophys. J.* **89**, 3508–3522 (2005).

399. P. Kapusta, R. Macháň, A. Benda, M. Hof, Fluorescence Lifetime Correlation Spectroscopy (FLCS): concepts, applications and outlook. *Int. J. Mol. Sci.* **13**, 12890–12910 (2012).

400. S. Padilla-Parra, N. Audugé, M. Coppey-Moisan, M. Tramier, Dual-color fluorescence lifetime correlation spectroscopy to quantify protein-protein interactions in live cell. *Microsc. Res. Tech.* **74**, 788–793 (2011).

401. K. Bacia, P. Schwille, Practical guidelines for dual-color fluorescence cross-correlation spectroscopy. *Nat. Protoc.* **2**, 2842–56 (2007).

402. X. Ma, Y. H. Foo, T. Wohland, Fluorescence cross-correlation spectroscopy (FCCS) in living cells. Fluorescence Spectroscopy and Microscopy (Eds. Y. Engelborghs, A. Visser) in *Methods in Molecular Biology* (Humana Press, Totowa, NJ), pp. 557–573 (2014).

403. C. Joo, H. Balci, Y. Ishitsuka, C. Buranachai, T. Ha, Advances in single-molecule fluorescence methods for molecular biology. *Annu. Rev. Biochem.* **77**, 51–76 (2008).

404. A. A. Deniz, *et al.*, Single-pair fluorescence resonance energy transfer on freely diffusing molecules: observation of Förster distance dependence and subpopulations. *Proc. Natl. Acad. Sci.* **96**, 3670–3675 (1999).

405. X. S. Xie, J. K. Trautman, Optical studies of single molecules at room temperature. *Annu. Rev. Phys. Chem.* **49**, 441–480 (1998).

406. A. Orte, R. Clarke, S. Balasubramanian, D. Klenerman, Determination of the fraction and stoichiometry of femtomolar levels of biomolecular complexes in an excess of monomer using single-molecule, two-color coincidence detection. *Anal. Chem.* **78**, 7707–7715 (2006).

407. D. R. Whiten, *et al.*, Single-Molecule Characterization of the Interactions between Extracellular Chaperones and Toxic α-Synuclein Oligomers. *Cell Rep.* **23**, 3492–3500 (2018).

408. X. Ren, *et al.*, Analysis of human telomerase activity and function by two color single molecule coincidence fluorescence spectroscopy. *J. Am. Chem. Soc.* **128**, 4992–5000 (2006).

409. A. Coullomb, *et al.*, QuanTI-FRET: a framework for quantitative FRET measurements in living cells. *Sci. Rep.* **10**, 6504 (2020).

410. S. Pelicci, A. Diaspro, L. Lanzanò, Chromatin nanoscale compaction in live cells visualized by acceptor-to-donor ratio corrected Förster resonance energy transfer between DNA dyes. *J. Biophotonics* **12**, e201900164 (2019).

411. C. Zhang, *et al.*, Automated E-FRET microscope for dynamical live-cell FRET imaging. *J. Microsc.* **274**, 45–54 (2019).

412. U. Kubitscheck, *et al.*, Fluorescence resonance energy transfer on single living cells. Application to binding of monovalent haptens to cell-bound immunoglobulin E. *Biophys. J.* **60**, 307–318 (1991).

413. H. Fukagawa, T. Shimizu, Y. Iwasaki, T. Yamamoto, Operational lifetimes of organic light-emitting diodes dominated by Förster resonance energy transfer. *Sci. Rep.* **7**, 1735 (2017).

414. L. Tosatto, *et al.*, Single-molecule FRET studies on α-synuclein oligomerization of Parkinson's disease genetically related mutants. *Sci. Rep.* **5**, 16696 (2015).

415. F. Dingfelder, S. Benke, D. Nettels, B. Schuler, Mapping an Equilibrium Folding Intermediate of the Cytolytic Pore Toxin ClyA with Single-Molecule FRET. *J. Phys. Chem. B* **122**, 11251–11261 (2018).

416. M. Axmann, J. B. Huppa, M. M. Davis, G. J. Schütz, Determination of interaction kinetics between the T cell receptor and peptide-loaded MHC class II via single-molecule diffusion measurements. *Biophys. J.* **103**, L17-9 (2012).

417. M. L. Dustin, D. Depoil, New insights into the T cell synapse from single molecule techniques. *Nat. Rev. Immunol.* **11**, 672–684 (2011).

418. J. Diao, *et al.*, A single-vesicle content mixing assay for SNARE-mediated

membrane fusion . *Nat. Commun.* **1**, 54 (2010).

419. J. Diao, Y. Ishitsuka, W.-R. Bae, Single-molecule FRET study of SNARE-mediated membrane fusion. *Biosci. Rep.* **31**, 457–463 (2011).

420. A. Brunger, K. Weninger, M. Bowen, S. Chu, Single-Molecule Studies of the Neuronal SNARE Fusion Machinery. *Annu. Rev. Biochem.* **78**, 903–928 (2009).

421. D. K. Sasmal, L. E. Pulido, S. Kasal, J. Huang, Single-molecule fluorescence resonance energy transfer in molecular biology. *Nanoscale* **8**, 19928–19944 (2016).

422. P. Arosio, T. P. J. Knowles, S. Linse, On the lag phase in amyloid fibril formation. *Phys. Chem. Chem. Phys.* **17**, 7606–7618 (2015).

423. S. I. A. Cohen, M. Vendruscolo, C. M. Dobson, T. P. J. Knowles, From macroscopic measurements to microscopic mechanisms of protein aggregation. *J. Mol. Biol.* **421**, 160–171 (2012).

424. P. Gracia, J. D. Camino, L. Volpicelli-daley, N. Cremades, Multiplicity of α -Synuclein Aggregated Species and Their Possible Roles in Disease. *Int. J. Mol. Sci.* (2020).

425. M. Schweighauser, *et al.*, Structures of α-synuclein filaments from multiple system atrophy. *Nature* **585**, 464–469 (2020).

426. T. Strohäker, *et al.*, Structural heterogeneity of α-synuclein fibrils amplified from patient brain extracts. *Nat. Commun.* **10**, 1–12 (2019).

427. M. Delenclos, *et al.*, Cellular models of α-synuclein toxicity and aggregation. *J. Neurochem.* **150**, 566–576 (2019).

428. J. Pronchik, X. He, J. T. Giurleo, D. S. Talaga, In vitro formation of amyloid from α-synuclein is dominated by reactions at hydrophobic interfaces. *J. Am. Chem. Soc.* **132**, 9797–9803 (2010).

429. C. Wang, N. Shah, G. Thakur, F. Zhou, R. M. Leblanc, α-Synuclein in α-helical conformation at air-water interface: Implication of conformation and orientation changes during its accumulation/aggregation. *Chem. Commun.* **46**, 6702–6704 (2010).

430. S. Campioni, *et al.*, The presence of an air-water interface affects formation and elongation of α-synuclein fibrils. *J. Am. Chem. Soc.* **136**, 2866–2875 (2014).

431. A. K. Buell, *et al.*, Solution conditions determine the relative importance of nucleation and growth processes in α-synuclein aggregation. *Proc. Natl. Acad. Sci. U. S. A.* **111**, 7671–7676 (2014).

432. C. Galvagnion, *et al.*, Lipid vesicles trigger α-synuclein aggregation by stimulating primary nucleation. *Nat. Chem. Biol.* **11**, 229–234 (2015).

433. C. Galvagnion, *et al.*, Chemical properties of lipids strongly affect the kinetics of the membrane-induced aggregation of α-synuclein. *Proc. Natl. Acad. Sci. U. S. A.* **113**, 7065–7070 (2016).

434. M. Necula, C. N. Chirita, J. Kuret, Rapid anionic micelle-mediated α-synuclein fibrillization in vitro. *J. Biol. Chem.* **278**, 46674–46680 (2003).

435. L. Giehm, C. L. P. Oliveira, G. Christiansen, J. S. Pedersen, D. E. Otzen, SDS-Induced Fibrillation of α-Synuclein: An Alternative Fibrillation Pathway. *J. Mol. Biol.* **401**, 115–133 (2010).

436. S. Ray, *et al.*, α-Synuclein aggregation nucleates through liquid-liquid phase separation. *Nat. Chem.* **12**, 705–716 (2020).

437. M. Sunde, *et al.*, Common core structure of amyloid fibrils by synchrotron X-ray diffraction. *J. Mol. Biol.* **273**, 729–739 (1997).

438. S. Mukherjee, P. Chowdhury, F. Gai, Infrared study of the effect of hydration on the amide i band and aggregation properties of helical peptides. *J. Phys. Chem. B* **111**, 4596–4602 (2007).

439. K. Griebenow, A. M. Klibanov, Lyophilization-induced reversible changes in the secondary structure of proteins. *Proc. Natl. Acad. Sci.* **92**, 10969–10976 (1995).

440. E. J. Castillo, J. L. Koenig, J. M. Anderson, J. Lo, Protein adsorption on hydrogels. II. Reversible and irreversible interactions between lysozyme and soft contact lens surfaces. *Biomaterials* **6**, 338–345 (1985).

441. C. M. Baronio, A. Barth, Correction to "The Amide I Spectrum of Proteins-Optimization of Transition Dipole Coupling Parameters Using Density Functional Theory Calculations". *J. Phys. Chem. B* **124**, 2730 (2020).

442. J. L. Arrondo, A. Muga, J. Castresana, F. M. Goñi, Quantitative studies of the structure of proteins in solution by Fourier-transform infrared spectroscopy. *Prog. Biophys. Mol. Biol.* **59**, 23–56 (1993).

443. S. Thirunavukkuarasu, E. A. Jares-Erijman, T. M. Jovin, Multiparametric Fluorescence Detection of Early Stages in the Amyloid Protein Aggregation of Pyrene-labeled α-Synuclein. *J. Mol. Biol.* **378**, 1064–1073 (2008).

444. G. Zandomeneghi, M. R. H. Krebs, M. G. McCammon, M. Fändrich, FTIR reveals structural differences between native β-sheet proteins and amyloid fibrils. *Protein Sci.* **13**, 3314–3321 (2009).

445. Antonino Natalello and Silvia M. Doglia, *Insoluble Proteins* in Methods in Molecular Biology (Ed. E. García-Fruitós), Springer (New York, NY) **1258**, 347-369 (2015).

446. L. A. Munishkina, C. Phelan, V. N. Uversky, A. L. Fink, Conformational behavior and aggregation of α-synuclein in organic solvents: Modeling the effects of membranes. *Biochemistry* **42**, 2720–2730 (2003).

447. V. L. Anderson, W. W. Webb, A desolvation model for trifluoroethanol-induced aggregation of enhanced green fluorescent protein. *Biophys. J.* **102**, 897–906 (2012).

448. A. Barth, C. Zscherp, What vibrations tell us about proteins. *Q. Rev. Biophys.* **35**, 369–430 (2002).

449. W. Dzwolak, R. Ravindra, C. Nicolini, R. Jansen, R. Winter, The diastereomeric assembly of polylysine is the low-volume pathway for preferential formation of beta-sheet aggregates. *J. Am. Chem. Soc.* **126**, 3762–3768 (2004).

450. A. K. Buell, Stability matters, too – the thermodynamics of amyloid fibril formation. *Chem. Sci.* Advance article (2022).

451. A. J. Baldwin, *et al.*, Metastability of native proteins and the phenomenon of amyloid formation. *J. Am. Chem. Soc.* **133**, 14160–14163 (2011).

452. H. A. Lashuel, C. R. Overk, A. Oueslati, E. Masliah, The many faces of α-synuclein: from structure and toxicity to therapeutic target. *Nat. Rev. Neurosci.* **14**, 38–48 (2013).

453. D. Ami, P. Mereghetti, A. Natalello, Contribution of Infrared Spectroscopy to the Understanding of Amyloid Protein Aggregation in Complex Systems. *Front. Mol. Biosci.* **9**, 822852 (2022).

454. Y. Lin, Y. Fichou, Z. Zeng, N. Y. Hu, S. Han, Electrostatically Driven Complex Coacervation and Amyloid Aggregation of Tau Are Independent Processes with Overlapping Conditions. *ACS Chem. Neurosci.* **11**, 615–627 (2020).

455. M. C. Hardenberg, *et al.*, Observation of an α-synuclein liquid droplet state and

its maturation into Lewy body-like assemblies. *J. Mol. Cell Biol.* **13**(4), 282-294 (2021).

456. P. J. Flory, Thermodynamics of High Polymer Solutions. *J. Chem. Phys.* **10**, 51–61 (1942).

457. B. Y. Zaslavsky, V. N. Uversky, In Aqua Veritas: The Indispensable yet Mostly Ignored Role of Water in Phase Separation and Membrane-less Organelles. *Biochemistry* **57**, 2437–2451 (2018).

458. B. Y. Zaslavsky, L. A. Ferreira, A. L. Darling, V. N. Uversky, The solvent side of proteinaceous membrane-less organelles in light of aqueous two-phase systems. *Int. J. Biol. Macromol.* **117**, 1224–1251 (2018).

459. S. E. Reichheld, L. D. Muiznieks, F. W. Keeley, S. Sharpe, Direct observation of structure and dynamics during phase separation of an elastomeric protein. *Proc. Natl. Acad. Sci. U. S. A.* **114**, E4408–E4415 (2017).

460. J. D. Camino, P. Gracia, N. Cremades, The role of water in the primary nucleation of protein amyloid aggregation. *Biophys. Chem.* **269**, 106520 (2021).

461. I. M. van der Wateren, T. P. J. Knowles, A. K. Buell, C. M. Dobson, C. Galvagnion, C-terminal truncation of α-synuclein promotes amyloid fibril amplification at physiological pH. *Chem. Sci.* **9**, 5506–5516 (2018).

462. W. Hoyer, *et al.*, Dependence of α-synuclein aggregate morphology on solution conditions. *J. Mol. Biol.* **322**, 383–393 (2002).

463. L. Nielsen, *et al.*, Effect of environmental factors on the kinetics of insulin fibril formation: Elucidation of the molecular mechanism. *Biochemistry* **40**, 6036–6046 (2001).

464. E. J. King, The colorimetric determination of phosphorus. *Biochem. J.* **26**, 292–297 (1932).

465. G. K. Bains, S. H. Kim, E. J. Sorin, V. Narayanaswami, The extent of pyrene excimer fluorescence emission is a reflector of distance and flexibility: analysis of the segment linking the LDL receptor-binding and tetramerization domains of apolipoprotein E3. *Biochemistry* **51**, 6207–6219 (2012).

466. M. Nishihara, *et al.*, Arginine magic with new counterions up the sleeve. *Org. Biomol. Chem.* **3**, 1659 (2005).

467. S. F. Banani, H. O. Lee, A. A. Hyman, M. K. Rosen, Biomolecular condensates: organizers of cellular biochemistry. *Nat. Rev. Mol. Cell Biol.* **18**, 285–298 (2017).

468. S. Alberti, D. Dormann, Liquid–Liquid Phase Separation in Disease. *Annu. Rev. Genet.* **53**, 171–194 (2019).

469. A. L. Darling, Y. Liu, C. J. Oldfield, V. N. Uversky, Intrinsically Disordered Proteome of Human Membrane-Less Organelles. *Proteomics* **18**, 1700193 (2018).

470. H.-X. Zhou, V. Nguemaha, K. Mazarakos, S. Qin, Why Do Disordered and Structured Proteins Behave Differently in Phase Separation? *Trends Biochem. Sci.* **43**, 499–516 (2018).

471. J. R. Simon, N. J. Carroll, M. Rubinstein, A. Chilkoti, G. P. López, Programming molecular self-assembly of intrinsically disordered proteins containing sequences of low complexity. *Nat. Chem.* **9**, 509–515 (2017).

472. A. A. Bhopatkar, V. N. Uversky, V. Rangachari, Granulins modulate liquid–liquid phase separation and aggregation of the prion-like C-terminal domain of the neurodegeneration-associated protein TDP-43. *J. Biol. Chem.* **295**, 2506–2519 (2020).

473. S. Farina, F. Esposito, M. Battistoni, G. Biamonti, S. Francia, Post-Translational Modifications Modulate Proteinopathies of TDP-43, FUS and hnRNP-A/B in Amyotrophic Lateral Sclerosis. *Front. Mol. Biosci.* **8** (2021).

474. A. Arenas, *et al.*, Lysine acetylation regulates the RNA binding, subcellular localization and inclusion formation of FUS. *Hum. Mol. Genet.* **29**, 2684–2697 (2020).

475. P. P. Gopal, J. J. Nirschl, E. Klinman, E. L. F. Holzbaur, Amyotrophic lateral sclerosis-linked mutations increase the viscosity of liquid-like TDP-43 RNP granules in neurons. *Proc. Natl. Acad. Sci.* **114**, E2466–E2475 (2017).

476. D. Pakravan, G. Orlando, V. Bercier, L. Van Den Bosch, Role and therapeutic potential of liquid–liquid phase separation in amyotrophic lateral sclerosis. *J. Mol. Cell Biol.* **13**, 15–28 (2021).

477. B. S. Johnson, *et al.*, TDP-43 Is Intrinsically Aggregation-prone, and Amyotrophic Lateral Sclerosis-linked Mutations Accelerate Aggregation and Increase Toxicity. *J. Biol. Chem.* **284**, 20329–20339 (2009).

478. I. Grundke-Iqbal, *et al.*, Abnormal phosphorylation of the microtubule-associated protein tau (tau) in Alzheimer cytoskeletal pathology. *Proc. Natl. Acad. Sci.* **83**, 4913–4917 (1986).

479. L. Buée, T. Bussière, V. Buée-Scherrer, A. Delacourte, P. R. Hof, Tau protein isoforms, phosphorylation and role in neurodegenerative disorders. *Brain Res. Brain Res. Rev.* **33**, 95–130 (2000).

480. M. Nagaishi, H. Yokoo, Y. Nakazato, Tau-positive glial cytoplasmic granules in multiple system atrophy. *Neuropathology* **31**, 299–305 (2011).

481. L. Pan, L. Meng, M. He, Z. Zhang, Tau in the Pathophysiology of Parkinson's Disease. *J. Mol. Neurosci.* **71**, 2179–2191 (2021).

482. S. Boyko, X. Qi, T.-H. Chen, K. Surewicz, W. K. Surewicz, Liquid–liquid phase separation of tau protein: The crucial role of electrostatic interactions. *J. Biol. Chem.* **294**, 11054–11059 (2019).

483. Y.-H. Lin, J. P. Brady, J. D. Forman-Kay, H. S. Chan, Charge pattern matching as a 'fuzzy' mode of molecular recognition for the functional phase separations of intrinsically disordered proteins. *New J. Phys.* **19**, 115003 (2017).

484. Y. Lin, *et al.*, Liquid-Liquid Phase Separation of Tau Driven by Hydrophobic Interaction Facilitates Fibrillization of Tau. *J. Mol. Biol.* **433**, 166731 (2021).

485. A. Aguzzi, M. Altmeyer, Phase Separation: Linking Cellular Compartmentalization to Disease. *Trends Cell Biol.* **26**, 547–558 (2016).

486. K. Arima, *et al.*, Cellular co-localization of phosphorylated tau- and NACP/α-synuclein-epitopes in Lewy bodies in sporadic Parkinson's disease and in dementia with Lewy bodies. *Brain Res.* **843**, 53–61 (1999).

487. T. Ishizawa, P. Mattila, P. Davies, D. Wang, D. W. Dickson, Colocalization of Tau and A-Synuclein Epitopes in Lewy Bodies. *J. Neuropathol. Exp. Neurol.* **62**, 389–397 (2003).

488. L. K. Clinton, M. Blurton-Jones, K. Myczek, J. Q. Trojanowski, F. M. LaFerla, Synergistic Interactions between A , Tau, and -Synuclein: Acceleration of Neuropathology and Cognitive Decline. *J. Neurosci.* **30**, 7281–7289 (2010).

489. B. Roy, G. R. Jackson, Interactions between Tau and α-synuclein augment neurotoxicity in a Drosophila model of Parkinson's disease. *Hum. Mol. Genet.* **23**, 3008–3023 (2014).

490. J. L. Guo, *et al.*, Distinct α-Synuclein Strains Differentially Promote Tau Inclusions in Neurons. *Cell* **154**, 103–117 (2013).

491. B. I. Giasson, *et al.*, Initiation and Synergistic Fibrillization of Tau and A-Synuclein. *Science* **300**, 636–640 (2003).

492. U. Sengupta, *et al.*, Pathological Interface Between Oligomeric A-Synuclein and Tau in Synucleinopathies. *Biol. Psychiatry* **78**, 672–683 (2015).

493. A. Siegert, *et al.*, Interplay between tau and α-synuclein liquid–liquid phase separation. *Protein Sci.* **30**, 1326–1336 (2021).

494. V. I. Stsiapura, *et al.*, Thioflavin T as a molecular rotor: fluorescent properties of thioflavin T in solvents with different viscosity. *J. Phys. Chem. B* **112**, 15893–15902 (2008).

495. N. Amdursky, Y. Erez, D. Huppert, Molecular rotors: what lies behind the high sensitivity of the thioflavin-T fluorescent marker. *Acc. Chem. Res.* **45**, 1548–1557 (2012).

496. A. F. Drake, G. Siligardi, W. A. Gibbons, Reassessment of the electronic circular dichroism criteria for random coil conformations of poly(l-lysine) and the implications for protein folding and denaturation studies. *Biophys. Chem.* **31**, 143–146 (1988).

497. S. Park, *et al.*, Dehydration entropy drives liquid-liquid phase separation by molecular crowding. *Commun. Chem.* **3**, 83 (2020).

498. A. A. M. André, E. Spruijt, Liquid–Liquid Phase Separation in Crowded Environments. *Int. J. Mol. Sci.* **21**, 5908 (2020).

499. M. Kang, C. A. Day, A. K. Kenworthy, E. DiBenedetto, Simplified Equation to Extract Diffusion Coefficients from Confocal FRAP Data. *Traffic* **13**, 1589–1600 (2012).

500. M. Drescher, EPR in protein science : intrinsically disordered proteins. *Top. Curr. Chem.* **321**, 91–119 (2012).

501. N. Le Breton, *et al.*, Exploring intrinsically disordered proteins using site-directed spin labeling electron paramagnetic resonance spectroscopy . *Front. Mol. Biosci.* **2** (2015).

502. I. García-Rubio, EPR of site-directed spin-labeled proteins: A powerful tool to study structural flexibility. *Arch. Biochem. Biophys.* **684**, 108323 (2020).

503. W. Chen, *et al.*, Fluorescence Self-Quenching from Reporter Dyes Informs on the Structural Properties of Amyloid Clusters Formed in Vitro and in Cells. *Nano Lett.* **17**, 143–149 (2017).

504. G. S. Kaminski Schierle, *et al.*, A FRET sensor for non-invasive imaging of amyloid formation in vivo. *Chemphyschem* **12**, 673–680 (2011).

505. K.-J. Choi, *et al.*, A Chemical Chaperone Decouples TDP-43 Disordered Domain Phase Separation from Fibrillation. *Biochemistry* **57**, 6822–6826 (2018).

506. J. D. Camino, *et al.*, The extent of protein hydration dictates the preference for heterogeneous or homogeneous nucleation generating either parallel or antiparallel β-sheet α-synuclein aggregates. *Chem. Sci.*, 11902–11914 (2020).

507. M. Grabenauer, *et al.*, Spermine Binding to Parkinson's Protein α-Synuclein and Its Disease-Related A30P and A53T Mutants. *J. Phys. Chem. B* **112**, 11147–11154 (2008).

508. C. W. Bertoncini, *et al.*, Release of long-range tertiary interactions potentiates aggregation of natively unstructured α-synuclein. *Proc. Natl. Acad. Sci. U. S. A.*

102, 1430–1435 (2005).

509.   N. M. Lewandowski, *et al.*, Polyamine pathway contributes to the pathogenesis of Parkinson disease. *Proc. Natl. Acad. Sci.* **107**, 16970–16975 (2010).

510.   J. A. Riback, *et al.*, Stress-Triggered Phase Separation Is an Adaptive, Evolutionarily Tuned Response. *Cell* **168**, 1028-1040.e19 (2017).

511.   V. Verdile, E. De Paola, M. P. Paronetto, Aberrant Phase Transitions: Side Effects and Novel Therapeutic Strategies in Human Disease. *Front. Genet.* **10** (2019).

512.   B. E. Ackermann, G. T. Debelouchina, Heterochromatin Protein HP1α Gelation Dynamics Revealed by Solid-State NMR Spectroscopy. *Angew. Chemie Int. Ed.* **58**, 6300–6305 (2019).

513.   N. M. Kanaan, C. Hamel, T. Grabinski, B. Combs, Liquid-liquid phase separation induces pathogenic tau conformations in vitro. *Nat. Commun.* **11**, 2809 (2020).

514.   S. Biswas, B. Mukherjee, B. Chakrabarti, Thermodynamics of droplets undergoing liquid-liquid phase separation, *arXiv* preprint arXiv:2104.00651 (2021).

515.   S. Ranganathan, E. I. Shakhnovich, Dynamic metastable long-living droplets formed by sticker-spacer proteins. *Elife* **9**, e56159 (2020).

516.   A. Khedr, A. Striolo, Quantification of Ostwald Ripening in Emulsions via Coarse-Grained Simulations. *J. Chem. Theory Comput.* **15**, 5058–5068 (2019).

517.   W. E., K. Pope, X. Duan, Droplet Coalescence in Liquid/Liquid Separation. *J. Fluids Eng.* **142** (2020).

518.   A. W. Folkmann, A. Putnam, C. F. Lee, G. Seydoux, Regulation of biomolecular condensates by interfacial protein clusters. *Science* **373**, 1218–1224 (2021).

519.   J. P. Quinn, N. J. Corbett, K. A. B. Kellett, N. M. Hooper, Tau Proteolysis in the Pathogenesis of Tauopathies: Neurotoxic Fragments and Novel Biomarkers. *J. Alzheimers. Dis.* **63**, 13–33 (2018).

520.   A. M. Küffner, *et al.*, Sequestration within biomolecular condensates inhibits Aβ-42 amyloid formation. *Chem. Sci.* **12**, 4373–4382 (2021).

521.   V. G. KrishnaKumar, S. Gupta, Simplified method to obtain enhanced expression of tau protein from *E. coli* and one-step purification by direct boiling. *Prep. Biochem. Biotechnol.* **47**, 530–538 (2017).

522.   S. Stoll, A. Schweiger, EasySpin, a comprehensive software package for spectral simulation and analysis in EPR. *J. Magn. Reson.* **178**, 42–55 (2006).

523.   M. Kjaergaard, F. M. Poulsen, Sequence correction of random coil chemical shifts: correlation between neighbor correction factors and changes in the Ramachandran distribution. *J. Biomol. NMR* **50**, 157–165 (2011).

524.   L. Wang, Bharti, R. Kumar, P. F. Pavlov, B. Winblad, Small molecule therapeutics for tauopathy in Alzheimer's disease: Walking on the path of most resistance. *Eur. J. Med. Chem.* **209**, 112915 (2021).

525.   M. R. Duff, Jr., J. Grubbs, E. E. Howell, Isothermal Titration Calorimetry for Measuring Macromolecule-Ligand Affinity. *J. Vis. Exp.*, 2–5 (2011).

526.   J. Ries, Z. Petrášek, A. J. García-Sáez, P. Schwille, A comprehensive framework for fluorescence cross-correlation spectroscopy. *New J. Phys.* **12**, 113009 (2010).

527.   A. N. Kapanidis, *et al.*, Fluorescence-aided molecule sorting: Analysis of structure and interactions by alternating-laser excitation of single molecules. *Proc. Natl. Acad. Sci. U. S. A.* **101**, 8936–8941 (2004).

528.   G. Fusco, *et al.*, Structural basis of membrane disruption and cellular toxicity by α-synuclein oligomers. *Science* **000**, 1–4 (2017).

529. F. van Diggelen, *et al.*, Two conformationally distinct α-synuclein oligomers share common epitopes and the ability to impair long-term potentiation. *PLoS One* **14**, e0213663 (2019).

530. J. M. Froula, *et al.*, Defining α-synuclein species responsible for Parkinson's disease phenotypes in mice. *J. Biol. Chem.* **294**, 10392–10406 (2019).

531. B. Winner, *et al.*, In vivo demonstration that -synuclein oligomers are toxic. *Proc. Natl. Acad. Sci.* **108**, 4194–4199 (2011).

532. J. M. Froula, *et al.*, Correction: Defining α-synuclein species responsible for Parkinson's disease phenotypes in mice. *J. Biol. Chem.* **295**, 1142 (2020).

533. S. W. Chen, N. Cremades, Preparation of α-Synuclein Amyloid Assemblies for Toxicity Experiments. Amyloid Proteins in *Methods in Molecular Biology* (Eds E. Sigurdsson, M. Calero, M. Gasset), Humana Press (New York, NY) **1779**, 45-60 (2018) .

534. U. Meseth, T. Wohland, R. Rigler, H. Vogel, Resolution of Fluorescence Correlation Measurements. *Biophys. J.* **76**, 1619–1631 (1999).

535. M. D. Tuttle, *et al.*, Solid-state NMR structure of a pathogenic fibril of full-length human α-synuclein. *Nat. Struct. Mol. Biol.* **23**, 409–415 (2016).

536. N. Cremades, S. W. Chen, C. M. Dobson, Structural Characteristics of α-Synuclein Oligomers. *Int. Rev. Cell Mol. Biol.* **329**, 79–143 (2017).

537. B. Bolognesi, *et al.*, ANS binding reveals common features of cytotoxic amyloid species. *ACS Chem. Biol.* **5**, 735–740 (2010).

538. S. W. Chen, *et al.*, Structural characterization of toxic oligomers that are kinetically trapped during α-synuclein fibril formation. *Proc. Natl. Acad. Sci.* **112**, E1994–E2003 (2015).

539. A. A. Desai, *et al.*, Rational affinity maturation of anti-amyloid antibodies with high conformational and sequence specificity. *J. Biol. Chem.* **296**, 100508 (2021).

540. R. Ştefănescu, L. Lupu, M. Manea, R. E. Iacob, M. Przybylski, Molecular characterization of the β-amyloid(4-10) epitope of plaque specific Aβ antibodies by affinity-mass spectrometry using alanine site mutation. *J. Pept. Sci. an Off. Publ. Eur. Pept. Soc.* **24** (2018).

541. J. M. Perchiacca, A. R. A. Ladiwala, M. Bhattacharya, P. M. Tessier, Structure-based design of conformation- and sequence-specific antibodies against amyloid β. *Proc. Natl. Acad. Sci. U. S. A.* **109**, 84–89 (2012).

542. L. Olejko, I. Bald, FRET efficiency and antenna effect in multi-color DNA origami-based light harvesting systems. *RSC Adv.* **7**, 23924–23934 (2017).

543. K. Walczewska-Szewc, P. Bojarski, S. d'Auria, Extending the range of FRET--the Monte Carlo study of the antenna effect. *J. Mol. Model.* **19**, 4195–4201 (2013).

544. A. Lionnet, *et al.*, Does Parkinson's disease start in the gut? *Acta Neuropathol.* **135**, 1–12 (2018).

545. H. Braak, U. Rüb, W. P. Gai, K. Del Tredici, Idiopathic Parkinson's disease: possible routes by which vulnerable neuronal types may be subject to neuroinvasion by an unknown pathogen. *J. Neural Transm.* **110**, 517–536 (2003).

546. P. Brundin, R. Melki, Prying into the Prion Hypothesis for Parkinson's Disease. *J. Neurosci. Off. J. Soc. Neurosci.* **37**, 9808–9818 (2017).

547. S. Peña-Díaz, *et al.*, ZPD-2, a Small Compound That Inhibits α-Synuclein Amyloid Aggregation and Its Seeded Polymerization. *Front. Mol. Neurosci.* **12**, 306 (2019).

548. J. Pujols, *et al.*, High-throughput screening methodology to identify α-synuclein

aggregation inhibitors. *Int. J. Mol. Sci.* **18** (2017).

549. S. T. Kumar, S. Donzelli, A. Chiki, M. M. K. Syed, H. A. Lashuel, A simple, versatile and robust centrifugation-based filtration protocol for the isolation and quantification of α-synuclein monomers, oligomers and fibrils: Towards improving experimental reproducibility in α-synuclein research. *J. Neurochem.* **153**, 103–119 (2020).

550. V. Muñoz, L. Serrano, Elucidating the folding problem of helical peptides using empirical parameters. *Nat. Struct. Biol.* **1**, 399–409 (1994).

551. J. Schymkowitz, *et al.*, The FoldX web server: an online force field. *Nucleic Acids Res.* **33**, W382-8 (2005).

552. D. Eisenberg, R. M. Weiss, T. C. Terwilliger, The hydrophobic moment detects periodicity in protein hydrophobicity. *Proc. Natl. Acad. Sci.* **81**, 140–144 (1984).

553. I. C. Brás, M. Xylaki, T. F. Outeiro, Mechanisms of α-synuclein toxicity: An update and outlook. *Prog. Brain Res.* **252**, 91–129 (2020).

554. M. G. Erkkinen, M.-O. Kim, M. D. Geschwind, Clinical Neurology and Epidemiology of the Major Neurodegenerative Diseases. *Cold Spring Harb. Perspect. Biol.* **10** (2018).

555. G. M. Halliday, J. L. Holton, T. Revesz, D. W. Dickson, Neuropathology underlying clinical variability in patients with synucleinopathies. *Acta Neuropathol.* **122**, 187–204 (2011).

556. K. M. Danzer, *et al.*, Exosomal cell-to-cell transmission of α synuclein oligomers. 1–18 (2012).

557. P. Desplats, *et al.*, Inclusion formation and neuronal cell death through neuron-to-neuron transmission of α-synuclein. *Proc. Natl. Acad. Sci. U. S. A.* **106**, 13010–13015 (2009).

558. W. Peelaerts, *et al.*, α-Synuclein strains cause distinct synucleinopathies after local and systemic administration. *Nature* **522**, 340–344 (2015).

559. Y. J. Lee, R. Savtchenko, V. G. Ostapchenko, N. Makarava, I. V Baskakov, Molecular structure of amyloid fibrils controls the relationship between fibrillar size and toxicity. *PLoS One* **6**, e20244 (2011).

560. A. Scior, *et al.*, Complete suppression of Htt fibrilization and disaggregation of Htt fibrils by a trimeric chaperone complex. *EMBO J.* **37**, 282–299 (2018).

561. E. Nachman, *et al.*, Disassembly of Tau fibrils by the human Hsp70 disaggregation machinery generates small seeding-competent species. *JBC* (2020) https:/doi.org/10.1101/2019.12.16.876888.

562. A. F. Budia, Disaggregation of aS by dequenching.

563. N. K. Polinski, *et al.*, Best practices for generating and using α-synuclein pre-formed fibrils to model Parkinson's disease in rodents. *J. Parkinsons. Dis.* **8**, 303–322 (2018).

564. R. Cascella, *et al.*, The release of toxic oligomers from α-synuclein fibrils induces dysfunction in neuronal cells. *Nat. Commun.* **12**, 1814 (2021).

565. G. Musteikytė, *et al.*, Interactions of α-synuclein oligomers with lipid membranes. *Biochim. Biophys. acta. Biomembr.* **1863**, 183536 (2021).

566. D. J. Lichlyter, S. A. Grant, O. Soykan, Development of a novel FRET immunosensor technique. *Biosens. Bioelectron.* **19**, 219–226 (2003).

567. M. Drescher, *et al.*, Spin-label EPR on α-synuclein reveals differences in the membrane binding affinity of the two antiparallel helices. *Chembiochem* **9**, 2411–

2416 (2008).

568. A. Franco, *et al.*, All-or-none amyloid disassembly via chaperone-triggered fibril unzipping favors clearance of α-synuclein toxic species. *Proc. Natl. Acad. Sci. U. S. A.* **118** (2021).

569. A. Franco, *et al.*, Unzipping the secrets of amyloid disassembly by the human disaggregase. *Cells* **10**, 1–16 (2021).

570. A. Franco, *et al.*, Truncation-Driven Lateral Association of α-Synuclein Hinders Amyloid Clearance by the Hsp70-Based Disaggregase. *Int. J. Mol. Sci.* **22** (2021).

571. S. Fujiwara, *et al.*, Dynamic Properties of Human α-Synuclein Related to Propensity to Amyloid Fibril Formation. *J. Mol. Biol.* **431**, 3229–3245 (2019).

572. J. Tittelmeier, E. Nachman, C. Nussbaum-Krammer, Molecular Chaperones: A Double-Edged Sword in Neurodegenerative Diseases. *Front. Aging Neurosci.* **12**, 581374 (2020).

573. A. K. Buell, *et al.*, Probing small molecule binding to amyloid fibrils. *Phys. Chem. Chem. Phys.* **13**, 20044–20052 (2011).

574. P. Alam, L. Bousset, R. Melki, D. E. Otzen, α-synuclein oligomers and fibrils: a spectrum of species, a spectrum of toxicities. *J. Neurochem.* **150**, 522–534 (2019).

575. J. A. Fernández-Higuero, A. Muga, J. M. G. Vilar, Extraction and Refolding Determinants of Chaperone-Driven Aggregated Protein Reactivation. *J. Mol. Biol.* **432**, 3239–3250 (2020).

576. D. L. Floyd, S. C. Harrison, A. M. van Oijen, Analysis of kinetic intermediates in single-particle dwell-time distributions. *Biophys. J.* **99**, 360–366 (2010).

577. J. M. G. Vilar, C. C. Guet, S. Leibler, Modeling network dynamics: the lac operon, a case study. *J. Cell Biol.* **161**, 471–476 (2003).

578. B. Dennis, G. P. Patil, The gamma distribution and weighted multimodal gamma distributions as models of population abundance. *Math. Biosci.* **68**, 187–212 (1984).

579. P. Gracia and N. Cremades (2021), Single-Particle Analysis of the Interaction between Small Molecules and Protein Aggregated Species by Dual-Color Time-Resolved Fluorescence Spectroscopy. *Methods Mol. Biol.*, in press (2021).